DOE/BC/14852-15
Distribution Category UC-122

Scale-up of Miscible Flood Processes for Heterogeneous Reservoirs

Final Report

By
Franklin M. Orr, Jr.

April 1996

Work Performed Under Contract No. DE-FG22-92BC14852

Prepared for
U.S. Department of Energy
Assistant Secretary for Fossil Energy

Jerry Casteel, Project Manager
Bartlesville Project Office
P.O. Box 1398
Bartlesville, OK 74005

Prepared by
Stanford University
65 Green Earth Sciences Building
Stanford, CA 94305-2220

MASTER

DISTRIBUTION OF THIS DOCUMENT IS UNLIMITED

1. Introduction

When gas is injected into an oil reservoir at high pressure, a richly complex set of physical interactions begins. Components transfer between oil and gas phases, viscous fingers form, geological heterogeneities control flow pathways in wonderfully complicated ways, and capillary and gravity forces modify flows driven by pressure gradients between injection and production wells. In this report, we examine the scaling of the interactions of those mechanisms. The goal of the work is to provide a base of physical understanding upon which can be built the design of gas injection processes for heterogeneous reservoirs.

In Chapter 2 we consider how multicontact miscibility develops in multicomponent systems. Standard theory for development of miscibility is based on analysis of three-component systems, and minimum miscibility pressures (MMP's) or minimum enrichments for miscibility (MME's) are often calculated by mixing cell methods that determine when either the injection gas or displaced oil lies on a critical tie line. Those methods fail for systems with more than three components if development of miscibility is controlled by tie lines other than the injection or initial tie lines. That situation arises for condensing/vaporizing gas drives, which occur in many CO_2 floods and in the displacement underway at Prudhoe Bay, for example. In Chapter 2 we extend and apply the theory to several systems. We report an analysis of the behavior of nitrogen displacements that is consistent with results reported by other investigators concerning the effect of changes in oil or injection gas composition on MMP. In Section 2.2 we apply the theory to a CO_2 displacement of a synthetic oil containing ten components [131].That section shows how to use the MOC approach to understand displacement behavior of crude oils, which can contain many more than three or four components. Sections 2.3 and 2.4 examine the mathematical structure of the MOC theory for systems with equilibrium K-values that are independent of composition. Because nearly all the important features of the mathematical structure carry over to systems with variable K-values, the constant K-values analysis provides the basis for understanding the behavior of crude oil systems as well. Finally, in Section 2.5 we describe a new technique for direct calculation of the MMP for such situations. The new method works well for condensing/vaporizing gas drives, and it is significantly more efficient than other approaches in widespread use.

In Chapter 3, we turn to the question of viscous instability. It has long been known that when viscous oil is displaced by a less viscous gas, the flow is hydrodynamically unstable, and the less viscous fluid "fingers" through the oil. In Chapter 3, we make use of a particle-tracking technique to study the interplay of fingering, gravity segregation, and reservoir heterogeneity. The results presented show clearly that two-dimensional flow calculations do not necessarily reproduce what happens in three-dimensional flows when viscous and gravity forces are of comparable importance. Gravity forces turn out to be more important in three-dimensional flows than in two-dimensional cross-sections. Additional results reinforce our previous conclusion that reservoir heterogeneity, the spatial distribution of permeability, has a significant effect on flow patterns — fingers adapt happily to preferential flow paths. The transition from gravity-dominated flow at low flow rate to viscous- or permeability-dominated flow at high flow rate is also strongly affected by heterogeneity. Finally, we examine approximations that can be used to try to account for viscous fingering in compositional gas injection processes.

In Chapter 4 we describe an efficient technique for calculating the performance of a gas injection process in a heterogeneous reservoir. The method is a version of a streamtube technique, in which the effects of heterogeneity in a two-dimensional porous medium are represented by flow through a series of streamtubes, while the effects of the displacement process, whether it is a miscible flood, a waterflood or a compositional displacement, are represented by a one-dimensional

the chromatographic separations that then can be used to design efficient oil recovery processes. In the context of describing the mechanisms of those processes, Eqs. 2.4 (or the equivalent molar conservation equations when volume change is included [52]) have been solved repeatedly for ternary systems by investigators of alcohol flooding, surfactant flooding and gas displacement processes, and the theory of three-component flows is largely complete. An extensive set of references to that literature is given by Johansen [96]. Investigations of four-component problems have been limited to gas/oil displacements. Four-component solutions were first reported by Monroe *et al.* [135], and the properties of those solutions and many others were subsequently explored in detail by Dindoruk [45] and Johns [103] (see also [105, 46, 148]). Four-component solutions were also reported by Bedrikovetsky [11] for displacement processes with constant K-values. All those investigations showed that a solution to a Riemann problem, which can be represented as a sequence of shocks and rarefactions that generate a path through the state space, Γ, must lie on surfaces of tie lines illustrated in Fig. 2.21. One surface is associated with the left state (injection composition) and the other with the the right state (initial composition). This section provides additional evidence that it is the geometry of tie lines in those surfaces that controls the structure of solutions.

On the mathematical side, much work has been devoted to questions of existence and uniqueness and to describing the wave structure of solutions. Investigations that have much in common with the problems considered here have been reported by Johansen and Winther [98, 99, 100].

In the analysis of polymer flooding [98, 99] and three-component, two-phase flow problems [100, 103], it has proved useful to rewrite the problem in terms of dependent variables that yield an eigenvalue problem for a triangular matrix. In that form, the analysis of wave structure is much more straightforward than it is for the eigenvalue problems associated with Eqs. 2.4. In this section we employ the same strategy: we ask under what circumstances can a problem with triangular structure be obtained by a suitable model representation. We then consider what types of phase behavior produce triangular structure and show that only a small set of phase behavior types is allowed. However, we show that the types that do produce triangular structure are consistent with simplifying assumptions commonly used to describe the behavior of surfactant and gas/oil systems. It is also important to note, however, that the models considered here are always hyperbolic, even if the structure is not triangular [187].

For triangular models, the solution path in Γ lies on a sequence of easily defined surfaces of tie lines, and the solution wave structure can be described in a straightforward manner. While the assumptions required to make the problem triangular are fairly restrictive, the properties of the resulting solutions provide considerable guidance about solutions to more general problems, and hence the structures described here are a useful step toward understanding of truly multicomponent flows by extending the techniques employed in the analysis of multicomponent polymer flows [99].

In the sections that follow, we state and prove a theorem about tie line geometry. We then show that expressions for eigenvalues and eigenvectors can be obtained easily for four-component conservation equations with global triangular structure, and we examine the wave structure of solutions. We show that triangular structures result when equilibrium K-values are independent of composition. We conclude with a discussion of other approximate phase behavior models that would also yield triangular structure.

2.3.1 Global Triangular Structure

It is convenient for analysis to write the conservation equations in terms of the properties of tie lines, which control solution structure and behavior. To do so, we represent the equation of a general tie line as

$$C_2 = \alpha(\xi,\eta)C_1 + \phi(\xi,\eta), \tag{2.10}$$

The initial and boundary conditions are specified as left (L) and right (R) states,

$$C_i(z,0) = \begin{cases} C_i^L, & z \le 0, \\ C_i^R, & z > 0. \end{cases} \tag{2.67}$$

2.4.2 Nontie-line Path Integration for a Ternary System

We choose S and x_1 as primary variables, which yields the following version of Eq. 2.64,

$$\frac{\partial}{\partial t}\begin{bmatrix} S \\ x_1 \end{bmatrix} + \begin{bmatrix} \frac{df}{dS} & a_3 \\ 0 & b_3 \end{bmatrix} \frac{\partial}{\partial z}\begin{bmatrix} S \\ x_1 \end{bmatrix} = \begin{bmatrix} 0 \\ 0 \end{bmatrix}, \tag{2.68}$$

where a_3 and b_3 are algebraic expressions involving the K-values,

$$a_3 = \frac{(K_2-K_1)(K_3-K_1)(f-s)}{x_1(K_2-K_1)(K_3-K_1) - [1+(K_1-1)s](K_2-1)(K_3-1)}, \tag{2.69}$$

and

$$b_3 = \frac{F_1+h}{C_1+h}, \tag{2.70}$$

where

$$h = -\frac{(K_1-K_2)(K_1-K_3)}{(K_2-1)(K_3-1)}x_1^2. \tag{2.71}$$

The ordinary differential equation describing the nontie-line path is found from the eigenvector that points in the direction of the nontie-line path,

$$\begin{aligned} \frac{dx_1}{dS} &= \frac{(1-f')}{(f-S)}x_1 \\ &- \frac{(K_2-1)(K_3-1)(1-f')[1+(K_1-1)S]}{(K_2-K_1)(K_3-K_1)(f-S)} \\ &- \frac{(K_1-1)(K_2-1)(K_3-1)}{(K_2-K_1)(K_3-K_1)}. \end{aligned} \tag{2.72}$$

Eq. 2.72 can be integrated to obtain an expression for the nontie-line path as a function of saturation.

$$\begin{aligned} x_1 &= \frac{(f_0-S_0)x_1^0}{f-S} + \frac{(K_2-1)(K_3-1)}{(K_2-K_1)(K_3-K_1)} \\ &- \frac{(K_2-1)(K_3-1)(f_0-S_0)}{(K_2-K_1)(K_3-K_1)(f-S)} \\ &+ \frac{(K_1-1)(K_2-1)(K_3-1)}{(K_2-K_1)(K_3-K_1)(f-S)}\Big[(Sf-S_0f_0) - 2\int_{S_0}^{S} f\,dS\Big]. \end{aligned} \tag{2.73}$$

Here (x_1^0, S_0) is some starting point for the integration.

The final form of the expression for the nontie-line path depends on the integral of the fractional flow expression in Eq. 2.73. The fractional flow function we use for the example that follows

$$f(S) = \frac{S^2}{S^2 + M(1-S-S_{or})^2}. \tag{2.74}$$

3. Viscous Fingering, Gravity Segregation and Reservoir Heterogeneity in Gas injection Processes

Viscous fingering, gravity segregation and reservoir heterogeneity have long been known to affect the performance of gas injection processes. This chapter we report results of an extended effort to understand the interplay of those factors. Section 3.1 presents a study of the interaction of viscous fingering, gravity segregation and reservoir heterogeneity in 2D and 3D media using particle tracking simulation technique. We show that 3D flow behavior differs substantially from the 3D flow behavior for displacements in which either gravity or viscous forces dominate. Reservoir heterogeneity can reduce the effect of gravity segregation, and hence the difference between 2D and 3D flow behavior. These results strengthen further our previous conclusion that reservoir permeability distribution often dominate flow behavior. In Section 3.2 we describe compositional simulations conducted to investigate the effects of phase behavior on the development of viscous fingering and gravity segregation in heterogeneous media. We show that slightly submiscible displacements can be more efficient than completely miscible ones, because mobility ratios are more favorable in the submiscible displacements.

3.1 Interactions of Viscous Fingering, Permeability Heterogeneity and Gravity Segregation in 2D and 3D Flow in Porous Media

H. A. Tchelepi and F. M. Orr, Jr.

Viscous fingering, gravity segregation, and reservoir heterogeneity have long been known to affect the performance of the collection of gas injection processes known as miscible floods [171]. Numerical simulations of viscous fingering and gravity segregation have been performed by some investigators to examine the transition from gravity-dominated flow, in which a single gravity tongue forms and early breakthrough of injected fluid occurs, to flow dominated by viscous fingering. Most calculations have been performed only for two-dimensional cross sections, however.

Only recently have investigations of 3D fingering begun. Withjack *et al.* [196] presented 3D computed tomography images from a series of unstable miscible displacement experiments in a 5-spot geometry such that buoyancy in the vertical plane was in competition with the viscous forces in the horizontal plane. They found that recovery correlations for 5-spot geometry based on 2D information overestimate the observed 3D recoveries from the experiments.

Zimmerman [209] simulated growth of viscous fingers in homogeneous porous media in the absence of gravity segregation under conditions of isotropic dispersion using a spectral technique. He found that transversely averaged concentration profiles were similar in 2D and 3D simulations. Christie *et al.* [34] investigated both fingering and gravity segregation in homogeneous media as well as those in which a distribution of shales was also present. In all their calculations, buoyancy forces were quite strong. They found that breakthrough occurred slightly earlier and recovery was slightly lower in 3D flow than in 2D flow. Christie *et al.* [34] did not investigate the transition from gravity-dominated to viscous-dominated flow.

Chang *et al.* [28] performed 2D and 3D simulations of laboratory displacement experiments and found that calculated recovery curves differed only slightly. Mohanty and Johnson [132] simulated corefloods performed in heterogeneous cores. They found that 2D simulations were not good

approximations for layered systems with only modest contrast in permeability between layers and found better agreement when 3D simulations were performed.

Because 3D simulations are significantly more expensive to perform than 2D simulations, it would be useful to know when 2D calculations can be used with confidence to predict performance of reservoir displacement processes. In this paper we report results of simulations that examine when 2D simulations reproduce the behavior of 3D flow and, more importantly, when they do not.

The simulations described here were performed with a particle-tracking technique described in detail by Araktingi and Orr [6], Tchelepi and Orr [180], and Tchelepi *et al.* [181]. Brock and Orr [24] showed that the simulator reproduces accurately the transition from flow controlled by viscous fingering in a 2D homogeneous porous medium to flow controlled by the permeability distribution in heterogeneous porous media. Araktingi and Orr [5] showed that the simulator accurately represents the effects of gravity in 2D flow as well. Thus, the simulator used has been tested extensively against experimental data where available and has been shown to model accurately the effects of heterogeneity, viscous instability, and gravity segregation. In the remainder of this paper, we examine a succession of unstable 2D and 3D displacements to determine when 3D flow differs substantially from 2D flow.

Simulations were performed for flow in a rectangular porous medium with width equal to the height. Unless otherwise stated, the aspect (length to height) ratio was set to L/H = 4. The 3D simulations were performed on 128 x 64 x 32 grids, with 64 particles taken to represent a unit concentration. For 2D simulations, 128 x 64 grids were used. Extensive grid refinement tests showed that no significant changes in results were observed for finer grids. The grids used here were significantly finer in the vertical and transverse horizontal directions than those used by previous investigators. Longitudinal and transverse Peclet numbers were set to 505 and 3750, respectively, a dispersion anisotropy of 30. The computations were performed on massively parallel machines with 8192 or 4096 processors (MasPar, Inc.). The algorithms that implement the model were designed to take advantage of the speed of parallel processing in moving particles. Typical simulation times for the 3D computations were about 5 hours of CPU time.

3.1.1 Homogeneous Porous Media

Displacements without Gravity. A comparison of 2D and 3D displacements in a homogeneous porous medium with viscosity ratio, M, set to 30 is shown in Fig. 3.1. It compares the pattern of viscous fingers in a 2D simulation with several horizontal and vertical slices through the 3D porous medium. Fig. 3.1 shows that in both 2D and 3D, fingers have dimensions and spacing that are nearly the same, though fingers have penetrated slightly farther in 3D. Furthermore, in the absence of gravity, the numbers of fingers and their widths are essentially equal in the horizontal and vertical directions. That result is reasonable because finger dimensions are determined by the level of transverse dispersion, mobility ratio and flow length, factors that act equivalently in 2D and 3D flow.

Another comparison of 2D and 3D fingering is given in Fig. 3.2. It compares concentration profiles obtained by averaging the concentrations of fluid present at a given longitudinal position, again for M = 30. Fig. 3.2 shows that the longitudinal concentration distributions are remarkably similar in 2D and 3D flow in the absence of gravity. The 2D distributions are noisier, presumably because concentrations are averaged over fewer fingers in 2D than in 3D, but otherwise the distributions do not differ in any significant way.

Displacements with Gravity. When gravity is added to the picture, the equivalence of 2D and 3D flow disappears for some displacements. In both 2D and 3D flow, of course, viscous forces that drive the hydrodynamic instability compete with buoyancy forces that act to create a gravity tongue. If the flow is slow enough that gravity forces dominate, then fingering will be

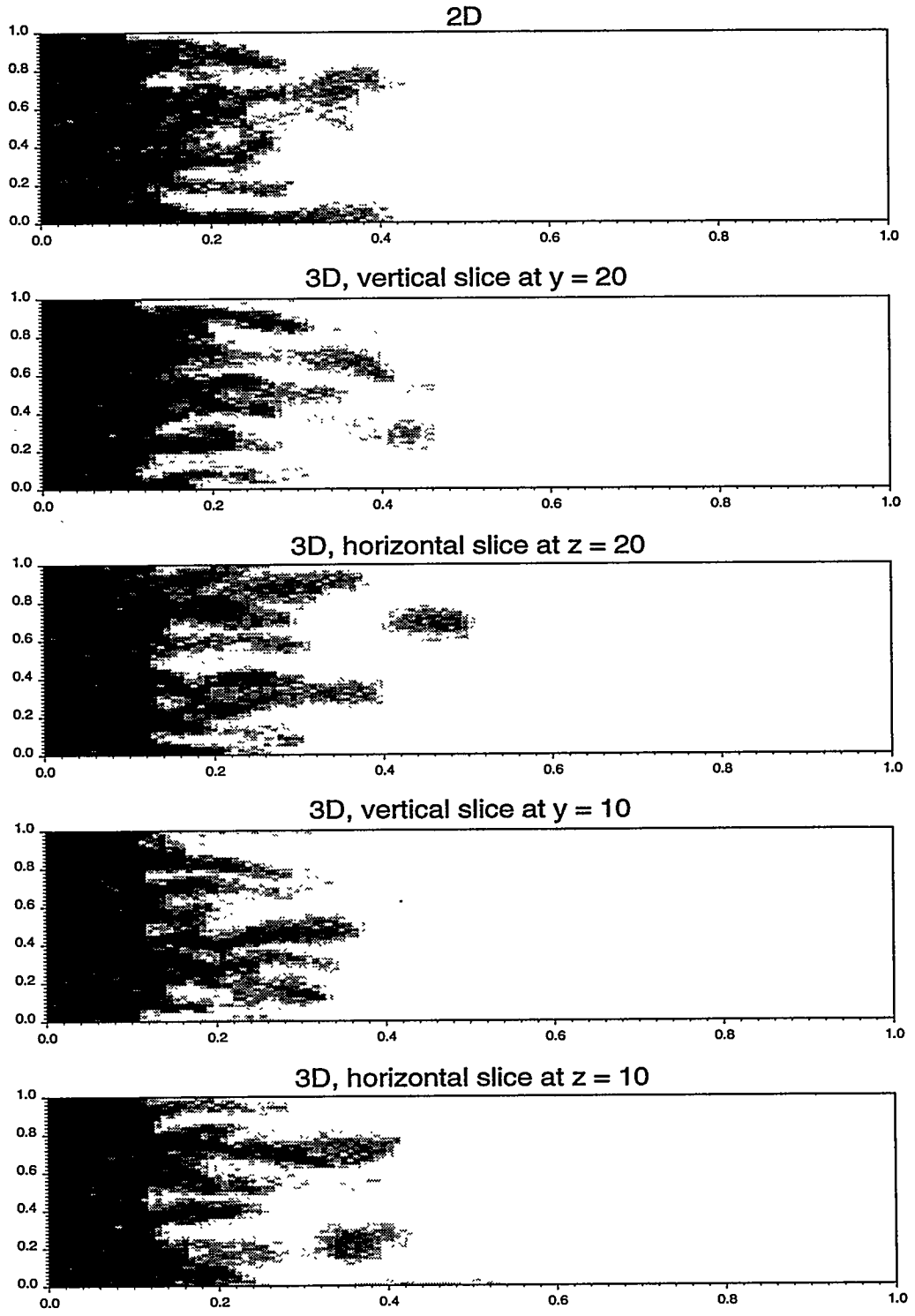

Figure 3.1: Comparison at 0.2 PVI of 2D and 3D displacements with M = 30 in a homogeneous porous medium in the absence of gravity.

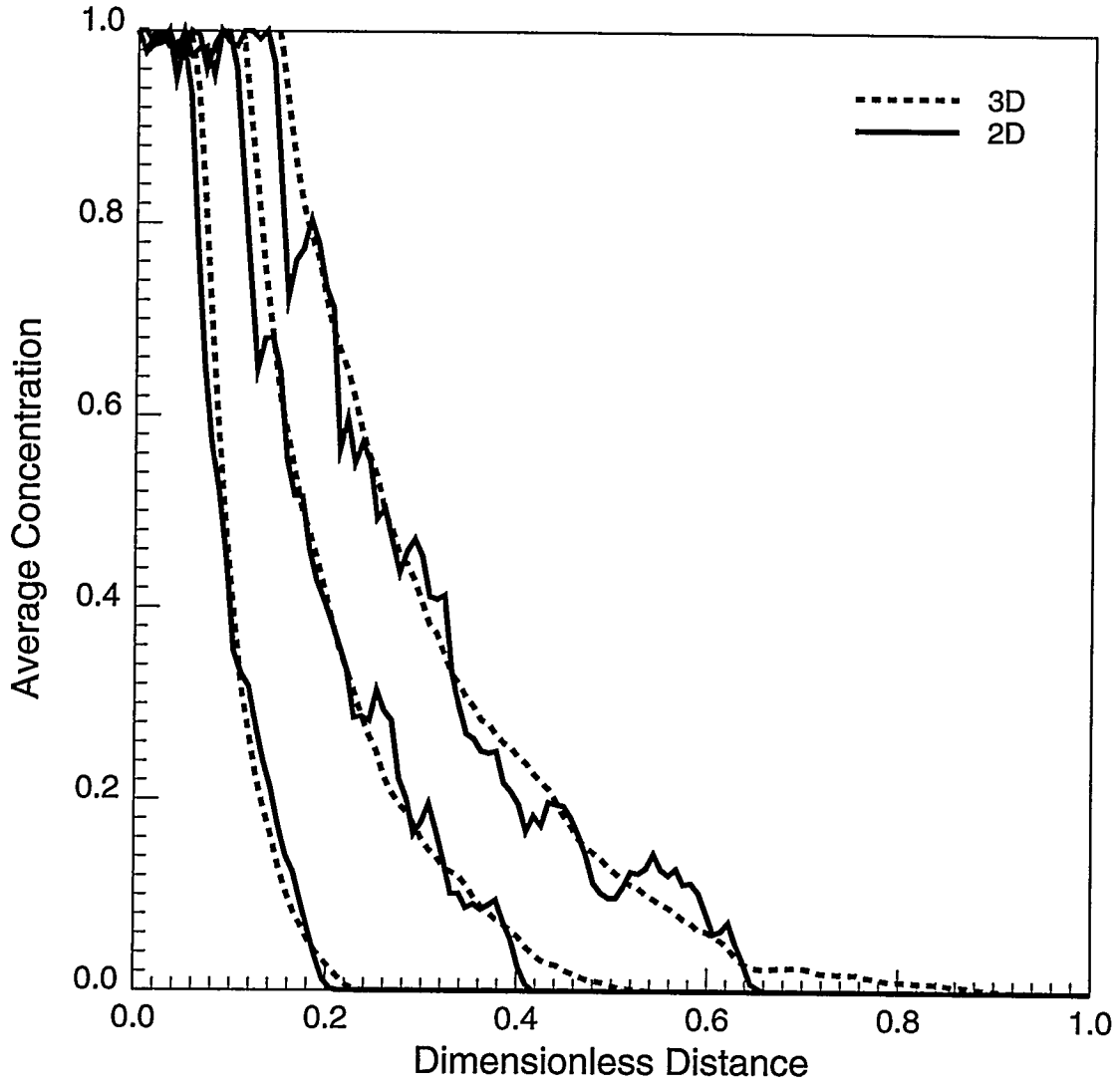

Figure 3.2: Comparison of transversely averaged concentrations of injected fluid in 2D and 3D displacements with M = 30 at 0.1, 0.2 and 0.3 PVI in a homogeneous porous medium in the absence of gravity.

suppressed. If the flow is fast enough that viscous forces dominate, then fingers form and the gravity tongue is suppressed. The relative importance of viscous and gravity forces is measured by a viscous to gravity ratio, $R_{v/g}$. Here we use the definition of Fayers and Muggeridge [64],

$$R_{v/g} = 2\frac{v\Delta\mu}{\Delta\rho g k_z}\frac{H}{L}. \tag{3.1}$$

$R_{v/g}$ as defined in Eq. 3.1, without the leading coefficient of 2, can be rigorously derived from the governing equations. $R_{v/g}$ is interpreted as a ratio of characteristic times. It is the ratio of the time it takes a particle to traverse the height of the model, to the time it takes the particle to cover the length of the medium when driven by the mean viscous force at $\overline{u}$. In addition to the obvious fact that segregation requires a density difference, the viscous-to-gravity ratio, $R_{v/g}$, indicates that the following factors, when dispersion is negligible, add to the effectiveness of buoyancy. (1) slow average displacement velocities, (2) large vertical communication and (3) longer, thinner domains.

The transition from flow dominated by a single gravity tongue to flow dominated by viscous fingering is illustrated for 2D flow in Fig. 3.3. At $R_{v/g} = 1$ and 2, the flow is strongly influenced by gravity-driven vertical flow, which causes a thin gravity tongue to form. As $R_{v/g}$ is increased further, however, viscous fingers begin to form, and the gravity tongue loses strength and becomes smaller. The $R_{v/g} = 5$ and $R_{v/g} = 10$ displacements in Fig. 3.3 are in the transition region where buoyancy and viscous fingering compete for dominance. Finally, when $R_{v/g} = 20$, viscous fingering dominates the flow.

Fig. 3.4 compares 2D and 3D flow for M = 30 and $R_{v/g} = 20$. While there is no evidence of a gravity tongue in the 2D flow, all three vertical slices of the 3D flow show some evidence of gravity override. Fig. 3.5 is a 3D perspective at 0.3 PVI of the M = 30 displacement when $R_{v/g}$ = 20. The presence of a gravity tongue is evident in Figs.3.4 and 3.5. In addition, some of the fingers below the gravity tongues in the 3D flow appear to have been deflected upward by gravity. Apparently, gravity segregation remains important at $R_{v/g} = 20$ for M = 30 in 3D flow, while its effect in 2D flow is virtually absent.

Another indication of the larger effect of gravity in 3D flow is given in Fig. 3.6, which reports recovery at breakthrough of injected solvent for both 2D and 3D flows. In 2D flow, breakthrough recovery increases with $R_{v/g}$ up to about $R_{v/g} = 10$. In 3D flow, however, breakthrough recovery is lower than that for 2D flow (at the same value of M), and the effect of gravity persists to higher values of $R_{v/g}$. In fact, only above $R_{v/g} = 100$ does the effect of gravity on breakthrough recovery disappear.

The effect of gravity on recovery after breakthrough is shown for M = 30 in Fig. 3.7. It shows that for L/H = 4, there is little difference between the 2D and 3D displacements after breakthrough for $R_{v/g} = 5$. As the flow length is increased, the weaker influence of buoyancy in 2D flow gives way to the effects of lateral dispersion and viscous fingering. Hence, when L/H is increased to 16, there is a substantial difference between 2D and 3D flow, as the longer flow length provides more time for gravity segregation, which is more effective for a given $R_{v/g}$ in 3D than in 2D, to take effect.

Fig. 3.8 provides further evidence of the increased effectiveness of gravity segregation in 3D than in 2D at the same value of $R_{v/g}$. Fig. 3.8 is a 3D snapshot for M = 30 and L/H = 4 for $R_{v/g}$ = 100 just before breakthrough. The effect of buoyancy on 3D flow at this high viscous-to-gravity ratio is reflected in preferred fingering near the top of this relatively short model. We saw in Fig. 3.3 that buoyancy was no longer effective in 2D flow at M = 30 and L/H = 4 when $R_{v/g}$ was 20. The enhanced effectiveness of gravity segregation in 3D flow was experimentally observed by Withjack *et al.* [196] in unstable miscible displacements in a 5-spot geometry.

We offer the following explanation for the difference between 2D and 3D flow behavior in the transition region of $R_{v/g}$ where both gravity and viscous forces influence the flow. In unstable 2D flow (see Fig. 3.3) at intermediate values of $R_{v/g}$, the effect of gravity is to cause upward flow of

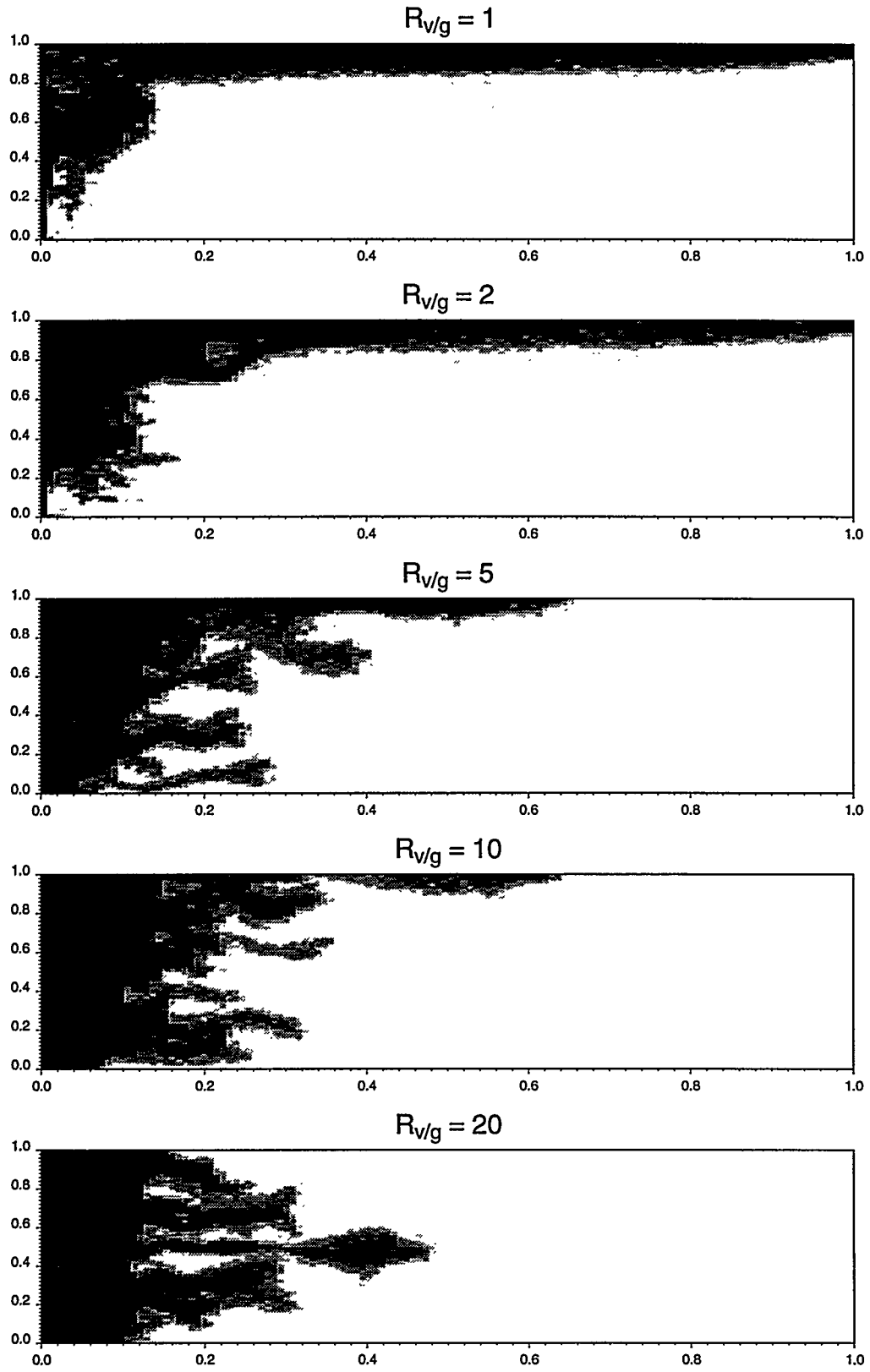

Figure 3.3: Effect of viscous to gravity ratio, $R_{v/g}$, in 2D displacements for M = 30 at 0.2 PVI.

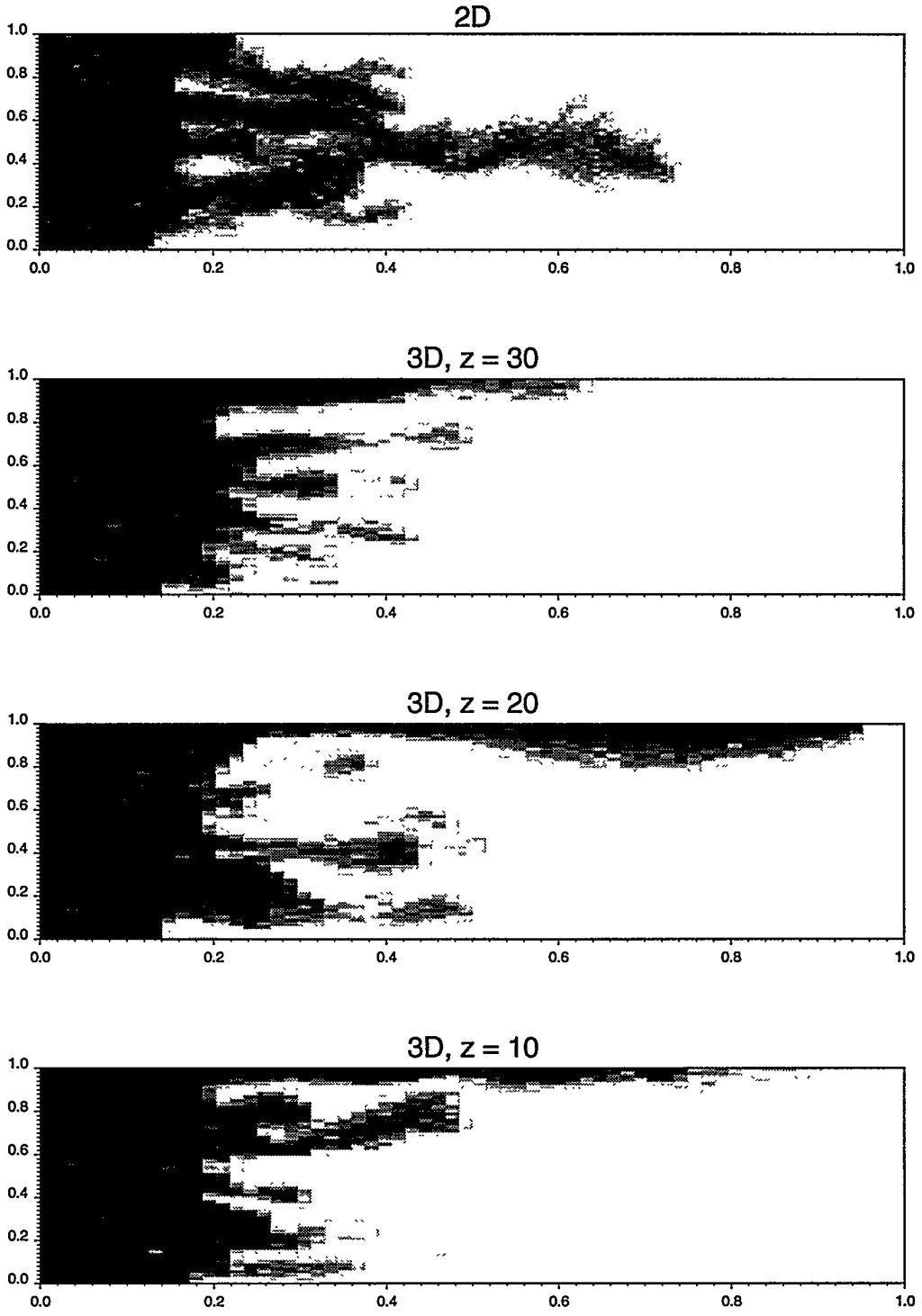

Figure 3.4: Comparison at 0.3 PVI of 2D and 3D displacements with M = 30 and $R_{v/g} = 20$ in a homogeneous porous medium.

M = 30, Rvg = 20, PVI = 0.3

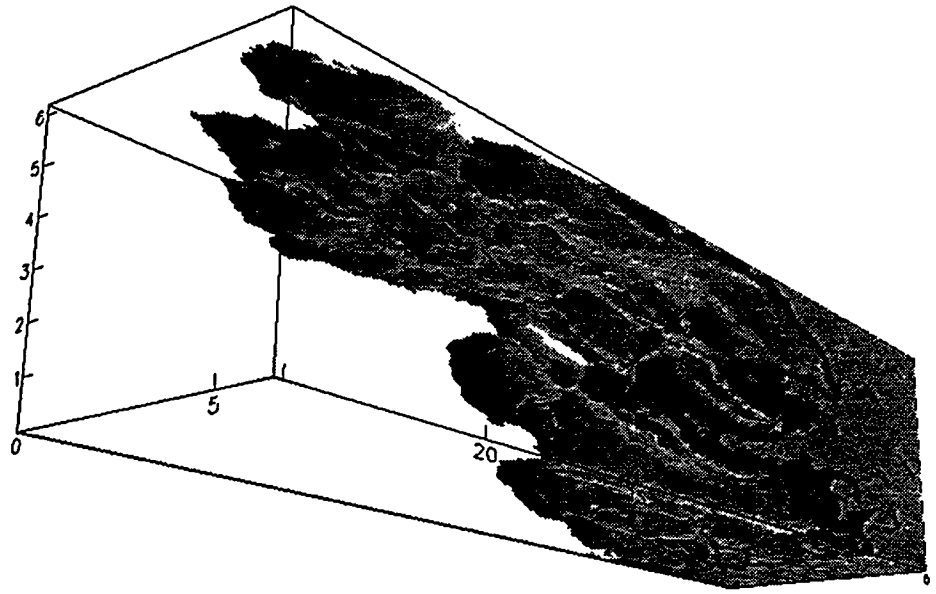

Figure 3.5: A 3D snapshot for M = 30 and $R_{v/g}$ = 20 in a homogeneous porous medium at 0.3 PVI.

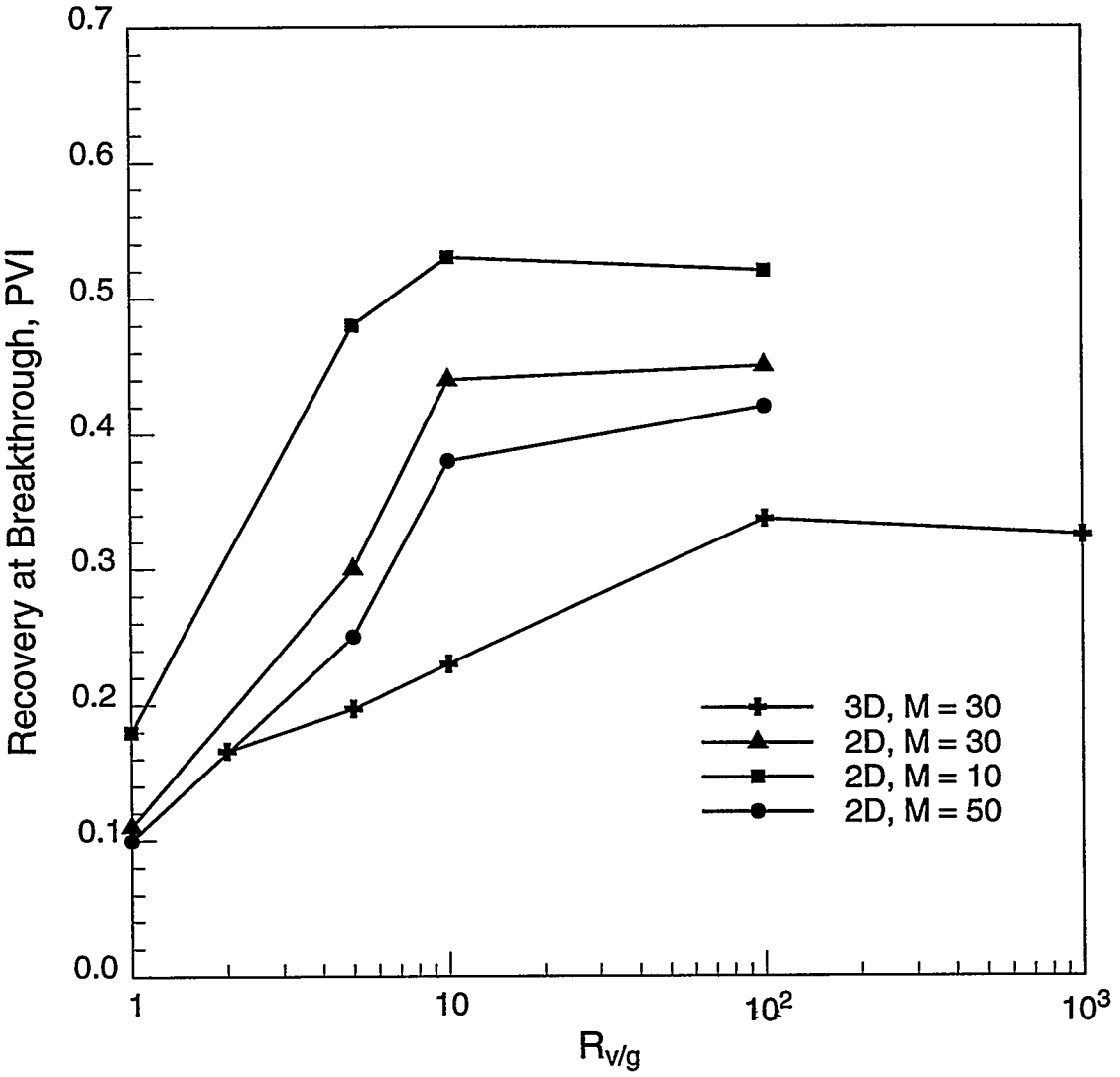

Figure 3.6: Effect of viscous to gravity ratio, $R_{v/g}$, on breakthrough recovery for 2D and 3D displacements when L/H = 4.

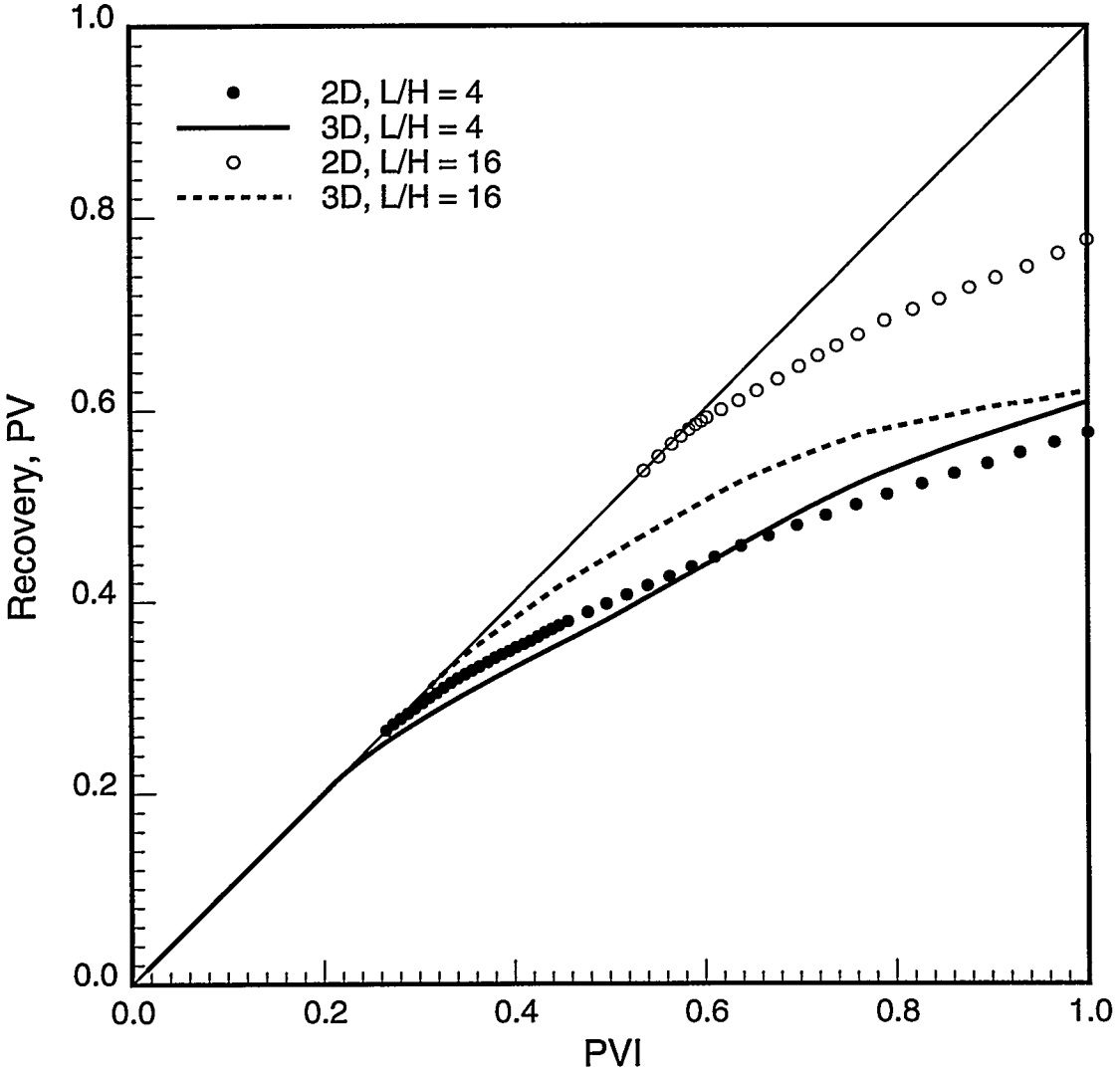

Figure 3.7: Comparison of calculated oil recovery for 2D and 3D simulations in homogeneous porous media for $R_{v/g} = 5$.

M = 30, Rvg = 100, PVI = 0.33

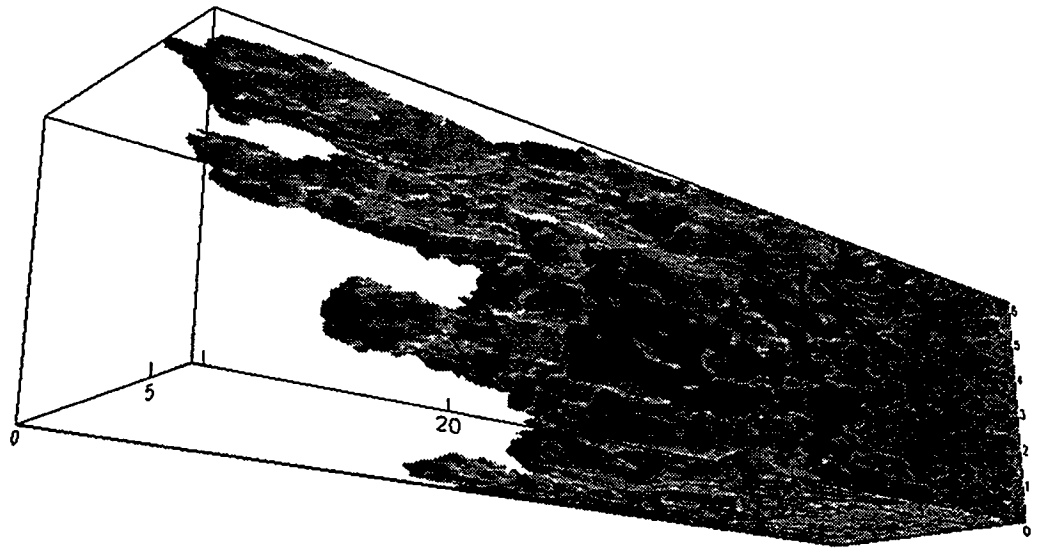

Figure 3.8: A 3D snapshot for M = 30, L/H = 4 and $R_{v/g} = 100$ in a homogeneous porous medium at 0.33 PVI.

injected fluid within the fingers and downward flow of the resident, more viscous fluid between the fingers. In 2D flow, the vertical displacement must cause mixing of the two fluids because the flow can only occur in a single plane. That mixing reduces the local contrasts in viscosity and density, which limits the driving force for vertical transport.

In 3D flow, however, vertical flow need not take place in a single plane. Instead, downward flow of the heavy, more viscous fluid can take place between fingers. As a result, less mixing takes place, the viscosity and density contrasts remain higher than in 2D flow, and hence, segregation remains important at higher values of $R_{v/g}$. Thus, 2D calculations can yield inaccurate predictions when $R_{v/g}$ is in the transition region and L/H is large, as it is likely to be in field-scale flows.

3.1.2 Heterogeneous Porous Media

To investigate how the presence of permeability heterogeneities affects the interplay of gravity segregation and viscous fingering, a series of computations was performed for 2D and 3D correlated permeability distributions for Dykstra-Parsons coefficients $V_{DP} = 0.2$, 0.4, and 0.8 and dimensionless correlation lengths $\lambda_D = 0.05$, 0.1 and 0.2. Here we illustrate the results for $V_{DP} = 0.8$ and $\lambda_D = 0.2$. The permeability distributions were generated by Gaussian sequential simulation, and the 2D and 3D distributions were generated independently. Simulations were performed for mobility ratios of 10, 30, and 50.

When the permeability field was nearly uncorrelated (small λ_D), fingering behavior was nearly the same in 3D flow as that observed for 2D flow, and both were similar to the behavior described above for homogeneous porous media. Simulations with gravity were not performed for those fields, but we speculate that gravity would also have effects similar to those for homogeneous porous media.

When the correlation length is longer ($\lambda_D = 0.2$), the resulting permeability fields contain preferential flow paths that interact strongly with viscous forces to determine where injected fluid flows most easily. Fig. 3.9 shows transversely averaged concentration profiles for displacements with M = 1 and M = 10 in 2D and 3D porous media (labeled 2DF6 and 3DF6) with $\lambda_D = 0.2$ in all coordinate directions. Gravity effects are not included in the displacements of Fig. 3.9. The displacement at M = 1 shows how much spreading of the transition zone arises from the permeability distribution. Dispersion also contributes to that spreading, but its effect is small compared to that of the permeability distribution. Here again, the averaged profiles are similar for the 2D and 3D flows, though the 3D profiles are smoother, probably because they are averaged over more flow paths in 3D. When the displacement is unstable at M = 10, the transition zone is longer still, as viscous forces amplify the effects of the heterogeneity. When gravity effects are absent, the differences between 2D and 3D flow are small in this example in which the mean flow direction is parallel to one of the principal axes of the correlation structure. In simulations in which the mean flow direction was not so aligned, 2D simulations did not match the results of 3D simulations even when gravity effects were not included.

Fig. 3.10 gives another view of the effect of heterogeneity on the flow. Fig. 10a compares the averaged concentration profile for unstable (M = 30) 3D flow without gravity for permeability field 3DF6 with that for a homogeneous porous medium. The effect of the heterogeneity is to lengthen the transition zone substantially. In this case viscous fingers find and flow along the preferential flow paths present in field 3DF6 that are oriented more or less parallel to the mean flow direction. Fig. 10b shows the effect of gravity in the homogeneous displacement along with the profile for field 3DF6 without gravity. In the homogeneous porous medium, a significant gravity tongue forms, though it still does not lengthen the transition zone as much as heterogeneity alone in 3DF6.

The effect of gravity in field 3DF6 is shown in Fig.3.10c, which gives profiles for $R_{v/g} = 0.1$, 5, 10 and 20. At those values of $R_{v/g}$, a significant gravity tongue forms in a 3D homogeneous

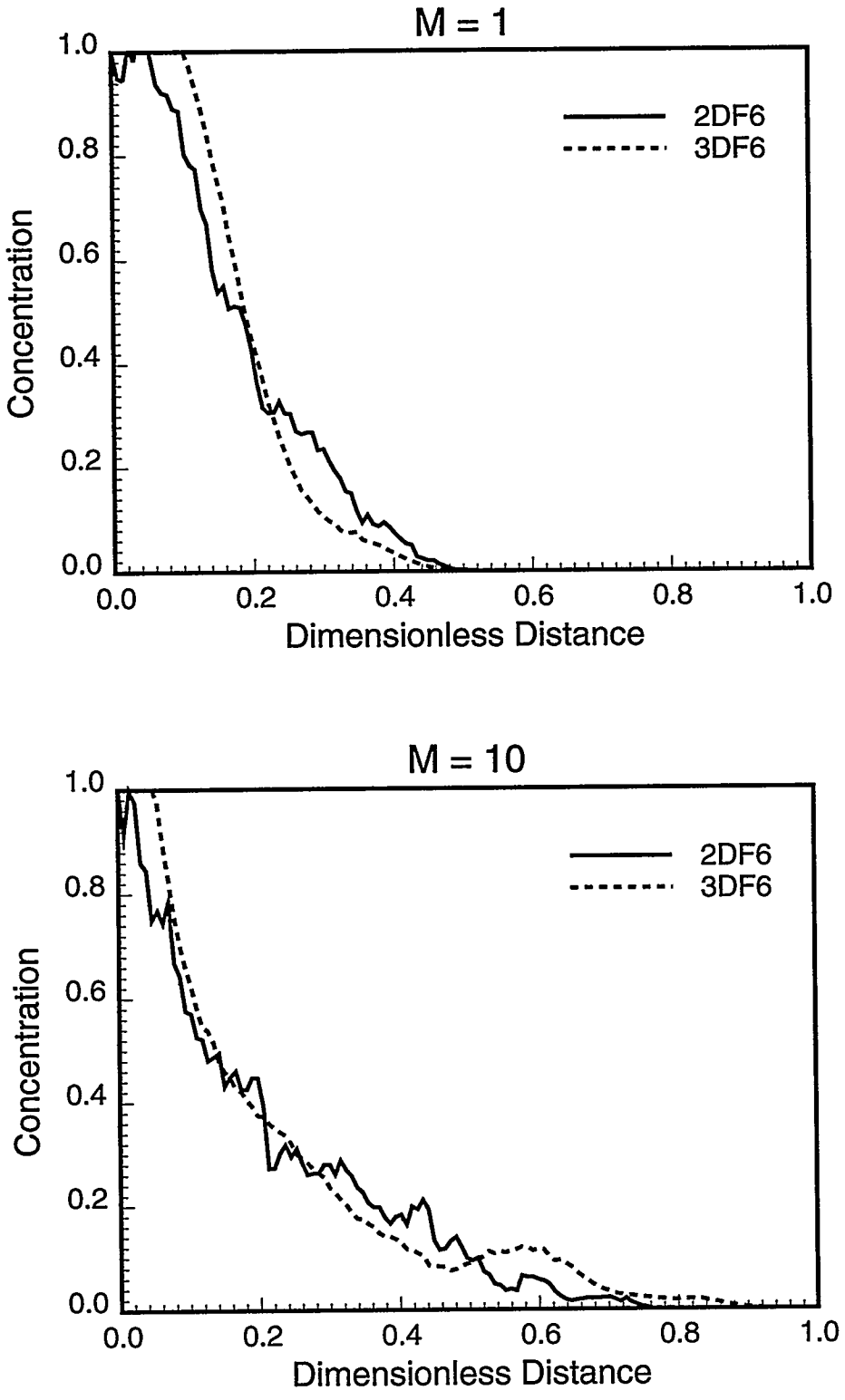

Figure 3.9: Comparison at 0.2 PVI of transversely averaged concentration profiles for M = 1 and M = 10 from simulations using 2DF6 and 3DF6 with no gravity segregation effects.

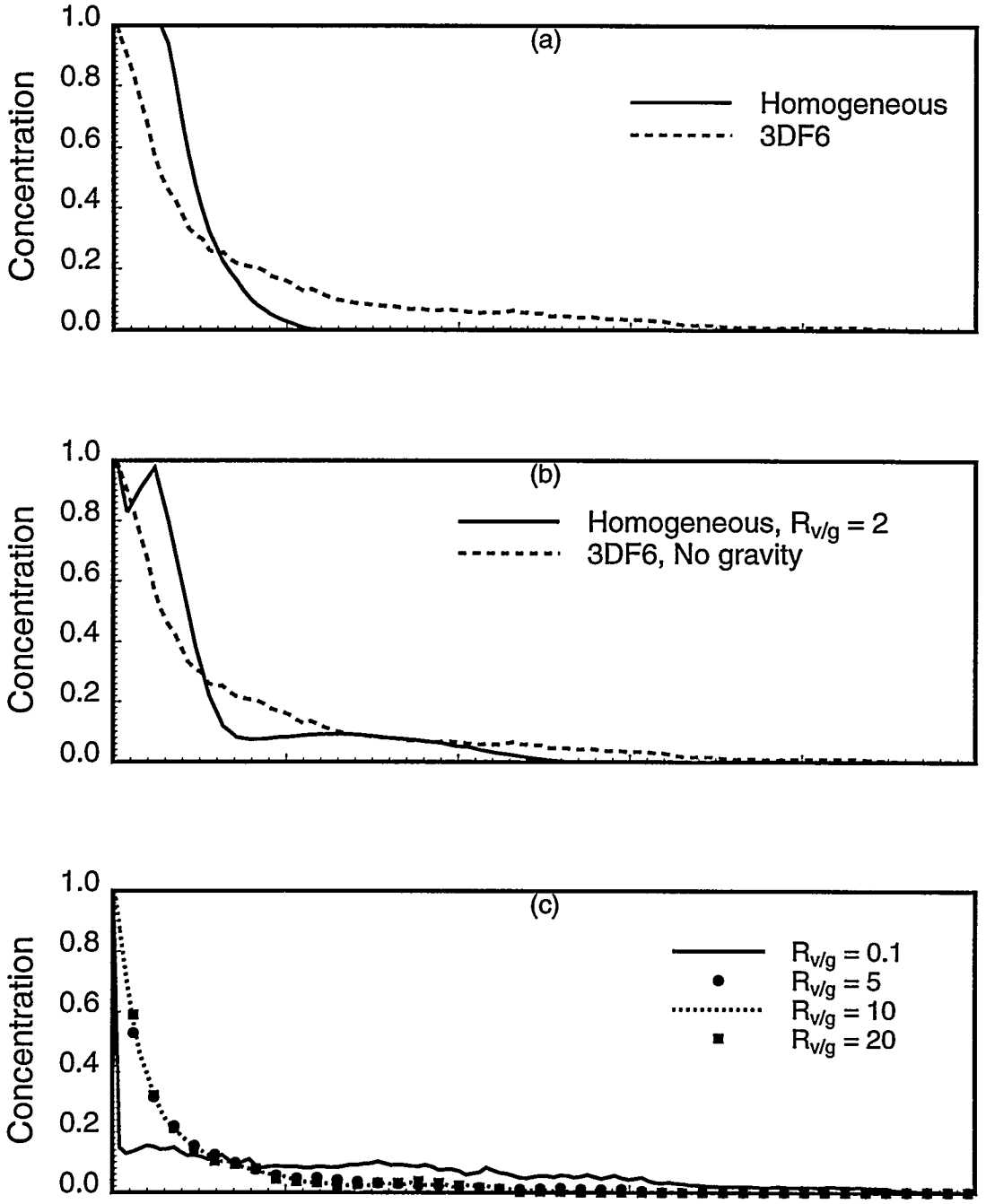

Figure 3.10: Comparison of transversely averaged concentration profiles for displacements for M = 30 in homogeneous and heterogeneous porous media with and without gravity effects. Figures (a) and (b) at 0.2 PVI and figure (c) at 0.1 PVI.

porous medium. In 3DF6, however, the profiles for $R_{v/g}$ = 5, 10, and 20 are indistinguishable. Figs. 3.11 and 3.12 are 3D snapshots at breakthrough for displacements in field 3DF6 at $R_{v/g}$ of 100 and 5, respectively. At $R_{v/g}$ = 100 (Fig. 3.11), two high-permeability channels join near the bottom of the model and the system breaks through along the bottom of the model. When $R_{v/g}$ is 5 (Fig. 3.12), some of the flow is reallocated to the top depriving the high permeability channels near the bottom from some of the flow. When $R_{v/g}$ = 5, breakthrough occurs near the top of the model. While the details of the flow are altered as $R_{v/g}$ is lowered from 100 to 5 in 3DF6, the average behavior in terms of sweep is not significantly affected. In Fig.3.10c, only at the lowest value, $R_{v/g}$ = 0.1, is evidence of a significant gravity tongue apparent. Fig. 3.13 is a 3D snapshot of the M = 30 displacement in 3DF6 for $R_{v/g}$ = 0.1 at breakthrough. Thus, for field 3DF6, the gravity viscous transition occurs for values of $R_{v/g}$ between 0.1 and 5 for M = 30, in contrast to the behavior of a homogeneous porous medium, for which the transition occurs in the range $1 < R_{v/g} < 100$.

We argue that the difference in behavior between homogeneous and heterogeneous porous media is the result of restrictions to vertical flow in the heterogeneous medium. Evidently, the variations in permeability place some zones of low permeability in locations that slow gravity-driven vertical flow, while high permeability zones amplify the effects of viscous forces in the horizontal flow. As a result, the transition region occurs for lower values of $R_{v/g}$ when the heterogeneities of field 3DF6 are present. Here again, for displacements in the transition region, 2D simulations are unlikely to reproduce accurately the fluid distribution and recovery behavior of the 3D flow.

3.1.3 Discussion

The examples presented indicate that results of unstable displacements in 3D porous media can be very different from those obtained for 2D porous media when the combined effects of gravity segregation, heterogeneity, and viscous instability are considered. The differences are largest for systems with high values of L/H when the value of $R_{v/g}$ is in the transition region from gravity-dominated flow to viscous-dominated flow. If either gravity segregation or viscous forces dominate, however, 2D and 3D simulations produce similar results as long as the 2D permeability field represents adequately the correlated permeability structure of the 3D field. Thus, use of some 3D simulations to assess the relative importance of viscous and gravity forces is desirable, though it is clear that such computations will continue to be limited by the computation time required and by the availability and resolution of 3D reservoir descriptions. The particle-tracking technique used here is a relatively efficient technique that can be used to determine whether extensive 3D simulations are required, for example to investigate optimum injection rates, or whether 2D representations are adequate.

3.1.4 Conclusions

Comparison of 2D and 3D simulations of unstable displacements leads to the following conclusions:

Homogeneous Porous Media

(i) If gravity effects are absent, 2D and 3D simulations predict similar finger dimensions and averaged concentration profiles.

(ii) 3D flow behavior differs substantially from 2D flow behavior for displacements in which neither gravity forces nor viscous forces dominate ($1 < R_{v/g} < 100$).

F6, M = 30, Rvg = 100, PVI = 0.105 (BT)

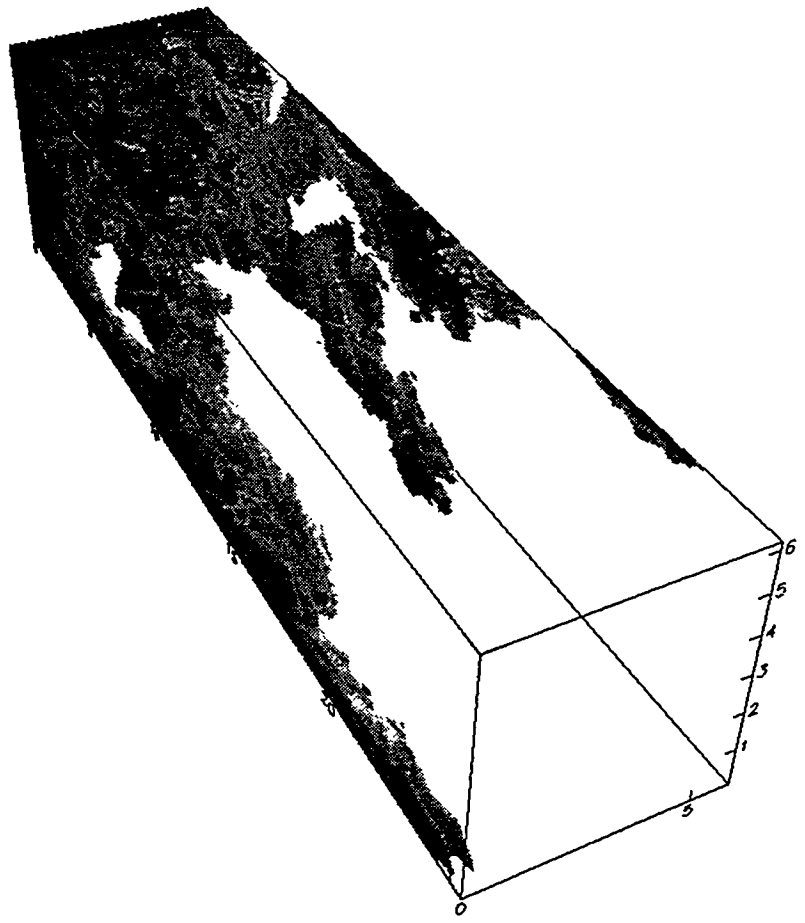

Figure 3.11: A 3D snapshot for M = 30 in permeability field 3DF6 with $R_{v/g} = 100$ at breakthrough (0.105 PVI).

F6, M = 30, Rvg = 5, PVI = 0.07 (BT)

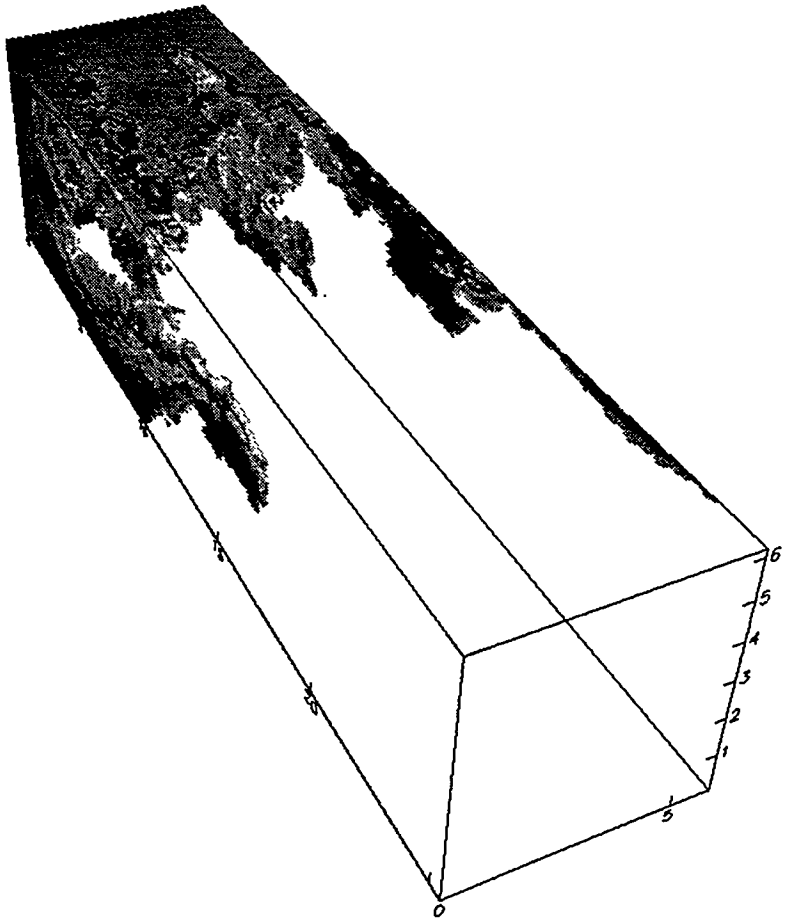

Figure 3.12: A 3D snapshot for M = 30 in permeability field 3DF6 with $R_{v/g} = 5$ at breakthrough (0.07 PVI).

F6, M = 30, Rvg = 0.1, PVI = 0.04 (BT)

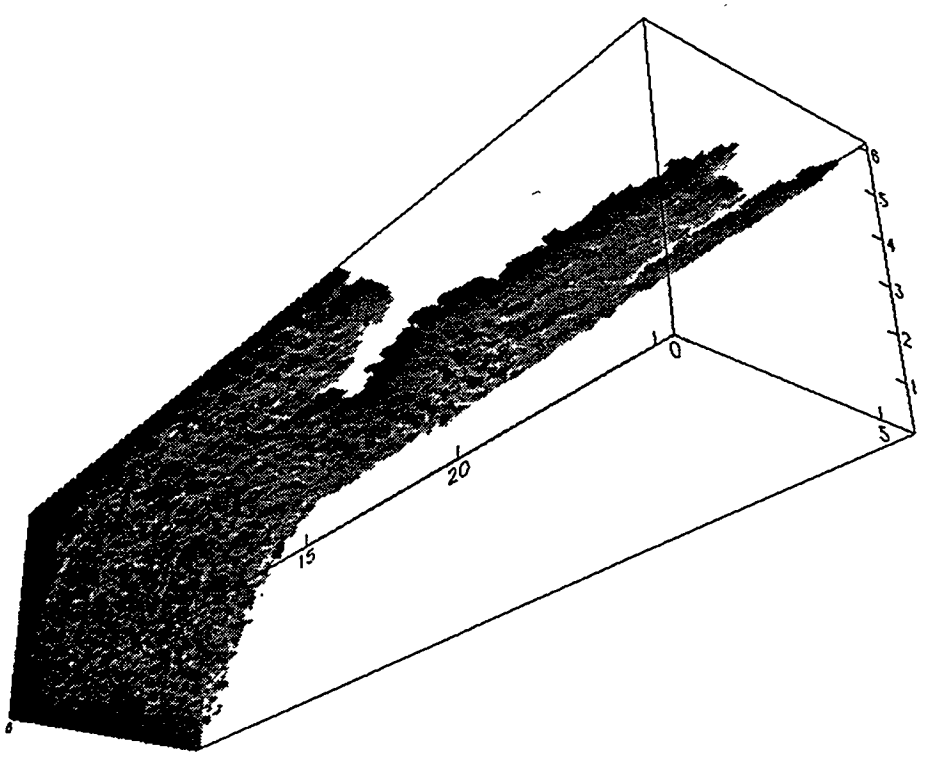

Figure 3.13: A 3D snapshot for M = 30 in permeability filed 3DF6 with $R_{v/g} = 0.1$ at breakthrough (0.04 PVI).

(iii) In correlated permeability fields in the absence of gravity, 2D and 3D simulations agree well as long as the principal axes of the correlation structure are aligned with the mean flow direction.

(iv) The presence of correlated heterogeneities can significantly alter the range $R_{v/g}$ over which the transition from gravity-dominated flow to flow controlled by viscous forces is observed.

3.2 Compositional Displacements in Heterogeneous Systems

F. J. Fayers, B. Aleonard, and F. Jouaux

The flow studied in Section 3.1 focussed on the physics of unstable flow, but neglected the influence of phase behavior, shown to be so important in Chapter 2. In this section we describe research to obtain a better understanding of how phase behavior, adverse viscosity ratio, viscous fingering, heterogeneity and gravity interact in compositional modeling of gas displacement processes. One of the difficulties in understanding such problems arises from the fact that in a multicontact process leading to miscibility, the two phases move quickly towards equality in composition, so that density and viscosity contrasts are substantially reduced. However, at positions away from the mixing zone, the injected and *in situ* phases retain their original contrasts in properties. This led to the Todd and Longstaff method [186] for modeling viscous fingering in such systems, where the problem is represented in terms of a mixing rule with effective properties for the phases. This formulation neglects phase behavior and is based on the hypothesis that the system behaves very similarly to a first-contact miscible process. More recent studies have indicated that multicontact processes do not generally attain miscibility (see for example [105]), and that dispersion effects can lead to submiscible behavior with some detrimental effects on oil displacement. Another factor relates to heterogeneity, where it is increasingly evident [6] that reservoir heterogeneity has a strong effect on fingering patterns, although the magnitude of the adverse viscosity ratio also influences the behavior. The appropriate way to adjust the Todd and Longstaff mixing parameter for heterogeneity is poorly understood. Because heterogeneity forces the displacing fluid to take preferred paths, the sweep characteristics are very different from the homogeneous case, and the assumptions of uniform mixing within large grid blocks are highly erroneous. For these reasons, the α-correction procedures were introduced by Barker and Fayers [9] into compositional modeling to compensate for the nonuniformities in phase behavior and component transport associated with the use of large grid blocks.

In the present studies, we will set up a "mildly" heterogeneous problem and study the attributes of various ways of representing its behavior under nearly miscible displacement. Understanding how to use compositional models to predict gas displacement more reliably in heterogeneous applications has become an important question. We will assume that the scale size involved is sufficiently large that capillary forces and diffusion processes are negligible. At the laboratory and somewhat larger scales, these effects cannot be neglected in nearly miscible processes [63], but their omission may be appropriate at the reservoir scale.

Two major simulators have been used in this work. The first code, MISTRESS, is a fast high resolution simulator developed by Christie *et al.* [33] at BP Research, which models a two-component first-contact miscible process. Its high resolution is achieved through fine gridding and use of an FCT-algorithm [32] for controlling numerical dispersion. It has been used to understand the physics of viscous fingering in homogeneous systems [65], and also some work has been done in heterogeneous systems [67]. The second code MORE, is a commercial compositional simulator developed by Young [199] at Reservoir Simulation Research Inc. It has high speed efficiency for

Table 3.1: The parameters for the PR equation

Component	M_w (g/mol)	P_c (Psi)	T_c (F)	Ω —	Parachors —	%Mole Oil/Mis. Gas
C_1	16	671.17	117.07	0.1592	77.1	36.92/32.77
C_2+	41	769.81	142.79	0.013	141	11.55/67.23
C_5+	189	322.89	775	0.6736	588	42.81/0
$C_{30}+$	451	171.07	1136.59	1.0259	1453	8.71/0

finely gridded problems, and is very fast on the Cray YMP computer used in this work. It does not have special features for controlling numerical dispersion, and the unquantified influence of this in compositional problems will be partially examined in these studies. We will also be looking at some special features associated with variable interfacial tensions, which have been programmed into MORE through the Elf Geosciences Center.

3.2.1 The Permeability Field

Permeability distributions have been generated using the moving average technique in 2D, based on averages within an ellipse (major and minor axes give the anisotropic correlation lengths α_l and α_t). Random permeabilities are first normally generated using a random number generator on a fine (128 $\times$ 64) grid, with further points generated for averaging outside the rectangle of interest. The moving averages are taken on the fine grid, and thence a log transformation is used to give a log normal distribution. The distribution shown in Fig. 3.14 was the principal realization studied, which was generated using the parameters: L/W = 3.0, α_l/L = 0.2, α_t/W = 0.06 and σ_{lnk} = 0.69. The distribution was intentionally chosen to give rather long and thin permeability zones, thought to be more appropriate to real geology. We also wished to create a distribution which was reasonably statistically homogeneous as a function of x (clearly not so) and to be not too heterogeneous (the Dykstra-Parsons index for this problem is V_{DP} = 0.50). A reduced grid of permeability values (64 $\times$ 32) was also formed by performing a simple renormalization based on a 2 $\times$ 2 column and row averaging procedure (see Fig. 3.14b).

3.2.2 Phase Behavior

Three types of phase behavior have been studied as follows :

(i) First contact miscible displacements with μ_o/μ_g = 20 and ρ_o = 49.2 lb/ft^3, ρ_g = 24.5 lb/ft^3.

(ii) A four-component model of slightly submiscible displacement, using the data of [105] with a C_2+ enrichment of 67.23 mol% for the injected gas. The parameters for the Peng Robinson equation are listed in Table 3.1. These properties give viscosities and densities close to those in (1) for the initial fluids.

(iii) A twelve-component model from which the values in the four-component model were consistently derived [105]. The PR-parameters are given in Table 3.2.

The parameters in (2) and (3) are associated with slightly submiscible displacement [105] but nevertheless the phase behavior ensures a reasonably efficient oil displacement, of the type which probably occurs in many "miscible" condensing/vaporizing displacements [208].

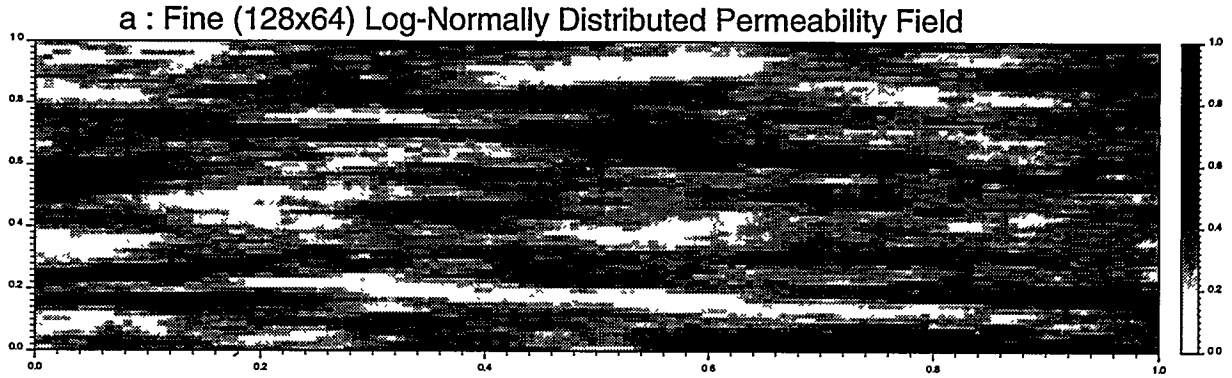

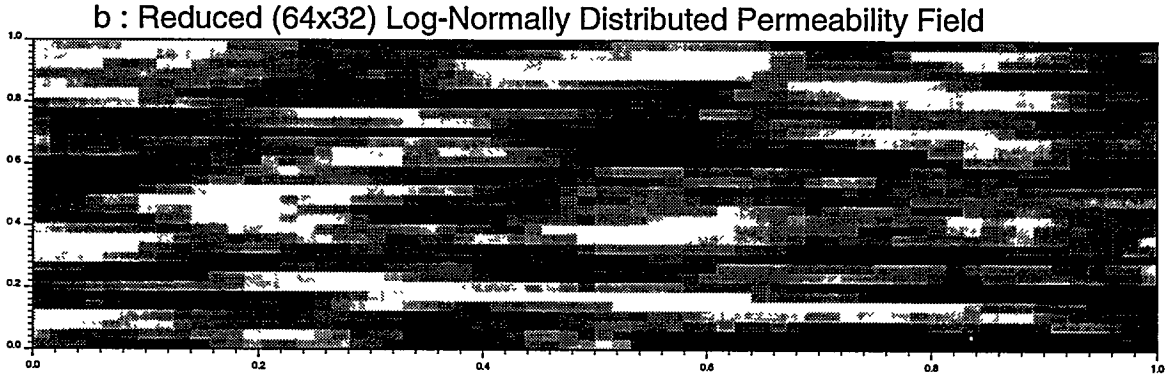

Figure 3.14: The permeability distribution used in this work.

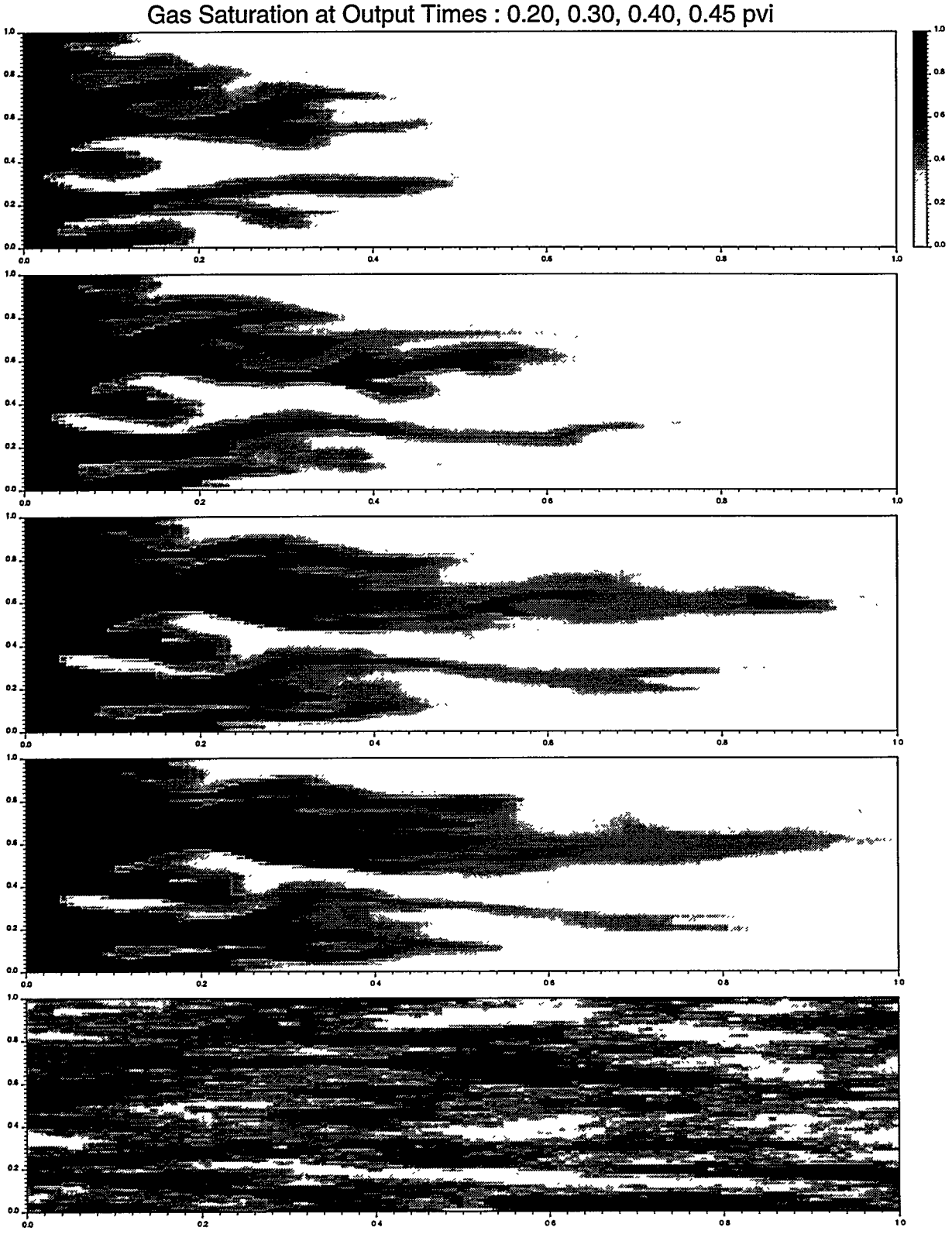

Figure 3.15: MORE four-component run on the fine grid (no gravity).

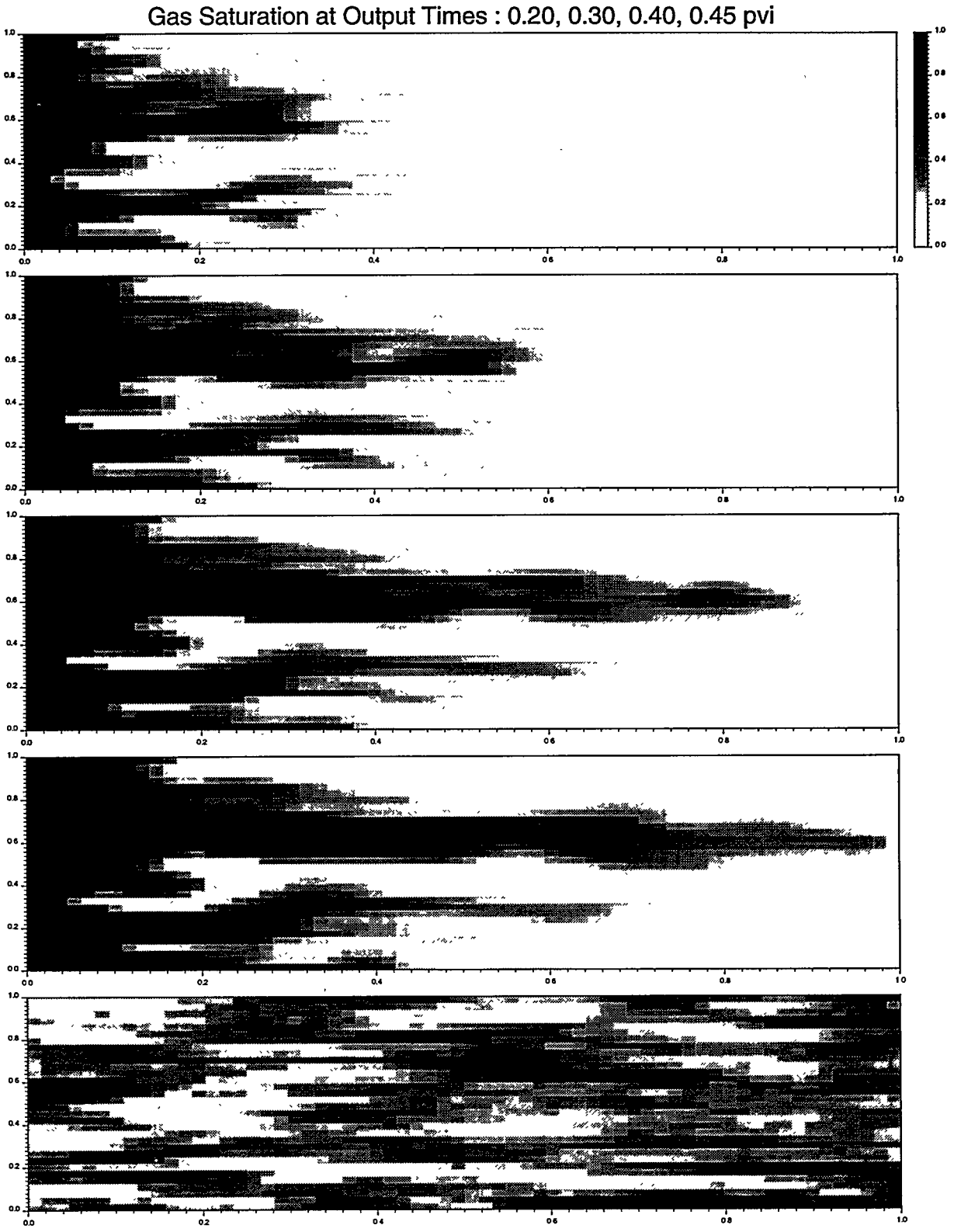

Figure 3.16: MORE four-component run on the reduced grid (no gravity).

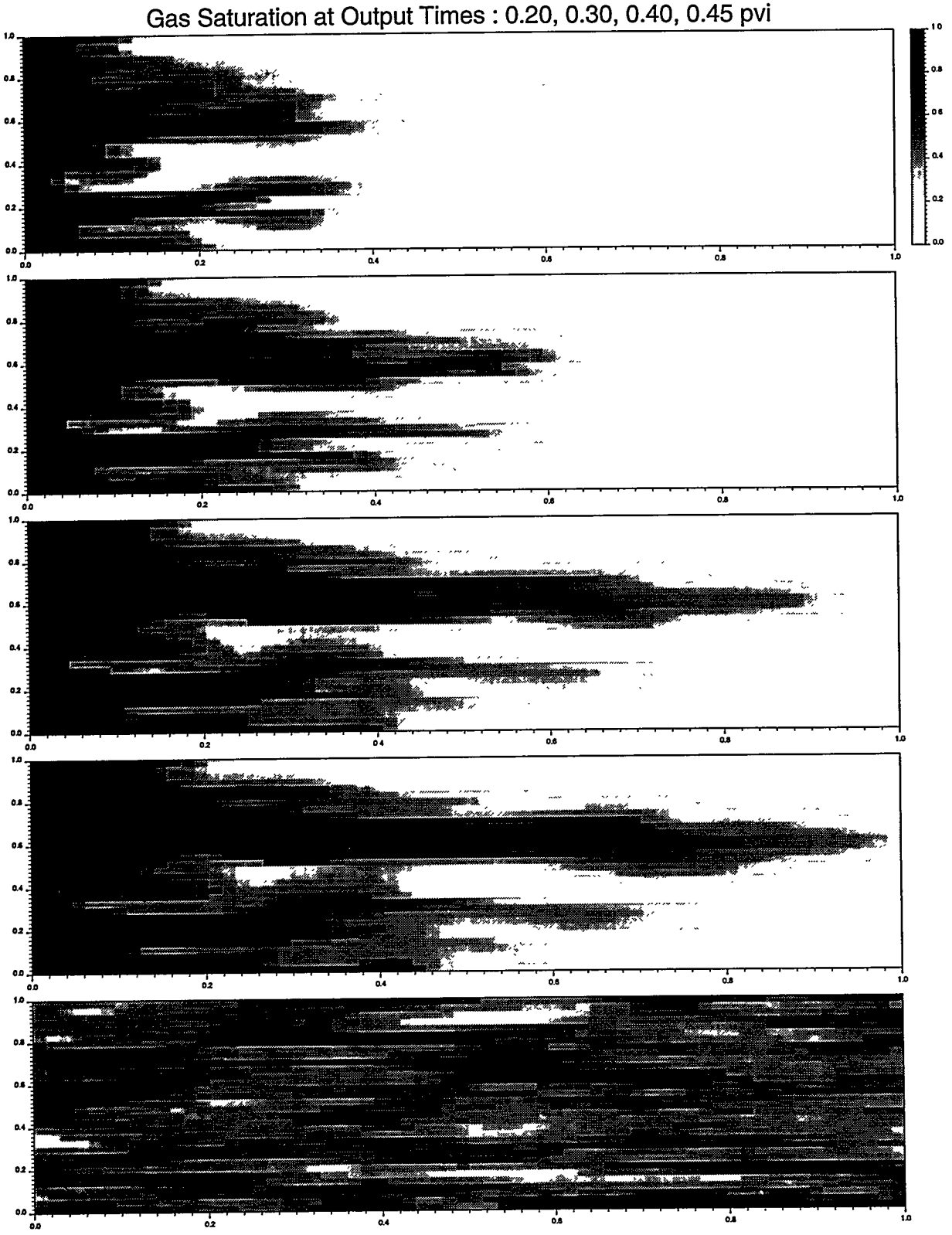

Figure 3.17: MORE twelve-component run on the reduced grid (no gravity).

Table 3.2: The PR-parameters used in this work

Component	M_w (g/mol)	P_c (Psi)	T_c (F)	Ω —	% Mole Oil /Mis. Gas
CO_2	44	1071.34	87.56	0.225	4.48/20.81
CH_4N_2	16	671.17	117.07	0.013	36.92/32.77
C_2	30	708.35	89.72	0.0986	3.21/20.08
C_3	44	617.38	205.82	0.1524	2.33/22.23
C_4	58	543.31	294.58	0.187	1.53/ 4.11
C_5	72	475.28	366.46	0.2523	0.88/0
C_6	86	419.54	439.41	0.3138	1.27/0
C_7+	108	417.69	584.35	0.3739	9.17/0
$C_{10}+$	152	407.14	670.78	0.5489	11.19/0
$C_{14}+$	213	314.34	808.24	0.755	11.22/0
$C_{20}+$	312	205.28	954.6	0.875	9.09/0
$C_{30}+$	451	171.07	1136.59	1.0259	8.72/0

3.2.3 Results without Gravity

Base Case MORE Calculations. A base case was run with the MORE four-component model on the fine grid. The gas saturation distribution is shown in Fig. 3.15. There is no evidence of injected gas components moving ahead of the S_g-values, since C_1 remains fixed at the *in-situ* value ahead of the gas front. The gas phase distribution is strongly controlled by the heterogeneities. Use of the reduced grid was expected to cause two sources of smoothing error, namely reduced permeability spread due to averaging and increased truncation errors in the finite difference method. Fig. 3.16 indicates that the consequent errors are tolerable, with the reduced grid still giving a fair reproduction of the main characteristics from the fine grid, including only a small error in breakthrough time. The effects of a more accurate representation of phase behavior were tested using the twelve-component model where comparison of Figs. 3.16 and 3.17 indicates almost no changes, i.e. the four-component approximation is more than adequate. In view of this, no further cases were run with twelve components. These results confirm the view that satisfactory compositional simulation in reservoir applications can often be performed with relatively few components (e.g. four to six). The relative permeabilities used in MORE have been based on $k_{ro} = S_o^{*2}$, $k_{rg} = S_g^{*2}$ with $S_{org} = 0.15$ and $S_{gc} = 0.05$. Thus high oil recovery is primarily driven by phase behavior. We also examined $k_{ro} = S_o^*$, $k_{rg} = S_g^*$ with $S_{org} = 0$ and $S_{gc} = 0$, i.e. straight lines assuming almost miscible behavior. The results shown in Fig. 3.18 indicate a very high degree of dispersion at low gas saturations. This must be partly physically driven by the much larger gas mobility at low saturation, but there may be exaggerated numerical dispersion errors due to the absence of any self-sharpening character in the fractional flow. It is interesting that the method of characteristics solutions for 1D flows suggest that there is only a weak dependency on fractional flow when the system is close to miscibility. Instead of solving by the method of characteristics, accurate 1D MORE solutions for gas saturations were obtained using 500 gridblocks for the two forms of relative permeabilities. These are compared in Fig. 3.19, which demonstrates that the straight line form will be more dispersed, although the numerical dispersion errors are now much reduced. There is also a light component front now moving ahead of the gas front. Recently completed Elf modifications to MORE which allow relative permeability adjustment with interfacial tension have

also been examined. The interfacial tension is calculated by the Mcleod-Sugden correlation

$$\sigma^{1/4} = \sum_{i}^{N_c} P_{ic} \left(\frac{\rho_o x_i}{M_o} - \frac{\rho_g y_i}{M_g} \right) \tag{3.2}$$

where ρ_o and ρ_g are oil and gas phase densities and M_o, M_g the corresponding molecular weights. P_{ic} is the Parachor for component i. The parachor values used in this study are listed in Table 3.1. The default option in the Elf extension to MORE satisfies the following rules: For phase j

$$k_{rj} = [1 - f(r)]\, k_{rj}^{im} + f(r) k_{rj}^{m} \tag{3.3}$$

where im and m imply the limiting immiscible and miscible relative permeabilities, and the weighting function $f(r)$ is defined by

$$f(r) = (1 - r) exp(-r) \tag{3.4}$$

where $r = min\left(\frac{\sigma}{\sigma_o}\right)$. The magnitude of the switching parameter σ_o, determines the interfacial tension at which the weighting towards straight-line relative permeabilities will commence. With σ_o set to a threshold of 0.01 dyne/cm, and then to 0.1 dyne/cm, the results were almost identical to those from immiscible relative permeabilities in Fig. 3.16. The trend towards straight lines starts to occur using $\sigma_o = 1.0$ dyne/cm. The results shown in Fig. 3.20 are now somewhat closer to Fig. 3.18, but still similar to Fig. 3.16. This value for σ_o is probably too high in terms of expectation of a real change to immiscible relative permeabilities. Thus for nearly miscible processes in heterogeneous systems, the use of the unmodified immiscible relative permeabilities appears to be justified.

Equivalencing First-Contact Miscible Calculations to Compositional Results. It would be very convenient if compositional calculations could be replaced by appropriate first-contact miscible calculations in the consistent heterogeneous geometry. The MISTRESS code has been run for the fine and reduced permeability models to test this possibility. The fine grid results for $\mu_o/\mu_g = 20$ are shown in Fig. 3.21 which should be compared with Fig. 3.15 for the equivalent four-component MORE calculation. This shows finer fingers with MISTRESS and an earlier breakthrough. Thus the first-contact process in a heterogeneous system is more unstable than its submiscible compositional counterpart. The last calculation was replaced with the reduced grid, as shown in Fig. 3.22. This indicates a solution with a similar character, but now the breakthrough time is surprisingly, slightly more advanced. To test the effects of numerical dispersion in the MORE code, a method was found to allow this code to simulate a first-contact MISTRESS calculation. This entailed choosing the same properties for each component in a two-component model in the input data to MORE, and then adjusting the z_c-critical factors to cause the correct viscosity ratio in the Lohrenz-Bray-Clark correlation, i.e. 20:1. This gives a flatter mixing behavior than the 1/4-power mixing law. The MORE calculation is shown in Fig. 3.23 for the reduced grid, which shows some exaggerated numerical dispersion, but less dispersive than Fig. 3.18. However, the general character is similar to MISTRESS, and the breakthrough time is only delayed slightly. Although the effects of numerical dispersion in two-component miscible models are different from multicomponent models with phase behavior, the above MORE results give encouragement about the nondominance of dispersion errors in MORE. It therefore seems unlikely that the numerical dispersion is a significant feature in reducing the instability of the compositional displacement. All of the first-contact miscible solutions are consistent with an effective mobility ratio which is too high. One method for fixing up the effective mobility ratio is to choose M_e consistent with the Koval value, arguing that viscosity mixing dominates in the channels of the heterogeneity. This approach is sometimes used in streamtube models. The Koval effective ratio is $M_e = 2.3$. The MISTRESS calculation run with this ratio is shown in Fig. 3.24. The delay in breakthrough is now too great, and this result is not a satisfactory compromise. A second method for choosing the appropriate mobility

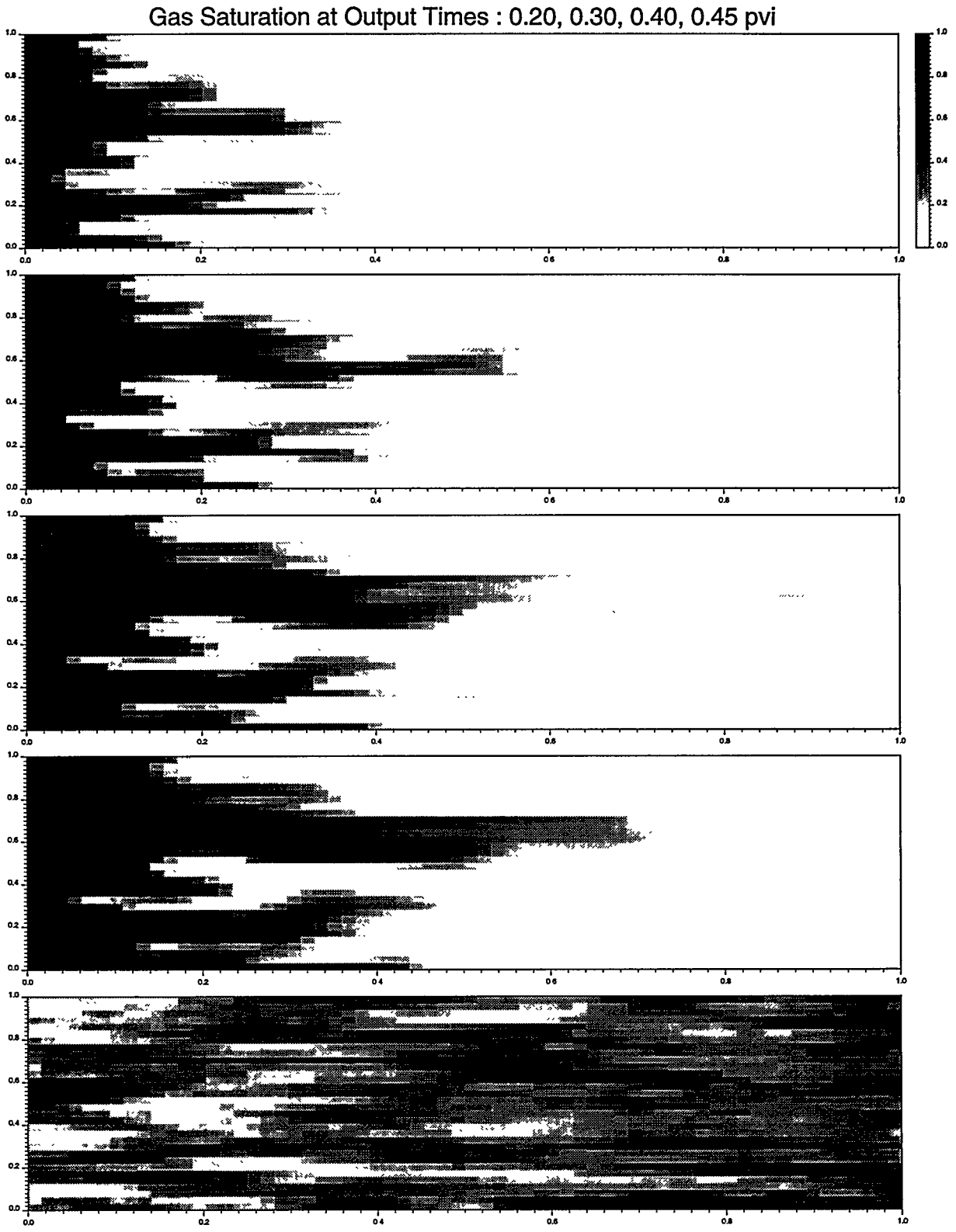

Figure 3.18: MORE four-component run on the reduced grid (no gravity) with straight line relative permeabilities.

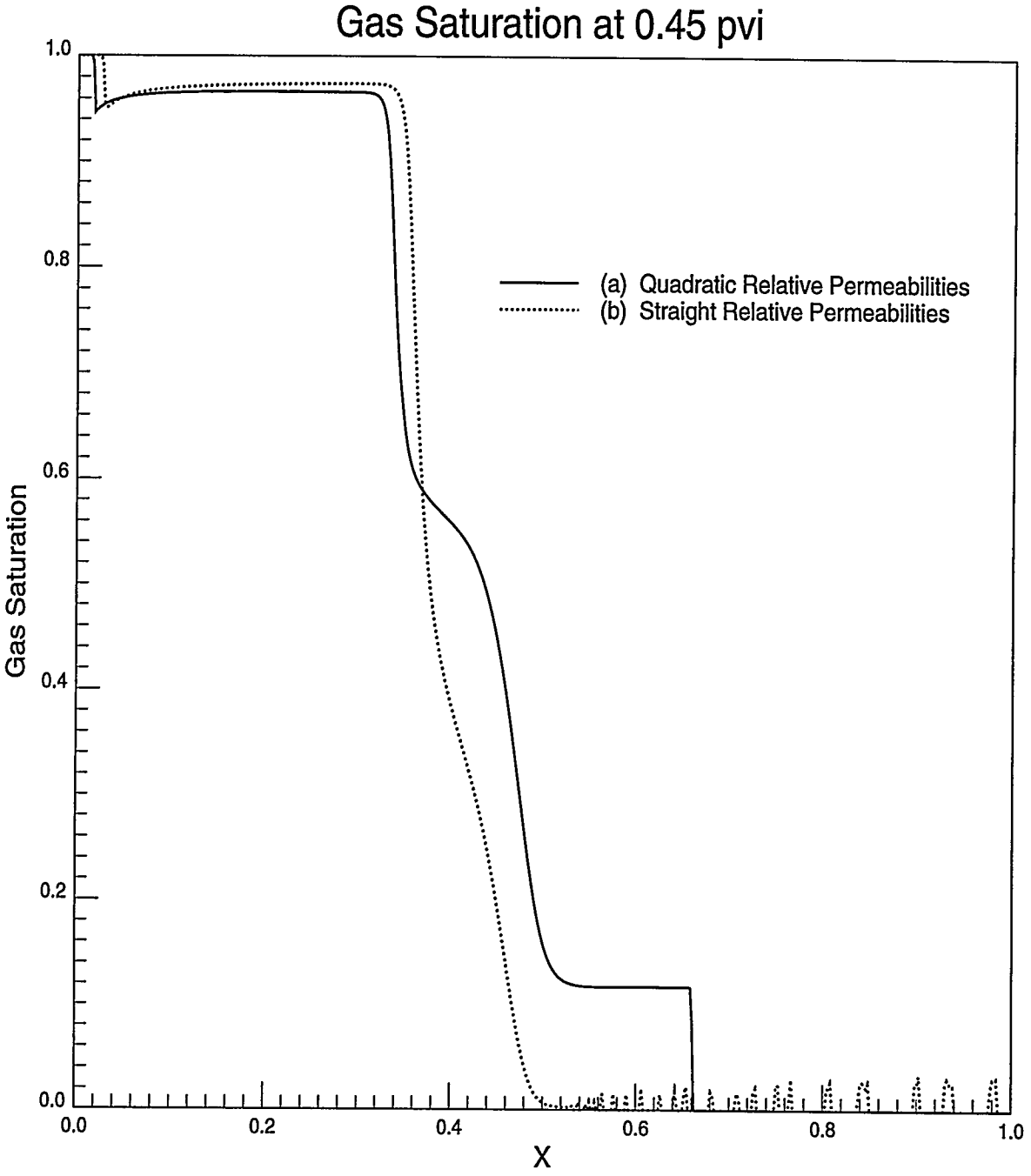

Figure 3.19: MORE four-component run on a homogeneous 1D grid (500 grid blocks).

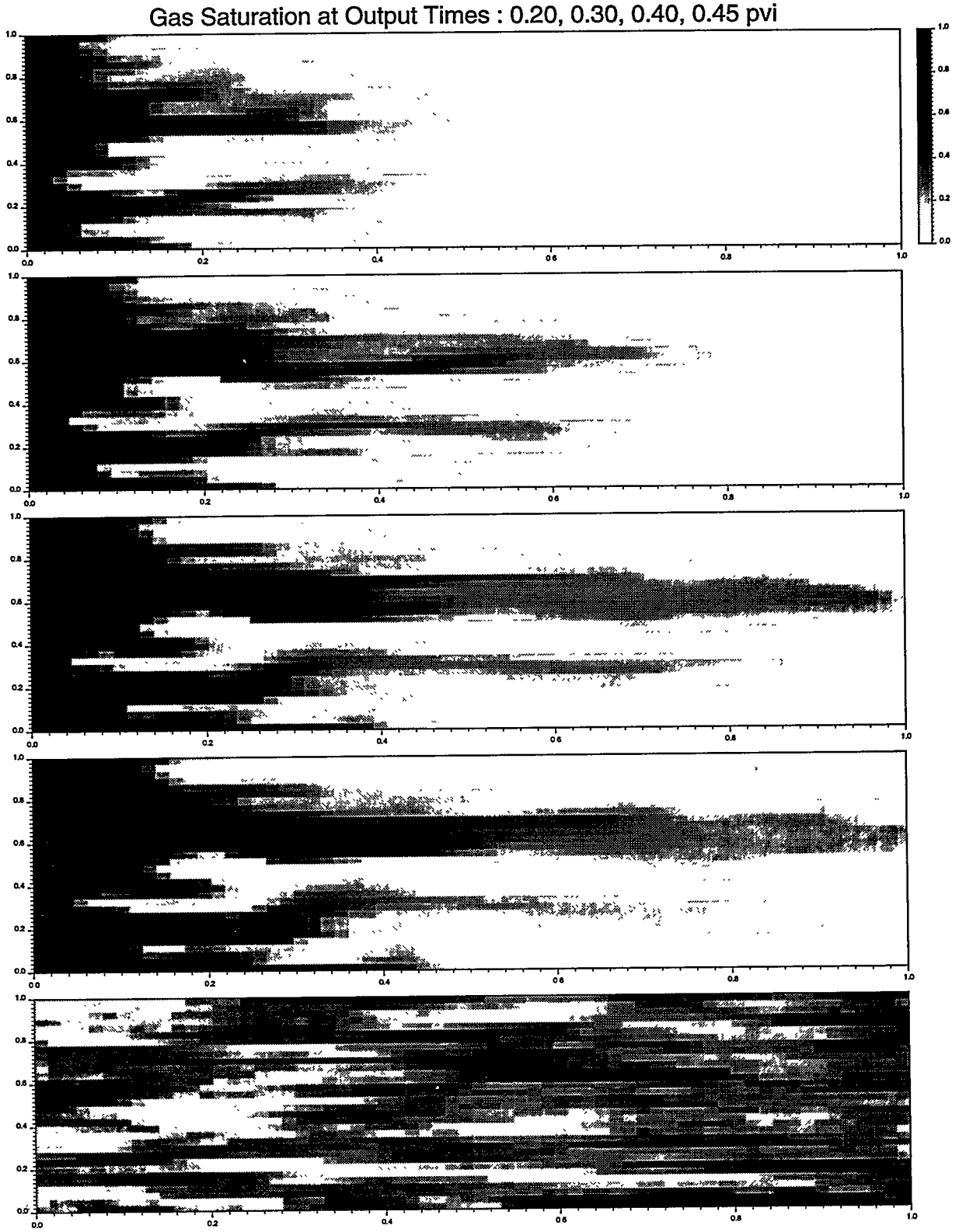

Figure 3.20: MORE four-component run on the reduced grid with IFT-adjusted relative permeabilities (σ_o = 1.0 dyne/cm).

ratio is based on the results of Rubin *et al.* [163] for viscous fingering in compositional problems in homogeneous media. They suggest that the fingering is primarily controlled by the mobility ratio across the principal shock of the analytic 1D solution. The saturations and compositions for curve (a) of Fig. 3.19 in the 500 point 1D calculation were used to estimate the variations in λ_t, the total mobility, as indicated in Fig. 3.25. It is seen that the primary variation occurs between $\lambda_t = 0.44$ and $\lambda_t = 2.20$ giving $M_e \sim 5.0$. A MISTRESS calculation run with this ratio, illustrated in Fig. 3.26, now gives reasonably close agreement with the MORE four-component result in Fig. 3.15. Further examples are needed to test the generality of this equivalencing in heterogeneous problems.

3.2.4 Results with Gravity

Calculations with gravity are known to be sensitive to the effects of heterogeneity, because of the competition between mixing processes. Mixing governs $\Delta\rho$ and therefore controls gravity override, but mixing also controls the viscous drive through high permeability channels, which prevents large scale mixing and therefore modifies phase behavior. In general, we do not expect compositional and first-contact miscible models to be compatible when gravity is important. Cases for the same permeability models have been run for a vertical cross section, again with L/W = 3.0. We use the definition of gravity number given by:

$$N_g = \frac{q(M-1)W}{\Delta\rho g L\sqrt{\bar{k}/\mu_g}} \tag{3.5}$$

where $\Delta\rho$ is the density difference between injected and *in-situ* phases, μ_g is the injected gas phase viscosity and q is the injection rate per unit area at the left boundary. We have used the arithmetic average permeability for our heterogeneous problem. The MORE calculation with $N_g = 2.0$ did not show much gravity effect (contrary to what would be expected for a homogeneous problem [66]; see also Section 4.1). However, results for $N_g = 1.0$ shown in Fig. 3.27 now show significant differences from Fig. 3.16. There is a very early breakthrough caused by the thin gravity tongue in the top layer. Using the fine grid gives much the same results, as seen in Fig. 3.28, but with an even finer tongue. It is necessary to decrease the flow rate by another factor of 5 to give $N_g = 0.2$, before gravity essentially overcomes heterogeneity (Fig. 3.29). The permeability distribution creates asymmetry in the effective horizontal and vertical permeabilities, so that $k_{evff}/k_{heff} < 1.0$. This implies N_g in Eq. 3.5 should be rescaled by, which would probably cause the rescaled N_g in the last case to move closer to 0.5, the value at which gravity override is expected to completely overcome viscous fingering in homogeneous cross sections [66].

A first-contact miscible (FCM) calculation for the case $N_g = 1.0$ run on MORE, illustrated in Fig. 3.30, shows considerably less gravity override than observed in the four-component result in Fig. 3.28. The more pronounced gravity effect arises in the immiscible case because the two phases have different densities which give a finite segregation term in the fractional flow equation. The density difference is largest at the small gas saturation values, which therefore gives a significant upward dispersion appearance to the results in Fig. 3.28. We believe this is a real physical effect, and not an artifact arising from numerical dispersion. At $N_g = 0.2$, the FCM-calculation with MORE shown in Fig. 3.31, is nearly dominated by gravity, but nevertheless by not quite as much as in the four-component result in Fig. 3.29.

It would be useful to find an effective density difference, or effective vertical permeability, for equivalencing a MISTRESS calculation with gravity effects to the equivalent MORE four-component model. We first ran MISTRESS with trial values of $N_g = 0.33$ and M = 20, as illustrated in Fig. 3.32. The gravity override is too severe and the fingers are too thin. Since M = 5.0 gave the appropriate equivalencing of the mobility ratio in the nongravity case, the next MISTRESS case in Fig. 3.33 was for $N_g = 0.33$ and M = 5.0. The magnitude of gravity override is now

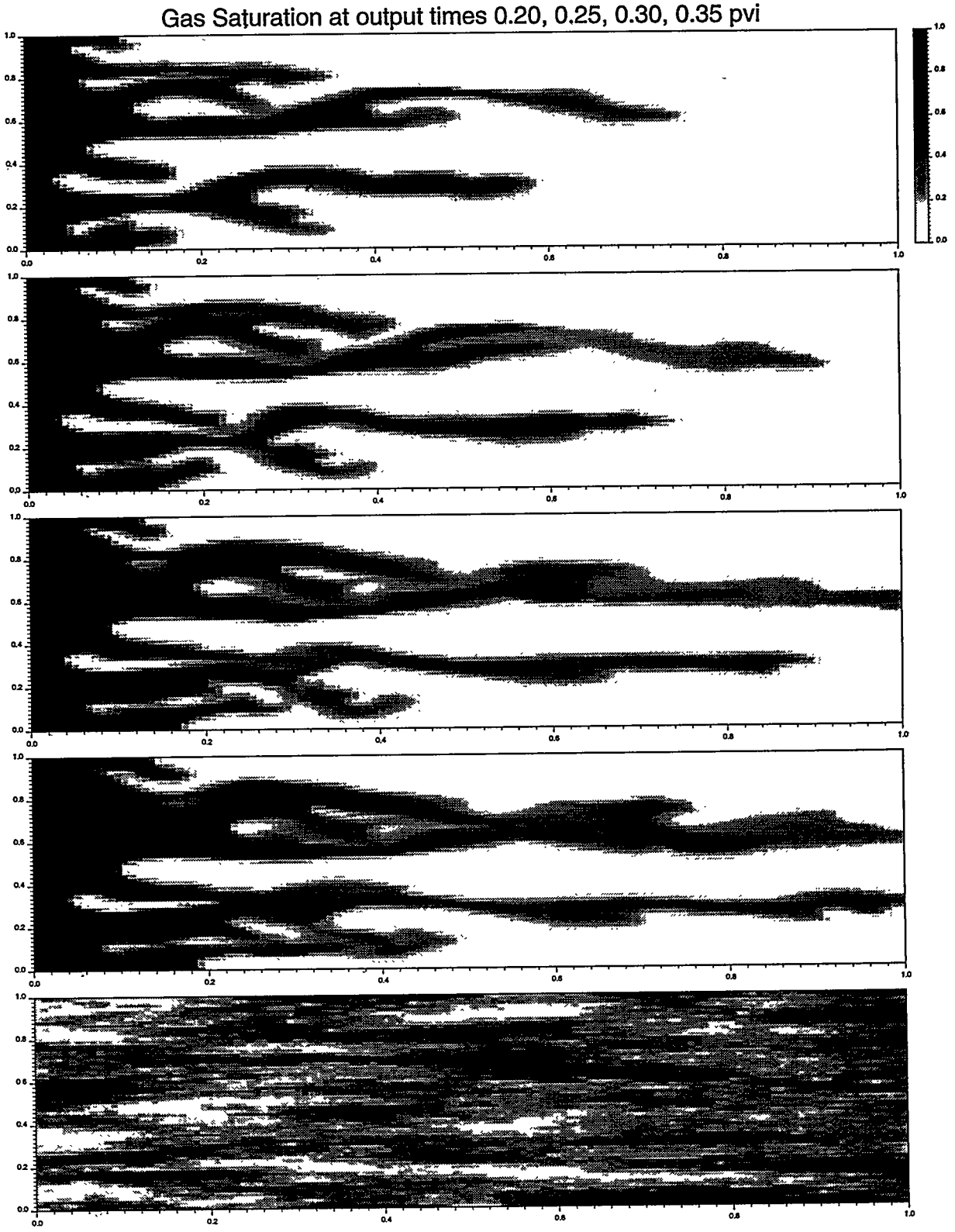

Figure 3.21: MISTRESS run with M = 20 on the fine grid (no gravity).

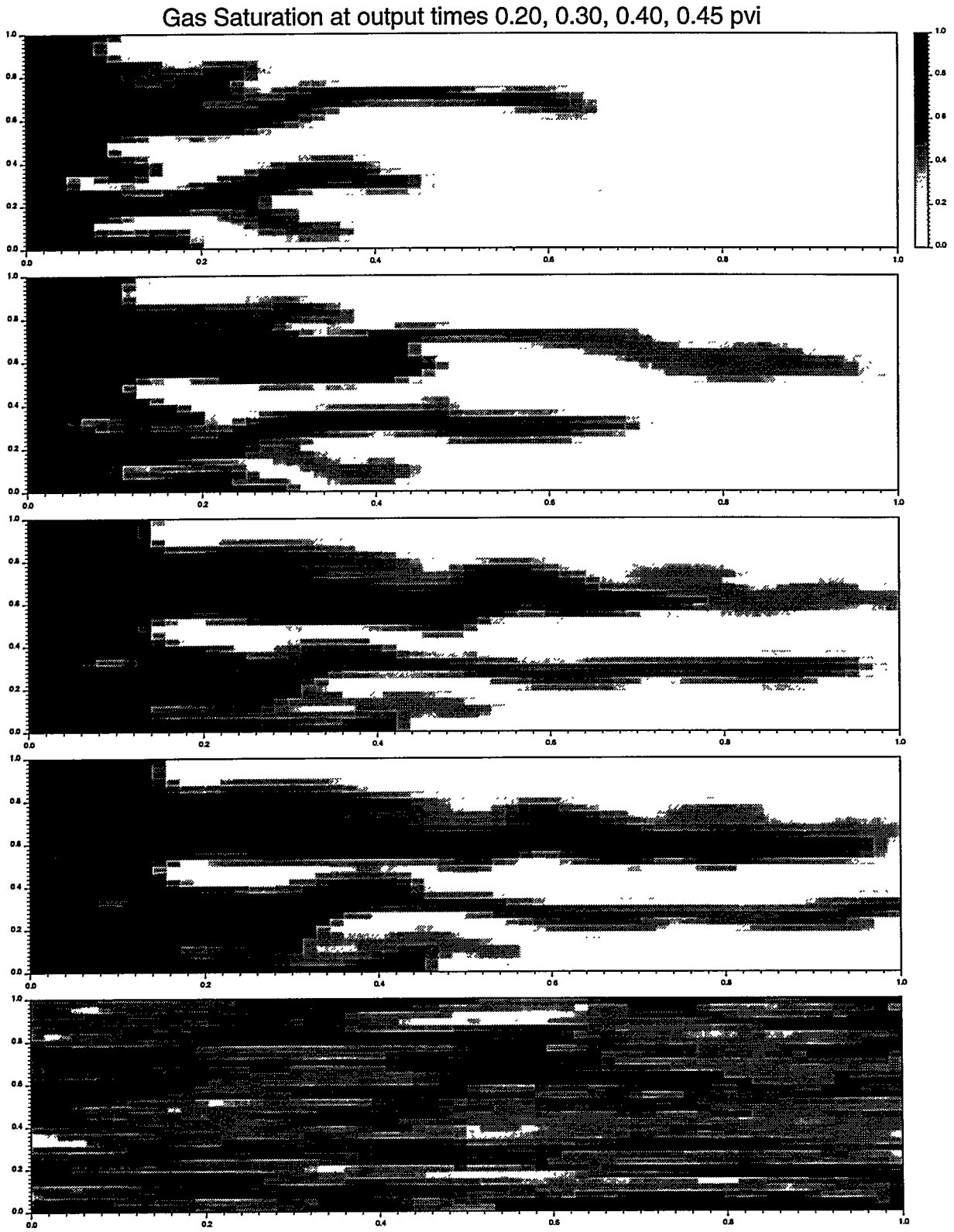

Figure 3.22: MISTRESS run with M = 20 on the reduced grid (no gravity).

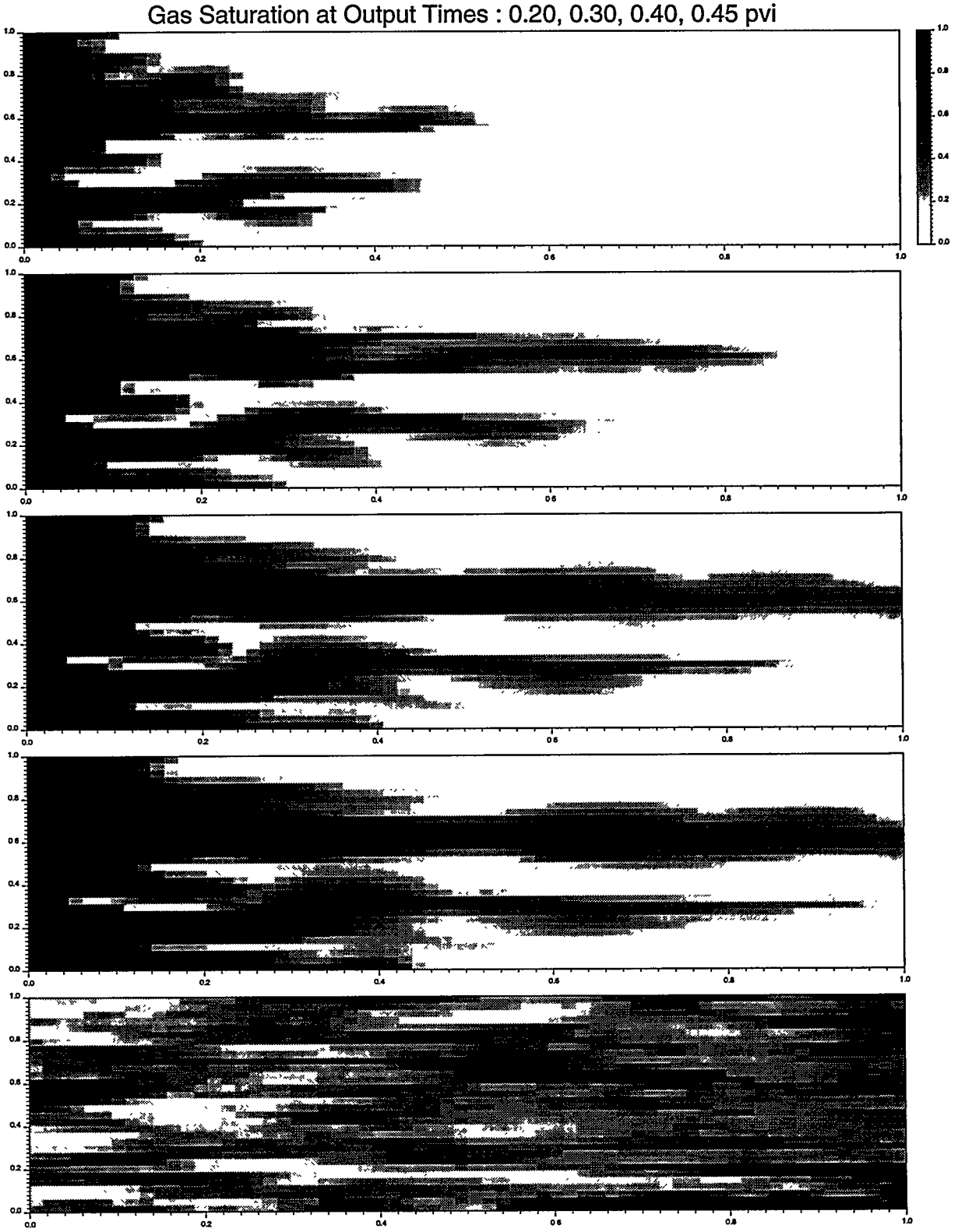

Figure 3.23: MORE "first-contact miscible" run on the reduced grid (M = 20 and no gravity).

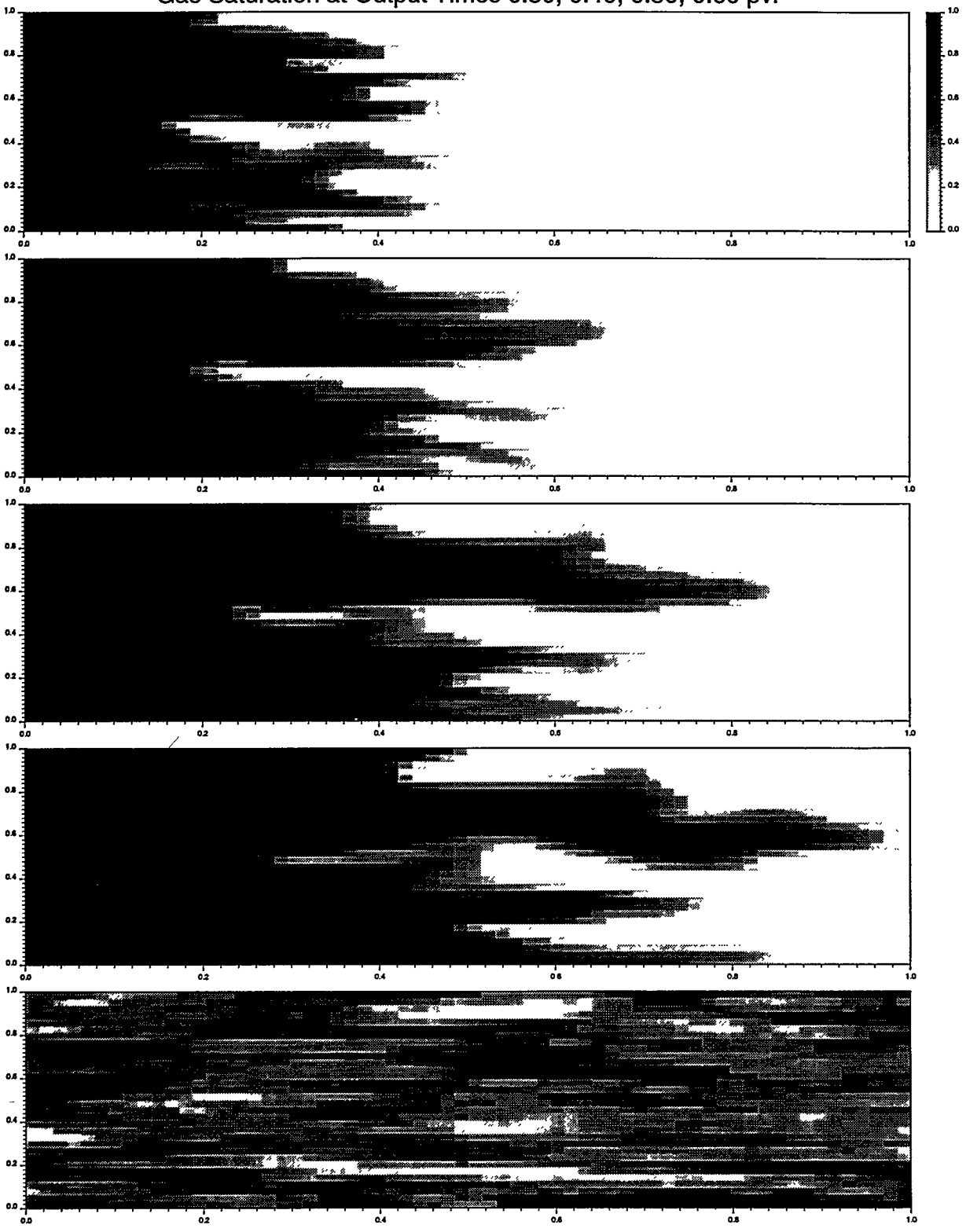

Figure 3.24: MISTRESS run with M = 2.3 on the reduced grid (no gravity).

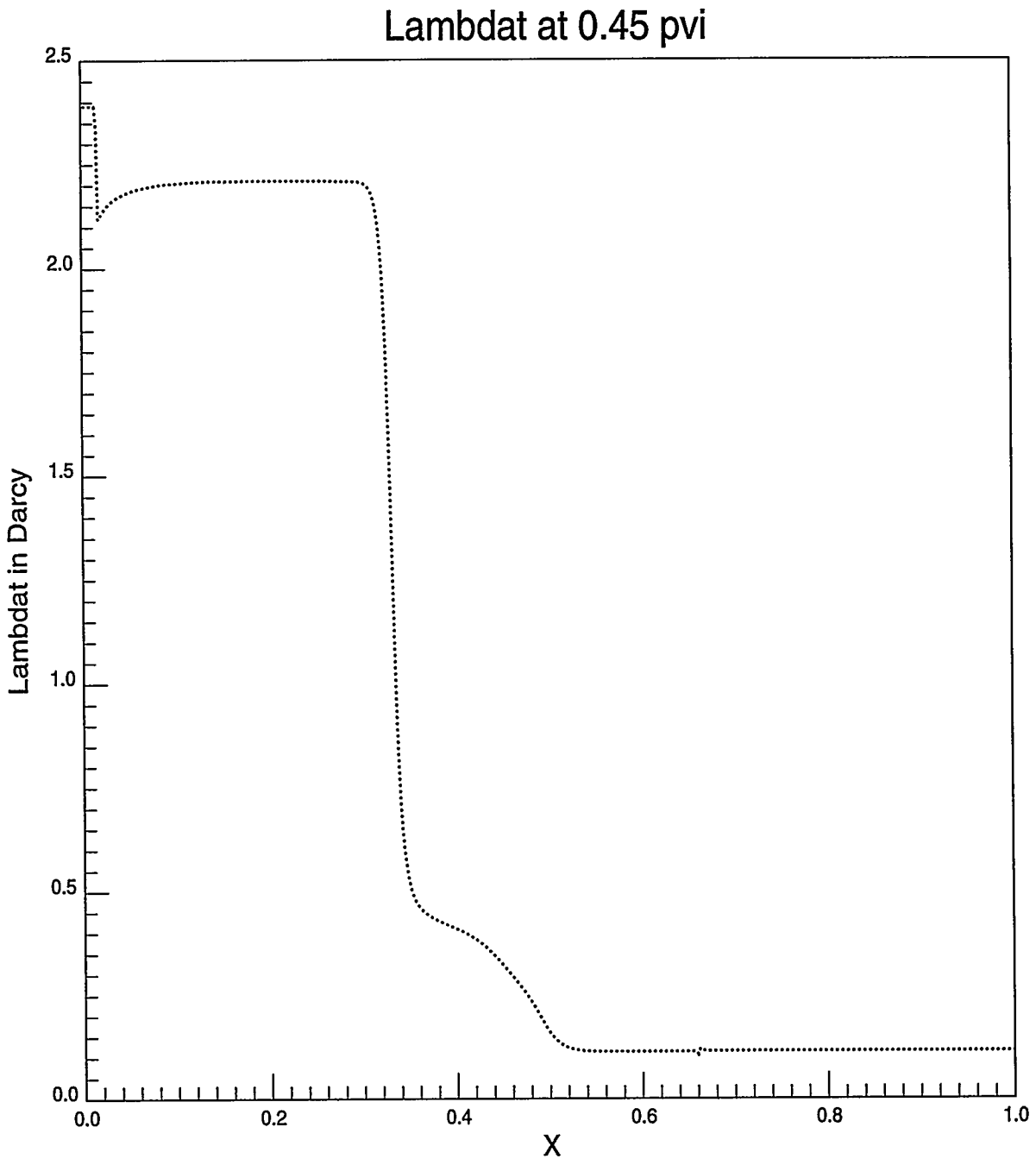

Figure 3.25: MORE four-component run on a homogeneous 1D grid (500 grid blocks).

somewhat reduced; that is decreasing the mobility ratio causes the growth rate of the gravity tongue to be reduced in favor of the fingers caused by the heterogeneous channels. An FCM-calculation in Fig. 3.34, run on MORE with M = 5.0, N_g = 0.33, gives a result slightly closer in appearance to the four-component model in Fig. 3.28, where the additional numerical dispersion helps the comparison. Thus we have found an *ad hoc* correction to the gravity number, which when combined with an appropriate mobility ratio, allows the FCM-calculation to essentially reproduce the compositional behavior. In summary, for cross sections with gravity effects, this work illustrates that enhanced gravity segregation rates can occur with a submiscible process, particularly at the lower gas saturations. The enhancement is of the order of a factor of three (i.e. very significant) in the problem studied. We have not yet found a simple method for predicting this equivalencing factor.

3.2.5 A Simple One-Dimensional Approximation for Heterogeneous Flows Without Gravity

We have seen that a 2D-heterogeneous MISTRESS calculation can be made to represent a MORE 2D-heterogeneous compositional problem provided an appropriate mobility ratio is used. This mobility ratio was chosen from the change in total mobility across the mobility front in Fig. 3.25, implying the need to perform a 1D-compositional calculation as a precursor to the 2D first-contact miscible case. A further step in simplifying these problems can now be contemplated. The Koval model contains the empirical parameter H, which is recommended as a measure of heterogeneity, to correct the effective mobility ratio M_e appropriate to viscous fingering in a heterogeneous system. The Koval fractional flow is given by

$$F = \frac{C}{C + (1 - C)/HM_e} \tag{3.6}$$

C is the average solvent concentration across any y-section of the 2D fingering pattern, and M_e is the Koval effective mobility ratio, given by

$$M_e = \mu_o \left(0.22\mu_g^{-1/4} + 0.78\mu_o^{-1/4}\right)^4 \tag{3.7}$$

For homogeneous (H = 1.0) viscous fingering problems, Eq. 3.6 represents the average fractional flow behavior and the consequent average C(x) profiles very well. For the submiscible problem studied in this paper, the appropriate mobility ratios are M = 5 and M_e = 1.512 from Eq. 3.7. It remains to determine the appropriate value for H for our mildly heterogeneous example. Koval recommended that H be determined by fitting to the results of a displacement calculation for the real heterogeneity distribution, run with M = 1.0. The unit mobility problem is simpler than a problem with $M \geq 1.0$, since the pressure solution (Laplace's equation) has only to be determined once. Fig. 3.35 shows MISTRESS average concentration distributions obtained for M = 1.0. These are compared with the Koval model for M = 1.0, with a reasonable choice, H = 1.5. This value of H appears to give quite a good fit. Referring back to the earlier M = 5 solution with MISTRESS in Fig. 3.26, the consequent plots of $C(x)$ and the Koval model with H = 1.5 and M_e = 1.512 are compared in Fig. 3.36. Equally good results are also obtained for M = 20, and higher mobility ratios. The need for an explicit M = 1 solution to determine an appropriate value of H could be avoided if there were some simple rule or correlation for calculating this quantity. Koval recommended use of a correlation graph, which is fitted by the equation

$$logH = \frac{V_{DP}}{(1 - V_{DP})^{0.2}} \tag{3.8}$$

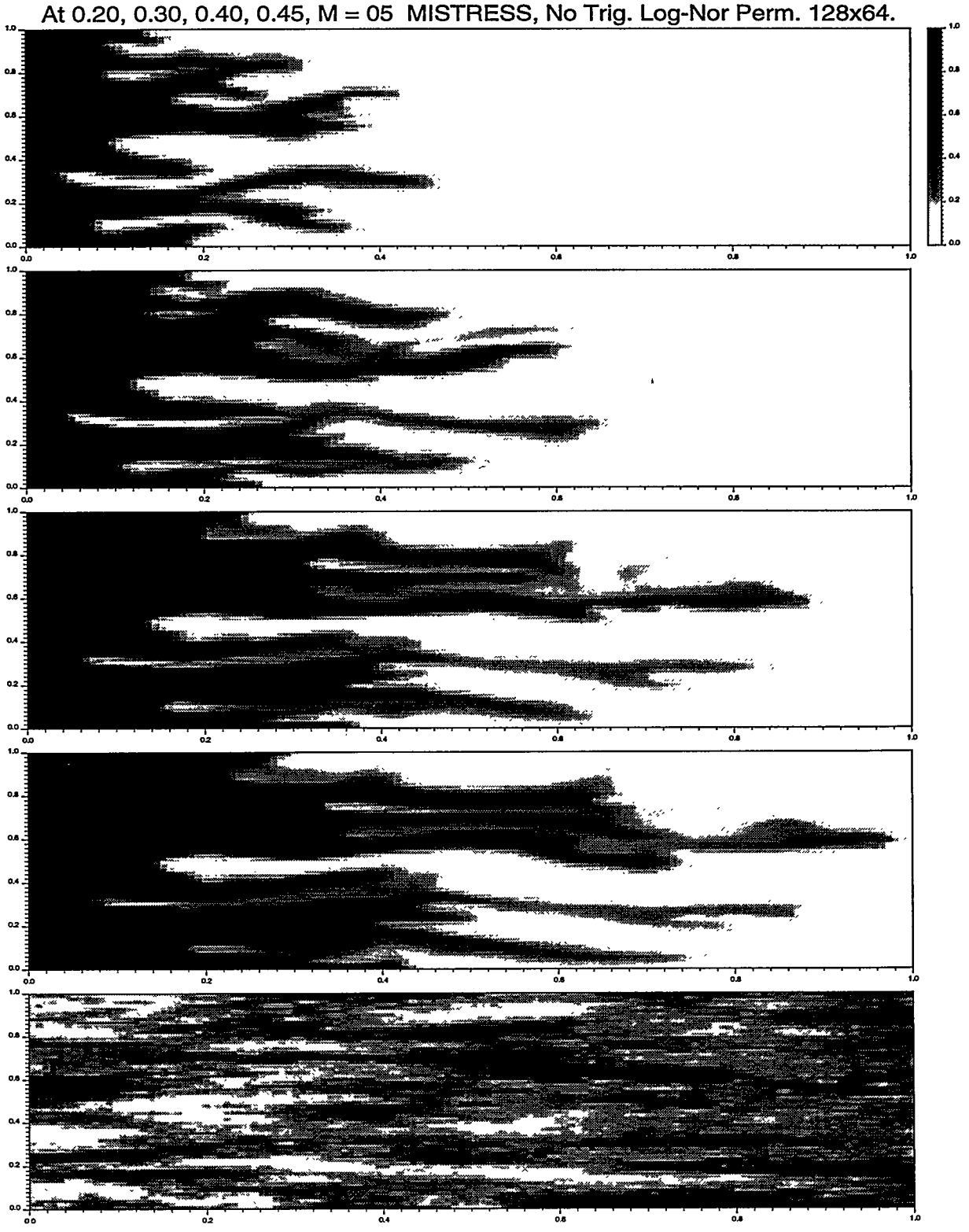

Figure 3.26: MISTRESS run with M = 5 on the fine grid (no gravity).

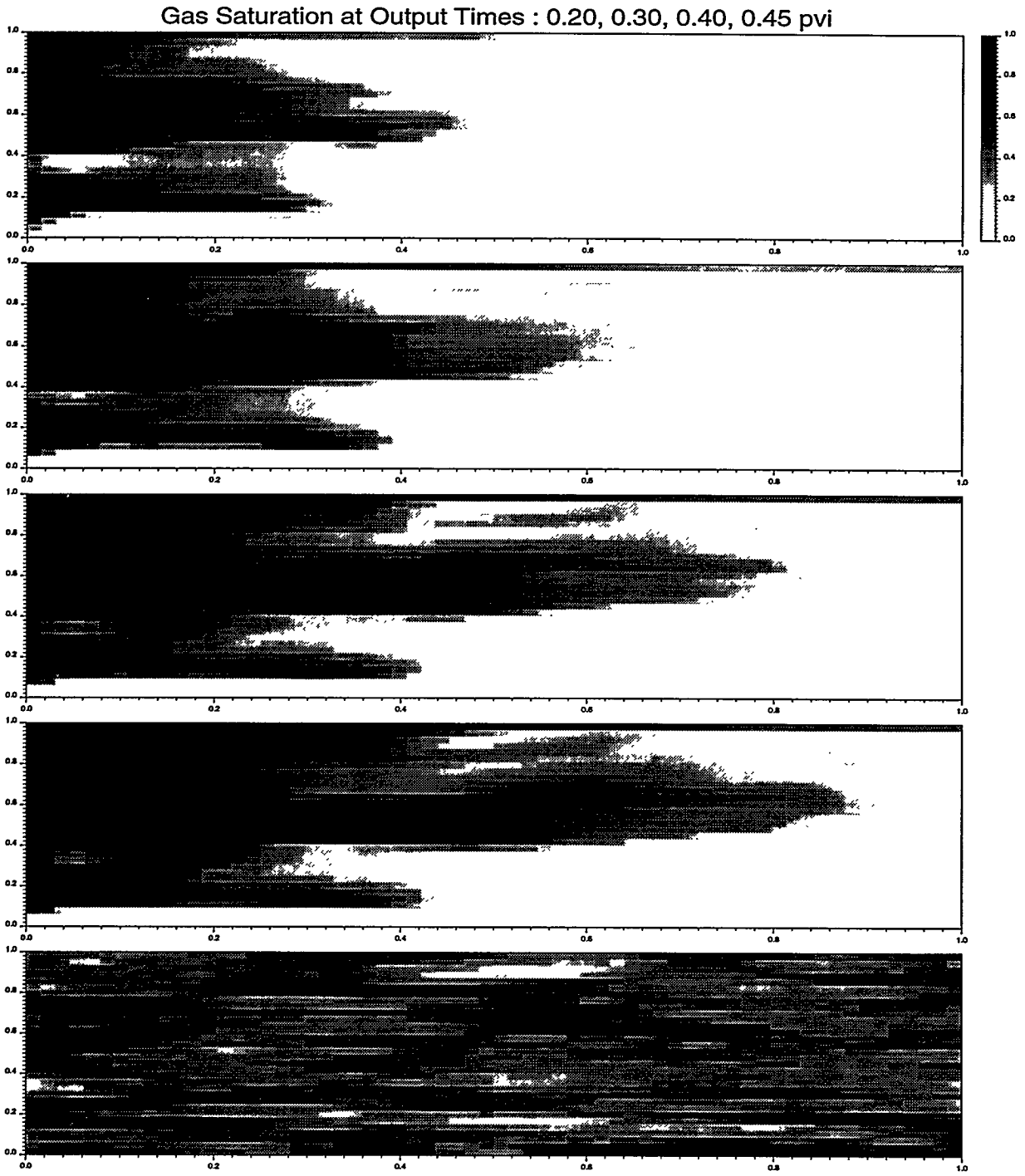

Figure 3.27: MORE four-component run on the reduced grid ($N_g = 1$).

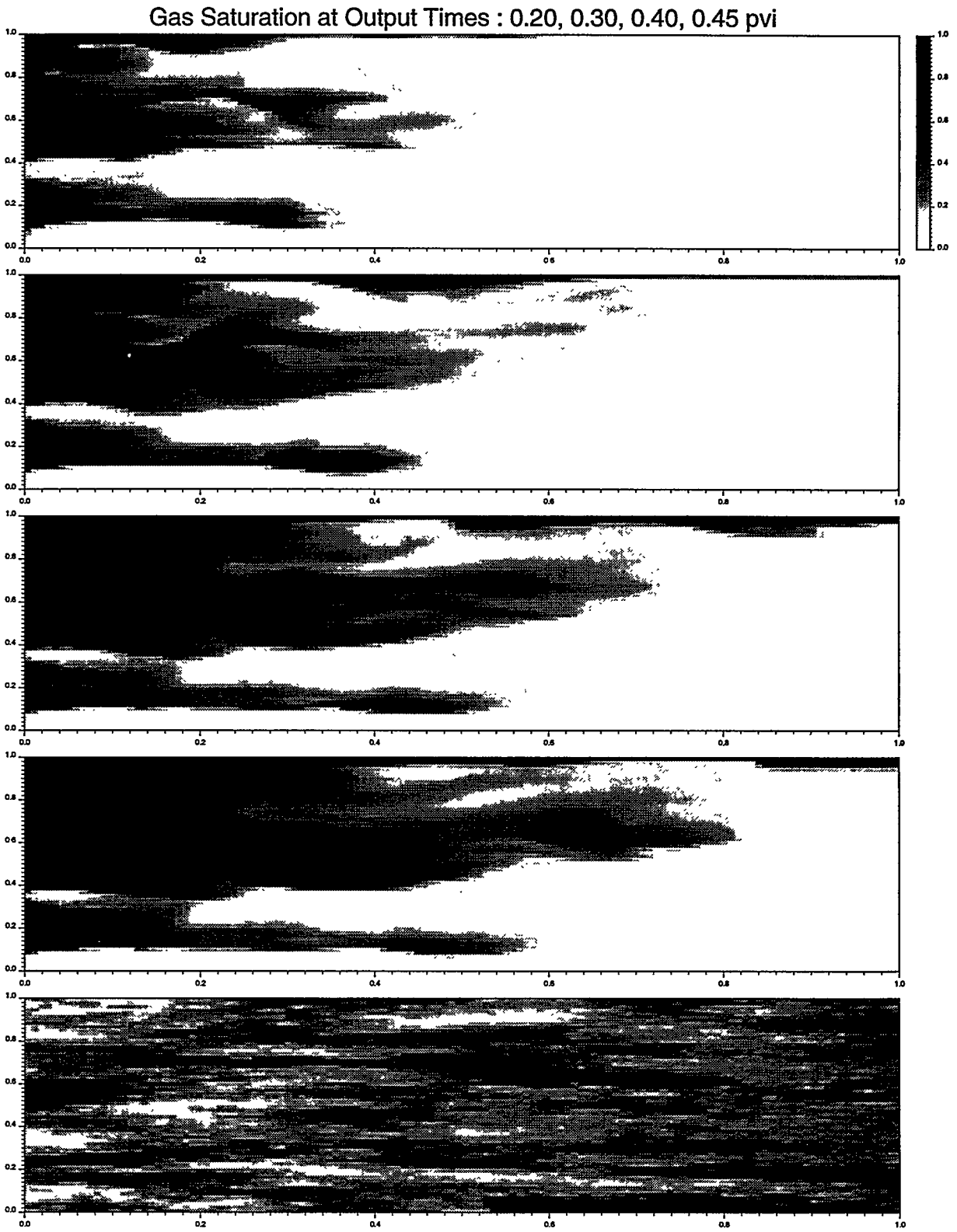

Figure 3.28: MORE four-component run on the fine grid ($N_g = 1$).

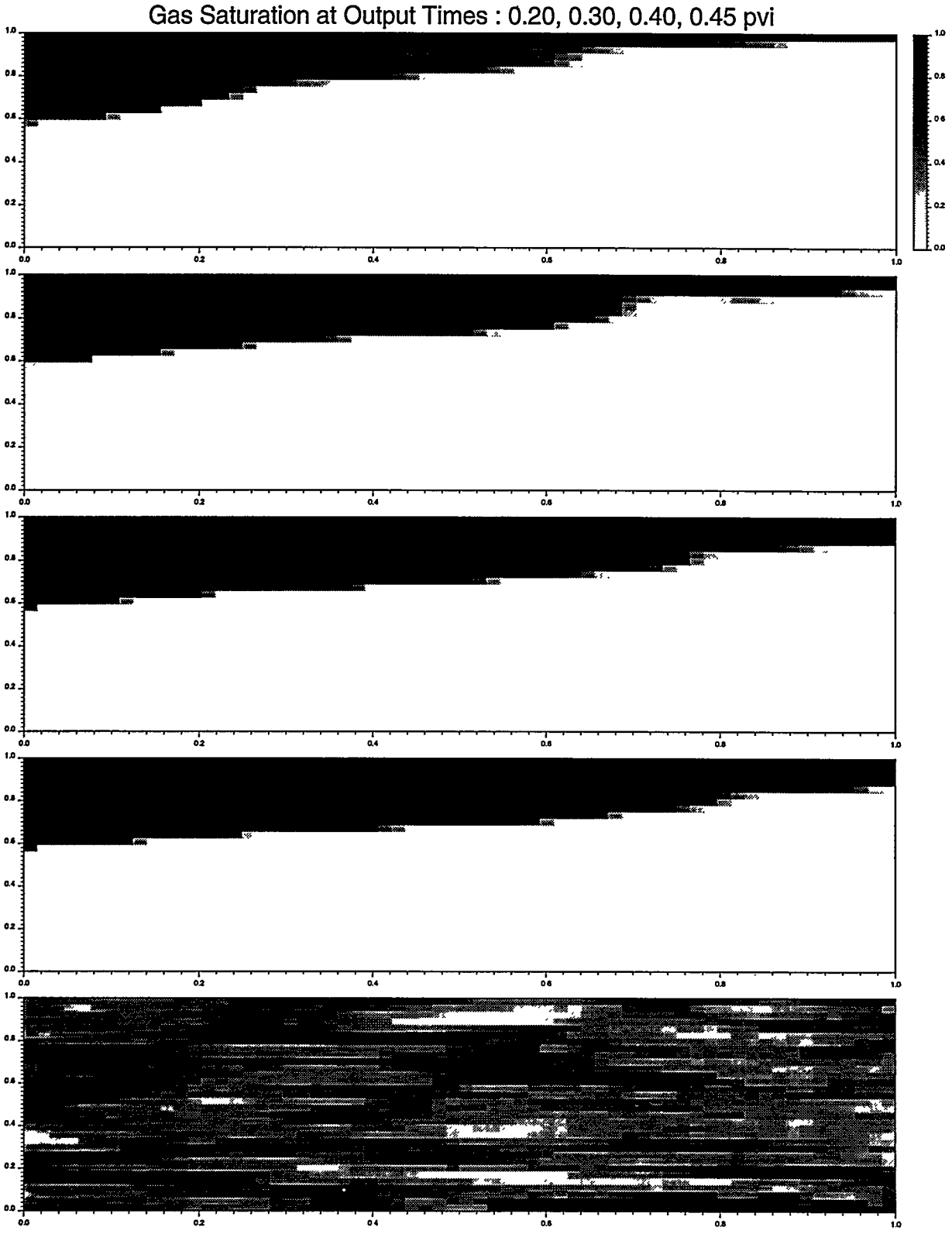

Figure 3.29: MORE four-component run on the reduced grid ($N_g = 0.2$).

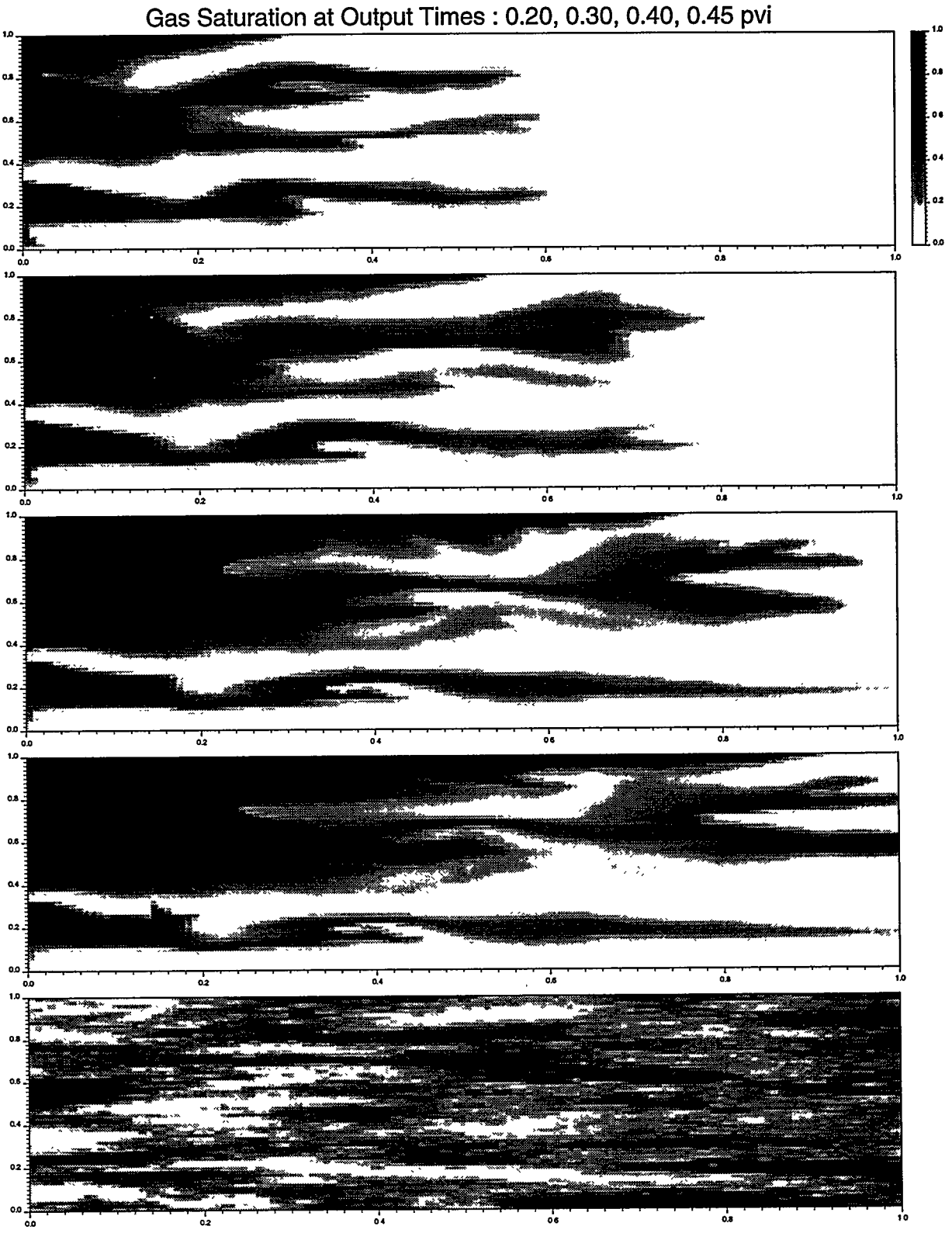

Figure 3.30: MORE "first-contact miscible" run (M = 20) on the fine grid ($N_g = 1$).

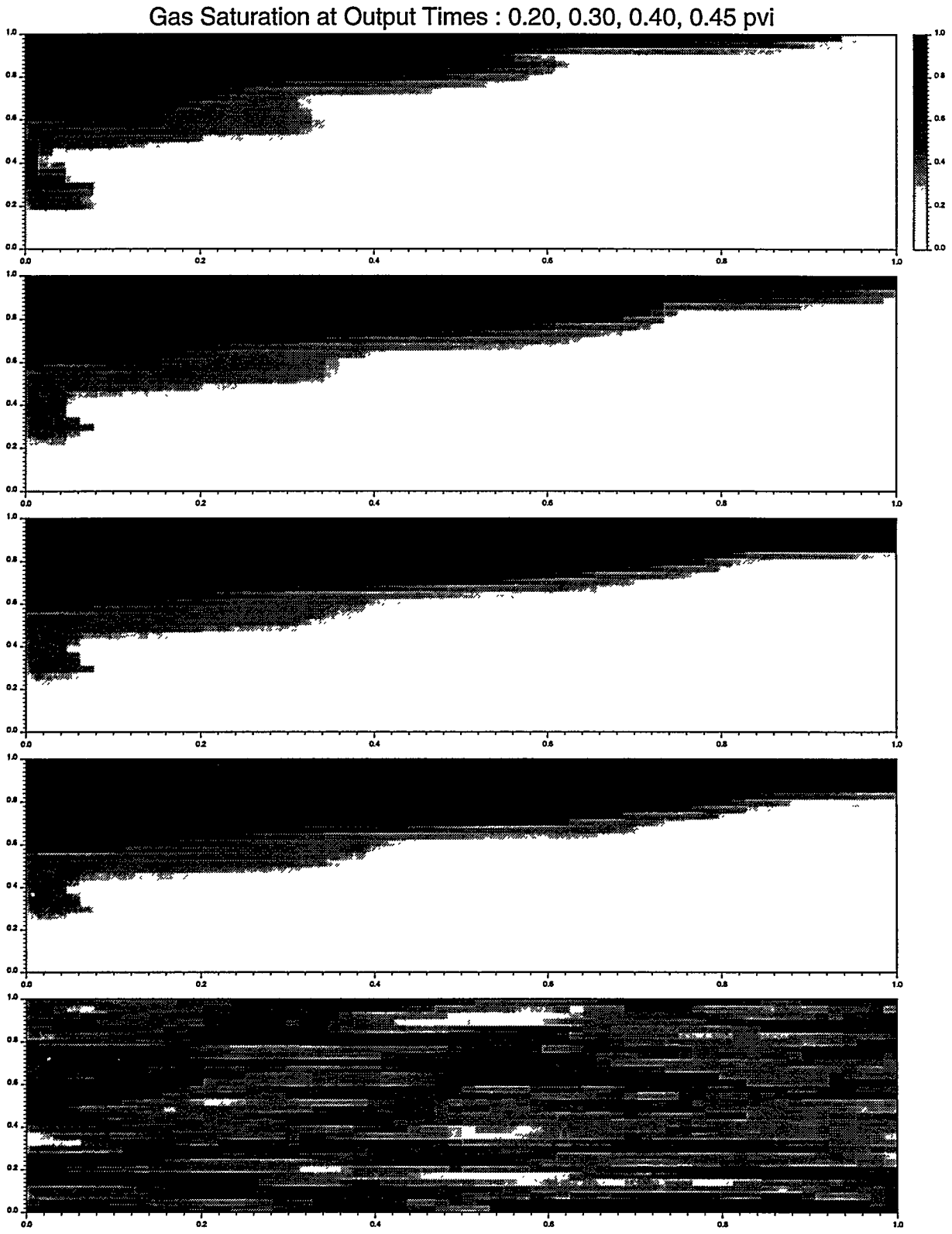

Figure 3.31: MORE "first-contact miscible" run (M = 20) on the reduced grid ($N_g = 0.2$).

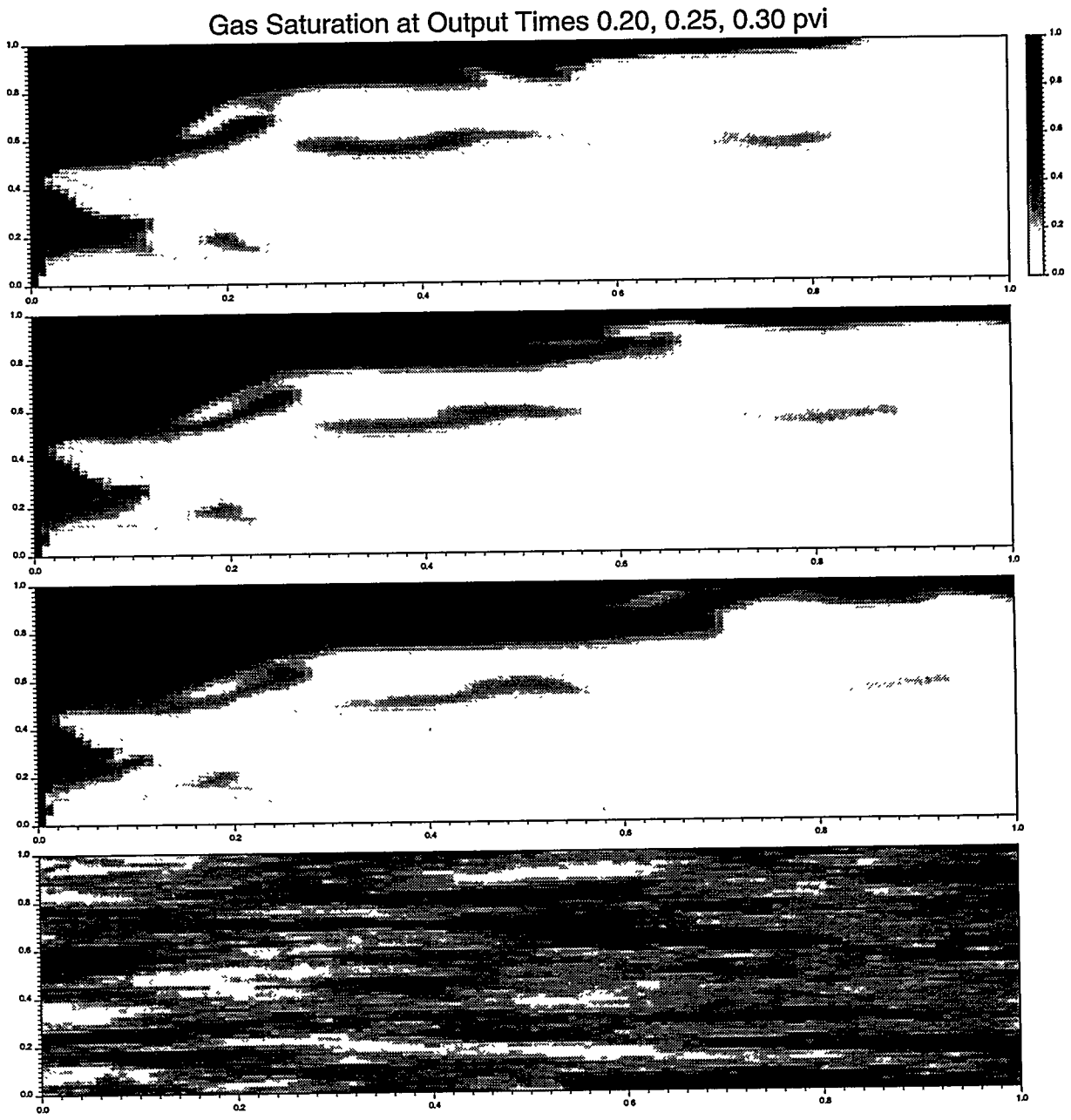

Figure 3.32: MISTRESS run with M = 20 on the fine grid ($N_g = 0.33$).

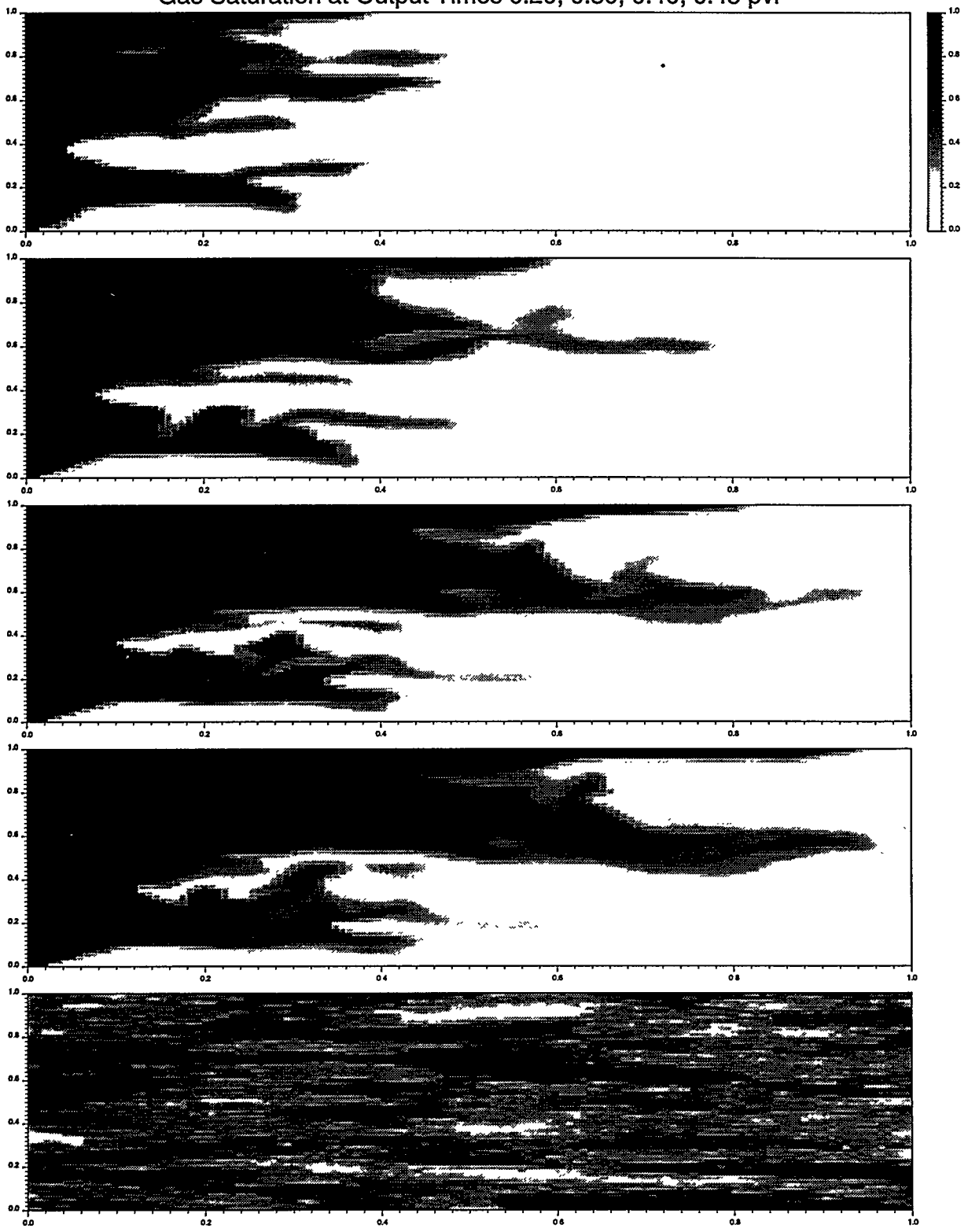

Figure 3.33: MISTRESS run with M = 5.0 on the fine grid ($N_g = 0.33$).

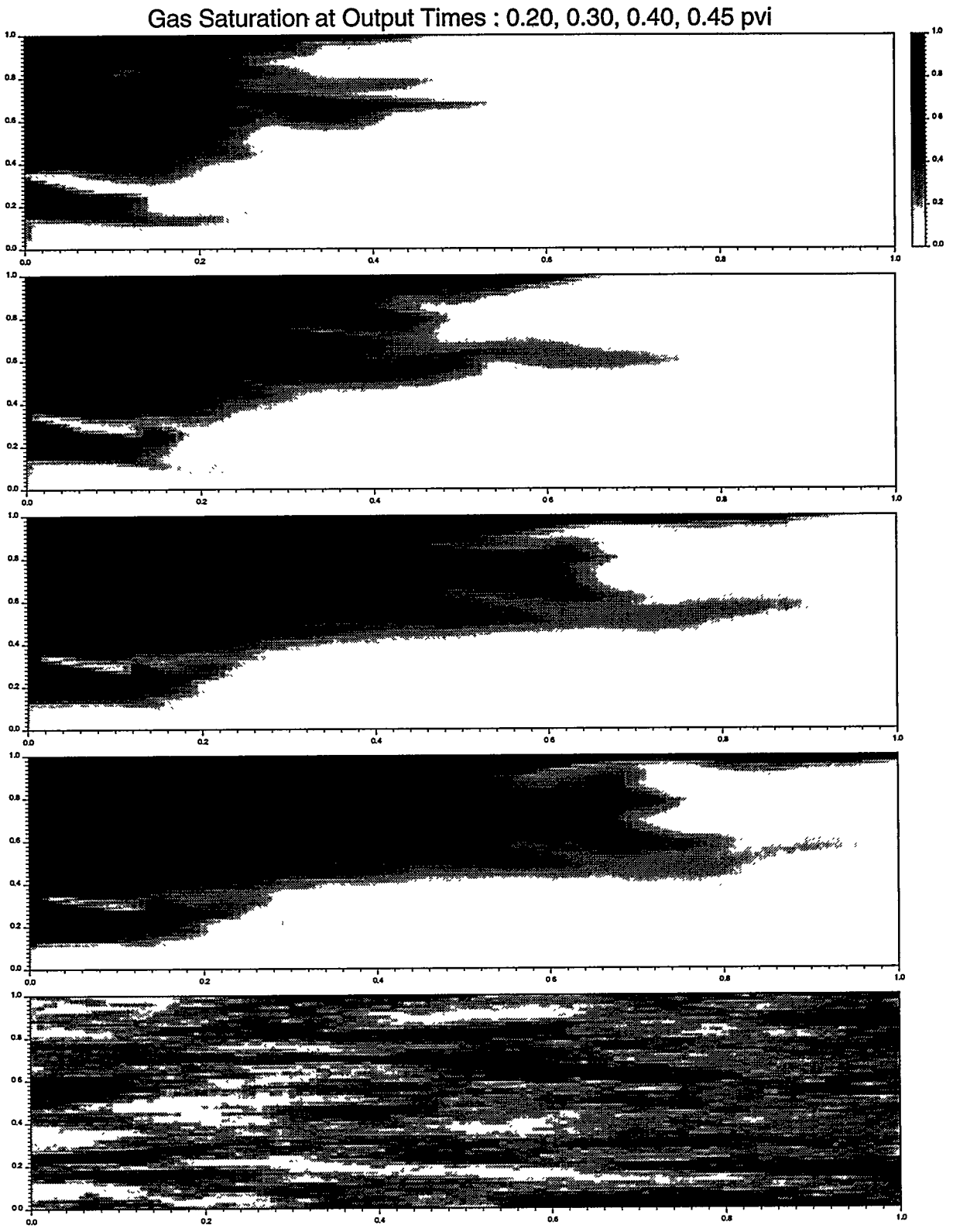

Figure 3.34: MORE "first-contact miscible" run (M = 5) on the fine grid ($N_g = 0.33$).

This result was largely based on studies for layered systems and for our problem would give 3.75, which is far too large. Araktingi and Orr [6] suggested that an important parameter is the heterogeneity index defined by

$$H_i = \sigma^2_{logk}\alpha_l/L. \tag{3.9}$$

This relation gives 0.095, which is below the cut-off suggested by Araktingi and Orr for heterogeneities to influence fingering significantly. It seems unlikely that H will be a simple function of H_i. For example, our results are for L/W = 3.0, and it is known that viscous fingering behavior is dependent on this ratio, and it will also depend on α_t/W, the dimensionless transverse correlation length.

3.2.6 Conclusions

The following conclusions apply to our results for a "mildly" heterogeneous problem, although other examples of heterogeneity would need to be studied:

(i) A multicomponent compositional calculation in a heterogeneous medium can be adequately represented by phase behavior from relatively few components (in the range 4-6).

(ii) A compositional simulator without special differencing methods [12] operated in a first-contact miscible mode, or in a multicomponent mode with straight-line relative permeabilities, will show severe numerical dispersion at low gas saturations, although this is less pronounced at higher saturations. When used with conventional immiscible relative permeabilities, a multicomponent calculation appears to give acceptable dispersion errors.

(iii) Near-miscible heterogeneous problems run in a compositional framework do not appear to give low enough interfacial tensions to justify use of modified relative permeabilities. This is not likely to be true for capillary pressures for problems at smaller scale sizes [63].

(iv) First-contact miscible calculations run at the initial fluid mobility ratio show much more adverse viscous fingering in a heterogeneous system than their compositional equivalent, i.e. miscible displacement is less unstable than initial estimates may suggest.

(v) An effective mobility ratio can be found for running a nongravity heterogeneous problem in a first-contact miscible mode. This mobility ratio is given by the shock front change in total mobility from an accurate 1D-solution.

(vi) The first-contact miscible solution for the nongravity heterogeneous problem is well represented by a Koval model with H chosen from the $M = 1$ solution. Better understanding is needed of the factors which control H.

(vii) Heterogeneities interact strongly with gravity segregation and reduce the magnitude of the latter. Increasing the mobility ratio increases the gravity override for a constant gravity number.

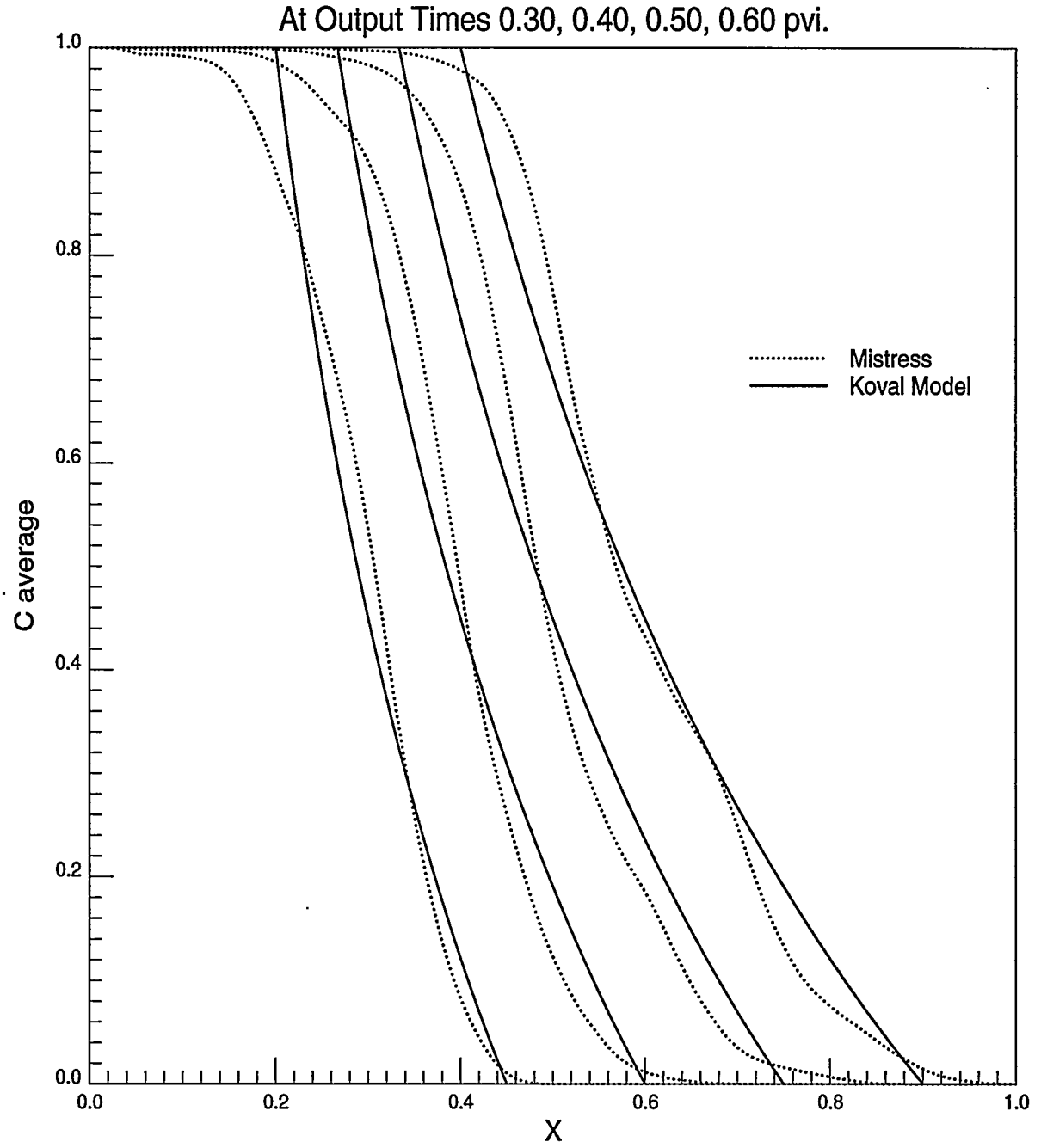

Figure 3.35: Comparison of MISTRESS average concentration profiles with Koval model for M = 1.0 and H = 1.5.

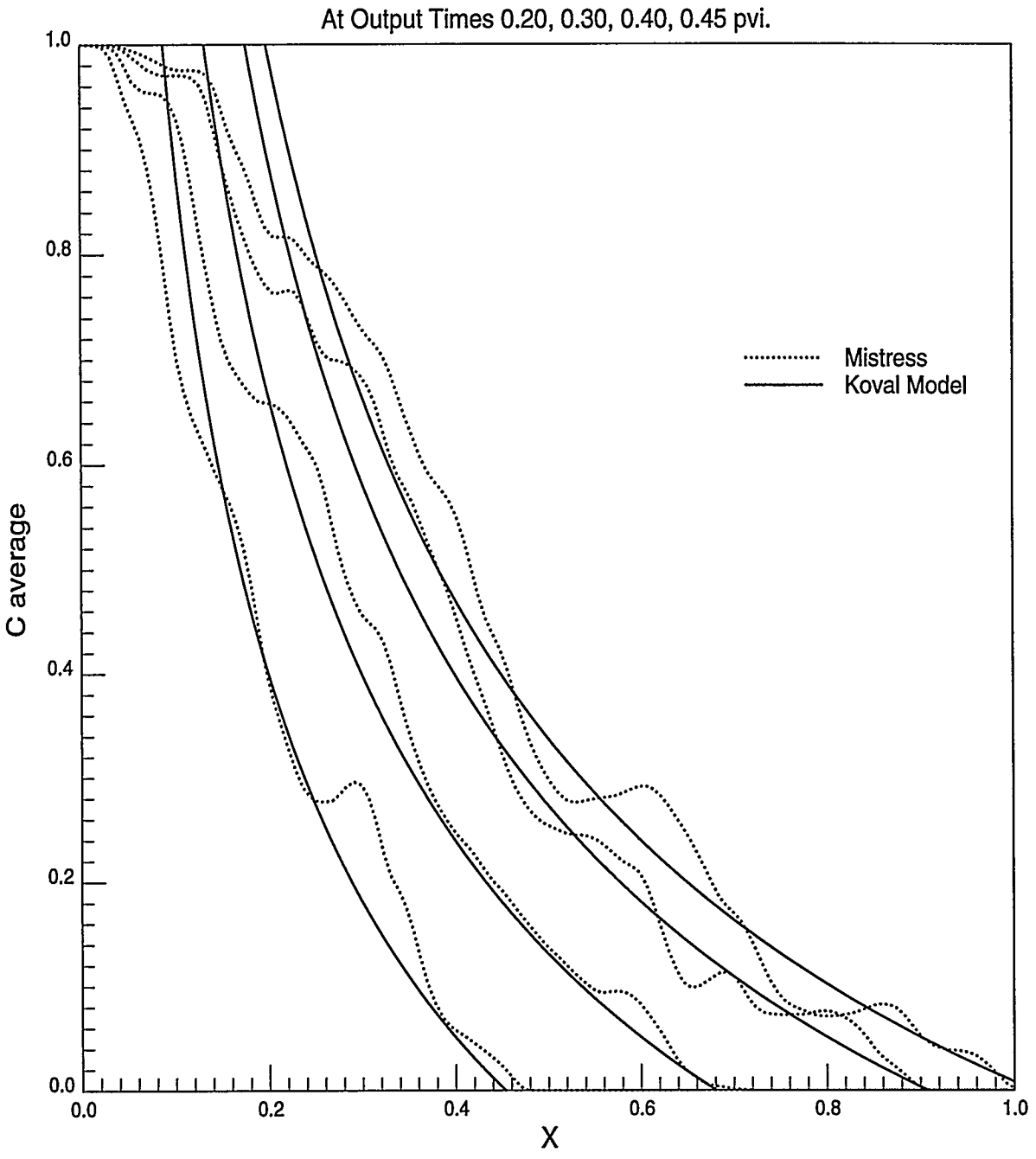

Figure 3.36: Comparison of MISTRESS average concentration profiles with Koval model for M = 5.0 and H = 1.5.

4. Modeling Multiphase Flow in Heterogeneous Media Using a Streamline/Streamtube Technique

The results of Chapter 3, along with the work of a variety of investigators [6, 134, 181, 179, 24, 192, 170] indicate that in many flow situations, the spatial distribution of permeability dominates the flow. Low viscosity injected fluid follows preferential flow paths created by heterogeneities rather than forming viscous fingers.

The particle-tracking method employed in Chapter 3 is an efficient way to explore the transition from viscous-dominated to permeability-dominated flow, but it is not suitable for multiphase flow problems because it does not capture the behavior of shocks that form when dispersion has small effect (see Chapter 2). In this chapter we explore use of related methods that make use of streamtubes and streamlines to create very fast simulation techniques for multiphase flow in heterogeneous systems. In Section 4.1 we consider single- and two-phase flow in two-dimensional heterogeneous porous media. Section 4.2 extends the approach to consider the kind of compositional displacements studied for one-dimensional flow in Chapter 2. Section 4.3 shows how to extend these ideas to three-dimensional flows.

The simulation approach outlined in this chapter has great promise because it is orders of magnitude faster than conventional simulations, and it is not subject to large errors due to numerical dispersion. It works best when the flow is dominated by the permeability distribution. The most important limitation is the restriction to processes in which gravity forces have limited effect. Research to remove that limitation is underway.

4.1 Modeling Flow in Heterogeneous Media Using Streamtubes: I. Miscible and Immiscible Displacements

M. R. Thiele, M. J. Blunt, and F. M. Orr, Jr.

The primary objective of the streamtube approach is to enable fast and accurate numerical solutions for displacements through heterogeneous systems. The fundamental assumption in our approach is that field-scale displacements are dominated by reservoir heterogeneity; flow paths are governed by the permeability distribution, while the fluid composition along these flow paths is similar to that seen in an equivalent one-dimensional displacement.

The motivation for this research originated from recent advances in the one-dimensional theory of multicomponent, two-phase, compositional displacements [104, 46, 148] (see Chapter 2) and a desire to extend these solutions to two-dimensional heterogeneous systems. Motivation for a fast numerical technique was also sparked by the now established statistical methods used in reservoir description [44]. It is possible to generate many equiprobable geostatistical realizations of a reservoir having several million gridblocks, conditioned possibly on log data, core analysis, and seismic data. However, simulation of multiphase displacements using conventional numerical models is limited to a few simulations on systems containing around half a million gridblocks or less for first-contact miscible displacements [180, 34, 31], and only around ten thousand gridblocks for compositional displacements [15, 27]. Estimating recovery from hundreds of detailed reservoir models to obtain a statistical spread in cumulative oil recovery is beyond current computational capabilities, forcing either the use of upscaling techniques [113, 114] or rapid but approximate solution techniques that adequately represent the dominant displacement process.

In this work, we explore the use of a streamtube method as an approximate but rapid and efficient solution technique to model multiphase flow in heterogeneous media. Streamlines and streamtubes have been used extensively in the past to model displacements in regular and irregular well patterns. Important contributions are from Higgins and Leighton [85, 86], Higgins *et al.* [87], Parsons [152], Martin and Wegner [126], Bommer and Schechter [20], Lake *et al.* [117], Emanuel *et al.* [56], and Hewett and Behrens [84]. A successful use of streamtubes has been demonstrated by Emanuel *et al.* [56], in which a conventional finite-difference simulator was used to compute the average fractional flow and total mobility for a representative, heterogeneous cross section as suggested by Lake *et al.* [117]. The one-dimensional solution resulting from the average fractional flow was then mapped along fixed streamtubes representing flow paths for a complex well pattern in an areal heterogeneous system. To account for the changing mobility field, the flux along each streamtube was varied in proportion to the total resistance of each streamtube [85, 86], but the streamtubes were fixed in time. This method reliably reproduced field performance in nine cases, including a CO_2 displacement.

In our work we use a different approach [183, 185]: the streamtubes are no longer fixed in time, but are recalculated periodically, thereby capturing the change in the flow field that can result due to large mobility contrasts. Fixed streamtubes can sometimes overestimate recovery and fail to represent adequately the changing velocity field. Although periodically updating the streamtubes allows representation of the inherent nonlinearity of the velocity field, it does introduce a difficulty concerning arbitrary initial conditions along streamtubes when moving one-dimensional solutions forward in time. No analytical solutions exist for such general, one-dimensional conservation problems, and solutions could only be constructed using a numerical approach [20] or a front-tracking approach along streamtubes [166, 47, 78, 22]. We propose a simplified method: for any new timestep, $t_D + \Delta t_D$, the solution along a streamtube is always found by using the same one-dimensional solution, which is known at the start of the displacement for all times and which was found using fixed initial conditions. This is an approximation that some of the initial conditions found along a streamtube at a particular time t_D may be different. Thus, our approach is different from a rigorous timestepping algorithm that would require to move a given concentration forward in time by considering its position at time t_D and using the local velocity for determining its new position at time $t_D + \Delta t_D$. But the appeal of our approach is given by the possibility of combining periodically changing streamtubes with any one-dimensional solution that can be determined *a priori* to estimate the performance of a displacement through a heterogeneous system. Although our method clearly involves assumptions in generating a solution, we will show that the error introduced by these assumptions is small and considerably less than the uncertainty introduced by the geostatistical description of the reservoir.

The streamtube approach is meant to solve problems that are dominated by reservoir heterogeneity and convective forces. We only consider cross-sectional problems with constant initial and injected conditions (Riemann boundary conditions) without gravity. Furthermore, the one-dimensional nature of the streamtubes requires the assumption that transverse flow mechanisms (normal to the streamtube boundaries) be of negligible importance. The extension of the streamtube method as described in this paper to three dimensions with gravity and transverse diffusion is the subject of ongoing research.

4.1.1 The Mathematics of Streamtubes

Streamtubes can be found by solving directly for the streamfunction using [10]

$$\frac{\partial}{\partial x}\left(\frac{1}{\lambda_y}\frac{\partial \Psi}{\partial x}\right) + \frac{\partial}{\partial y}\left(\frac{1}{\lambda_x}\frac{\partial \Psi}{\partial y}\right) = 0 \ , \tag{4.1}$$

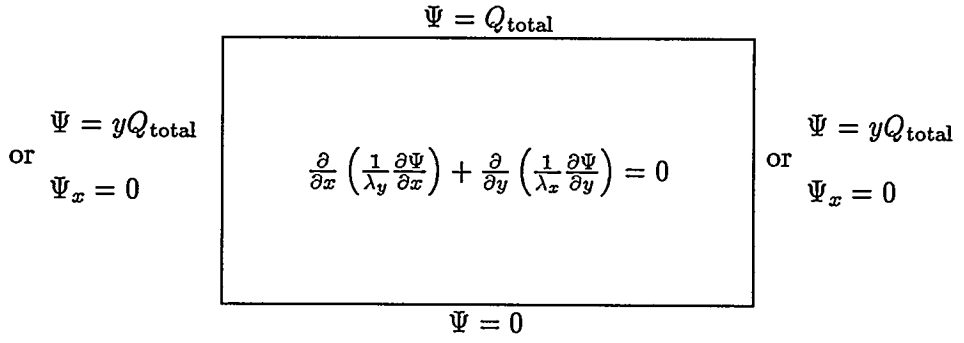

Figure 4.1: Possible boundary conditions of the streamfunction Ψ.

where λ_x and λ_y are the total mobilities in the x and y directions given by

$$\lambda_x = \sum_{j=1}^{N_p} \frac{k_x k_{rj}}{\mu_j} \quad ; \quad \lambda_y = \sum_{j=1}^{N_p} \frac{k_y k_{rj}}{\mu_j} \ . \tag{4.2}$$

j is the phase index, N_p is the total number of phases present, k_x and k_y are the absolute permeabilities in the x and y directions, respectively, k_{rj} is the phase relative permeability, and μ_j is the phase viscosity. For cross-sectional domains the boundary conditions for Eq. 4.1 are particularly easy to formulate (Fig. 4.1), since the flowrate between two streamlines is simply given by the difference in value of the streamfunction associated with each streamline. Since the top and bottom no-flow boundaries are themselves streamlines, the difference in the value of the streamfunction between the two must equal the total flowrate. An obvious choice then is to set the bottom boundary to $\Psi = 0$ and the top boundary to $\Psi = Q_{\text{total}}$ (clearly, the opposite choice is just as good). Similarly, a uniform rate distribution along the inlet or outlet face must be given by a linear distribution of Ψ from 0 to Q_{total}. Thus,

$$\Psi_{\text{in/out}} = yQ_{\text{total}} \ ; \ 0 \leq y \leq 1 \ . \tag{4.3}$$

To find the equivalent of a constant-pressure/total-rate boundary condition in terms of the streamfunction, it is sufficient to consider the Cauchy-Riemann equation,

$$\frac{1}{\lambda_y}\frac{\partial \Psi}{\partial x} = -\frac{\partial P}{\partial y} \ .$$

A constant-pressure boundary states that gradient in the y direction must be zero. For a nonzero coefficient λ_y^{-1} it follows that

$$\frac{\partial P}{\partial y} = 0 \quad \Longrightarrow \quad \frac{\partial \Psi}{\partial x} = 0 \ . \tag{4.4}$$

Total flow is automatically honored by the value associated with the top and bottom limiting streamlines. The possible boundary conditions for the the inlet and outlet ends are summarized in Fig. 4.1. Once the streamfunction has been solved for the particular heterogeneous domain of interest, streamtubes are defined by considering two adjacent streamlines. A system of N streamlines will therefore define $N-1$ streamtubes. A streamtube allows identification of slow and fast flow regions: thick sections of a streamtube correspond to slow-flow regions (low-permeability regions), thin sections to fast-flow regions (high-permeability regions). The heterogeneity of the system is therefore reflected in the geometry of the streamtubes, which capture the distribution of the flow velocity imposed by the underlying permeability field as demonstrated in Fig. 4.2.

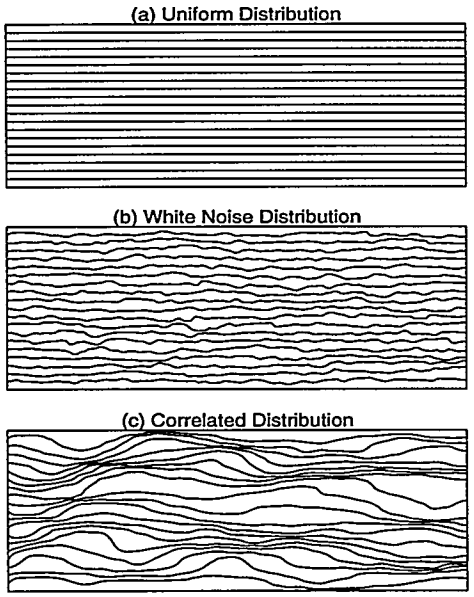

Figure 4.2: Streamtube geometries as a function of reservoir heterogeneity.

4.1.2 Stream Tubes as 1D Systems

The key idea in using streamtubes to model two-dimensional displacements is to treat each streamtube as a one-dimensional system. Higgins and Leighton [85, 86] showed that in order to map a one-dimensional solution along streamtubes, the solution must scale volumetrically. Treating each streamtube as a one-dimensional system automatically associates a pore volume with it, which must be a fraction of the total pore volume of the system. By definition, a streamtube will see a volumetric flowrate that is given by the difference in the value of the streamfunction associated with the bounding streamlines. Therefore, for each streamtube it is possible to use the common form of dimensionless time given by

$$t_{Di} = \frac{\int_0^t q_i d\tau}{\overline{V}_P} \ , \tag{4.5}$$

where q_i is the volumetric flowrate of streamtube i given by the difference $\Psi_{\mathcal{B}} - \Psi_{\mathcal{A}}$, with the subscripts $\mathcal{A}$ and $\mathcal{B}$ referring to the bounding streamlines, and $\overline{V}_P$ is an arbitrary pore volume used for scaling. If all streamtubes see the same $\Delta\Psi$ (i.e, the streamlines are found by interpolating using a constant $\Delta\Psi$), then

$$Q = \sum_i^N q_i = q \sum_i^N = qN \ , \tag{4.6}$$

where N is the number of streamtubes, and the dimensionless time for each streamtube can be written as

$$t_{Di} = \frac{\int_0^t q_i d\tau}{\overline{V}_P} = \frac{\int_0^t q d\tau}{\overline{V}_P} = \frac{\int_0^t Q d\tau}{N\,\overline{V}_P} \ . \tag{4.7}$$

Similarly, a dimensionless length can be associated with each streamtube given by

$$x_{Di} = \frac{\int_0^s \phi A_i(\zeta) d\zeta}{\overline{V}_P} \ , \tag{4.8}$$

where A_i is the cross-sectional area of the streamtube as a function of a one-dimensional coordinate, ζ, along a streamtube. The "best" choice for $\overline{V}_P$ is clearly

$$\overline{V}_P = \frac{V_{P_T}}{N} \quad , \tag{4.9}$$

where V_{P_T} is the total system pore volume and N is the number of streamtubes. In the limit of a homogeneous system each streamtube will have a dimensionless length of $x_D = 1$.

It is also possible to define a dimensionless velocity as

$$v_{Di} = \frac{x_{Di}}{t_{Di}} = \left(\frac{\int_0^s \phi A_i(\zeta) d\zeta}{\overline{V}_P}\right)\left(\frac{N\,\overline{V}_P}{\int_0^t Q d\tau}\right) = \frac{N \int_0^s \phi A_i(\zeta) d\zeta}{\int_0^t Q d\tau} \quad . \tag{4.10}$$

The importance of Eq. 4.10 lies in the fact that solutions that scale as x_D/t_D can now be mapped directly onto a streamtube simply by evaluating Eq. 4.10. Notice that $\overline{V}_P$ cancels out in Eq. 4.10, stating that the dimensionless velocity does not depend on the choice of $\overline{V}_P$ [84]. However, it is also true that to map the solutions along the streamtubes requires explicitly defining the dimensionless variables x_D and t_D. Thus, for actual calculation purposes a choice for $\overline{V}_P$ must be made.

4.1.3 Tracer Displacements

For tracer displacements the elliptic equation governing the potential flow field is decoupled from the mass-conservation equations. The mobility field does not change with time and consequently the streamtubes are fixed and need to be solved for only once. Two analytical solutions can be mapped along streamtubes in the tracer case: (1) a no-diffusion solution given by an indifferent wave traveling at unit velocity, expressed mathematically as

$$C_D(x_D, t_D) = \begin{cases} 1 & \text{for } x_D < t_D \\ 0 & \text{for } x_D > t_D \end{cases} \tag{4.11}$$

and (2) a convection-diffusion type solution. For a semi-infinite domain an approximate solution is given by [118]

$$C_D(x_D, t_D) = \frac{1}{2}\text{erfc}\left(\frac{x_D - t_D}{2\sqrt{\frac{t_D}{N_{Pe}}}}\right) \quad . \tag{4.12}$$

C_D, x_D, and t_D have the usual definitions of dimensionless concentration, distance, and time, and N_{Pe} is the Peclet number, a dimensionless number expressing the extent of physical diffusion/dispersion in the direction of flow. The Peclet number is defined as

$$N_{Pe} = \frac{uL}{K} \quad , \tag{4.13}$$

where u is the total flow velocity, L is the system length, and K is the diffusion/dispersion coefficient in the direction of flow. A velocity-dependent model is sometimes used to express the coefficient K as [118]

$$K = K_m + \alpha\,|u| \quad , \tag{4.14}$$

where K_m is the molecular diffusion coefficient and α is the dispersivity of the permeable medium. If the molecular diffusion coefficient is assumed to be small compared to the product $\alpha\,|u|$, then the Peclet number may be approximated as

$$N_{Pe} \approx \frac{L}{\alpha} \quad . \tag{4.15}$$

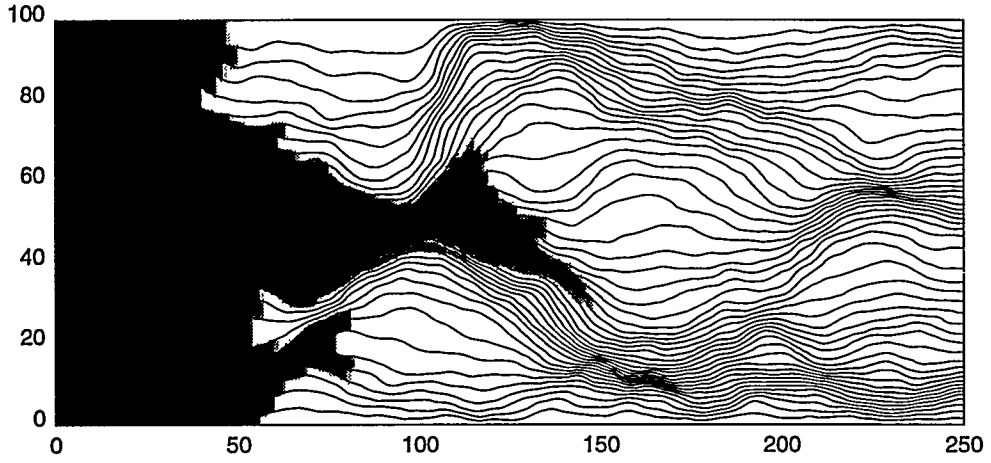

Figure 4.3: Example solution for a two-dimensional heterogeneous domain ($HI = 0.3$) with 250x100 gridblocks by mapping the diffusion-free tracer solution at $t_D = 0.3$ along streamtubes.

Thus, large values of the Peclet number correspond to less diffusion/dispersion, and as the Peclet number tends to infinity Eq. 4.12 tends to the no-diffusion solution given by Eq. 4.11. Field-scale Peclet numbers can range from 100 to 10,000 [7].

To quantify reservoir heterogeneity, we use the heterogeneity index, HI. The heterogeneity index originated from the work of Gelhar and Axness [73] and is defined as

$$HI = \sigma^2_{\ln k} \lambda_c \ , \tag{4.16}$$

where $\sigma^2_{\ln k}$ is the variance of the $\ln k$–field and λ_c is the correlation length in the main direction of flow. The higher HI, the more heterogeneous the system is said to be. The heterogeneity index is a better measure of reservoir heterogeneity than the Dykstra-Parsons coefficient, V_{DP}, because it combines information about the variability of the permeability field ($\sigma^2_{\ln k}$) with information about the correlation structure of the heterogeneity (λ_c). The traditional Dykstra–Parson coefficient, V_{DP}, can be recovered from HI by recalling that

$$\sigma_{\ln k} = -\ln(1 - V_{DP}) \ . \tag{4.17}$$

Even so, it is questionable whether the HI is a satisfactory parameter for quantifying the complex geological structure of a real reservoir. In particular, it does not account for anisotropy and field size.

An example tracer solution for a heterogeneous reservoir with 250x100 gridblocks using 50 streamtubes and the no-diffusion solution (Eq. 4.11) is shown in Fig. 4.3. The heterogeneity index for the permeability field is $HI = 0.3$ and the variance is $\sigma^2_{\ln k} = 1$. Generating the streamtube solution in Fig. 4.3 does not involve any timestepping, as is the case for finite difference approaches. Instead, because the dimensionless distance (Eq. 4.8) is known along each streamtube, the location of the tracer front can be positioned immediately in each streamtube by simply finding the $x_D = t_D$ point. All points along a streamtube associated with $x_D < t_D$ will see a tracer concentration of $C_D = 1$, whereas all points associated with $x_D > t_D$ will see a concentration of $C_D = 0$. To generate a solution at some later time then, the streamtube approach does not move the old front position by a Δt_D, but instead generates a solution for the new cumulative time $t_D + \Delta t_D$. Using Eq. 4.12, on the other hand, allows the addition of physical longitudinal diffusion. Example solutions at $t_D = 0.3$ for three Peclet numbers ($N_{Pe} \to \infty$, $N_{Pe} = 1000$, and $N_{Pe} = 100$) are shown in Fig. 4.4. It is important to realize that using Eq. 4.12 along streamtubes does not account for transverse diffusion, but only for longitudinal diffusion. On the other hand, in the streamtube

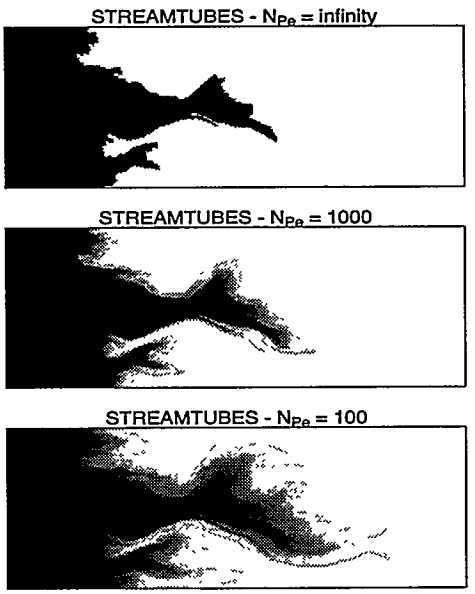

Figure 4.4: Including physical diffusion in a M=1 displacement by mapping the CD equation along 200 streamtubes at $t_D = 0.3$. Examples for $N_{Pe} \rightarrow \infty$, $N_{Pe} = 1000$, and $N_{Pe} = 100$.

approach longitudinal diffusion is truly specified along the total velocity vector, which is different from traditional simulation which specifies diffusion coefficients along the Cartesian directions of the underlying grid.

Mapping a CD-solution along field-scale streamtubes can be interpreted as an attempt to capture sub-tube heterogeneities by specifying an appropriate Peclet number. As such, it represents a nested approach to modeling heterogeneities that dominate at different scale: the streamtubes capture the large-scale heterogeneities of the reservoir, while the CD-solution models sub-gridblock/sub-streamtube features.

4.1.4 Numerical Diffusion

Mapping analytical solutions, such as Eq. 4.11 or Eq. 4.12, onto streamtubes results in two-dimensional solutions that are completely devoid of numerical diffusion. Streamtube solutions can therefore be used to quantify the extent of numerical diffusion in other numerical solutions obtained using finite-differences or finite-elements. An example of such a comparison is given in Fig. 4.5, which shows the tracer solution without physical diffusion at $t_D = 0.3$ compared to solutions with no physical diffusion (but some numerical diffusion) obtained using a BP research code with flux-corrected transport [33] (using a Courant–Friedrichs–Lewy number of 0.2) and Eclipse [94], a commercially available finite-difference reservoir simulator with single-point upstream weighting. As the number of streamtubes increases, the streamtube solution converges to the exact limiting solution for the no-diffusion case and can therefore be used to calculate the spatial error,

$$\Delta C_{\text{err}} = \mid C(x,y)_{\text{Stubes}} - C(x,y)_{\text{FD}} \mid \ , \tag{4.18}$$

where the subscript FD stands for finite-difference. A spatial rendering of ΔC_{err} is shown in Fig. 4.5, which demonstrates that numerical solutions are clearly affected by numerical diffusion, although the basic flow pattern dictated by the permeability field is the same in all cases. The reason for

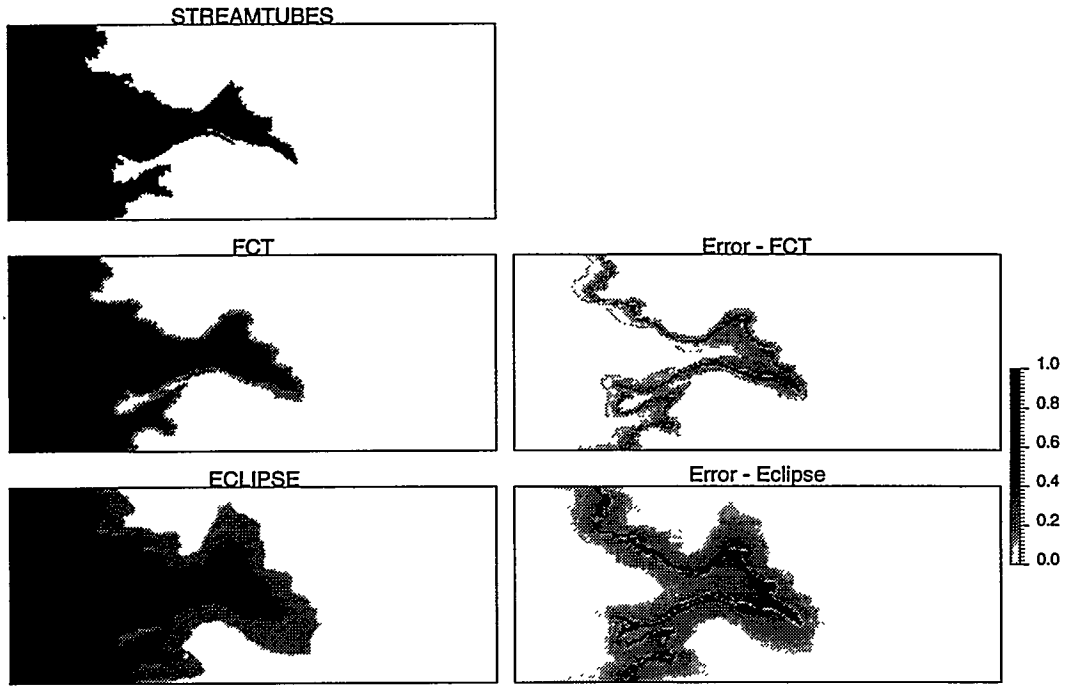

Figure 4.5: Comparison of concentration profiles and spatial error distribution showing extent of numerical diffusion in finite-difference simulators. Streamtube method versus a BP research code with flux-corrected transport (FCT) and Eclipse, a commercially available reservoir simulator with single-point upstream weighting and automatic timestep selection.

this, of course, is that for the tracer case the flow velocity is fixed in time and thus is unaffected by any level of diffusion/dispersion.

4.1.5 Immiscible Displacements

The one-dimensional, two-phase immiscible problem, also known as the Buckley-Leverett problem, is well documented in the petroleum literature [26, 38, 118] and is generally presented in its dimensionless form,

$$\frac{\partial S_w}{\partial t_D} + \frac{\partial f_w}{\partial x_D} = 0 \ , \tag{4.19}$$

where $t_D = tu_t/\phi L$ and $x_D = x/L$ are the usual definitions of dimensionless time and distance, respectively, u_t is the total (constant) Darcy velocity given by $u_t = u_w + u_o$, and f_w is the fractional flow of water given by

$$f_w = \frac{u_w}{u_w + u_o} = \frac{1}{1 + \frac{k_{ro}\mu_w}{k_{rw}\mu_o}} \ . \tag{4.20}$$

k_{ro}, k_{rw}, μ_o, and μ_w are the relative permeabilities and viscosities of oil and water as indicated by the subscripts. The solution to Eq. 4.19, subject to the Riemann conditions

$$S_w(x_D, 0) \begin{cases} S_{wl} & \text{for } x_D < 0 \\ S_{wr} & \text{for } x_D > 0 \end{cases} \ , \tag{4.21}$$

where the subscripts l and r refer to the left and right constant states of the discontinuity at $x_D = 0$, can be found easily using the method of characteristics [203, 123]. An example solution for a two-phase problem with an endpoint mobility ratio of 10 is shown in Fig. 4.6. Depending on

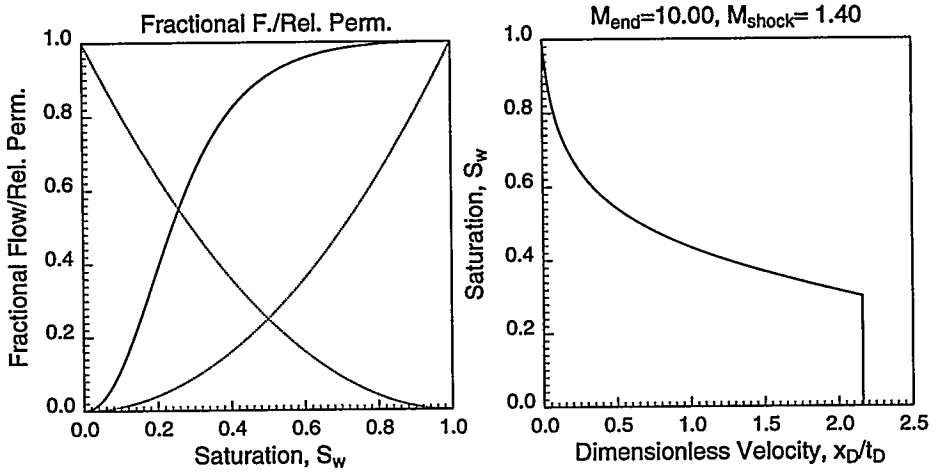

Figure 4.6: Relative permeability curves ($k_{rw} = S_w^2$, $k_{ro} = S_o^2$), corresponding fractional flow function for a viscosity ratio of 10 ($\mu_o/\mu_w = 10$), and BL analytical solution used for testing the new streamtube approach. The mobility ratio at the shock front is $M_{\text{shock}} = 1.36$.

the shape of the fractional flow curve, f_w, the solution can contain rarefaction waves and/or shocks [118].

The Higgins and Leighton Method. The streamtube approach originally proposed by Higgins and Leighton [85, 86, 87], and subsequently used and extended by many investigators [152, 126, 20, 117, 56, 84], centers on capturing the nonlinear behavior of the displacement by keeping the streamtube fixed but allocating the total flow into each streamtube in proportion to the total flow resistance as it changes with time. For areal problems, the Higgins and Leighton method has been shown to give good approximation of recovery for both homogeneous domains [48, 126] and heterogeneous domains [56, 129]. The total resistance along a streamtube i is given by

$$R_i = \int_0^S \frac{d\zeta}{A(\zeta)\lambda_t(\zeta)} \ , \tag{4.22}$$

where S is the total length of each streamtube (not to be confused with x_D, the dimensionless pore volume coordinate along a streamtube defined by Eq. 4.8) and λ_t is the total mobility. At any instant in time, the flow is then allocated in proportion to [84]

$$\frac{R_T}{R_i} \ , \tag{4.23}$$

where R_T is given by

$$\frac{1}{R_T} = \sum_{i=1}^{N_S} \frac{1}{R_i} \ . \tag{4.24}$$

Unlike finding the dimensionless pore volume along a streamtube using Eq. 4.8 — which is all that is required to map one-dimensional Riemann solutions along periodically changing streamtubes and is easily determined — evaluating the integral in Eq. 4.22 is more difficult. The reason is that to calculate R_i the product $A(\zeta)k(\zeta)$, where $k(\zeta)$ is the absolute permeability, must be determined along the streamline coordinate, ζ. For a general heterogeneous domain, in which the permeability field is specified by k_x and k_y components on a regular Cartesian grid, finding the directional permeability $k(\zeta)$ becomes a nontrivial exercise. Furthermore, if the streamtube encompasses more than one gridblock, then $k(\zeta)$ should really be an average of the directional permeabilities along $A(\zeta)$. Finding the area, $A(\zeta)$, is easier than finding $k(\zeta)$, but must be approximated as well.

Thus, the product $A(\zeta)k(\zeta)$ may involve a substantial error, which is then integrated along ζ using Eq. 4.22 to find R_i.

To find a two-dimensional solution using the Higgins and Leighton method then, the one-dimensional Buckley–Leverett solution shown in Fig. 4.6 is mapped along a (fixed) streamtube, with the total flux apportioned over time to each streamtube changing according to Eq. 4.23. In other words, each streamtube no longer sees the same volumetric rate. Figure 4.7 compares recoveries for the Higgins and Leighton method to recoveries found using Eclipse. Although the Higgins and Leighton method returns acceptable recoveries, the difficulty it has in capturing breakthrough time correctly with increasing mobility ratio suggests a weakness of the method in trying to model the changing velocity field (Fig. 4.8) with fixed streamtubes. Although acceptable in the immiscible case, the error can be substantial for strongly nonlinear first-contact miscible and compositional displacements, as we will show.

A New Streamtube Approach. The principal difference in our approach from that of Higgins and Leighton and other investigators lies in combining periodically changing streamtubes with one-dimensional solutions that are previously known. The solution along a streamtube for a new time level $t_D + \Delta t_D$ is not given by considering the initial conditions along the streamtube at time t_D, solving the one-dimensional problem with these conditions, and timestepping from t_D to $t_D + \Delta t_D$. Instead, we always use the same one-dimensional solution and simply go from 0 to $t_D + \Delta t_D$ along an updated streamtube. In other words, our approach centers on treating each streamtube as a true one-dimensional system on which the Buckley-Leverett solution, for example, is mapped repeatedly for different times, even though the streamtubes are updated periodically.

The motivation for this new approach came from the desire to capture the changing velocity field in multiphase flow while retaining the detailed representation of the physics of flow embedded in one-dimensional analytical solutions. Updating the streamtubes is an appealing solution because the changing streamtubes reflect the nonlinearity of the problem, while the original definition of a streamtube as carrying a volumetric rate equal to the difference in the values of its bounding streamlines is maintained. However, as mentioned in the introduction, updating the streamtubes poses one problem related to the initial conditions associated with each streamtube: each time a streamtube is updated, the initial conditions along the new streamtube will not correspond exactly to the initial conditions along the old streamtube. The resulting (hyperbolic) problem that must be solved in order to move the solution forward in time correctly by a Δt_D along each streamtube is therefore one with general type initial conditions, which in general can be solved only by (a) using a standard one-dimensional finite-difference solution along each streamtube [20], or (b) by using a moving interface, front-tracking algorithm [127, 126, 159, 166, 47, 78, 22]. We side-step the problem of general initial conditions that arises with streamtube updating by choosing to use the same one-dimensional solution for all times. Although our approach involves an assumption in terms of how it moves a two-dimensional solution forward in time, we show that the resulting error is small and largely offset by the lack of numerical diffusion, increased speed, ability to capture the changing velocity field as well as the uncertainty in the geological description.

Validation. We tested our approach by the following numerical experiment. The saturation and velocity fields of a standard finite-difference simulator [94] were stored at regular increments of dimensionless time. From each velocity field, the corresponding streamtubes were then constructed and used to find the saturation profiles by mapping a Buckley–Leverett solution along the streamtubes for that particular time, t_D. The saturation profiles obtained by this method were then compared to the saturation profiles obtained by the new streamtube approach we propose here.

The Buckley–Leverett solution used in the numerical experiment is shown in Fig. 4.6. Notice that although the endpoint mobility ratio is 10, the shock–front mobility ratio is only 1.36, leading to a more stable displacement than suggested by the endpoint value alone. This is generally true for many waterfloods with reasonable relative permeability curves: the frontal mobility ratio is of

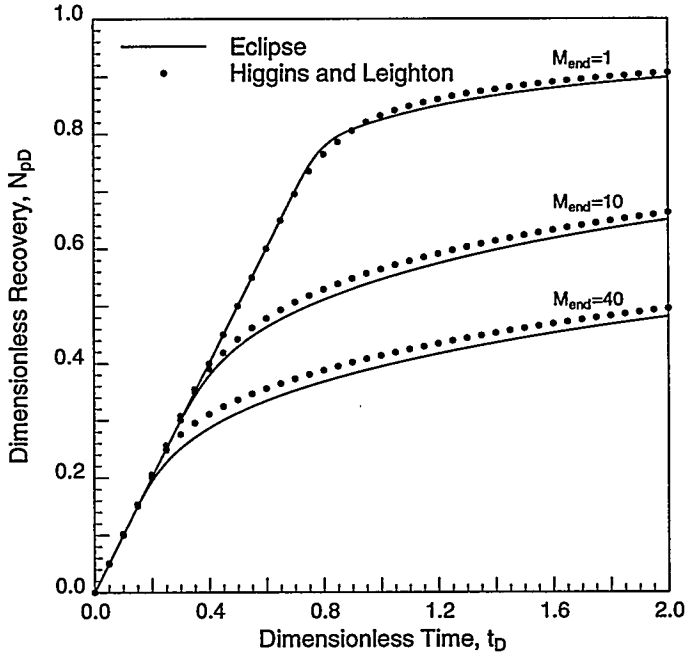

Figure 4.7: Comparison of recovery curves found using Eclipse and the Higgins and Leighton method. The same permeability field as the one used in Fig. 4.3 was used here.

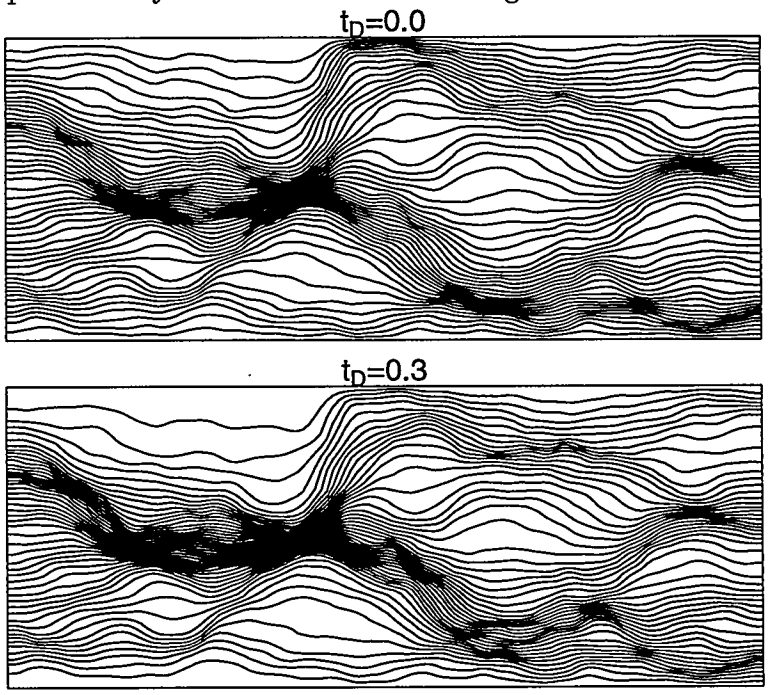

Figure 4.8: Streamtube geometries at different times for the $M = 10$ displacement.

order 1 even though the endpoint can be of order 10 or 100, leading to a weak nonlinearity in the total velocity.

Figure 4.9 displays example solutions at $t_D = 0.2$ and $t_D = 0.4$. The upper row shows saturation maps obtained directly from Eclipse; the middle row shows maps obtained using the velocity from Eclipse but mapping the one-dimensional solution as in our approach; and the last row shows profiles obtained by using the new streamtube approach only. As demonstrated in Fig. 4.9, the solution found using our method agrees well with the mixed solution found using Eclipse. Both solutions have no numerical diffusion because an analytical one-dimensional solution is used along the streamtubes. A direct comparison of the saturation maps (Fig. 4.9), as well as the integrated response (Fig. 4.10), demonstrates that the difference between the two solutions (Eclipse velocity field + 1D solution and our approach) is indeed small. In fact, it is interesting to note that numerical diffusion causes a larger difference in recovery than the approximation introduced by the new streamtube approach. This conclusion can be drawn from the fact that the velocity fields for the Eclipse solution and the mixed method are identical, and therefore the difference must be attributed to numerical diffusion. This numerical experiment suggests that the error is indeed small compared to traditional finite-difference solutions, and in particular, numerical diffusion is shown to cause larger errors than the assumptions in our method.

Recovery curves using different endpoint mobility ratios are compared to recoveries found using Eclipse in Fig. 4.11. Compared to the Higgins and Leighton approach, breakthrough is now predicted correctly in all cases, clearly demonstrating that the nonlinearity of the problem is captured by updating the streamtubes. The improvement compared to the Higgins and Leighton method for the M=40 case (Fig. 4.7) is substantial.

Convergence for Immiscible Displacements. In the streamtube approach there is no discretization of the conservation equations, and therefore there is no Courant-Friedrichs-Lewy (CFL) [123] condition to worry about. Instead, the question of how many times the streamtubes must be updated to consider the solution converged arises naturally and is addressed by solving a problem repeatedly with an increasing number of streamtube updates over a fixed period of time. We consider the problem converged when the recovery curve no longer changes with increasing number of streamtube updates. Recovery curves for 1, 10, 20, 40, and 100 streamtube updates over two pore volumes injected are shown in Fig. 4.12. Only 20 solves are sufficient to consider the problem converged. With 20 updates, the new approach represents a reduction in computation time by two orders of magnitude compared to the thousands of solves needed by a traditional finite-difference simulator like Eclipse. For this particular problem ($M_{\text{end}} = 10$), Eclipse required 1,600 solves, which translates into a speed-up of 8,000% .

4.1.6 First-Contact Miscible Displacements

Unstable first-contact miscible (FCM) displacements in heterogeneous systems have been studied by many authors [6, 34, 192, 180]. The strong interest in unstable FCM displacements is motivated principally by the possibility of learning more about displacements that are near-miscible, such as natural-gas and carbon-dioxide flooding. The assumptions used in FCM flow isolate the convective part of the displacement problem from any phase-behavior considerations and allow study of the interaction of reservoir heterogeneity with the nonlinearity of the velocity field. Although the absence of any phase-behavior and multiphase flow aspects simplifies the physics, it does enhance the nonlinearity of the problem. Diffusive mechanisms, such as molecular diffusion and pore-scale mixing, are the only physical mechanisms available to mitigate the original mobility contrast. As a result, FCM displacements are very challenging to simulate numerically and are far more difficult than two-phase immiscible problems. High mobility contrasts lead to extreme velocity variations and sufficient gridblocks must be used to ensure that numerical diffusion is as

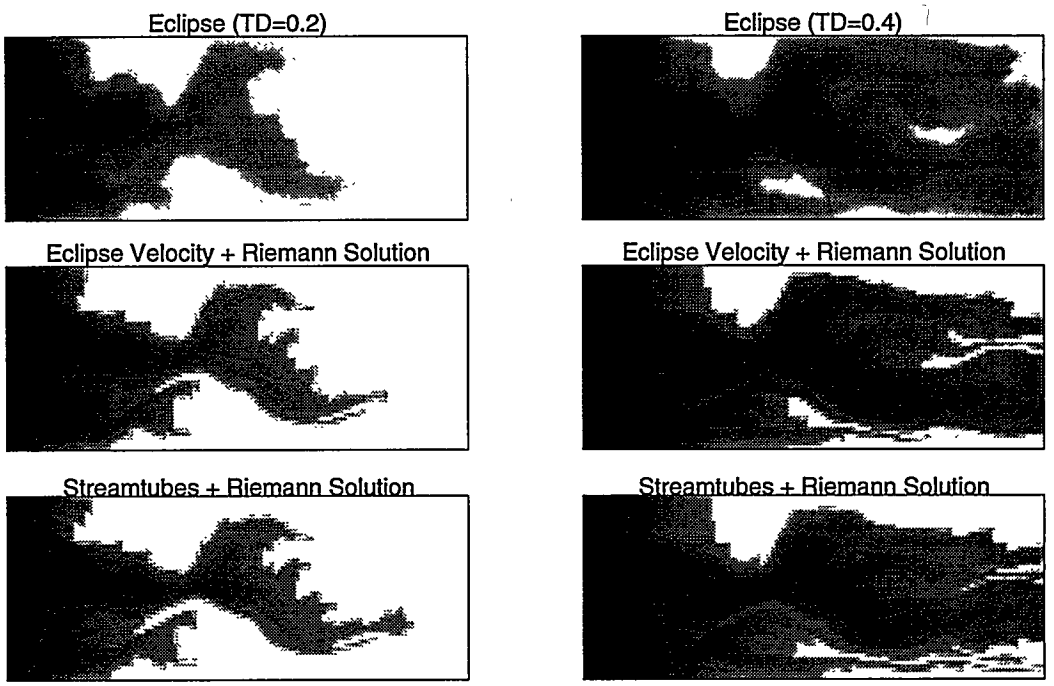

Figure 4.9: Saturation maps at times $t_D = 0.2$ and $t_D = 0.4$. From top to bottom: profiles obtained directly from Eclipse; profiles obtained by using the velocity field from Eclipse but mapping a Riemann solution along streamtubes; profiles obtained by the method proposed in this work.

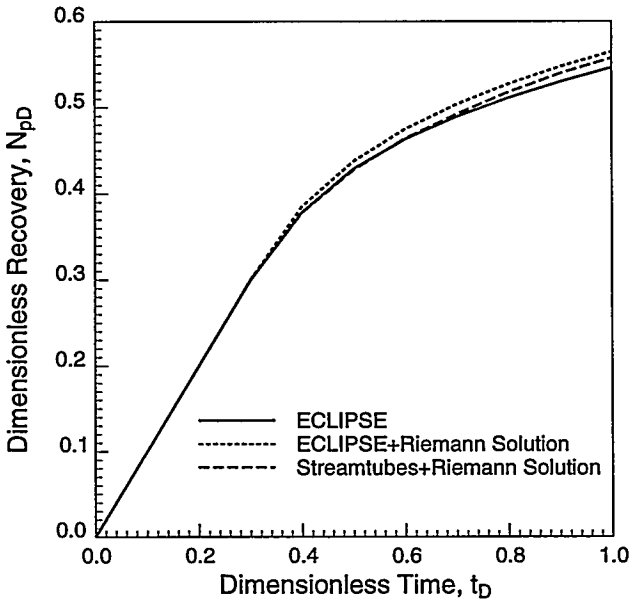

Figure 4.10: Recovery curves for the three different solution methods used to generate the profiles in Fig. 4.9.

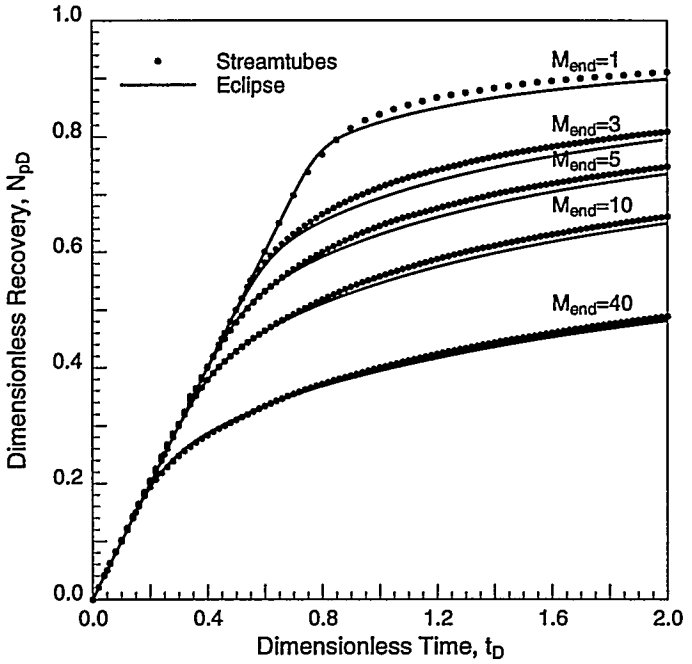

Figure 4.11: Comparison of recovery curves found using Eclipse and the new streamtube approach suggested here. The agreement is superior to that obtained by the Higgins and Leighton method shown in Fig. 4.7.

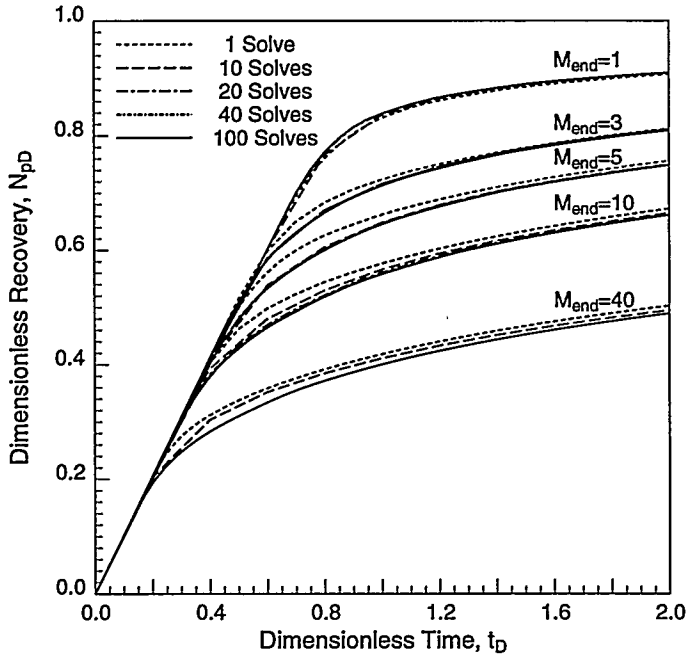

Figure 4.12: Recovery curves for 1, 10, 20, 40, and 100 streamtube updates over two pore volumes injected ($t_D = 2$), showing that the problem can be considered converged if more than 20 updates are used.

close as possible to representing true physical diffusion at the gridblock scale. Physically meaningful simulations of FCM displacements require substantial computer resources [180].

1D Viscous Fingering Solutions. Unlike the two-phase immiscible problem, the ideal miscible case has a subtle one-dimensional solution. The solution to the governing PDE (with no diffusion),

$$\frac{\partial C_D}{\partial t_D} + \frac{\partial C_D}{\partial x_D} = 0 \ , \tag{4.25}$$

with initial data of the type

$$C_D(x_D, 0) = \begin{cases} 1 & \text{for } x_D < 0 \\ 0 & \text{for } x_D > 0 \end{cases} \ , \tag{4.26}$$

where C_D is a normalized concentration, gives rise to an indifferent wave solution traveling at unit velocity (as for the tracer case). For favorable mobility ratios ($M < 1$), the physical solution is indeed a wave traveling at unit velocity, although the wave is no longer indifferent but self-sharpening. For unfavorable mobility ratios, on the other hand, the solution to Eq. 4.25 is misleading because it still gives a piston-like displacement, when the system is in fact unstable. The problem, of course, is that the displacement model given by Eq. 4.25 is unable to distinguish between stable and unstable displacements since it is linear; by not having concentration dependent coefficients, the solution cannot account for any viscosity-induced mobility contrast as a function of x_D and t_D. Furthermore, Eq. 4.25 has no characteristic length scale, resulting in a sharp, but unstable front at all length scales and for all times. A physically meaningful solution, on the other hand, would require some cut-off length scale across which the frontal instability is mitigated.

Although adding a cut-off length scale can be done mathematically by retaining a second-order diffusion term, implying that the cut-off length scale is given by the diffusive length scale associated with N_{Pe}, it is unlikely that at the field scale molecular diffusion and pore level mixing are first-order type physical processes that mitigate instabilities. Convective mixing at the macroscale, such as viscous fingering and channeling, are probably more important. To account for such phenomena in an averaged, one-dimensional sense, an analogy to two-phase flow was first proposed by Koval [116]. In the Koval model, straight-line relative permeabilities and a quarter-power mixing rule are combined to define a flux function $f(C_D)$ that models convective mixing of the fluids. The governing PDE for Koval's model is

$$\frac{\partial C_D}{\partial t_D} + \frac{\partial f(C_D)}{\partial x_D} = 0 \ , \tag{4.27}$$

where $f(C_D)$ is given by

$$f(C_D) = \frac{1}{1 + \frac{1-C_D}{C_D}\frac{1}{M_{\text{eff}}}} \ . \tag{4.28}$$

M_{eff} is the effective mobility ratio defined as

$$M_{\text{eff}} = \left(0.78 + 0.22 M^{1/4}\right)^4 \ , \tag{4.29}$$

and $M = \mu_o/\mu_s$ is the usual definition of the mobility ratio for FCM flow. Koval's original model also includes a heterogeneity factor H. This factor has been set to $H = 1$ (homogeneous), since the model is used along homogeneous, one-dimensional streamtubes.

A similar one-dimensional model is the Todd–Longstaff formulation. The Todd–Longstaff model [186] includes Koval's model as a special case and is a single-parameter function given by

$$f(C_D) = \frac{1}{1 + \frac{1-C_D}{C_D}\left(\frac{1}{M}\right)^{1-\omega}} \ . \tag{4.30}$$

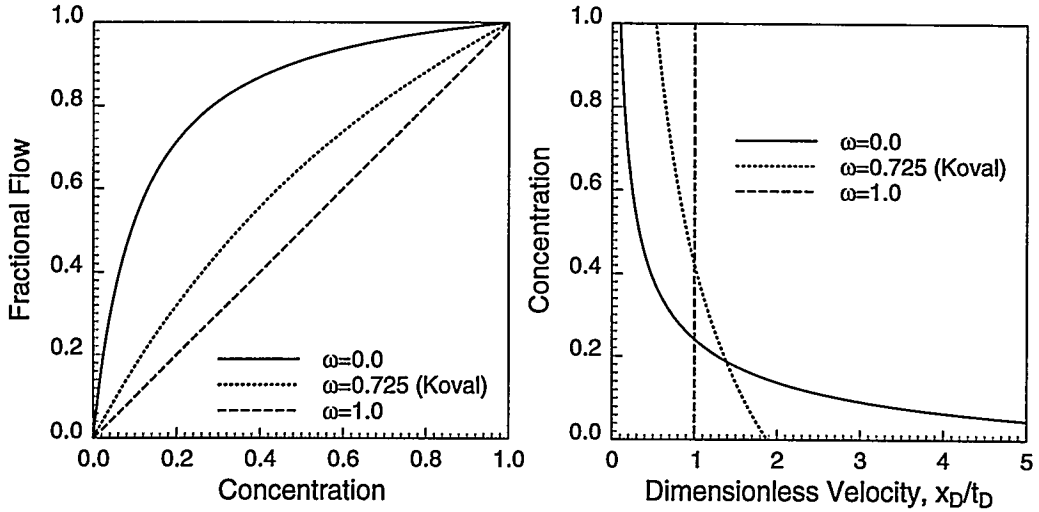

Figure 4.13: Fractional flow curves and corresponding velocity profiles for $M = 10$ and different values of ω in the Todd–Longstaff model.

By choosing ω as

$$\omega = 1 - 4\frac{\ln\left(0.78 + 0.22M^{1/4}\right)}{\ln M}\ , \tag{4.31}$$

the Todd–Longstaff model is equivalent to Koval's model [186]. As shown in Fig. 4.13, setting $\omega = 1$ gives the piston-like, no-diffusion solution, while $\omega = 0$ returns the equivalent two-phase problem using straight-line relative permeabilities.

Two-Dimensional Solutions. Fig. 4.14 shows example $M = 10$ solutions through several cross sections with 250x100 blocks and varying degree of heterogeneity at $t_D = 0.4$. The left column shows concentration maps found using the streamtube method, while the right column shows reference solutions found using a finite-difference simulator with flux-corrected transport (FCT) [33]. A value of $\omega = 0.725$ is used (equivalent to Koval's model) to capture the viscous-fingering-induced mixing along each streamtube. This value of ω was chosen so that the method would yield the correct recovery for the limiting homogeneous case. However, we found the solutions to be only a weak functions of ω, with values between 0.5 to 0.8 resulting in almost identical recoveries and concentration maps for the heterogeneous cases we studied.

Figure 4.14 shows that the streamtube approach is able to capture the same large-scale displacement features seen in the FCT solutions. One interesting question raised by the comparisons is whether the streamtube solutions and the reference solutions are indeed on the same scale. All FCT solutions have some viscous fingering features, whereas all the fingering in the streamtube solutions is assumed to take place within the streamtubes and captured in an averaged one-dimensional sense. As such, the streamtube technique, as for the CD solution, represents a nested approach to modeling displacements through heterogeneous systems: the streamtubes capture the large scale channels, while the 1D solution captures the viscous fingering taking place within these channels.

Total recoveries for the six different permeability distributions are summarized in Fig. 4.15. The recovery for the very short correlation length system (PERM 5) is expected to be good, since it amounts to the recovery predicted by the one-dimensional Koval solution. For the other cases, the recovery curves tell an interesting story, particularly for the permeability fields with a heterogeneity index of $HI = 0.0625$ (PERM 2) and $HI = 0.64$ (PERM 3).

The PERM 2 permeability field has a correlation length of $\lambda_c = 0.25$, but only a standard deviation of $\sigma_{\ln k} = 0.5$. In other words, the system is only mildly heterogeneous and although there are preferential flow channels, the streamtube solution sees a rather homogeneous reservoir. The FCT solution, on the other hand, allows fingers to grow along these channels. The predicted

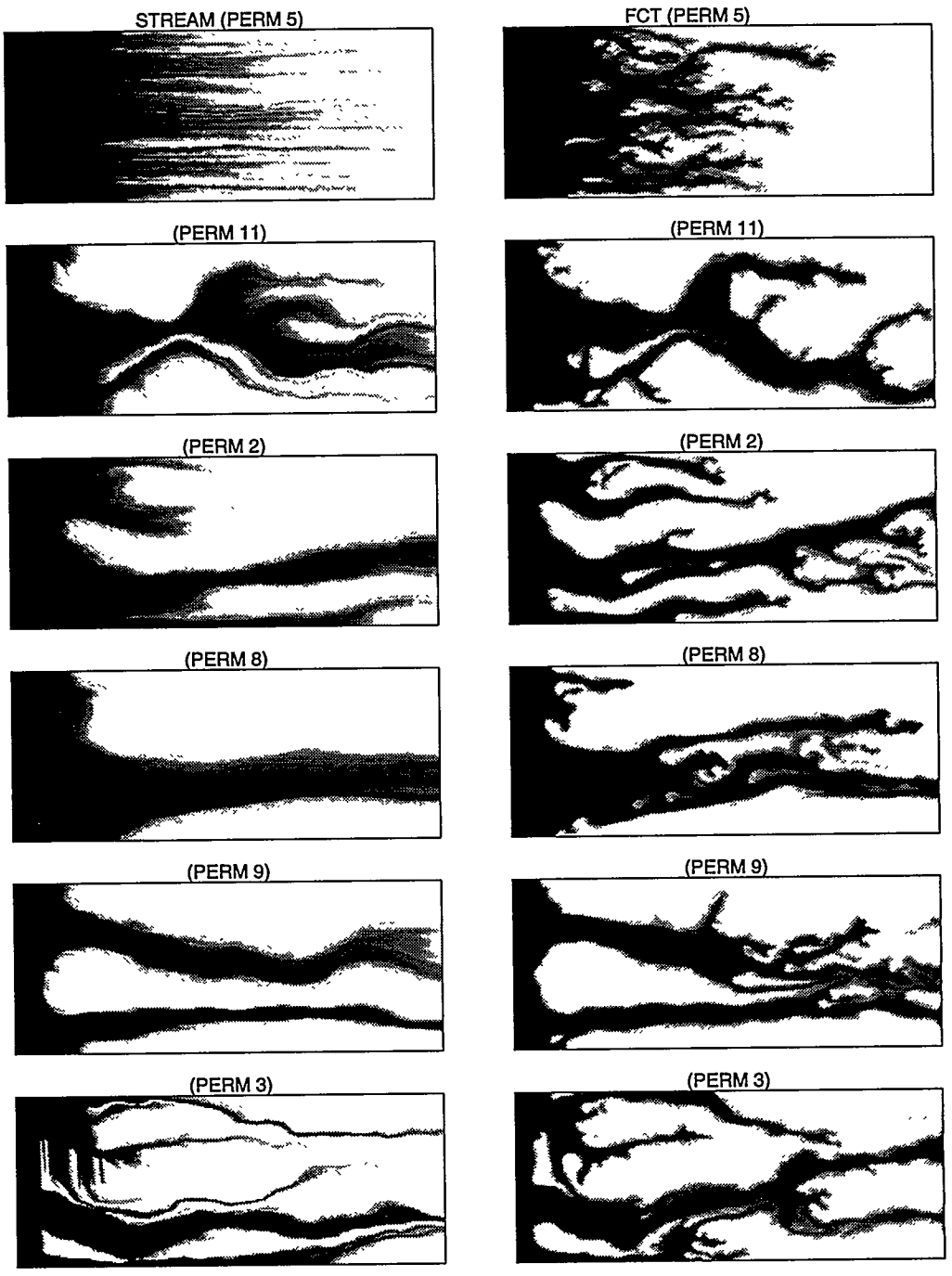

Figure 4.14: Concentration maps for $M = 10$ displacements in six different, 250x100-block heterogeneous reservoirs at $t_D = 0.4$

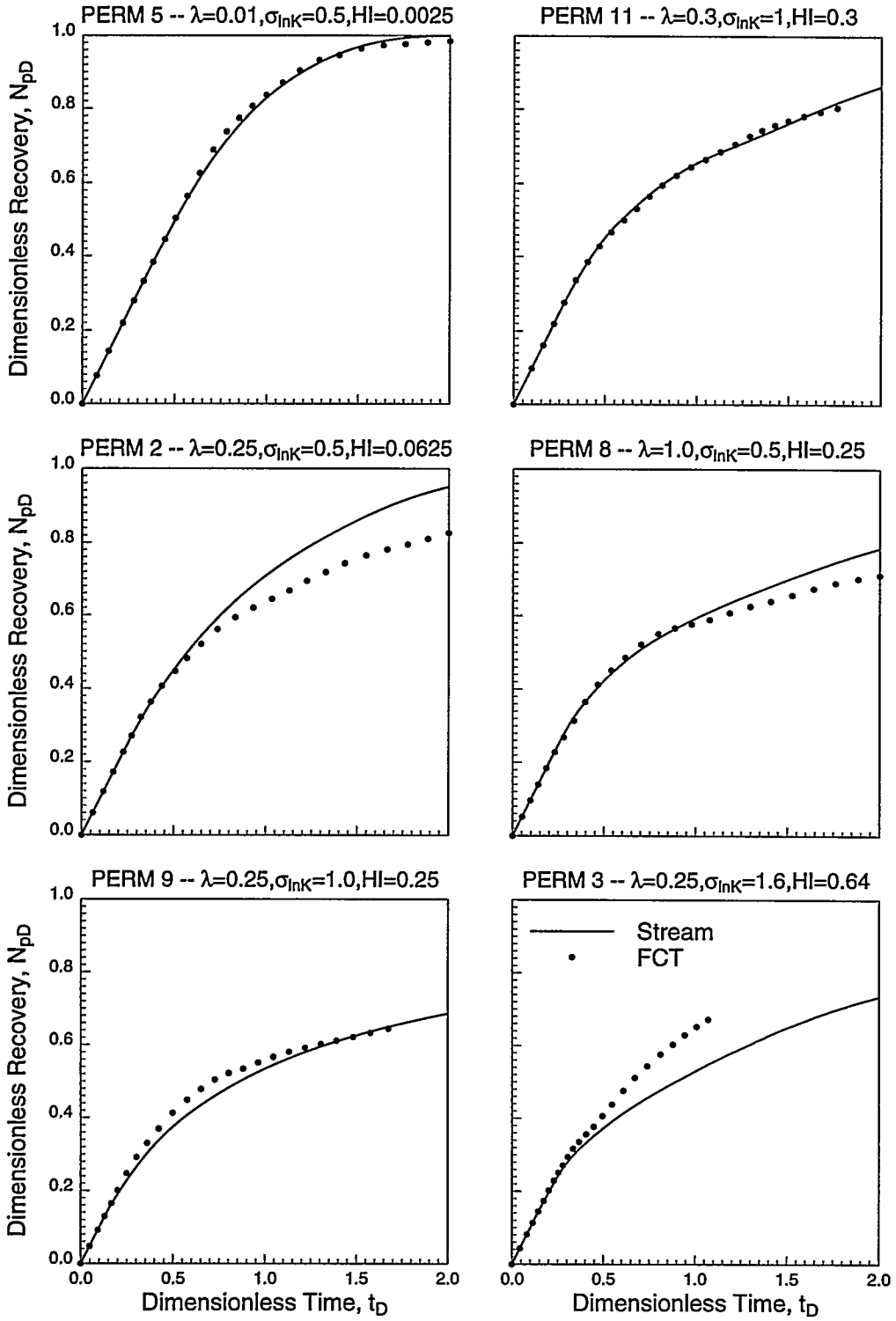

Figure 4.15: Recovery curves for the displacements shown in Fig. 4.14.

recoveries are, accordingly, higher for the more homogeneous streamtube solution and lower for the viscous-fingering-dominated FCT solution. This identifies a flow regime for which the streamtube approach probably fails to capture the dominant displacement mechanism: field-scale fingering induced by a mildly heterogeneous system.

The much more heterogeneous PERM 3 case, on the other hand, behaves quite differently. Heterogeneity clearly dominates the flow in this displacement, which the streamtube method is able to capture. The FCT solution also resolves the heterogeneity, but the flow channels are thicker, probably due to some transverse numerical diffusion as well as finger coalescence, inducing sufficient mixing to lower the mobility contrast. As a result, the recoveries for the FCT solution are higher than for the streamtube solution. It is worth pointing out that PERM 3 is a difficult permeability field to use for simulation and, in fact, the FCT simulation had some numerical difficulties due to the extreme permeability contrasts, causing the run time to exceed 14,000 Cray seconds, which was set as cap for all simulations. In the remaining cases, the streamtube and FCT recoveries match, demonstrating the ability of the streamtube approach to capture overall recovery and the main displacement features.

As in the two-phase immiscible case, an alternative to updating the streamtubes to capture the nonlinearity of the displacement is to keep the streamtubes fixed and allocate the flow according to the total flow resistance of each streamtube. Although the Higgins and Leighton approach gave reasonably good recovery curves in the immiscible case, the error in breakthrough time is much more significant for FCM flow because of the stronger nonlinearity of the formulation, as shown in Fig. 4.16. King *et al.*[111] modified the Higgins and Leighton approach and found "boost" factors for each streamline by calculating the total flow resistance as an integration from the inlet to the isobar located at the tip of the leading finger, rather than using the total length of the streamline from inlet to outlet as required in Eq. 4.22. King *et al.* realized that at early times the resistance, R_i, would be dominated by the unswept part of the streamtube, thus underestimating the nonlinearity of the displacement. Although the placement of an isobar at the leading finger is a clever way to reduce the influence of the unswept region on flow resistance, and may be an alternative to the Higgins and Leighton method, it clearly has some problems as well. For example, it may be difficult to pick the correct leading finger at early times; choosing the wrong finger will cause convergence to the wrong solution, because it will force the smallest flow resistance on the chosen finger and allow it to grow the fastest. The problem could possibly be corrected by using an isobar that is removed from the leading finger by some appropriate length (although that in turn raises the question by how much to remove the isobar from the leading finger). It is worth noting that the difficulties found by King *et al.* were anticipated by Martin *et al.* [127], who found that immiscible displacement with favorable mobility ratios (i.e., piston-like displacements with a mobility discontinuity) was not predicted as well as unfavorable mobility ratio displacement by using fixed streamtubes.

Convergence for FCM Displacements. As was mentioned previously, the streamtube approach does not have the equivalent of a CFL condition: there is no numerical limitation to the size of the timestep and the solution is always numerically stable. We consider a solution converged when the overall recovery does not change with increasing number of updates over a fixed time interval.

All the solutions presented so far implicitly used "sufficient" updates for a converged solution. Figure 4.17 shows overall recoveries as a function of mobility ratio and number of streamtube updates for one of the permeability fields used (PERM 11) in Fig. 4.14. In both cases, the solution can be considered converged by using between 40 and 100 streamtube updates over two pore volumes injected. In fact, the big difference in recovery occurs by going from a single solve (tracer case) to 10 streamtube updates. Even by using only 20 updates an acceptable solution can be obtained, with breakthrough being predicted correctly. Compared to the many thousands of pressure solves required by a traditional numerical formulation, the speed-up in finding the solution is by two to

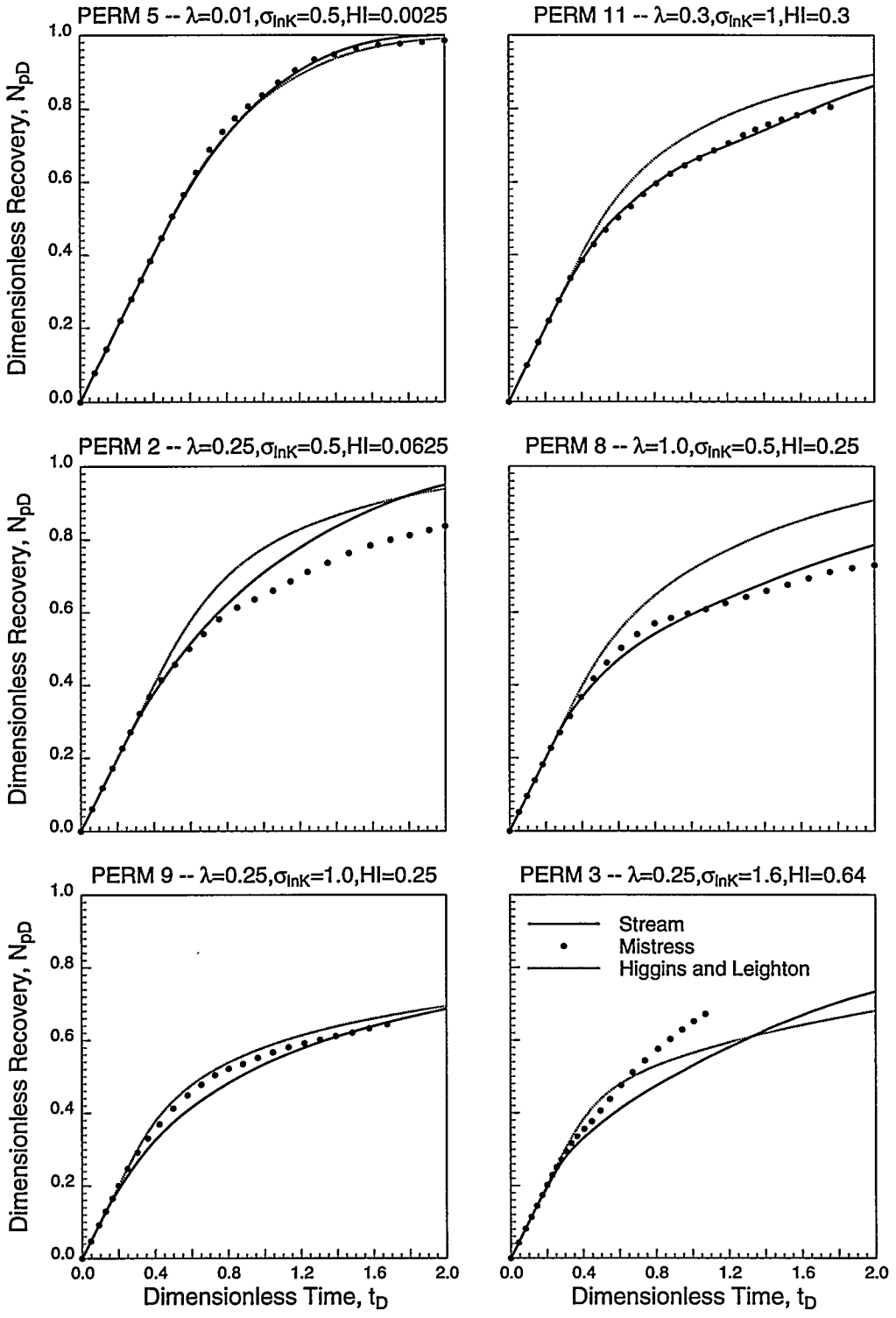

Figure 4.16: Comparison of recovery curves for a FCM displacement with $M = 10$ found using a FCT finite-difference simulator and the Higgins and Leighton method. The underlying permeability field has 250x100 gridblocks.

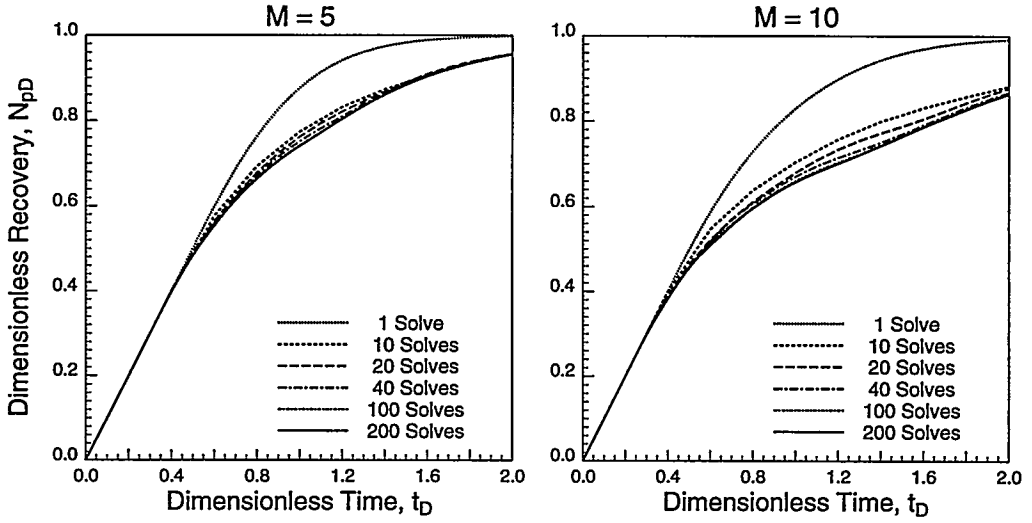

Figure 4.17: Convergence of the 2D solution for the ideal miscible case for endpoint mobility ratios of 5 and 10 over two pore volumes injected. The permeability has 250x100 gridblocks with $HI = 0.3$, $\lambda_c = 0.3$, and $\sigma_{\ln k} = 1$.

three orders of magnitude. Herein lies the great advantage of the streamtube approach: although it makes assumptions in generating the two-dimensional solutions and does not capture the subtleties of viscous fingering, it is able to find solutions that contain all the main features imposed by the large-scale heterogeneity and return accurate overall recoveries, particularly breakthrough times, using orders of magnitude less CPU time than a traditional finite-difference or finite-element approach.

4.1.7 Applications

The real power of the streamtube approach lies in its ability to produce solutions that capture the main features imposed by the underlying permeability field while using orders of magnitude less CPU time than traditional simulation techniques. Its strength is not in resolving the details of the displacements, although the control on numerical diffusion may suggest it, but in being able to produce accurate recoveries very quickly. As such, it is ideally suited for a statistical approach to reservoir forecasting. A large number of statistically identical permeability realizations can be processed to generate a spread in recovery for a particular combination of reservoir geology and displacement mechanisms. The streamtube approach may also be used as a filter: permeability fields that returned the maximum and minimum recoveries can be singled out and used in a much more expensive finite-difference simulation to confirm the spread in recovery.

The speed of the streamtube approach can be used in many ways, but becomes particularly appealing when the parameter space of interest includes reservoir heterogeneity, in which case many simulations are required to obtain a statistically meaningful answer. An example of a parameter space that has received considerable attention recently [180, 6, 192] has been in the area of unstable displacements through heterogeneous systems. In its simplest representation, the parameter space is given by the endpoint mobility ratio (instability) and heterogeneity index (heterogeneity), although HI is clearly not a completely satisfactory parameter for quantifying the complex geologic structure of a real reservoir. Nevertheless, HI can give some indication of the degree of heterogeneity of the reservoir, particularly if it is used in a statistical sense. An example sweep of the parameter space is shown in Fig. 4.18. There are 30 recovery curves for each of the six M-HI pairs. Mobility ratio increases from left to right and heterogeneity increases from top to bottom. All underlying

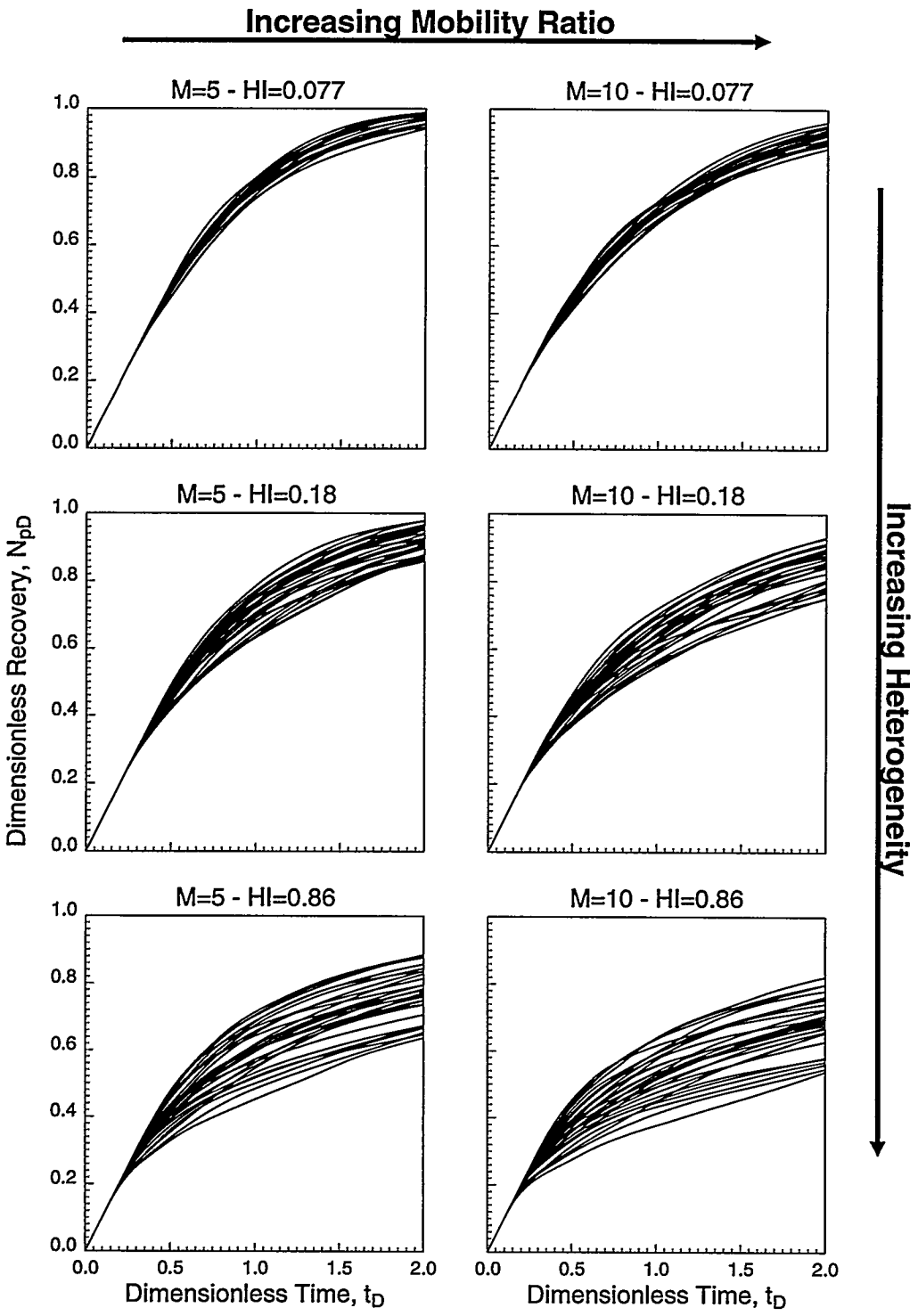

Figure 4.18: 180 recovery curves used in an example sweep of the M-HI parameter space to illustrate how nonlinearity and heterogeneity interact.

permeability fields have 125x50 gridblocks.

Fig. 4.18 is particularly interesting in that it quantifies how nonlinearity in the velocity field and heterogeneity interact, but does so statistically, rather than using a single recovery for each case. As a result, the weakness of HI as a parameter is traded for a more convincing spread in recovery given by the 30 curves for each case. Some interesting observations may be made from Fig. 4.18: (a) nonlinearity and reservoir heterogeneity interact to create a spread in recovery that increases with increasing mobility ratio and increasing heterogeneity; (b) of the two parameters, heterogeneity is clearly the dominant factor in establishing recovery; and (c) recovery envelopes partially overlap from one case to the next. A higher heterogeneity index or mobility ratio does not automatically lead to lower recoveries compared to a system with lower heterogeneity or mobility ratio, although on average this conclusion does hold. For example, an ($M = 5$,$HI = 0.86$) pair exists that will return a higher recovery than an ($M = 10$,$HI = 0.86$) pair.

Generating the 180 recoveries of Fig. 4.19 would have taken a prohibitively long time with a traditional finite-difference approach. Instead, if the streamtube approach is used as a filter for the 180 images, the number of solutions required to establish firmly the spread in recoveries is just six — two per case — as is shown in Fig. 4.19.

4.1.8 Limitations of the Streamtube Approach

As with all numerical techniques, the streamtube approach presented here has its limitations. The most serious limitation arises from using the same one-dimensional solution for all times. If a representative one-dimensional solution does not exist, then our approach, in its present form, is clearly not applicable. This may occur for domains that have non-constant initial conditions, problems with flow reversal, gravity-dominated displacements, or problems in which the boundary conditions change with time. In an areal domain, for example, where wells are routinely shut in, new infill wells are introduced, and flow rates vary, a one-dimensional solution that can be used for all the streamtubes does not exist.

It is possible to remove the limitation of arbitrary initial conditions along changing streamtubes by considering a numerical, one-dimensional solution along each streamtube as proposed by Bommer and Schechter [20] to move the solution forward in time for each Δt_D. We are currently pursuing this avenue as a way to generalize the streamtube approach.

Another key assumption in the streamtube method is the dominance of the heterogeneity in determining the flow response. If the reservoir is only mildly heterogeneous, then viscous fingering, which the streamtube approach cannot model explicitly, may dominate the displacement mechanism. For such cases, the streamtube approach would not be the correct numerical technique to use.

The biggest outstanding challenge in the streamtube approach is accounting for gravity. It is unclear what the representative one-dimensional solution is, and in multiphase flow there is an additional complication, because the velocity vectors for each phase do not point in the direction of the total velocity. Thus, a streamtube would not be representative of the flow direction of any one phase. We are actively pursuing the extension of our approach to gravity-dominated displacements and three-dimensional flow [17].

4.1.9 Summary and Conclusions

The underlying assumption in applying the streamtube method to describe two-phase immiscible and first-contact miscible flow in heterogeneous porous media is that field-scale displacements are dominated by reservoir heterogeneity and convective forces. Flow paths are captured by streamtubes, the geometry of which reflects the distribution of high and low flow regions in the reservoir. Each streamtube is treated as a one-dimensional system along which solutions to

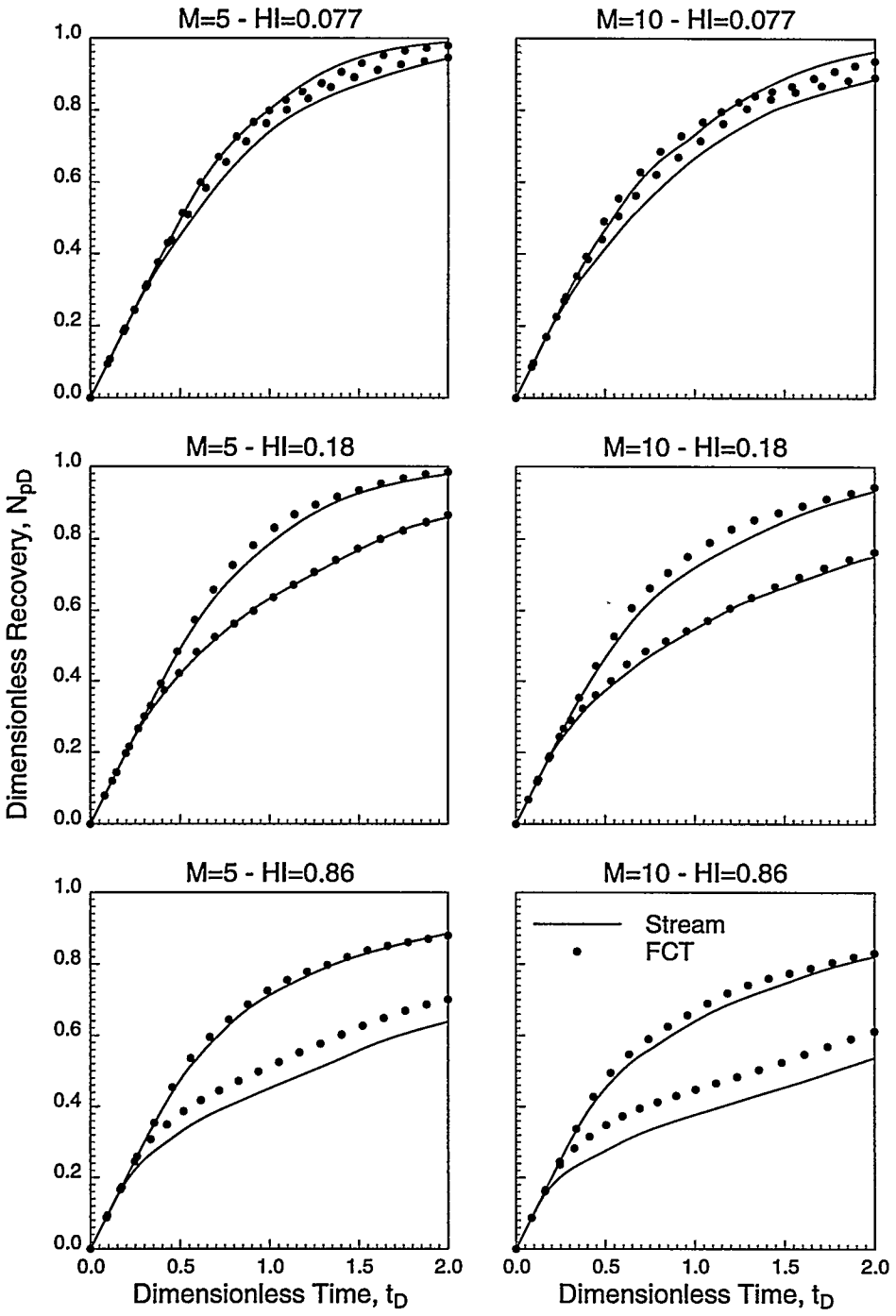

Figure 4.19: Confirming the spread in recoveries predicted by the streamtube approach by using a FCT finite-difference simulator on permeability fields associated with the maximum and minimum recoveries for each case predicted by the streamtube approach.

mass-conservation equations for different displacement mechanisms can be mapped. The streamtube approach effectively decouples the channeling imposed by the reservoir heterogeneity from the actual displacement mechanism taking place. In other words, regardless of the displacement type, the assumption is that there are predefined flow paths that will dominate the two-dimensional solution. The fluid velocity along these flow paths is reflected by the geometry of the streamtubes, and the inherent nonlinearity in the underlying velocity field is captured by periodically updating the streamtubes.

For a particular displacement type, the same one-dimensional solution is mapped along streamtubes, allowing to timestep by integrating from 0 to $t_D + \Delta t_D$. This approach allows analytical and numerical solutions to conservation equations to be mapped along periodically updated streamtubes, but does not account for general-type initial conditions along streamtubes that arise from the changing location of the streamtubes over time.

Fast, accurate, and robust solutions. The streamtube approach produces fast, accurate, and robust solutions to displacements that are dominated by reservoir heterogeneity. Streamtube geometries capture the impact of heterogeneity on the flow field, while the one-dimensional solutions mapped along them retain the essential physics of the displacement mechanism. Speed-up is by two to three orders of magnitude for two-phase immiscible and first-contact miscible displacements. The absence of any convergence criteria as well as accounting for all the essential physics in the one-dimensional solution leads to particularly robust solutions.

Statistical reservoir forecasting. The speed of the streamtube approach makes it an ideal tool for statistical reservoir forecasting: hundreds of geostatistical images can be processed in a fraction of the time required by traditional reservoir simulators. Application to first-contact miscible displacement show a substantial uncertainty in overall recovery due to the combined effects of reservoir heterogeneity and the inherent nonlinearity of the displacements. As reservoir heterogeneity and nonlinearity increase, so does the uncertainty in overall recovery. The streamtube approach allows to quantify this uncertainty, which can then be confirmed by a more expensive traditional approach by using only the two geostatistical images that produce maximum and minimum recoveries. Although the streamtube method makes assumptions in generating the two-dimensional solutions, the uncertainty in recovery because of heterogeneity is shown to be substantially larger than the error introduced by our approach.

Weak nonlinearity of Ψ. For all displacements, the number of necessary updates for the streamtubes to converge onto a solution are shown to be many orders of magnitude less than the equivalent number of pressure solves in traditional numerical simulation approaches. For all the displacements investigated here, 20 to 40 streamtube updates over two pore volumes injected were sufficient to give accurate overall recoveries.

4.2 Modeling Flow in Heterogeneous Media Using Streamtubes: II. Compositional Displacements

M. R. Thiele, M. J. Blunt, and F. M. Orr, Jr.

Thermodynamic considerations add a substantial degree of complexity to compositional displacements compared to the simpler two-phase immiscible and first-contact miscible displacements described in Section 4.1 [184]. The local equilibrium assumption requires a flash calculation for each gridblock at every timestep, while the traditional difficulties associated with numerical diffusion and frontal instabilities remain. Simulations become enormously expensive and yet may yield less than satisfactory solutions. Compared to the "simple" physics described by two-phase relative

permeabilities in immiscible displacements or the quarter-power mixing rule in first-contact miscible displacements, phase equilibrium and its coupling to multiphase flow poses daunting numerical difficulties, forcing very large computation times. As a result, most compositional simulations are performed on coarse grids and may have substantial amount of numerical diffusion. The problem of numerical diffusion is particularly subtle in compositional simulation, because it interacts with the phase-behavior to alter displacement performance, sometimes substantially. In multicontact miscible (MCM) flow a small amount of numerical diffusion is sufficient to induce two-phase flow by pulling the composition path into the two-phase region thus hindering development of true miscibility.[105, 193, 149]

The streamtube approach presented in Section 4.1 is a powerful tool for investigating compositional displacements. With a one-dimensional solution known, the two-dimensional solution for a heterogeneous system can be constructed with the same ease as for a tracer, immiscible, or first-contact miscible displacement as outlined in Section 4.1. Furthermore, because the one-dimensional solution may be calculated numerically using a large number of gridblocks, or analytically for some special cases [104, 46] (also see Chapter 2), numerical diffusion is minimized or even completely absent. Computation times are reduced dramatically, since beyond the savings resulting from the comparably small number of streamtube updates required to capture the nonlinear convective part of the displacement, all the phase-behavior is contained within the one-dimensional solution that is mapped along the streamtubes. This means that the phase-behavior is completely decoupled from the underlying Cartesian grid used to describe reservoir heterogeneity and to solve for the local flow velocity, and flash calculations are no longer necessary for each gridblock. The simplicity of the streamtube approach is in stark contrast to traditional compositional simulation, which faces significant numerical difficulties, particularly in strongly heterogeneous systems where extreme differences in local flow velocities impose very small timesteps and can cause convergence problems.

4.2.1 One-Dimensional Solutions

As for the displacements discussed in Section 4.1, applying the streamtube technique to model compositional flow in heterogeneous systems centers on the availability of a one-dimensional solution. Substantial progress on analytical solutions has been reported recently [104, 46, 135, 148], and analytical solutions have been presented for multicomponent problems that have constant initial and injected conditions (Riemann conditions) with either no volume change on mixing [104] (see Chapter 2) or volume change on mixing [46]. Compositional solutions subject to Riemann boundary conditions (constant left and right states) will be composed of shocks, constant states, and rarefaction waves.

Although all 1D solutions presented here could have been obtained analytically, we calculated them numerically to guarantee consistency in the phase-behavior representation between the one-dimensional solutions used along the streamtubes and the two-dimensional reference solutions found using the same compositional simulator in 2D. In other words, the two-dimensional compositional solutions used for comparing the streamtube solutions were obtained simply by increasing the number of blocks in the second dimension and specifying the heterogeneous permeability field, while leaving the PVT data untouched.

4.2.2 Heterogeneity and Phase Behavior

A key issue in multiphase, multicomponent flow through heterogeneous porous media revolves around the question of how phase-behavior and reservoir heterogeneity interact to define the displacement of resident hydrocarbons. Although several investigators have studied the problem, many questions remain, particularly with regard to conclusions drawn from numerical simulations

because of the limited number of gridblocks generally used in published studies. Numerical investigations of compositional displacements include the work by Gardner and Ypma [70], who simulated CO_2 displacements in uncorrelated, mildly heterogeneous systems on 100x10 and 40x10 grids; Chang *et al.*[27], who studied the displacement of a Maljamar separator oil by pure CO_2 at 1,200 psia and 90°F through a variety of different heterogeneous systems using an 80x20 mesh and a third-order finite-difference scheme; Fayers *et al.*[62] (Section 3.2), who simulated slightly sub-miscible gas displacements on 128x64 and 64x32 grids; and Blunt *et al.*[15], who present a theory for compositional viscous fingering that was validated against numerical solutions obtained using a high-order total-variation-diminishing (TVD) scheme on grids of up to 400x150 blocks.

In all these studies, the large parameter space introduced by the phase-behavior description (number of pseudocomponents, equation-of-state model, viscosity correlations, etc.) coupled with the well-known difficulties introduced by numerical diffusion and the uncertainties in the relative two- and three-phase flow properties as well as reservoir heterogeneity, combine to give a highly nonlinear, uncertain problem formulation that makes it difficult to separate what is physically meaningful from what is a purely numerical artifact. Besides proposing our streamtube approach as an alternative to conventional finite-difference/finite-element techniques in certain cases, one of the central issues of this paper is also to attempt to understand what traditional numerical solutions may be expressing about the physical interaction of phase-behavior and reservoir heterogeneity. We will show by comparing finite-difference solutions to ones obtained using the streamtube approach that even for simple three- and four-component systems, an adequate representation of the solution with finite differences requires hundreds of gridblocks in each dimension, even when a high-order numerical scheme is used. Hence our preliminary conclusion is that unless order 10^4 to 10^5 gridblocks (and probably more) are used in two dimensions, the resulting displacement predictions are unlikely to be accurate and will yield optimistic recoveries. In three dimensions, the number of gridblocks is likely to be in the order of 10^6 to 10^8. Unfortunately, such simulations are either outright impossible or may take a prohibitive amount of CPU time with current resources, and certainly cannot be done on a routine basis. Even with repeated upscaling to a coarsely gridded model, an attempt to determine a statistical spread in recovery because of the uncertainty in the description of the reservoir remains beyond current computer capabilities. In contrast, the simple streamtube method allows rapid and robust construction of approximate solutions for compositional flow in heterogeneous domains, preserving the sequence of composition fronts and avoiding difficulties associated with numerical diffusion interacting with the phase-behavior representation.

4.2.3 Three-Component Solution

An example of a high-volatility-intermediate (HVI) ternary system is given by CH_4 / CO_2 / C_{10} at 1,600 psia and 160°F[103]. The name high volatility intermediate refers to the strict ordering of the K-values, $K_{CH_4} > K_{CO_2} > K_{C_{10}}$, for all compositions and the fact that the intermediate component K-value is greater than one ($K_{CO_2} > 1$). This means that CO_2 will preferentially reside in the more mobile gas phase. An HVI system can give rise to either a condensing or vaporizing drive, depending on the initial and injected compositions. The displacement of a 30/70 (in mole fractions) CH_4/C_{10} oil by pure CO_2, for example, is a condensing gas drive. One-dimensional numerical solutions for the $CH_4/CO_2/C_{10}$ system found using 100 and 500 gridblocks and a third-order TVD scheme are shown in Fig. 4.20. The solutions in Fig. 4.20 were found using the Peng-Robinson equation of state[154], the Lohrenz-Bray-Clark correlation for the phase viscosities[125], and Corey-type relative permeabilities with an exponent of 2 and a residual oil saturation of 0.2. The numerical simulator used here was UTCOMP (V3.2)[189], an implicit-pressure, explicit-saturation (IMPES) type, isothermal, three-dimensional compositional simulator developed at The University of Texas at Austin. The reason for finding the one-dimensional solution numerically, rather than

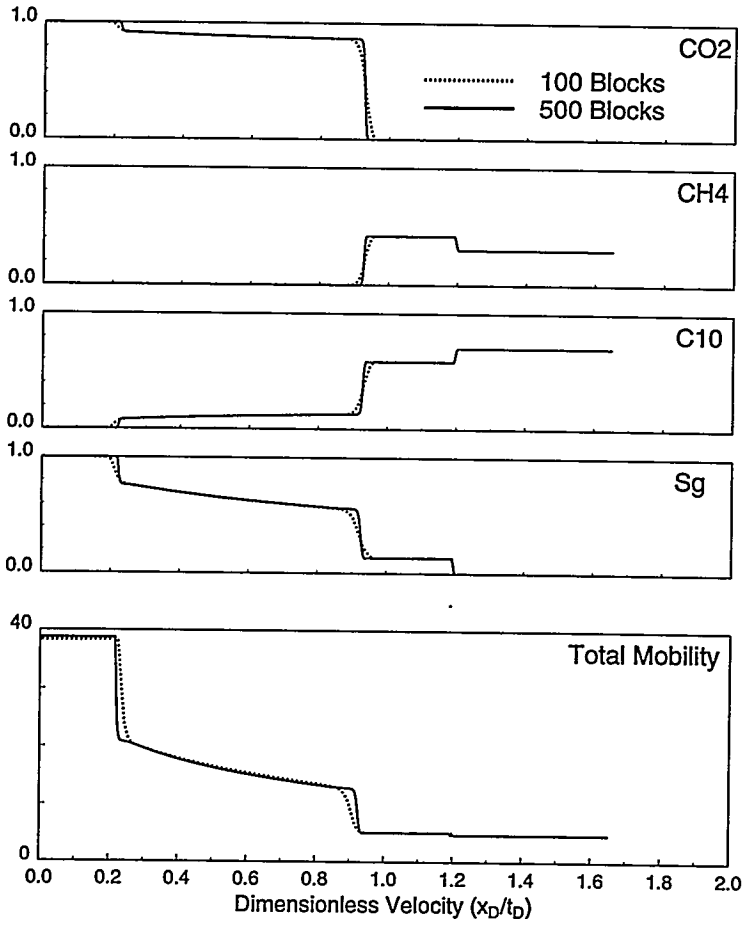

Figure 4.20: UTCOMP one-dimensional numerical solutions using 100 and 500 gridblocks and a third-order TVD scheme to control numerical diffusion for the $CH_4/CO_2/C_{10}$ condensing gas drive.

analytically, was to guarantee consistency in the phase-behavior representation between the one-dimensional solutions used along the streamtubes and the two-dimensional reference solutions found using the same compositional simulator in 2D.

The numerical solutions in Fig. 4.20 capture all the the essential shocks in the condensing gas drive, and in particular the 500-block solution has an acceptable level of numerical diffusion. For modeling purposes, the total mobility profile is the most important piece of information, because it indicates the strength of the nonlinearity of the total flow velocity and directly ties into the solution of the streamtubes. Thus, the total mobility profile is mapped along each streamtube, just like the concentration or saturation profiles, to find the new mobility field, which is then used directly in the solution of the elliptic PDE (Section 4.1, Eq. 4.1) for the streamfunction. For this particular case, although the endpoint mobility ratio is approximately 8, the mobility ratios across the two fronts, which are separated by a long rarefaction wave, are approximately 2 and 3. Thus, the endpoint mobility contrast is reduced considerably by the phase behavior alone.

2D Solutions. A compositional solution (almost free of numerical dispersion) for flow through a heterogeneous domain can now be found by mapping the 500-gridblock, third-order TVD solution shown in Fig. 4.20 along streamtubes. Composition and saturation maps for a 125x50-block heterogeneous reservoir at $t_D = 0.3$ are shown in Fig. 4.21. The heterogeneity field used here has a heterogeneity index of $HI = 0.3$ and a variance of $\sigma_{\ln k} = 1.0$ and corresponds to an upscaled version (using geometric averaging) of the 250x100 gridblock field used extensively in Section 4.1. The various composition fronts arising from chromatographic separation are clearly visible and,

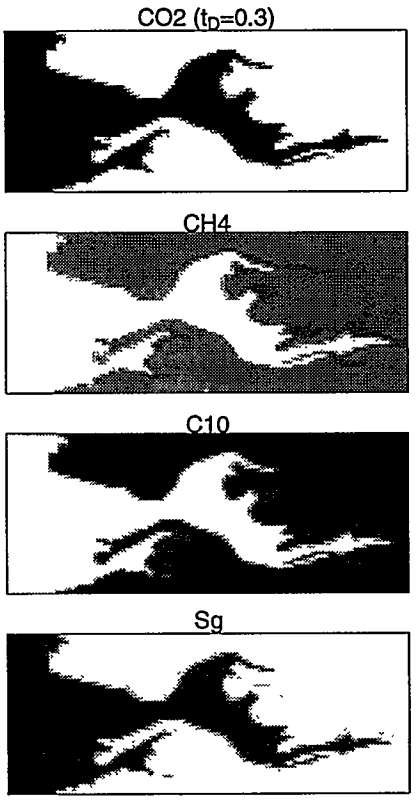

Figure 4.21: Two-dimensional, three-component condensing gas drive in a 125x50-mesh heterogeneous reservoir at $t_D = 0.3$. The one-dimensional solution used to generate the two-dimensional solution is shown in Fig. 4.20.

although the endpoint mobility ratio is $M \approx 8$, the displacement does not suffer from the instabilities that an equivalent first-contact miscible (FCM) displacement with the same endpoint mobility ratio would see. The reason for this is that the phase-behavior mitigates the initial mobility ratio contrast by creating two weaker fronts, which are separated by a long rarefaction wave.

A comparison of the approximate streamtube solution to a two-dimensional finite-difference solution (UTCOMP) found using a third-order TVD scheme is shown in Figs. 4.22 and 4.23. Fig. 4.22 compares composition and saturation profiles at $t_D = 0.4$, whereas Fig. 4.23 compares only the gas saturation profiles at $\Delta t_D = 0.1$ intervals. The agreement is good, particularly considering that UTCOMP required approximately 5,000 Cray seconds per 0.1PV injected, whereas the streamtube solution required less than 2 Cray seconds, a speed-up factor by over three orders of magnitude. Figs. 4.22 and 4.23 are encouraging, because they suggest that the streamtube approach detailed in Section 4.1 can be combined successfully with a one-dimensional compositional solution as well to model a two-dimensional displacement through a heterogeneous domain at a significantly reduced cost.

Nevertheless, even though the comparison between the finite-difference and the streamtube solutions is good, the leading front in the streamtube solution is at breakthrough, whereas it has advanced only two-thirds as far in the UTCOMP solution. This raises the question whether the difference is due to the assumptions inherent in our approach, which cannot model some physical phenomena, like transverse diffusion and mixing due to viscous crossflow, or whether it is due to numerical errors in the UTCOMP solution. Clearly, both numerical approaches involve some errors; the subtlety of the question really lies in trying to understand which of the two solutions is closest to the "true" solution.

The UTCOMP solution shown in Figs. 4.22 and 4.23 was obtained without explicitly adding

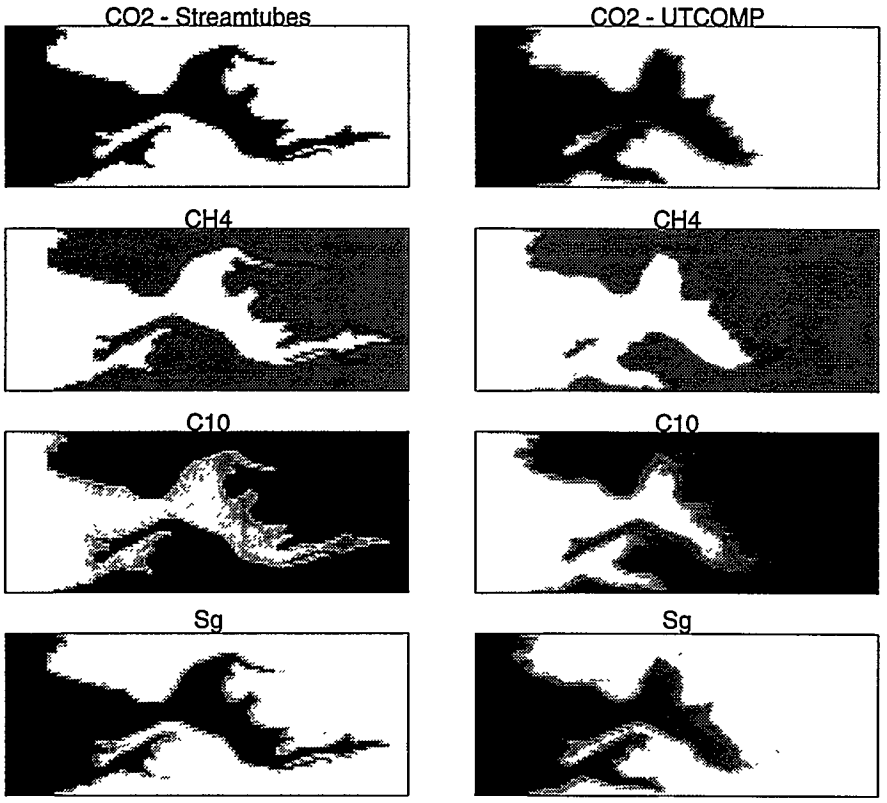

Figure 4.22: Comparison of the streamtube solution with the UTCOMP solution at $t_D = 0.4$. The UTCOMP solution was found using a third-order TVD scheme.

any diffusive terms like capillary pressure or physical diffusion/dispersion. Thus, the only remaining mechanisms that could lead to a reduction of the mobility contrast in the two-dimensional finite-difference solutions are transverse and longitudinal numerical diffusion and mixing resulting from viscous crossflow. Although the TVD scheme is certainly able to contain numerical diffusion, we know that some numerical diffusion must be present, particularly given that there are only 50 blocks in the transverse direction and 125 in the main direction of flow. It is also worth mentioning that a TVD scheme in 2D is not as efficient as in 1D [123]. Whether there is mixing because of viscous crossflow is difficult to say, particularly given that there seem to be no additional features in the saturation profiles compared to the streamtube solution that would indicate crossflow.

The streamtube solution, by definition, does not account for any transverse diffusion or mixing processes. Furthermore, it marches forward in time by always using the same one-dimensional solution and mapping it at $t_D + \Delta t_D$ along updated streamtubes. The net effect is that our method cannot account for physical mechanisms that may attenuate the original mobility contrast seen in the one-dimensional solution. As a result, the streamtube solution may be overly dominated by the mobility contrast seen in the one-dimensional solution causing a faster leading front and earlier breakthrough than in the finite-difference solution.

In order to evaluate the streamtube solution further, two additional simulations were performed: (1) a UTCOMP solution was found using a one-point upstream scheme to emphasize the effects of numerical diffusion (Fig. 4.24) and (2) a diffused one-dimensional compositional solution was mapped along the streamtubes in an attempt to include numerical longitudinal diffusion as a mitigating factor on the mobility contrast (Figs. 4.25 and 4.26). (A simulation with a refined 250x100 grid and a third-order TVD scheme, while maintaining the same heterogeneity structure, was attempted using UTCOMP as well, which would have allowed us to quantify the impact of numerical diffusion more directly. Unfortunately, excessive computation costs, $\approx$ 20hr per 0.1 PV,

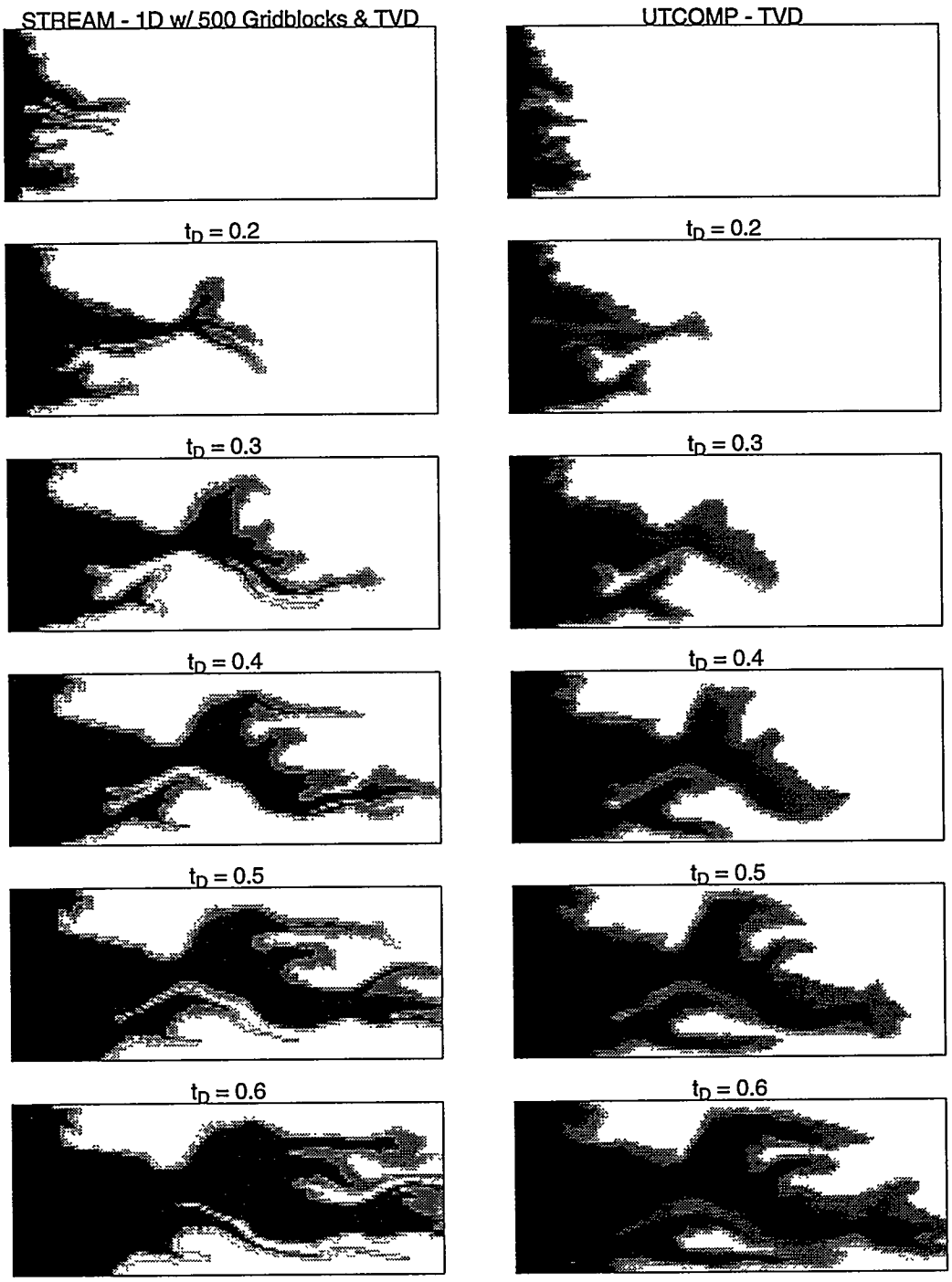

Figure 4.23: Comparison of the evolution in time of the gas saturation. The streamtube solution was found using a 500-gridblock one-dimensional solution, while the UTCOMP solution was found using a third-order TVD scheme.

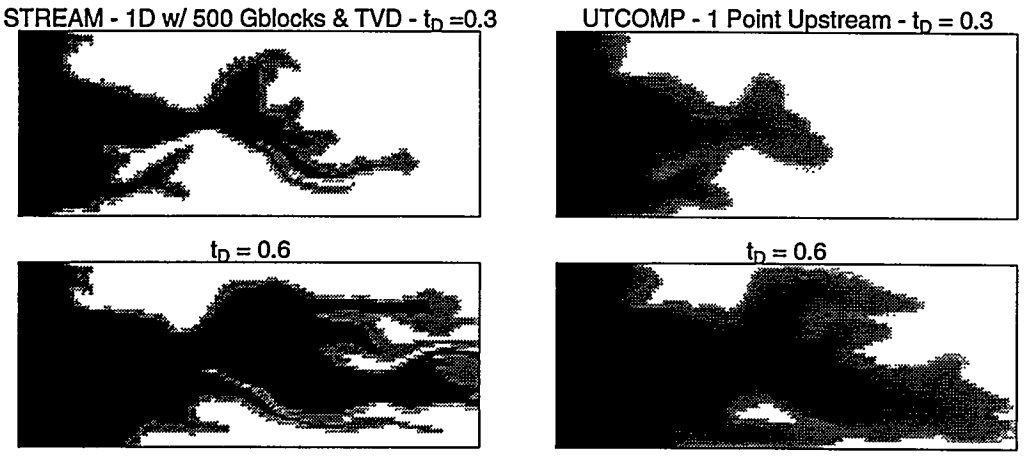

Figure 4.24: Comparison of the evolution in time of the gas saturation. The streamtube solution was found using a 500-gridblock one-dimensional solution, while the UTCOMP solution was found using a single-point upstream weighting scheme.

forced the simulation to be terminated.)

25x50 One-Point Upstream Solution. Fig. 4.24 compares a UTCOMP solution found using one-point upstream weighting to the same streamtube solution shown in Figs. 4.22 and 4.23. The degradation because of numerical diffusion in the UTCOMP finite-difference solution is considerable compared to the TVD solution (Fig. 4.23), and most importantly, the solution now has an even more stable character to it; the fronts are much more diffused and breakthrough occurs later than in the TVD solution. This is an indication that transverse and longitudinal numerical diffusion are mitigating the mobility contrast in the UTCOMP solution altering the nature of the instability of the displacement.

4.2.4 Diffused Streamtube Solution

If the frontal instability is mitigated principally by longitudinal numerical diffusion, then it should be possible to map a diffused one-dimensional solution along the streamtubes that would lead to a solution that would look similar to the UTCOMP solution of Figs. 4.22 and 4.23. On the other hand, if the instability is mitigated principally by transverse numerical diffusion, then it is unlikely that the UTCOMP solution can be matched by the streamtube method, since transverse phenomena are not accounted for in our approach. The one-dimensional solution used in the streamtube solution so far was obtained using 500 gridblocks and a third-order TVD scheme, which produced a solution with relatively sharp fronts (Fig. 4.20). To capture the fact that only 125 blocks are present in the main direction of flow in the two-dimensional heterogeneous domain, a one-dimensional solution using only 100 gridblocks and single-point upstream weighting was generated and mapped along streamtubes. A difficulty associated with mapping a diffused one-dimensional solution is that the solution is no longer scalable by x_D/t_D, as is shown in Fig. 4.25.

There are 10 curves in Fig. 4.25, each representing a solution at time increments of $\Delta t_D = 0.1$ (starting from $t_D = 0.1$). The solution clearly tends to sharpen up with time as we expect. To capture the time dependence of the diffused, one-dimensional solution in Fig. 4.25, the solution was mapped along the streamtubes for the corresponding time interval. In other words, the first curve was used in the streamtube simulator to find solutions in the range of $t_D = 0.0$ to $t_D = 0.1$, the second curve for solutions between $t_D = 0.1$ and $t_D = 0.2$, etc. Although this approach is only a rough attempt to include longitudinal numerical-type diffusion into the streamtube solution, it does mitigate the mobility contrast somewhat in the resulting two-dimensional solution. Fig. 4.26 shows

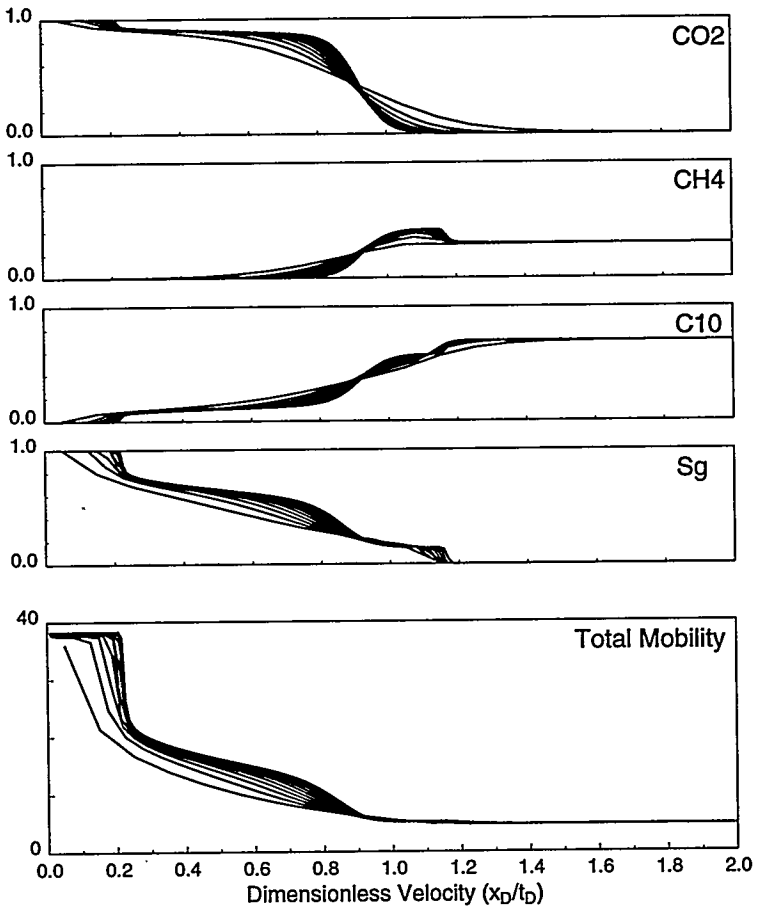

Figure 4.25: One-dimensional UTCOMP solution using 100 gridblocks and one-point upstream weighting. Each solution represents an increment of $\Delta t_D = 0.1$.

a comparison of the UTCOMP saturation maps to the saturation maps obtained by mapping the more diffused one-dimensional solutions of Fig. 4.25 onto streamtubes. Fig. 4.27 shows a summary of the gas saturation maps for the various cases. Although the streamtube displacement appears slightly more stable compared to the one found using 500 gridblocks (see Fig. 4.23), breakthrough still occurs earlier than in the UTCOMP solution, suggesting that other mixing phenomena must be present in the UTCOMP solution that are not present in the streamtube solution.

The very large difference in computation times, 3,000 to 5,000 Cray seconds per 0.1 PV injected depending on the numerical scheme for UTCOMP versus the 2 to 3 Cray seconds for the streamtube solution, makes the streamtube approach an attractive alternative, despite the underlying assumptions used in mapping the one-dimensional solutions along the streamtubes and the differences in the solution compared to one obtained using finite differences. Fig. 4.27 is particularly interesting in that it suggests that transverse and longitudinal numerical diffusion in finite-difference solutions may be able to mitigate substantially the instability of the displacement compared to what is seen in the equivalent one-dimensional solution. In turn, this raises the difficult question of whether the finite-difference solutions in Fig. 4.27 can indeed be considered converged and are capturing the true instability of the displacement.

Cumulative recoveries for the three-component problem are shown in Fig. 4.28. It is particularly revealing to note that the difference in recovery due to the different one-dimensional solutions used along the streamtubes (500 gridblocks and TVD versus 100 gridblocks and one-point upstream) is negligible. This reinforces the possibility that the mobility mitigation in the UTCOMP solution

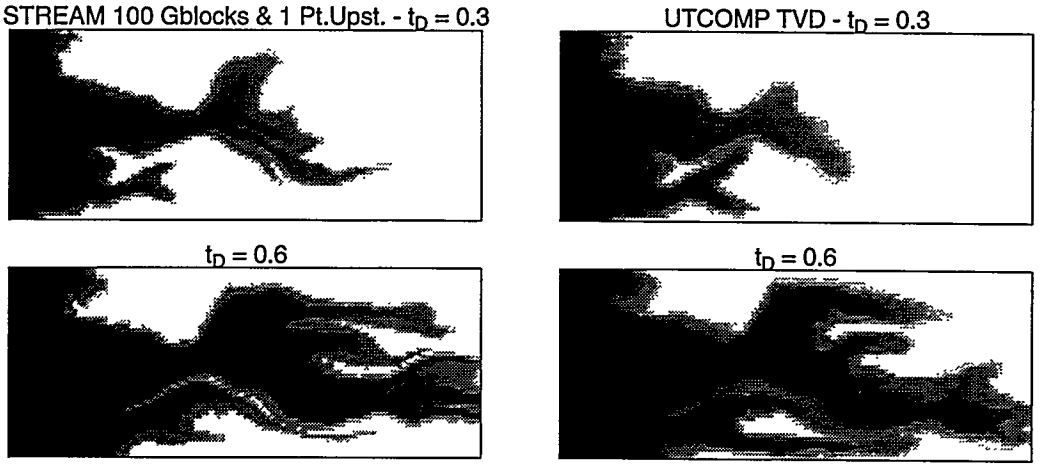

Figure 4.26: Comparison of the evolution in time of the gas saturation. The streamtube solution was found using a single-point upstream, 100-gridblock 1D solution, while the UTCOMP solution was found using a third-order TVD scheme on a 125x50 grid.

is unlikely to be an artifact of longitudinal-type diffusion, but rather from a transverse-type mixing mechanism, such as transverse diffusion or mixing due to viscous crossflow. The substantial difference between the UTCOMP and streamtube recoveries is in contrast to the good matches obtained for the immiscible and ideal miscible cases for the same permeability field (PERM 11) as shown in Section 4.1 (Figs. 4.10 and 4.14, respectively). We interpret this difference as an indication that a small amount of transverse mixing, either due to numerical diffusion or viscous crossflow or both, coupled with the phase-behavior of the system has a considerable impact on recovery. The one-dimensional recovery is also shown as a way to quantify the impact on recovery due to heterogeneity alone.

Fig. 4.29 shows the convergence of the streamtube solution. As in the FCM displacements discussed in Section 4.1 of this work, fewer than 40 streamtube updates are sufficient to capture the changing velocity field resulting from the nonunit mobility ratio of the displacement. In this case though, the speed-up compared to the finite-difference approach is by four orders of magnitude because in addition to reduced number of matrix inversions there are no phase-behavior calculations since all the phase-behavior is contained in the one-dimensional solution mapped along the streamtubes. How substantial the mitigation of the initial instability really is is quantified by the fact that the UTCOMP recovery falls between the streamtube solutions using a single update (tracer case) and ten updates of the streamtubes.

4.2.5 Four-Component Solution

The three-component system presented in the previous section was characterized by a condensing displacement mechanism. In this section, the displacement of a three-component oil ($CH_4/C_6/C_{16}$) by an enriched gas composed of a mixture of CH_4 and C_3, at 2,000 psia and 200°F is used as an example of a displacement exhibiting condensing behavior at the leading edge and vaporizing behavior at the trailing edge. The example is taken from Johns (p.194) [103]. The initial composition of the oil (in mole fractions) is $CH_4 = 0.2$, $C_6 = 0.4$, $C_{16} = 0.4$, and the injected composition of the enriched gas is $CH_4 = 0.65$ and $C_3 = 0.35$. The injected conditions are close to the minimum enrichment composition for miscibility ($CH_4 = 0.615$ and $C_3 = 0.385$), characterizing the system as near-miscible[103].

Fig. 4.30 shows the numerical one-dimensional solutions obtained from UTCOMP using 100 and 500 gridblocks and a third-order TVD scheme. Compared to the three-component solution

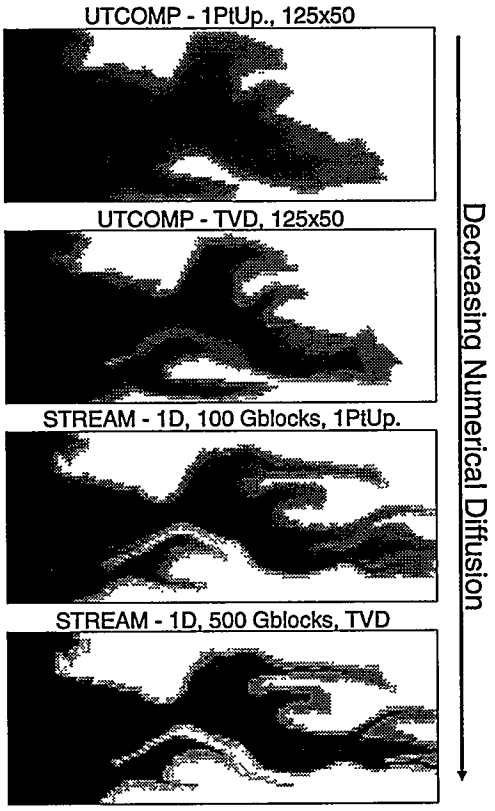

Figure 4.27: Summary of gas saturation maps at $t_D = 0.5$.

(Fig. 4.20), some numerical difficulties are evident for this example, as indicated by the more diffused fronts and the dip in the total mobility profile near the inlet. Nevertheless, the 500 gridblock solution does seem to capture the main feature of the displacement and sees the condition of near miscibility: the main part of the two-phase region is small and the total mobility profile shows a substantial mobility contrast across the two-phase region. The mobility profile is the main indicator of the instability that will control the displacement; for this case, the initial mobility contrast is $M \approx 8.4$, but unlike the three-component solution, which had a similar endpoint mobility ratio, the two main fronts are much closer to each other because of the condition of near miscibility and lead to a mobility contrast of $M \approx 6$ across the leading fronts. Thus, even though the endpoint mobility ratios are similar, the four-component streamtube solution is expected to be more unstable than the three-component solution discussed previously and therefore more difficult to model accurately in two dimensions.

The strong nonlinearity is clearly visible in Fig. 4.31, which compares the streamtube solution to a two-dimensional UTCOMP solution found using a third-order TVD scheme. The streamtube solution breaks through much earlier and the channeling is more pronounced than the finite-difference solution. As in the three-component case, the question arises whether the much more stable displacement predicted by the finite-difference formulation is a result of numerical diffusion or is, indeed, a genuine physical feature of the displacement mechanism. The possible impact of numerical diffusion is again studied by using single-point upstream weighting in UTCOMP, as well as a diffused one-dimensional solution along the streamtubes. (A simulation using a refined 250x100 grid with UTCOMP was attempted, but led to prohibitively high computation costs and had to be terminated.)

A comparison of UTCOMP saturation maps found using single-point upstream weighting

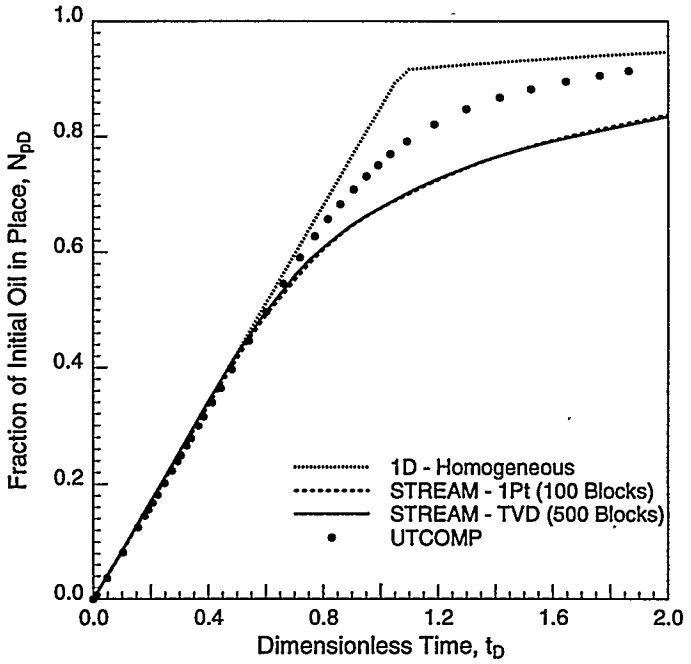

Figure 4.28: Recovery curves for the $CO_2/CH_4/C_{10}$ system.

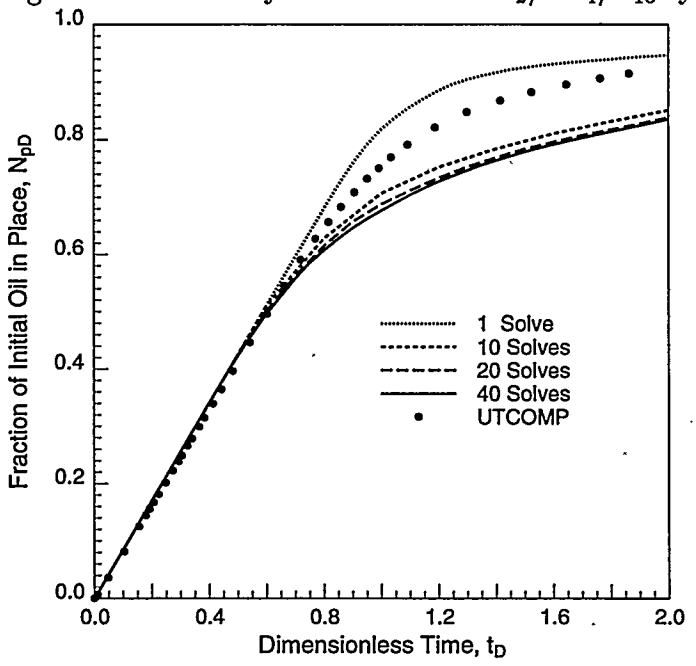

Figure 4.29: Convergence for the the $CO_2/CH_4/C_{10}$ system, showing that overall recovery can be predicted using fewer than 40 streamtube updates over 2 PV injected.

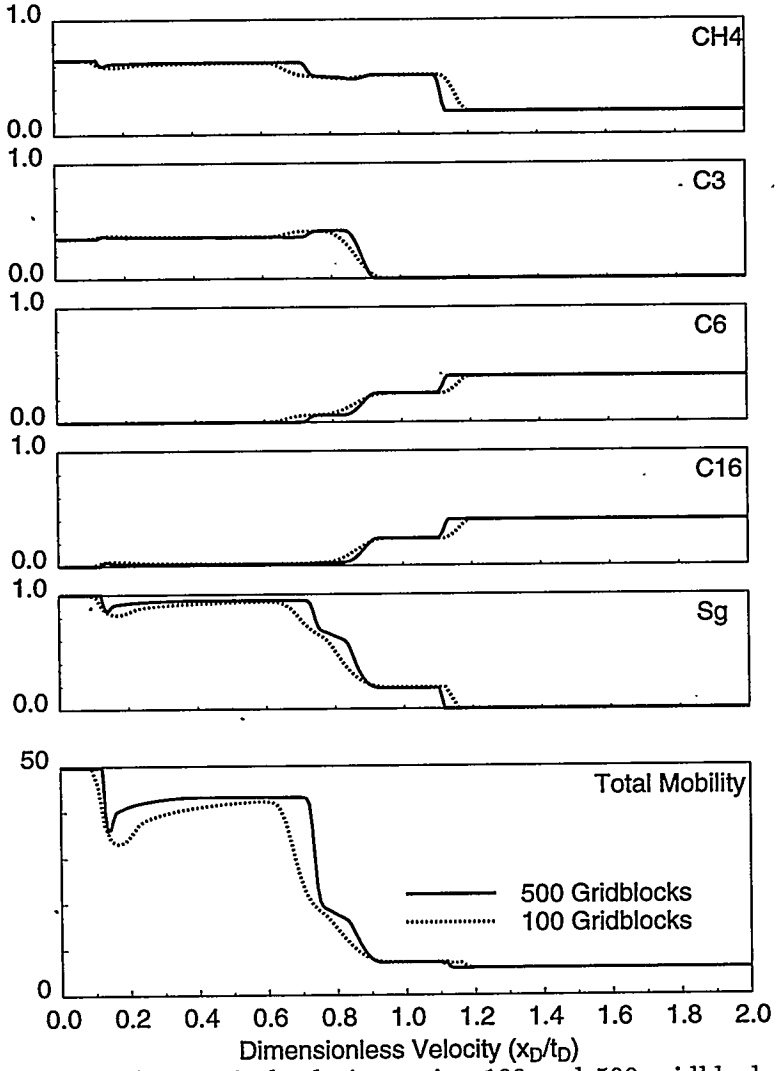

Figure 4.30: One-dimensional numerical solution, using 100 and 500 gridblocks and a third-order TVD scheme to control numerical diffusion for the $CH_4/C_3/C_6/C_{16}$ condensing/vaporizing gas drive.

and a third-order TVD scheme is shown in Fig. 4.32. The TVD solution shows a noticeable improvement in the resolution of the leading shock compared to the single-point upstream solution, indicating that numerical diffusion is affecting the displacement, but it does not show as good an improvement in capturing the instability of the displacement: the positions of the leading fronts in the two solutions shown in Fig. 4.32 are only marginally different. Thus, the mitigating effects longitudinal and transverse numerical diffusion have on the displacement by interacting with the phase-behavior of the system do not seem to be offset by the improved numerical resolution of the third-order TVD scheme. This points to an important aspect regarding control of numerical diffusion in compositional models: because numerical diffusion interacts in a complex way with the phase behavior of the system, doubling the number of cells and/or using an improved numerical scheme may not result in the same improvement in modeling the instability of the displacement as it would for ideal miscible or immiscible displacements. Furthermore, increasing the "complexity" of the phase-behavior description and the proximity to miscibility will decrease the efficiency of any numerical scheme to control numerical diffusion and its impact on displacement efficiency, particularly for higher mobility ratios. We interpret our results as indicating that the two-dimensional UTCOMP solutions are not likely to be fully converged, but rather represent intermediate solutions in a possible refinement sequence that would ultimately show a displacement with a stronger

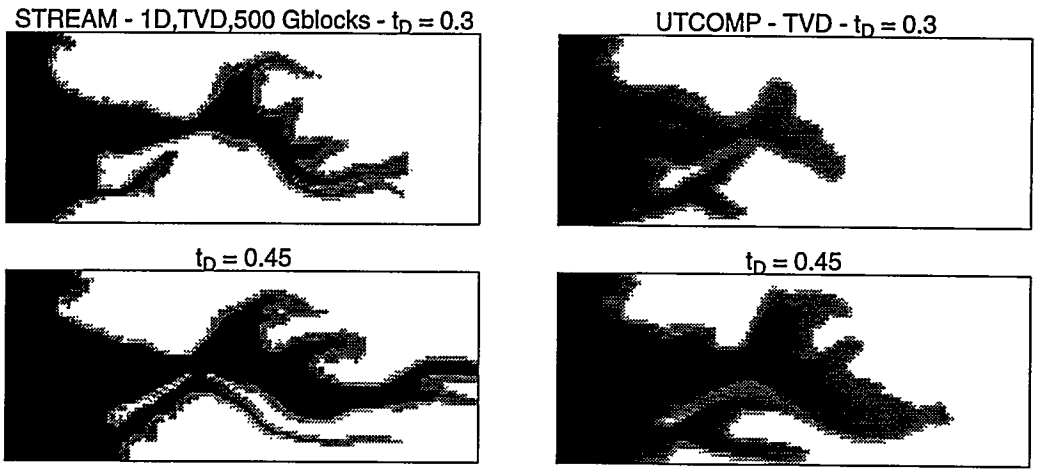

Figure 4.31: Saturation maps for the $CH_4/C_3/C_6/C_{16}$ displacement on a 125x50 gridblock heterogeneous domain. The UTCOMP solution was found using a third-order TVD scheme, while the streamtube solution used the 1D, 500-gridblock TVD solution.

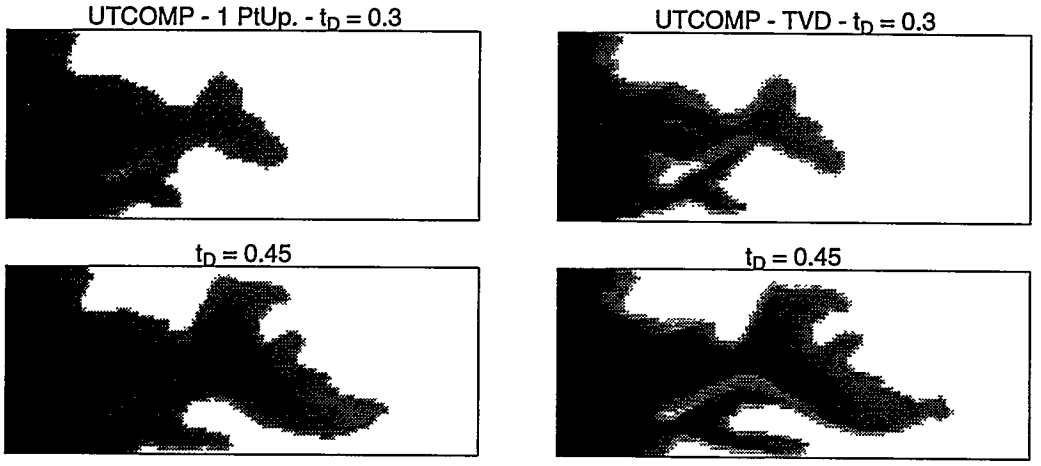

Figure 4.32: UTCOMP saturation maps for the $CH_4/C_3/C_6/C_{16}$ displacement at various times. The UTCOMP solutions were found using single-point upstream weighting and a third-order TVD scheme.

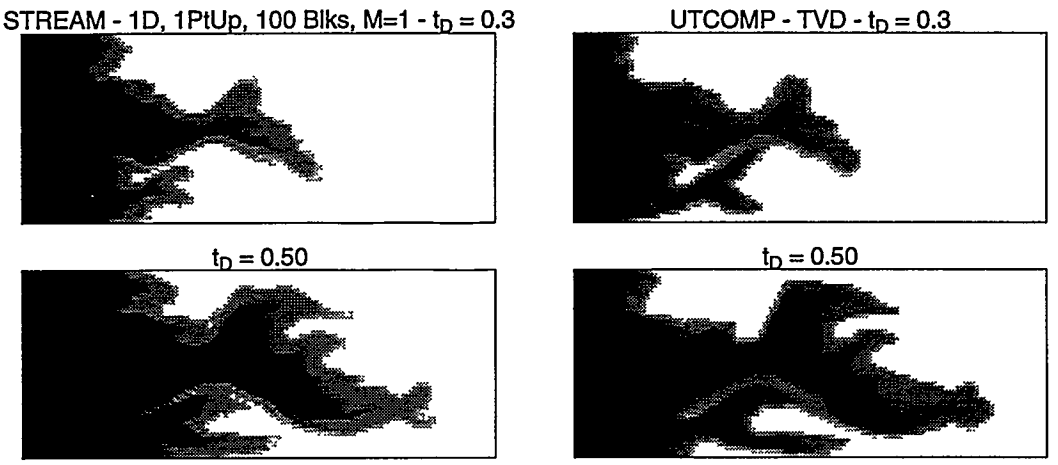

Figure 4.33: Saturation maps for the two-dimensional UTCOMP and streamtube solutions for the $CH_4/C_3/C_6/C_{16}$ displacement. In this example, the streamtube solution was found by using a 100-gridblock, 1D solution and $M = 1$. The UTCOMP solution is the same as shown in Fig. 4.32.

nonlinear behavior and substantial frontal instability.

The quantitative reduction in the inherent instability of the displacement in the finite-difference formulation is revealed by Fig. 4.33, which compares a "diffused" streamtube solution to the UTCOMP (TVD) solution. The streamtube solution was generated using a 1D, 100-gridblock, single-point upstream solution, but assuming a unit mobility ratio displacement ($M = 1$) throughout. In other words, the streamtubes were calculated only once, as in the tracer case, and used to describe the velocity field for the entire duration of the displacement, thereby ignoring any mobility contrast between the phases. The match in this case is much better than in any of the ones shown previously.

The comparisons in Fig. 4.33 are particularly revealing because they indicate that numerical diffusion and phase-behavior combine to mitigate substantially, or even completely eliminate, the original instability of a displacement. It is unlikely that any true physical crossflow mechanism could eliminate the entire mobility contrast of the displacement without altering in some way the fingering/channeling pattern. Furthermore, the speed-up is now by four to five orders of magnitude, since the streamtube solution uses a single matrix inversion versus the many thousand pressure solves and flash calculations required by the finite-difference formulation. The most dramatic conclusion to be drawn from these three- and four-component example solutions is that two-dimensional compositional solutions, particularly those generated on coarse grids and with a simple single-point upstream weighting scheme, are very likely not to be converged solutions, and will always predict optimistic recovery performance.

4.2.6 Summary and Conclusions

We show that for compositional displacements the streamtube approach is particularly powerful because of its simplicity, robustness, and speed. The speed-up compared to traditional finite-difference approaches can range from 3 to 5 orders of magnitude. Our results from example comparisons with finite-difference solutions suggest that numerical diffusion, particularly transverse numerical diffusion, can substantially reduce, or even completely eliminate, the mobility contrast seen in the equivalent one-dimensional solution.

Decoupling of phase-behavior from 2D grid. The streamtube approach becomes particularly

powerful for multiphase compositional displacement, because all the phase-behavior is now contained in the one-dimensional solution that is mapped along the streamtubes, thereby completely decoupling the underlying Cartesian grid used to specify reservoir heterogeneity from phase-behavior considerations. This is different from traditional approaches to reservoir simulation, which perform a flash calculation for each gridblock at each timestep. As a result, the streamtube approach makes for very robust and fast solutions in the case of compositional displacements.

Impact of numerical diffusion on compositional displacements. The examples presented indicate that numerical diffusion has a significant role in reducing the mobility contrast in traditional finite-difference solutions of compositional displacement. By comparing streamtube solutions to finite-difference solutions, we found that the original mobility contrast can be substantially reduced by the presence of numerical diffusion, particularly transverse numerical diffusion: the coupling of reservoir heterogeneity, phase behavior, and numerical diffusion may be so dominant in compositional displacements as to force only slow convergence with progressive grid refinement. As a result, many times the grid refinement used in FCM displacement may be necessary for compositional displacements, particularly if a single-point upstream weighting scheme is being used, to see the equivalent improvement in the solution. Thus, we argue that compositional displacements on coarse grids obtained using a single-point upstream weighting scheme, which are common in the published literature, are unlikely to be converged solutions in the sense of displaying the true instability of the displacement and must be interpreted with caution.

Weak nonlinearity of Ψ. For all displacements, the number of updates of streamtubes required to converge to a solution is shown to be many orders of magnitude fewer than the equivalent number of pressure solves in traditional numerical simulation approaches. As a result, updating the streamtubes only periodically (20 to 40 times per 2 pore volumes injected) and using a one-dimensional solution that captures the essential physics and nonlinearity of the displacement are sufficient to give accurate overall recoveries. As for the displacements described in Section 4.1, this offers the opportunity to quantify the impact of uncertainty in reservoir description on recovery without sacrificing the underlying physics of the displacement mechanisms to numerical errors.

4.3 A 3D Streamline Simulator

R. P. Batycky and M. J. Blunt

The results presented in Sections 4.1 and 4.2 were based on use of streamtubes to model flow in convection-dominated two-dimensional displacements. They show that streamtube calculations combined with mapping of any one-dimensional solution onto the streamtubes, results in accurate performance predictions using between 10 and 10000 times fewer matrix inversions than conventional approaches. The main focus of our work here is to extend that streamtube method to three-dimensional field scale systems with arbitrary well locations.

In this work, we trace streamlines in a three-dimensional flow field as opposed to calculating the streamtubes[1], although in 2-D our streamline method gives identical results to 2-D solutions reported in Section 4.1 and 4.2. As with the streamtube method, each streamline is treated as a one-dimensional homogeneous systems along which any one-dimensional solution can be mapped. The physics of the displacement is captured in the appropriate one-dimensional solution, while the effects of the heterogeneity are captured by the paths of the streamlines.

[1]Streamtubes do exist in 3-D, but calculating them can be quite involved (Matanga [128])

4.3.1 Tracing Streamlines and Mapping a One-Dimensional Solution

By definition, a streamline is a line in a velocity field that at any location is parallel to the local velocity vector. We trace streamline paths by a procedure similar to those documented in particle tracking and groundwater literature.

A summary of the streamline tracing and one-dimensional solution mapping method to arrive at a three-dimensional solution is shown below.

(i) Solve the pressure equation,

$$\nabla \cdot \lambda_t \nabla P = 0, \tag{4.32}$$

on a conventional finite difference grid with appropriate well locations and noflow outer boundaries. Here λ_t is the total mobility at any point in the grid and P is the pressure.

(ii) Solve for the velocity field at each gridblock face using Darcy's Law.

(iii) Apply the method derived by Pollock [155] for the analytical definition of a streamline path within a gridblock. In Pollock's method, he defined a piecewise linear interpolation of the velocity field in each direction, within a gridblock, based on the values at the block faces.

(iv) Trace streamlines from injectors to producers using the analytical expressions within each gridblock. For each block that a streamline passes through, record the time-of-flight. King *et al.* [111] defined the time-of-flight, tof_s, to any location, s, as the time it takes to move along a given streamline from the injector to location s,

$$tof_s = \int_0^s \frac{1}{V(\zeta)} d\zeta. \tag{4.33}$$

Here $V(\zeta)$ is the local interstitial velocity along the streamline.

(v) Map a one-dimensional solution along each streamline. These solutions (composition, saturation) typically scale by dimensionless velocity x_D/t_D. At any given elapsed time of the simulation, t_e, the following relationship holds,

$$\frac{tof}{t_e} = \frac{x_D}{t_D}. \tag{4.34}$$

So for a given elapsed time, any location along a streamline corresponds to a dimensionless velocity and hence, a unique composition and saturation.

We have integrated the above steps into a general 3-D streamline simulator, 3DSL, that can handle multiple wells in any location.

4.3.2 Current Results

In this section we use 3DSL for several simulations, and compare against ECLIPSE or analytical solutions where available. We look at tracer displacements, the application of 3DSL to multiple equiprobable realizations, and conclude with waterflood displacement comparisons on three different permeability fields.

Quarter Five-Spot Tracer Displacement. To validate our numerical method employed here, we first compare 3DSL results with the analytical solution of a tracer displacement in a quarter-five spot. The analytical streamline tracing technique combined with a 1-D tracer profile should yield "exact" results from 3DSL. The results on a 100X100 grid are shown in Figure 4.34[2]. Also included

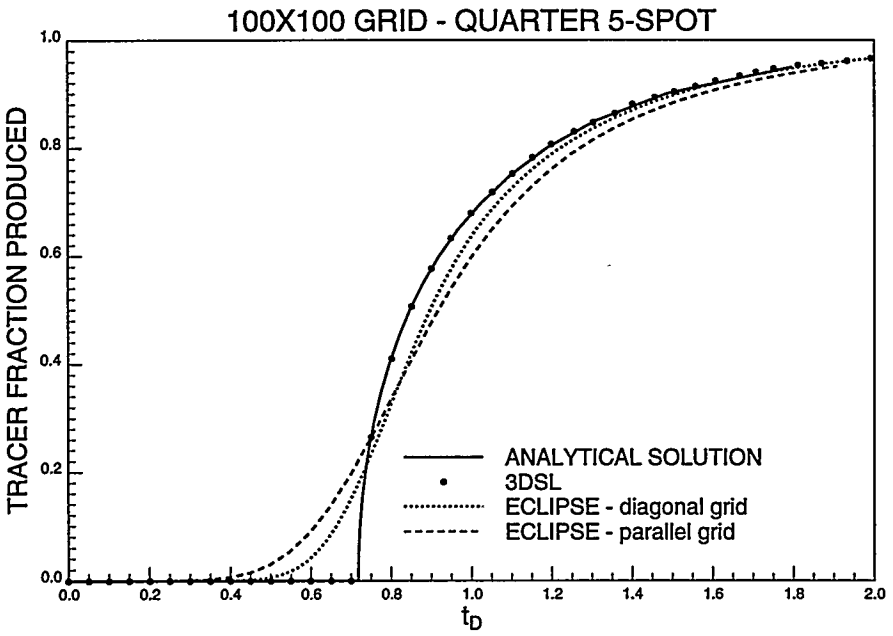

Figure 4.34: Tracer concentration at producer in a quarter-five spot.

are results from ECLIPSE for a diagonal and parallel grid. Clearly the 3DSL results are identical to the analytical solution and are free of numerical diffusion and grid orientation effects.

Three-Dimensional Tracer Simulations Because tracer results from 3DSL are exact, we can use this new simulator to quantify the level of numerical diffusion present in conventional ECLIPSE tracer simulations. Here we have generated a 40X40X10 permeability field using GSLIB. The field, as seen in Figure 4.35, is anisotropic with an on-trend correlation length of $\lambda_c = 0.5$ in the main horizontal direction, a transverse correlation length in the horizontal of $\lambda_c = 0.2$ and vertical correlation length of $\lambda_c = 0.1$.

We performed two quarter-five spot displacement experiments, one in the on-trend direction and one in the off-trend direction. The tracer recoveries for 3DSL and ECLIPSE are shown in Figure 4.36. The ECLIPSE results agree better with the actual solution (3DSL) when the main flow direction is off-trend as opposed to on-trend. The difference seen in the two solution methods is based strictly on the magnitude of numerical diffusion within ECLIPSE.

ECLIPSE has both longitudinal and transverse numerical diffusion while 3DSL has neither. Longitudinal diffusion along a streamline will smear the displacing tracer shock and act to reduce tracer recovery, while transverse diffusion will improve recovery. Clearly in the on-trend case transverse diffusion within ECLIPSE is more important than transverse convection. Tracer fingering through high permeability regions has the potential to diffuse into adjacent low permeability regions and remain there, giving overly optimistic recovery. When flow is off-trend the fluid takes a more tortuous path from injector to producer. Now transverse convective fluxes are large compared with transverse numerical diffusive fluxes, and the recovery curves are in closer agreement. However, there is still longitudinal diffusion that affects recovery during the first half of the displacement.

Using 3DSL with Multiple Realizations. The streamline method is suitable for quickly processing many equiprobable geological realizations generated using geostatistics. Here we show in Figure 4.37, the recovery curves from 3DSL for ten equiprobable geological models of a 200X200X10

[2]Similar results were presented by Fay & Pratts [60] in 1951 by solving numerically for the stream function directly, and then mapping a tracer solution to the calculated streamlines.

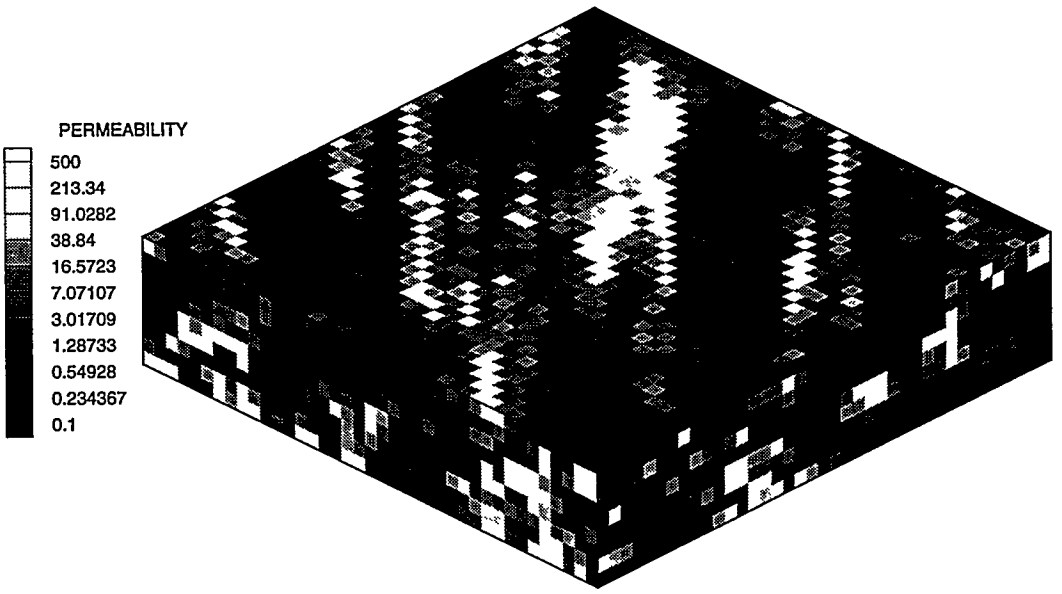

Figure 4.35: 40X40X10 correlated permeability field.

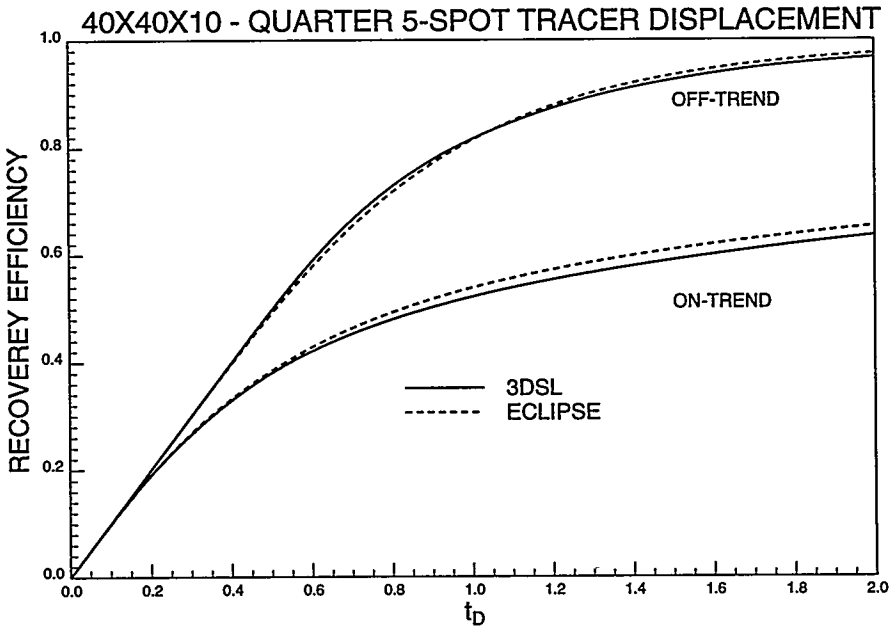

Figure 4.36: Recovery curves for tracer displacement in a quarter five-spot patter, for on-trend and off-trend directions.

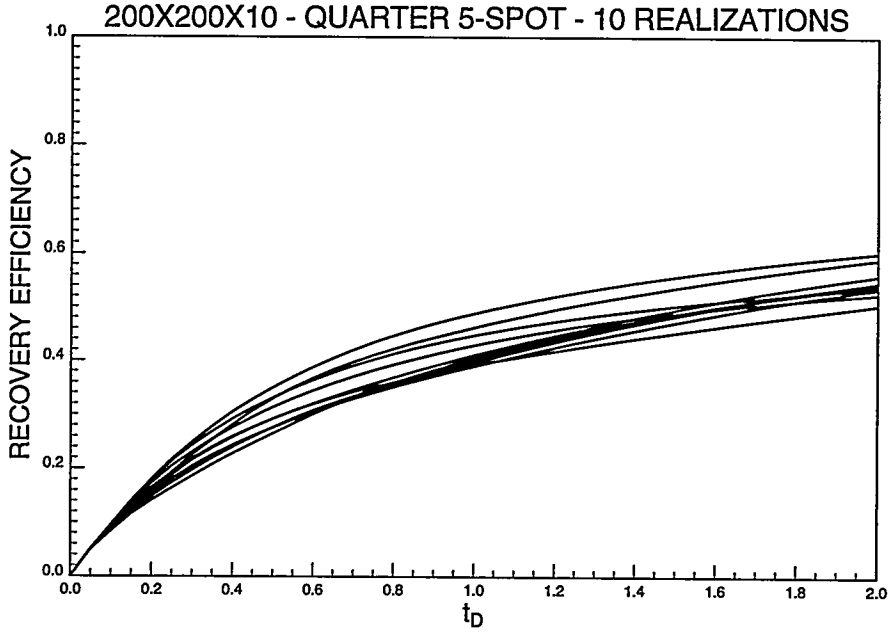

Figure 4.37: Recovery curves from 3DSL for ten equiprobable geological realizations of a quarter five-spot tracer displacement.

($4X10^5$ gridblocks) quarter five-spot tracer displacement. Note that it took less time to generate these 10 curves then is would have taken to generate one curve using a conventional finite difference approach. So by using 3DSL, one can quickly provide a distribution of recoveries based on the known uncertainty in any geological description.

Waterflooding in a Full Five-Spot Pattern. In the previous sections we mapped a one-dimensional tracer solution to each streamline. Here we map the Buckley-Leverett solution of a waterflood displacement to each streamline. Furthermore, to illustrate the generality of 3DSL, we consider a full five-spot pattern on a 50X50X20 grid with four corner producers and one central injector. The producers are completed in the upper 10 gridblocks while the injector is completed in the lower 10 gridblocks. We looked at three different fields with varying reservoir heterogeneity generated using GSLIB,

Case 1 A diagonally oriented permeability field with a correlation length of $\lambda_c = 0.3$ in the on-trend direction and $\lambda_c = 0.03$ in the off-trend direction. The vertical correlation length is $\lambda_c = 0.1$.

Case 2 An isotropic areal distribution with $\lambda_c = 0.4$ and a vertical correlation of $\lambda_c = 0.1$.

Case 3 A diagonally oriented field with $\lambda_c = 0.4$ in the main trend direction, an off-trend horizontal correlation with $\lambda_c = 0.1$, and a vertical correlation of $\lambda_c = 0.8$.

Figure 4.38 summarizes the oil recoveries under waterflooding for the three permeability fields. Clearly the results from the two simulation methods are in excellent agreement for all cases. Again ECLIPSE suffers from numerical diffusion which can lead to optimistic recoveries, depending on the interaction of major flow directions with permeability correlations. Note that the 3DSL solutions required between 10 and 20 times less CPU usage than the ECLIPSE solutions. So not only does 3DSL generate accurate results for waterfloods, but it does so in a fraction of the time.

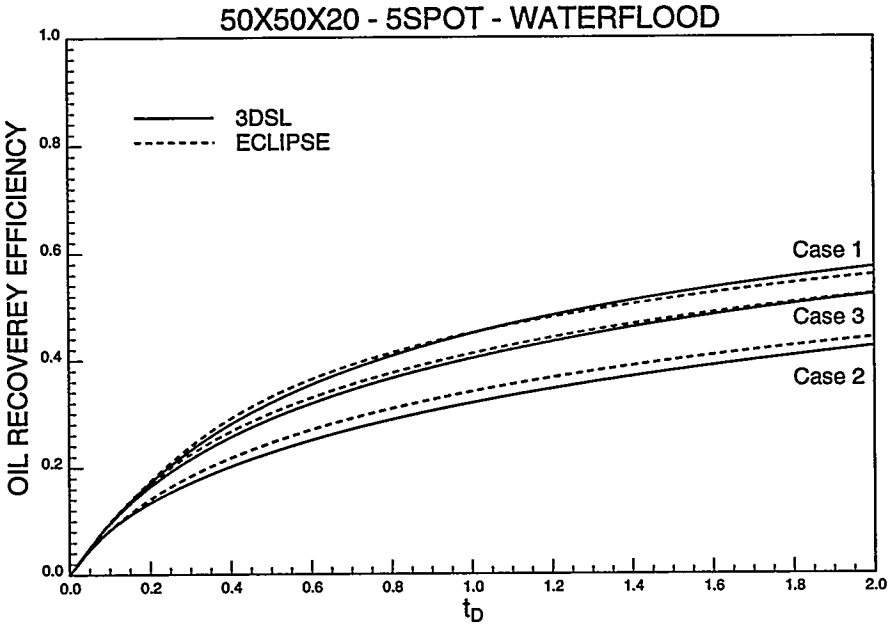

Figure 4.38: ECLIPSE and 3DSL recovery curves of a full five-spot waterflood displacement for three different permeability fields.

4.3.3 Conclusions

We have successfully extended streamtube methods of calculating two-dimensional displacements to three-dimensional systems by tracing streamlines from injectors to producers. The above examples highlight the advantage of the streamline technique over conventional finite difference results. The advantages are:

(i) 3DSL gives fast accurate results,

(ii) it is a useful tool for quantifying the effects of numerical diffusion in conventional simulations, and

(iii) 3DSL provides a way to analyze quickly equiprobable geological models thereby giving a distribution of possible recovery curves.

5. Interplay of Viscous, Gravity and Capillary Forces

The analysis of Chapter 2 indicates that essentially 100% displacement efficiency can be achieved in one-dimensional, dispersion-free flow if displacement pressure or gas composition is chosen appropriately. However, no real displacement meets completely the assumptions that make the analysis possible. The flows are not one-dimensional, dispersion is always present to some extent, and non-uniform flow and crossflow cause transverse mixing. All those mechanisms cause some two-phase flow in displacements that all multicontact miscible (MCM) according to the tie line criteria of Chapter 2. In real displacements, therefore, the residual saturation will not be zero. Instead, it will be determined by the interaction of phase behavior, capillary forces, viscous forces, and gravity forces. One effect of phase behavior is to cause low interfacial tensions (IFT's) for mixtures that are close in composition to a critical mixture. The mechanisms of multicontact miscibility produce just such mixtures. Hence a key issue is: what factors control residual oil saturations in near-critical (low IFT) systems? In this chapter, we examine that scaling question in some detail.

We begin in Section 5.1 by considering the combined effects of capillary, gravity and viscous forces on residual oil saturations. We develop simple models of the scaling behavior of entrapment and then test the theory with experiments. The result is a correlation with a reasonable theoretical basis for the combined effects of gravity, capillary and viscous forces on residual oil saturations.

In Section 5.2 we consider how high pressure CO_2 could be used to enhance gravity drainage of oil in fractured reservoirs. Experiments performed previously with analog oil/water/alcohol systems had indicted that significant recovery could be obtained if IFT's were lowered by phase behavor mechanisms. Here we report experimental evidence that similar behavior is observed in high pressure CO_2/crude oil systems. These results indicate that gas injection processes using low IFT gravity drainage can be applied to fractured reservoirs if the fracture network can be used to deliver gas, create the required gravity head, and collect the oil displaced from the matrix porosity.

In Section 5.3 we return to the more general problem of scaling behavior for a wide-range of multiphase flow problems that involve heterogeneity, gravity, viscous and capillary forces. We derive the appropriate dimensionless groups, and we review experimental and simulation evidence to determine the ranges of these parameters over which important transitions occur. A surprisingly consistent picture emerges, despite the complexity of the problem.

Finally, in Section 5.4, we return to the laboratory scale to interpret with simulations a set of low IFT imbibition experiments performed previously. Those experiments showed unexpectedly effective displacement behavior. We use the simulations (and their inadequacies) along with an analysis of imbibition mechanisms at the pore level to explain the observed behavior.

5.1 The Effects of Capillary, Gravity and Viscous Forces on Residual Oil Saturation

D. Zhou and F. M. Orr, Jr.

Tertiary oil recovery or aquifer remediation processes attempt to recover oil that is trapped by capillary forces. Displacement of a hydrocarbon phase by water alone is an immiscible displacement that cannot completely recover oil from reservoirs due to the interplay of capillary forces with heterogeneities of the media. Two types of heterogeneities are commonly dealt with: pore-level heterogeneity and macroscopic heterogeneity. Pore-level heterogeneity, such as pore size (grain size) and pore structure variations, controls the amount of oil left after the injected fluid has swept a

zone, whereas macroscopic heterogeneity determines zones that the injected fluid sweeps. In numerical simulation of a displacement process, macroscopic heterogeneity can be represented directly by assigning different rock properties (permeability and porosity) to certain grid blocks, given knowledge of the detailed structure of the medium. Because of the complex nature of pore entrapment mechanisms, however, the effects of pore level heterogeneity are represented by empirical correlations. One of the empirical correlations is the capillary desaturation curve (CDC), which defines the relationship of the residual oil saturation and the physical properties of a system. Accurate representation of the dependence of the CDC on fluid and rock properties is of great importance for simulations of enhanced oil recovery and spilled oil clean-up processes, because these processes must reduce the residual oil saturation to relatively low levels. This work describes theory and experiments that demonstrate the relative contributions of gravity, viscous and capillary forces in the correlation of residual oil saturation and the physical properties of water-wet systems.

The physical properties of a system are commonly represented by a capillary number, which is usually defined by one of the following equations

$$N_{c1} = \frac{\mu_w v}{\sigma}, \tag{5.1}$$

or

$$N_{c2} = \frac{k_w \bigtriangledown p}{\sigma} = \frac{\mu_w v_w}{\sigma k_{rw}}, \tag{5.2}$$

and a Bond number defined by

$$N_B = \frac{\Delta \rho g k}{\sigma}, \tag{5.3}$$

or

$$B = \frac{\Delta \rho g R^2}{\sigma}, \tag{5.4}$$

where μ_w is the viscosity of the displacing phase, v is Darcy velocity, $\bigtriangledown p$ is the pressure gradient, k is permeability, R is the radius of the grains composing the porous medium, $\Delta\rho$ is the density differences between the fluids, and σ is the interfacial tension (IFT) of the system. According to Darcy's law, the capillary numbers (N_{c1} and N_{c2}) are related by $N_{c2} = N_{c1}/k_{rw}$, where k_{rw} is the relative permeability of the displacing phase. The use of N_{c1} or N_{c2} in the literature depends on the application to specific situations. N_{c1}, for example, is likely to be used to correlate results of experiments with constant injection rates, whereas N_{c2} may be used to describe flows with constant pressure drop. In this section, however, we find that even for processes with constant injection rates, N_{c2} is a more appropriate form to represent the ratio of viscous forces to capillary forces. The Bond numbers B and N_B are related by the correlation of the permeability (k) and the grain sizes (R) of a medium.

There are two CDC's for a displacement system, depending on the continuity of the displaced fluid [118, 137, 205, 206]. A discontinuous nonwetting phase is more difficult to displace from a medium than a continuous nonwetting phase [118, 137]. In this work, we focus our attention on the displacement of continuous nonwetting phase from a porous medium, which is commonly involved in oil recovery processes with an oil bank. CDC's are generally obtained from laboratory measurements [71, 112, 137, 177], although attempts have been made to predict CDC's by statistical [119, 205] or deterministic theories [118, 172, 206]. Studies of CDC's have been largely focused on the balance of capillary and viscous forces [118, 161, 172, 205], which is measured by the capillary number. Consequently, gravity effects are neglected in CDCs used in most simulators of enhanced oil recovery processes, even though some studies [137, 194, 195] have shown that gravity effects can be significant. In this work, we examine the combined effects of gravity and viscous forces on oil entrapment in porous media, and we define conditions under which gravity forces can be neglected or must be included in the analysis.

5.1.1 Entrapment mechanisms

In order to identify the factors that influence oil entrapment during immiscible displacements, we first review entrapment mechanisms. Mohanty *et al.* [133] investigated the physics of oil entrapment in water-wet media, and identified two entirely different entrapment mechanisms, namely, a snap-off process that traps oil in a pore and a by-pass process caused by competition of flows between pores. Using detailed experimental observations, Chatzis *et al.* [29] determined that approximately 80% oil is entrapped by snap-off processes and 20% by the by-passing processes for consolidated, water-wet media.

Snap-off occurs in pores with large aspect ratios, the ratio of pore body and pore throat diameters. The large aspect ratio creates a significant lower wetting-phase pressure at the pore throat than that in the pore body. Hence, the wetting phase flows towards the pore throat, and forms a collar that grows and eventually breaks the nonwetting phase. Roof [161] derived a static criterion for snap-off in noncircular capillary tubes, based on the capillary force balance at the pore throat and the pore body. A noncircular capillary tube was used as a model of the irregularities of pores and the roughness of solid surface of the medium. Ransohoff *et al.* [158] extended Roof's static analysis to include the effects of viscous flow resistance in the water filled corners of the capillary tube. For a system shown in Fig. 5.1a, they obtained the static criterion for snap-off,

$$R_b \geq \frac{C_m R_o R_t}{R_o - R_t}, \tag{5.5}$$

where C_m is a dimensionless interfacial curvature, which is a function of the cross-sectional geometries, R_o is the pore neck radius, and R_t and R_b are the hydraulic radii of the pore throat and pore body respectively, as shown in Fig. 5.1A.

To include the dynamic effects of viscous flow, Ransohoff *et al.* [158] and Gauglitz *et al.* [72] calculated and measured experimentally the time required to transport enough fluid into the pore throat to have snap-off, and compared it to the time for the nonwetting phase to flow through the pore throat. If the time of transporting enough fluid to form a collar is less than the time required for the nonwetting phase to flow through the pore throat, snap-off would occur.

The random nature of the sizes and locations of pores in porous media incorporating the interconnections among the pores generates flow competition among pores. The displacing fluid in the fast flow pores can trap oil in pores in which flow is slow. This mechanism is referred to as by-passing. Pore doublet models (PDM) have been used both theoretically [29, 118] and experimentally [29] to demonstrate the by-pass mechanism. The PDM is based on the assumption that well-developed-Poiseuille flows compete in two parallel flow paths (pores) with different sizes (see Fig. 5.1B). The flow velocity in each flow path can be obtained by combining Poiseuille's law and the Young-Laplace equation [118]. The ratio of the velocities is an indication of the amount of fluid trapped in one pore. For an imbibition process, capillary forces draw the displacing phase into the smaller pore, while viscous forces make the fluid flow more rapidly in the larger pore. The result of this competition is that at low injection rate, the oil in the large pore would be trapped, with the reverse being true at high rates. Chatzis and Dullien's experiments [29] on a model of neck-bulge-neck pores showed that oil was trapped by the by-passing process.

By-passing processes can also be represented by network models for studies of entrapment mechanisms in porous media [13, 57, 58, 59, 194, 206]. Network models represent porous media by networks of pores with different sizes and connectivities. Another approach, percolation theory, has also been used to represent the random nature of the porous media, in which the flow path is fully random. In its original form, percolation theory represented only two-phase displacements when capillary forces dominate the flow process, and it did not account for the continuity of the flow path. Invasion percolation theory was then introduced to include both the randomness of the medium and the continuity of the fluids. In the following subsection, we review briefly effects of

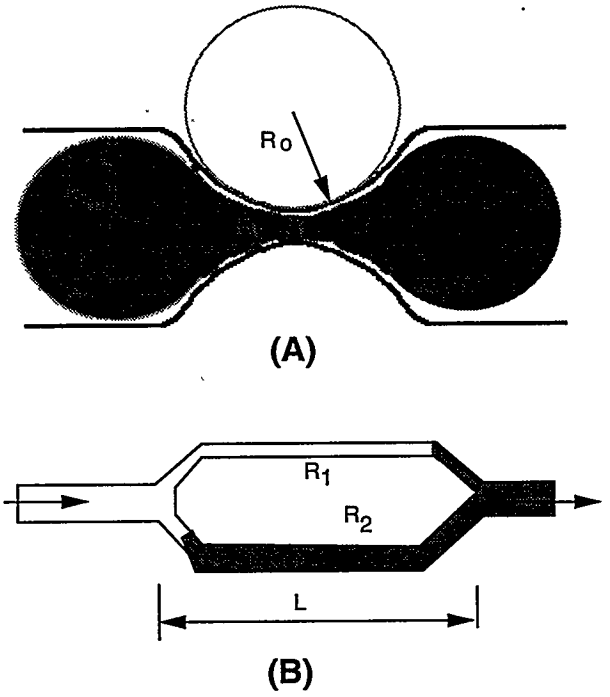

Figure 5.1: Commonly used snap-off model(A) and pore doublet model (B).

gravity in invasion percolation theory as well as the experimental results that demonstrate effects of gravity on residual nonwetting phase saturation.

Gravity Effects on Entrapment. The first theoretical investigation of gravity effects was reported by Wilkinson in an invasion percolation study [194]. Wilkinson neglected the snap-off process, and assumed that the nonwetting phase is only trapped by the by-passing process. Correlation lengths for both viscous and buoyancy forces were introduced to measure the relative magnitudes of viscous and buoyancy forces compared with capillary forces in the medium. A dimensionless viscous correlation length was defined as

$$\xi_V = \frac{L_{vm}}{R} \propto \left(\frac{N_{c1}}{k_w}\right)^{-\upsilon/(1+\upsilon)}, \tag{5.6}$$

where L_{vm} is the maximum length of oil clusters in the system during a viscous displacement, R is the grain size (radius) of the medium, $k_w = kk_{rw}/R^2$ and υ is a percolation exponent ($\upsilon = 0.88$ for three-dimensional percolation). They also defined a gravity correlation length (ξ_G),

$$\xi_G = \frac{L_{gm}}{R} \propto B^{-\upsilon/(1+\upsilon)}, \tag{5.7}$$

where B is the Bond number [137, 194], and L_{gm} is the maximum length of oil clusters in the system when gravity forces dominate. For gravity-dominated flow, the residual oil saturation S_{or} was related to the gravity correlation length by

$$S^*_{or} - S_{or} \propto \left(\frac{1}{\xi_G}\right)^{(1+\beta)/\upsilon} \propto B^{\lambda}, \tag{5.8}$$

where $\lambda = (1+\beta)/(1+\upsilon)$, which is a percolation constant ($\lambda = 0.77$ for three-dimensional percolation), β is also a percolation constant of 0.45 for three dimensional percolation, and S^*_{or} is

the residual oil saturation at very low capillary number and Bond number. For viscous-dominated cases, the residual oil saturation was correlated as

$$S^*_{or} - S_{or} \propto \left(\frac{1}{\xi_V}\right)^{(1+\beta)/\upsilon} \propto \left(\frac{N_{c1}}{k_w}\right)^{\lambda}. \tag{5.9}$$

For situations in which both viscous and gravity forces act, Wilkinson [195] assumed that capillary and gravity forces were additive, and that the residual oil saturation depends on $(N_{c1}/k_w + B)^{\lambda}$.

Blunt *et al.*[13] developed a network model to calculate the percolation constant for invasion percolation processes. For both imbibition and drainage processes, Blunt *et al.* showed good agreement between network simulations and percolation theory when the processes were dominated by gravity forces. They also demonstrated numerically that gravity forces (represented by the Bond number B) behave the same as viscous forces (N_{c2}). For cases in which both gravity and viscous forces are involved, Blunt *et al.* proposed an effective correlation length to correlate the residual oil saturation. The effective correlation length is defined as

$$\frac{1}{\xi} = \frac{1}{L} + \frac{1}{\xi_V} + \frac{1}{\xi_G}, \tag{5.10}$$

where L is the length of the system. For a porous medium of relatively large size, $1/L \approx 0$, and hence

$$\frac{1}{\xi} \approx \frac{1}{\xi_V} + \frac{1}{\xi_G}. \tag{5.11}$$

In terms of capillary and Bond numbers, the residual nonwetting phase saturation is

$$S^*_{or} - S_{or} \propto \left((Bk_{rw})^{\upsilon/(1+\upsilon)} + N_c^{\upsilon/(1+\upsilon)}\right)^{(1+\upsilon)/\upsilon}. \tag{5.12}$$

Eq. 5.12 indicates that the effective correlation length theory does not give a linear combination. Thus, for cases in which both gravity and viscous forces act, there are two very different correlations for residual oil saturations. We shall note that these correlations are two extrapolations of the invasion percolation theory, not from rigorous derivations. The pore-level models described in the next section support the linear combination of gravity and viscous forces in determining residual oil saturations.

Experimental studies [137, 138] indicate substantial effects of gravity on residual nonwetting phase saturation in glass-bead packs. The experiments were performed with beads of different diameters to obtain a wide variation of Bond numbers. Morrow *et al.* [138] correlated their results against a linear combination of N_{c1} and B,

$$S_{or} = f(N_{c1} + 0.001413B). \tag{5.13}$$

This correlation agrees with Wilkinson's results, although Wilkinson's theory neglected the snap-off process. In the following section, we demonstrate theoretically that there is a linear combination of gravity and viscous forces for both snap-off and by-passing processes.

5.1.2 Extended REV-Scale Models

Previously available models of snap-off and by-passing neglect the influence of gravity. In this section we extend such models to include gravity. In the following derivation of equations, we assume that the interface between oil and water phases is always in equilibrium, so that we can use the Young-Laplace equation to represent the pressure difference across an interface. Flow of both phases is assumed to be well-developed Poiseuille flow, and therefore, Poiseuille's law or Darcy's law is used to represent viscous pressure drops.

Snap-off Model. In past studies of snap-off processes, oil blob sizes were assumed to be smaller than the pore size. That assumption is known to be violated in displacements in real porous media. For example, Chatzis [29] observed the blobs could be several pore sizes in extent. In our analysis, we consider an oil blob occupying two pores in the vertical direction (see Fig. 5.2a). However, the analysis is not limited to two-pore lengths and could be easily extended to multipore arrangements. Consider the situation shown in Fig. 5.2, in which water flows into the pore from the bottom. We assume that water phase wets the walls with a film whose thickness remains constant in the pore body but varies in the pore neck. The pressures in the phases at the pore throat (A) are

$$P_o = P_i + \frac{C_m \sigma}{R_b} - \Delta P_{ov} - \rho_o g L, \tag{5.14}$$

and

$$P_w = P_i - \Delta P_{wv} - \rho_w g L, \tag{5.15}$$

where P_i is the pressure of the wetting phase at location (B), R_b is the pore body radius, C_m is the dimensionless interfacial curvature in the pore body and ΔP_{ov} and ΔP_{wv} are the viscous pressure drops of the oil and the wetting phase. Because of the continuity of the wetting phase, the wetting phase can reach the pore throat through other neighboring pores. Therefore, we use Darcy's law to calculate the viscous pressure drops for both phases. ΔP_{ov} and ΔP_{wv} are then expressed as $\Delta P_{wv} = (\mu_w v_w L)/(k k_{rw})$, and $\Delta P_{ov} = (\mu_o v_o L)/(k k_{ro})$. Thus, the pressure difference between the two phases at the pore throat (A) is

$$\Delta P_1 = (P_o - P_w)_1 = \frac{C_m \sigma}{R_b} + (\rho_w - \rho_o) g L + \frac{\mu_w v_w L}{k k_{rw}} - \frac{\mu_o v_o L}{k k_{ro}}. \tag{5.16}$$

At the pore throat, we can also obtain the pressure difference between the two phases from the Young-Laplace equation,

$$\Delta P_2 = (P_o - P_w)_2 = \frac{\sigma}{R_t} - \frac{\sigma}{R_o}, \tag{5.17}$$

where R_t is the oil throat radius, and R_o is the radius of the oil neck (see Fig. 5.2b).

Now we consider the following situations: $\Delta P_2 > \Delta P_1$ and $\Delta P_2 < \Delta P_1$. When $\Delta P_2 > \Delta P_1$, the fluids would flow in such a way as to reduce ΔP_2 to keep the two forces in balance. In order to decrease ΔP_2, the system would either increase R_t or decrease R_o. It is impossible to increase R_t much further, because of the solid pore structure. Thus, the system would reduce R_o. To reduce the value of R_o, capillary forces pump the wetting phase into the pore throat. Consequently, a wetting phase collar ring would forms at the pore throat [158]. The formation of the collar ring reduces the value of R_t, and results in snap-off. However, when $\Delta P_2 < \Delta P_1$, the system becomes stable. In order to balance the pressure difference in this case, the system would either reduce R_t or increase R_o. Reducing R_t is impossible, because the viscous pressure difference ΔP_1 would push oil into the pore throat and the interface moves outward to increase R_t. Thus, increasing the effective value of R_o is the only solution. To increase the effective value of R_o, the capillary forces push the wetting phase away from the pore throat and there is a reduced wetting phase at the pore throat. Therefore, there would be no snap-off. In summary, we argue that snap-off would occur if $\Delta P_2 \geq \Delta P_1$. We then obtain the following condition for snap-off to occur,

$$\frac{\sigma}{R_t} - \frac{\sigma}{R_o} \geq \frac{C_m \sigma}{R_b} + (\rho_w - \rho_o) g L + \frac{\mu_w v_w L}{k k_{rw}} - \frac{\mu_o v_o L}{k k_{ro}}. \tag{5.18}$$

Because v_o has positive values, the condition simplifies

$$\frac{\sigma}{R_t} - \frac{\sigma}{R_o} \geq \frac{C_m \sigma}{R_b} + (\rho_w - \rho_o) g L + \frac{\mu_w v_w L}{k k_{rw}}, \tag{5.19}$$

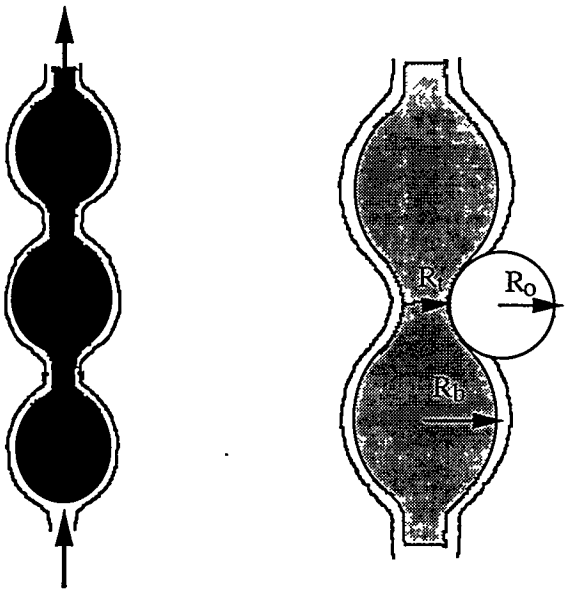

Figure 5.2: Vertically oriented snap-off model (a) and detailed pore structure (b).

or

$$N_{c1} + k_{rw}B \leq \frac{k}{R_t L} k_{rw} \left(1 - \frac{R_t}{R_o} - \frac{C_m R_t}{R_b}\right). \tag{5.20}$$

Eq. 5.20 suggests that mobility ratio would have minimal effect on the final residual nonwetting phase saturation, which agrees with experimental observations [1, 177].

If we set $N_{c1} = 0$ and $N_B = 0$, Eq. 5.20 simplifies to

$$R_b \geq \frac{C_m R_t R_o}{R_o - R_t}, \tag{5.21}$$

which is the same as Eq. 5.5.

Doublet Model. For vertically oriented doublet pores as Fig. 5.3 shows, we write down the pressure drops from point B to point A for each pore as following for a upflow (on the assumption that the tubes are cylindrical)

$$\Delta p_1 = \frac{8\mu_w v_1 L_1}{R_1^2} + \frac{8\mu_o v_1 (L - L_1)}{R_1^2} - \frac{2\sigma}{R_1} + L_1 \rho_w g + (L - L_1)\rho_o g, \tag{5.22}$$

and

$$\Delta p_2 = \frac{8\mu_w v_2 L_2}{R_2^2} + \frac{8\mu_o v_2 (L - L_2)}{R_2^2} - \frac{2\sigma}{R_2} + L_2 \rho_w g + (L - L_2)\rho_o g, \tag{5.23}$$

where R_i is the radius of tube i, and L_i is the distance the displacing fluid flows in tube i, L is the length of the tubes, and v_i is the flow velocity in tube i. Since the two pores have common junctions, the pressure drops Δp_1 and Δp_2 must be equal, $\Delta p_1 = \Delta p_2$. Therefore, we obtain the following expression in which the average velocity (v_a) of the doublet pores is $v_a = (R_1^2 v_1 + R_2^2 v_2)/(R_1^2 + R_2^2)$.

$$N_c m + (l_1 - l_2)\frac{f}{1+f} N_B = \frac{2k}{R_1 L} \frac{f}{1+f} (1 - \frac{R_1}{R_2}), \tag{5.24}$$

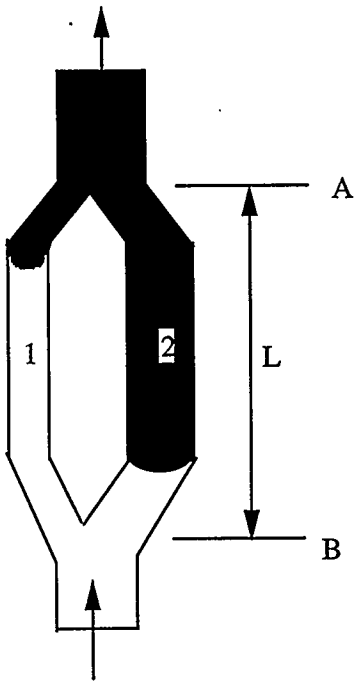

Figure 5.3: Vertically oriented pore doublet mode

where $l_i = L_i/L$, $\mu_r = \mu_o/\mu_w$, $f = R_2^2/R_1^2$, and

$$m = (1-\mu_r)\left((1+f-\frac{v_2}{v_a}f)l_1 f - \frac{v_2}{v_a}l_2\right) + \mu_r\left(f(1+f-\frac{v_2}{v_a}) - \frac{v_2}{v_a}\right). \tag{5.25}$$

The permeability of the PDM is defined as $(R_1^2+R_2^2)/8$ from Poiseuille's law.

To simplify the arguments, we assume the radius of pore 1 is smaller than that of pore 2, $R_1 < R_2$. Capillary forces draw the wetting phase into the smaller pore (pore 1), and viscous forces make fluid flow more easily in the larger pore (pore 2). At the same time, gravity forces reduce the velocity difference between pores. Reduction of viscous forces slows the flow in the larger pore, and results in more oil trapped in the larger pore. If the oil in pore 2 were completely trapped, we would have the following parameters: $v_2 = 0$, $l_1 = 1$ and $l_2 = 0$, and $m = f(1+f)$. Because the value of m decreases with increasing value of v_2, the system must have a value of m smaller that $f(1+f)$ to avoid entrapment of the nonwetting phase in pore 2 completely. Thus, the nonwetting phase would be trapped in pore 2 completely, if $m \geq f(1+f)$. Rearrangement of Eq. 5.24 gives

$$N_{c1} + CN_B \leq C\frac{2k}{R_1 L}(1-\frac{R_1}{R_2}), \tag{5.26}$$

where $C = 1/(1+f)^2$.

For a given system, Eq. 5.26 indicates that the nonwetting phase in the larger pore would be trapped due to by-passing when the combined effects of gravity and capillary forces are less than a certain value. The relative magnitude of gravity forces and viscous forces depends on the value of C, which represents the heterogeneity of the system. $C = R_1^4/(R_1^2+R_2^2)^2$ is the relative permeability of the displacing phase (the wetting phase), and can be derived as following with an

assumption that displacements in the tubes are piston-like,

$$C = \frac{R^4}{(R_1^2 + R_2^2)^2} = \frac{k_1 R_1^2}{k(R_1^2 + R_2^2)} = \frac{Q_1}{Q_t}, \tag{5.27}$$

where k_1 and k are the permeabilities of tube 1 and both tubes, Q_1 and Q_t are the flow rate in pore 1 and the total flow rate in both pores. According to Darcy's law, $Q_1 = Ak_{rw}k/(\mu\partial\Phi/\partial l)$, and $Q_t = Ak/(\mu\partial\Phi/\partial l)$ for a given flow area A and potential gradient $\partial\Phi/\partial l$. Therefore,

$$C = \frac{Q_1}{Q_t} = \frac{\frac{Akk_{rw}}{\mu}\frac{\partial\Phi}{\partial l}}{\frac{Ak}{\mu}\frac{\partial\Phi}{\partial l}} = k_{rw}, \tag{5.28}$$

and

$$N_{c1} + k_{rw}N_B \leq k_{rw}\frac{2k}{R_1 L}(1 - \frac{R_1}{R_2}). \tag{5.29}$$

Thus, Eq. 5.29 also suggests that a linear combination of the capillary and Bond numbers can be used to state a criterion for by-passing. Here again, the coefficient of the Bond number is the wetting-phase relative permeability.

Summary. In both snap-off and doublet models, we obtain criteria for entrapment of the non-wetting phase in porous media in terms of linear combinations of capillary and Bond numbers. Comparison of Eqs. 5.20 and 5.29 indicates that they have similar forms. In both cases, the relative contributions of capillary and Bond numbers are determined by the relative permeability of the displacing phase. Using the relationship between N_{c1} and N_{c2}, we obtain the following equations for snap-off and by-pass processes.

$$N_{c2} + N_B \leq \frac{k}{R_t L}(1 - \frac{R_t}{R_o} - \frac{2R_t}{R_b}), \tag{5.30}$$

and

$$N_{c2} + N_B \leq \frac{2k}{R_1 L}(1 - \frac{R_1}{R_2}). \tag{5.31}$$

The simplicity of Eqs. 5.30 and 5.31 suggests that N_{c2} is a more appropriate definition of capillary number than N_{c1} even for processes with constant injection rates.

5.1.3 Experiments

Experimental studies [137, 138] provide some evidence that a linear combination of capillary number and Bond number determines residual oil saturation. However, the Bond numbers were changed by varying the sizes of the beads used in packing their columns. We now investigate whether use of the linear combination is reasonable if we change Bond number by the variation of IFT and density differences of the fluids. In this section, we report results from experiments designed to examine these parameters.

All displacements were conducted in the same sand-pack column. The Bond number was varied by using different IFT's and density differences of the fluids. Fig. 5.4 is a schematic of the experimental apparatus. The HPLC pump provided constant injection rates ranging from 0.1 to 8.0 cc/min. The length of the sand-packed porous medium was 119.0 cm and the diameter 1.95 cm. The permeability was 48.5 Darcy and the porosity, 0.256. We used pre-equilibrated mixtures of brine, iso-octane (iC_8) and isopropanol (IPA) to generate fluid pairs of wide range of IFT and densities differences, This system has been well studied [138]. Four tie-lines were used to obtain IFTs varying from 0.1 to 38.1 mN/m and densities from 0.11 to 0.33 g/cc, which correspond to a range of capillary and Bond numbers from 10^{-6} to 10^{-3}. Table 5.1 lists the measured properties of the fluids used.

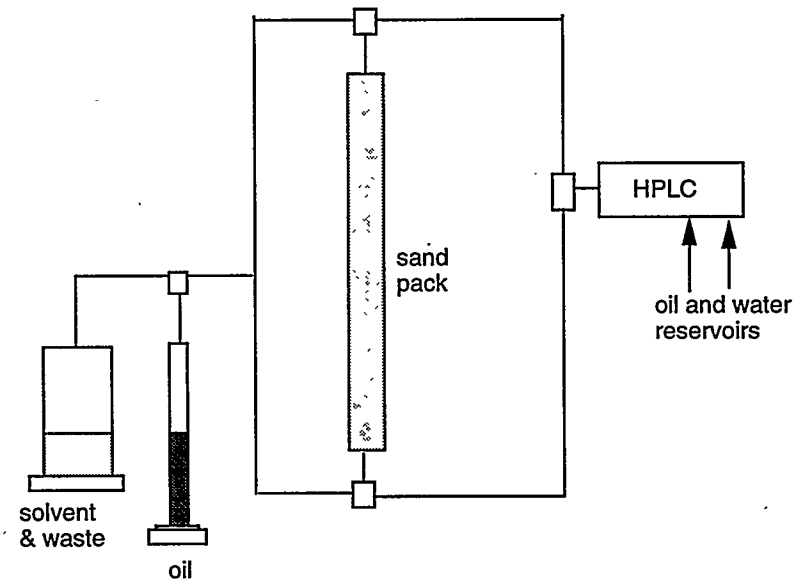

Figure 5.4: A schematic diagram of the experimental setup.

All the imbibition displacements were conducted with initial wetting phase saturations. These were established by first injecting the nonwetting phase into the top of the column that was fully saturated with the wetting phase. The initial wetting phase saturation varied from 0.19 to 0.26 of pore volume. The large variation of initial wetting phase saturations were results of large variations in mobility ratios in different runs. In this range of initial wetting phase saturation, repeated experiments showed that this variation of initial wetting phase saturation did not influence the residual nonwetting phase saturation. Therefore, the differences in the residual nonwetting phase saturation are the results of the capillary and Bond number variations. To study the directional effects of gravity forces, we conducted displacements by injecting the wetting phase from either bottom or top of the column. We refer to displacement from the bottom as gravity-favorable and that from the top as gravity-unfavorable, because the gravity forces stabilize the displacements when injected phase enters the column from the bottom. Table 5.2 summarizes the experimental results from both gravity-favorable and unfavorable displacements.

In all the displacements, we observed little additional recovery shortly after breakthrough, an observation that is consistent with the idea that the sand-pack was strongly-water wet. Following the common practice, we plot the final residual oil saturation against the capillary number alone

Table 5.1: Fluid properties.

fluid system	IFT (mN/m)	$\Delta\rho$ kg/m^3	N_B	Viscosity (cp) (wetting)	Viscosity (cp) (nonwetting)
#1	38.1	330	4.2×10^{-6}	0.98	0.48
#2	4.41	305	3.3×10^{-5}	2.80	0.49
#3	1.07	220	1.0×10^{-4}	3.25	0.52
#4	0.10	110	5.2×10^{-4}	2.60	0.70

Table 5.2: Summary of the displacement results

fluid system	flow rate (cc/min.)	S_{iw} favorable	S_{or} favorable	S_{iw} unfavorable	S_{or} unfavorable	N_{c1}
#1	0.5	0.19	0.181			6.6×10^{-7}
#1	1.0			0.22	0.257	1.4×10^{-7}
#1	2.0	0.23	0.181	0.19	0.248	2.7×10^{-6}
#1	4.0	0.23	0.181	0.19	0.248	5.4×10^{-6}
#1	8.0	0.20	0.171	0.24	0.19	1.1×10^{-5}
#2	0.1	0.24	0.16			3.4×10^{-5}
#2	0.5	0.25	0.152			1.6×10^{-5}
#2	1.0			0.26	0.19	3.3×10^{-5}
#2	2.0	0.26	0.138	0.27	0.15	6.7×10^{-5}
#2	4.0	0.24	0.124	0.22	0.123	1.3×10^{-4}
#2	8.0	0.25	0.10	0.27	0.11	2.7×10^{-4}
#3	0.1	0.25	0.12			1.6×10^{-5}
#3	0.5	0.25	0.11	0.24	0.178	8.5×10^{-5}
#3	1.0			0.25	0.14	1.7×10^{-4}
#3	2.0	0.24	0.10	0.22	0.11	3.2×10^{-4}
#3	4.0	0.20	0.086	0.14	0.09	6.2×10^{-4}
#3	8.0	0.22	0.067	0.23	0.07	1.3×10^{-3}
#4	0.1	0.23	0.096			1.4×10^{-4}
#4	0.5	0.25	0.08			6.9×10^{-4}
#4	1.0	0.25	0.067			1.4×10^{-3}
#4	2.0	0.23	0.048			2.8×10^{-3}
#4	4.0	0.23	0.038			5.5×10^{-3}
#4	8.0	0.25	0.02			1.0×10^{-2}

for all displacements in Fig. 5.5. From the results, the experimental data cannot be reasonably correlated by the capillary number alone. The experimental results also indicate, therefore, that gravity forces and the flow directions affect the residual nonwetting phase saturations.

5.1.4 Discussion

In the definitions of capillary number (N_{c1}) and Bond number N_B, five variables are involved: the injection rates (v), the IFT (σ), the density difference ($\Delta\rho$), the viscosity of the wetting phase (μ_w), and the permeability of the medium (kk_{rw}). In the experiments described in the previous section, we varied IFT and density differences, and injection rates to obtain a wide range of capillary and Bond numbers. To check the other parameters, we review the experimental results of Morrow and Songkran[137] and Morrow *et al.*[138] In both studies, they varied the capillary number and Bond number by changing different bead sizes and injection rates. Changing bead size changes the permeability of the bead pack. The permeability of a beadpack can be related to the bead size through the Kozeny-Carman equation

$$k = \frac{\phi^3}{k_z(1-\phi)^2 A_s^2}, \tag{5.32}$$

where A_s is the specific surface area per unit solid volume, for spherical bead $A_s = 3/R$, K_z is the Kozeny constant, which is approximately equal to 5 for bead packings, and ϕ is the porosity of the

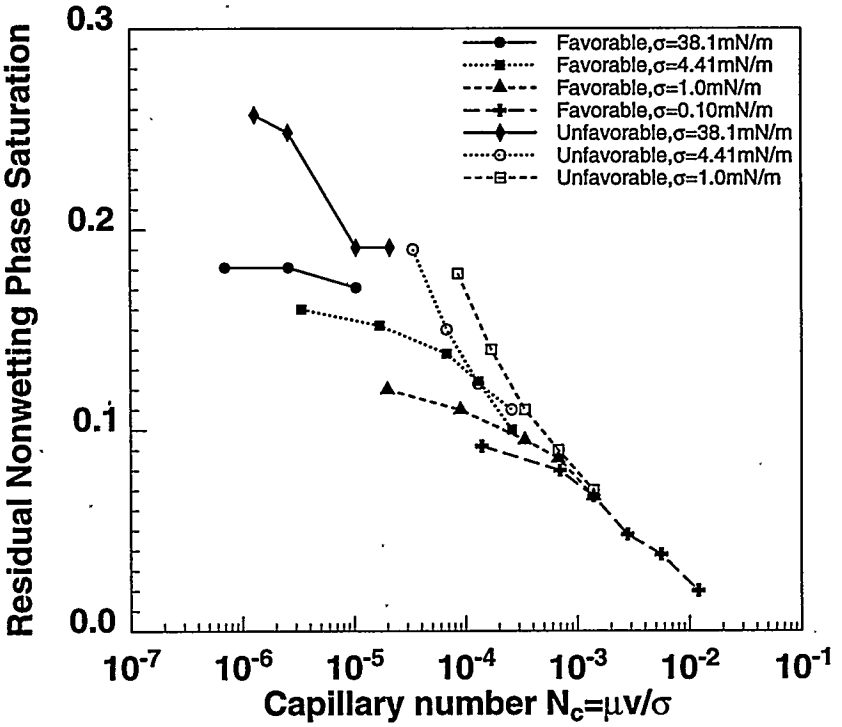

Figure 5.5: Correlation of residual nonwetting phase saturation with the capillary number alone for all displacements.

packing, which is about 0.38 for bead packings. Therefore, the permeability of a bead pack can be simply related to bead size as

$$k = 0.00317R^2. \tag{5.33}$$

Thus, the correlation given by Morrow and Songkran [137] and by Morrow *et al.* [138] can rearranged in terms of N_B as

$$S_{or} = f(N_{c1} + 0.445N_B). \tag{5.34}$$

Comparison of Eq. 5.34 with our theory indicates that the wetting-phase relative permeability at the trailing edge of the displacement front is about 0.445, which is consistent with the reported measurements for a similar system [137, 138] ($k_{rw} = 0.5$).

We used a procedure similar to that used by Morrow and Sougkran [137], and obtained a least-squares fit of our residual oil saturations from gravity-favorable displacements with an effective number defined as $N_e = N_{c1} + cN_B$. As Fig. 5.6 shows, a straight-line correlation on the semi-log plot exists when $c = 0.5$. The value of c is the relative permeability of the wetting phase according to Eqs. 5.20 and 5.29. This value is very close to the measured relative permeability by Morrow and Songkran [137] on a similar system. Again, our experiments suggest that a linear combination of the capillary and the Bond numbers correlates the residual oil saturations, and the appropriate coefficient is the wetting-phase relative permeability.

Using the same value of c, we correlated all our experimental results, as Fig. 5.7 shows, for both gravity-favorable and gravity-unfavorable displacements. At high values of N_e, the correlation is excellent, while it is less satisfactory when N_e is small. The difference between the gravity-favorable and unfavorable displacements may result partly from the accuracy of the flow rate and permeability measurements, because the subtraction of the two numbers enhanced the significance of the measurement error when these two values are comparable. In general, the correlation is good

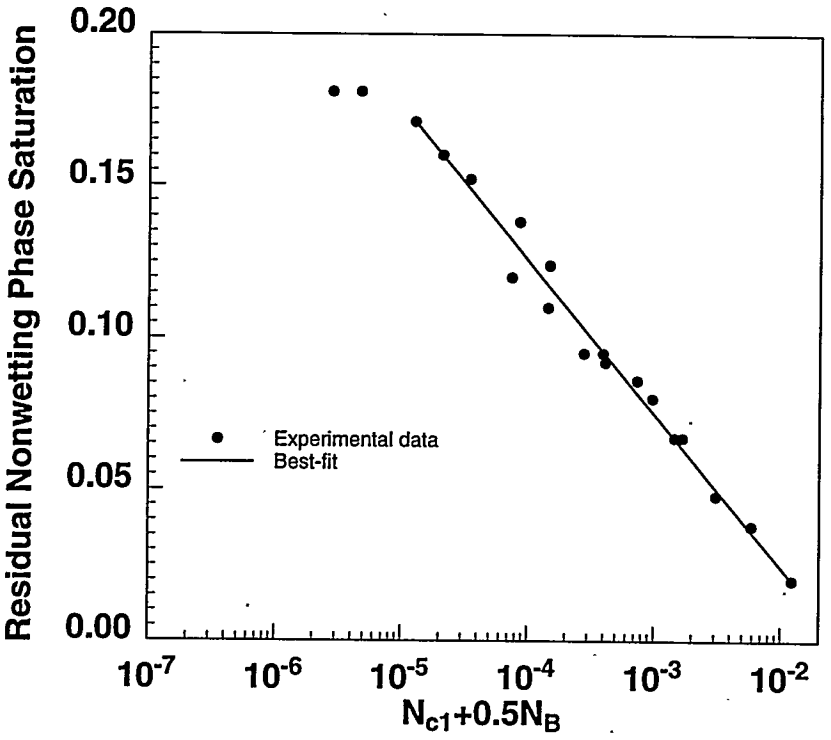

Figure 5.6: Correlation of the residual oil saturations and the sum of the capillary and Bond numbers for gravity-favorable displacements.

and we obtain the following correlation of the residual oil saturation with the capillary and the Bond numbers.

$$S_{or} = 0.02 + 0.0505 log(\frac{0.01227}{N_{c1} + 0.5N_B}). \tag{5.35}$$

Fig. 5.8 shows a comparison of the experimental data and the correlation given by Eq. 5.35. Fig. 5.8 also demonstrates the significant directional effects of gravity forces on residual nonwetting phase saturations. For a system with gravity forces comparable with viscous forces, gravity-favorable displacements have much lower residual oil saturation than do gravity-unfavorable displacements. This directional effect of gravity forces on residual oil saturation shows that gravity forces can reduce the residual oil saturations, as well as macroscopic sweep efficiency [207].

For a given system, it would be useful to determine which forces are most important. Therefore, we rearrange the linear combination to obtain

$$N_e = N_{c2}(1 + \frac{\Delta\rho g k}{\mu_w v}). \tag{5.36}$$

The relative magnitudes of N_{c2} and N_B in a system can be reflected by the gravity number

$$N_g = \frac{\Delta\rho g k}{\mu_w v}. \tag{5.37}$$

When $N_g > 1$, the Bond number is more important, whereas when $N_g < 1$, capillary number is the controlling parameter in determining the residual oil saturation.

We should note that the gravity number (N_g) is proportional to the medium permeability. Thus, flow in a high-permeability medium will have larger gravity effects than that in a low-permeability medium. To illustrate this concept, let us compare typical oil-spill and oil recovery

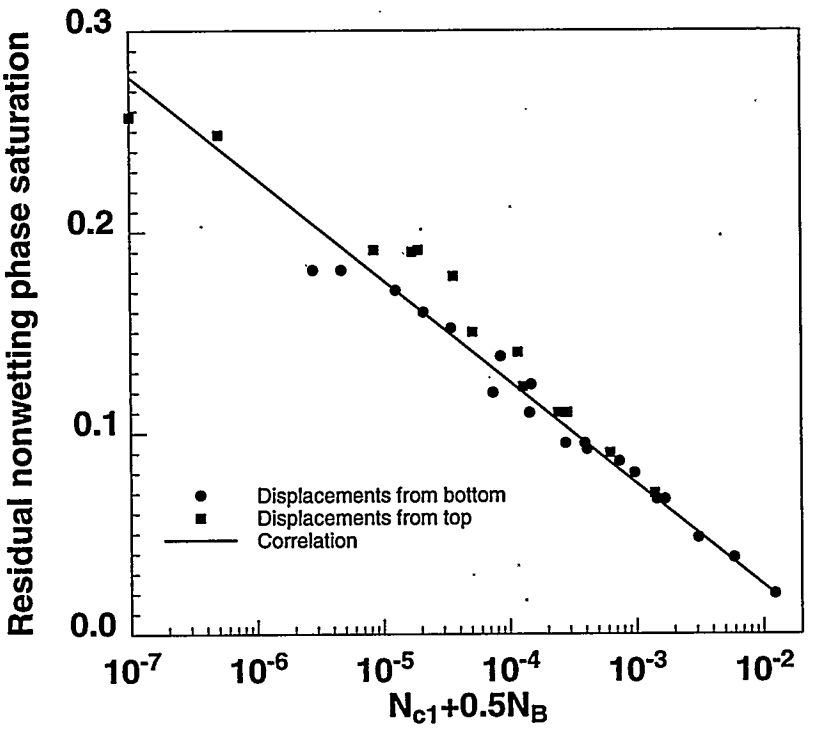

Figure 5.7: Correlation of residual oil saturations and the sum of capillary and Bond numbers from percolation theory and best-fit of the experimental data.

situations. The permeability of a typical soil is about 50 darcy, water viscosity is around $10^{-3}Ns$ (1 cp), and the flow rate can be estimated to be 1 ft/day, which is about 3.5 x $10^{-6}m/s$. We also assume that the density difference is about $300kg/m^3$ and the IFT is about 40 x $10^{-3}N/m$. The gravity number (N_g) is about 2.5, that is, the gravity forces are larger than the viscous forces in typical spilled-oil clean-up processes. For a waterflood oil recovery process, however, with a permeability of the order of 100 md and the same fluid properties, the gravity number is about 5×10^{-3}. Thus, the effects of density difference and flow direction will be more important in oil-spill applications than in typical waterflood situations.

5.1.5 Conclusions

In this work, we presented two different models of oil entrapment mechanisms, and experimental results from oil displacements with gravity forces assisting and impeding the oil recovery processes. We draw the following conclusions:

1. We demonstrated theoretically and experimentally that a linear combination of gravity and viscous forces can be used to correlate residual nonwetting phase saturations for both gravity-favorable and gravity-unfavorable displacements.

2. Changing the value of capillary and Bond numbers by varying interfacial tension, density difference and injection rate give similar effects on residual nonwetting phase saturations in our experiments.

3. When gravity forces are comparable to or larger than the viscous forces, gravity-unfavorable displacements have significantly higher residual nonwetting phase saturation than gravity-favorable displacements.

4. Because soils have much higher permeabilities than oil reservoirs, gravity effects on

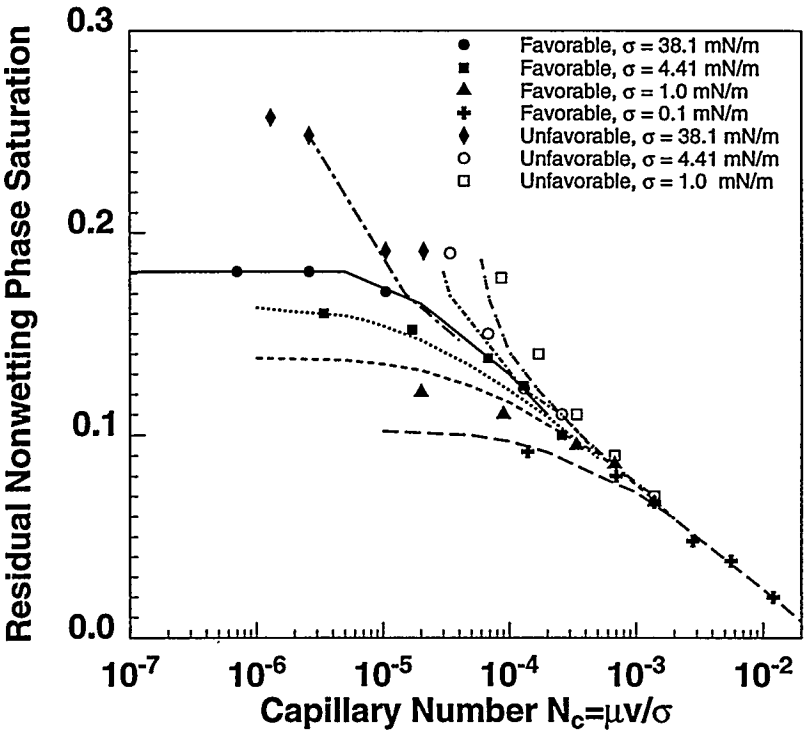

Figure 5.8: Comparison of the correlation with experimental data (lines are correlations and dots are the experimental data).

residual nonwetting phase saturations are much more significant in spilled-oil clean-up than in oil recovery processes.

5.2 Gravity Drainage of Crude Oil in the Presence of Carbon Dioxide

D. Zhou

Our recent experiments and theoretical analysis have demonstrated that gravity drainage at low interfacial tension could be an efficient oil recovery mechanism from vertically fractured reservoirs [165]. However, the analysis was based on experimental data from model fluid systems, such as a binary liquid mixture of C_1 and nC_7 used by Stensen *et al.* [173]. The question that one would ask when we apply the analysis to field design is whether the complex nature of crude oil leads to drainage behavior different from that of model systems. There are few data in the literature about crude oil drainage for injection gases that exhibit multicontact miscibility. One such gas is CO_2. In this section we report results of experiments to determine whether transfers of components between CO_2-rich and oil-rich phases can lead to gravity drainage of crude oil. In particular, we report experimental results for gravity drainage of Means/crude oil in the presence of high pressure CO_2.

When CO_2 is injected into a reservoir, mass transfer will occur between the CO_2 phase and the crude oil, because of the large solubilities of some hydrocarbon molecules in CO_2, and also the solubility of CO_2 in the crude oil. This mass exchange leads to the variations of phase properties such as interfacial tension and densities, which alters the relative magnitudes of the gravity and

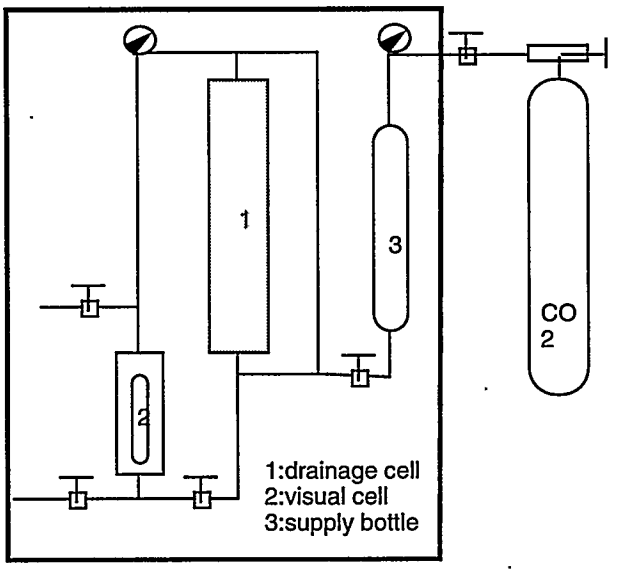

Figure 5.9: Schematic of the gravity drainage rig

capillary forces and influences the drainage rates of the oil phase. Gravity forces drain the heavier phase (crude oil) out of the rock, while capillary forces and the end effect act to retain oil in the core. The magnitude of gravity forces is proportional to the absolute length of the core. Therefore, relatively long cores are needed to investigate gravity drainage mechanisms in a way that is suitable for oil reservoirs. Our experimental setup was designed to use 2-ft long cores, which are significantly longer than the cores used in some past studies of gravity drainage experiments [173, 176].

5.2.1 Experimental Apparatus and Procedures

Fig. 5.9 is a schematic of the gravity drainage apparatus. The use of a visual cell enables us to measure the volume of oil drained at any given time without disturbing the system. The drainage apparatus was designed to operate up to 7,000 psia and 200°F. Fig. 5.10 shows the inside arrangement of the drainage cell. The annular space between the core and the cell wall is about 1 mm, a space that simulates an open fracture through which oil and gas can flow. We attempted to minimize the volume ratio of this space and the rock matrix in order to observe similar mass transfer mechanisms as in oil reservoirs. The inside dimensions of the drainage cell are height of 2 ft and a diameter of 2.5 in. In order to avoid oil displacement when gas flows into the cell, the cell was designed to allow gas flow into the cell from both ends.

Means stock tank crude was used for our studies, because it has been relatively well characterized in our laboratory [174, 79]. Because we used stock tank oil, we saturated cores at room temperature and pressure. We first saturated the core with water by evacuating it and then allowing water to imbibe into the core. Weighing the core before and after saturation gave the pore volume. The core was then moved into the core holder for oil displacements to establish initial water saturation. We considered the initial water saturation to be reached after injection of 1.5 pore volumes of crude oil, at which time the water production was small although it had not completely stopped. The amount of water produced was used to calculate oil saturation. The core was then weighed again to check the material balance.

The cell and CO_2 were then preheated to the desired temperature before inserting the

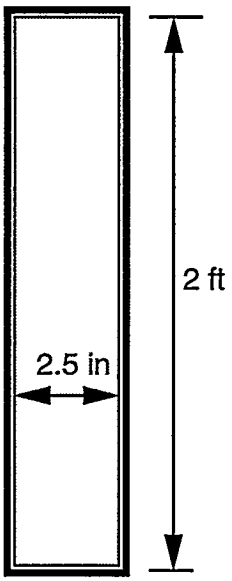

Figure 5.10: Schematic of the gravity drainage cell

saturated core into the drainage cell. The core was kept in the drainage cell for two days before the introduction of CO_2 in order to be sure that temperature equilibrium was achieved in the drainage cell.

Pure CO_2 was then introduced into the cell to replace the oil in the annulus. The pressure in the cell is controlled manually by periodically introducing additional CO_2 into the cell.

The difference in density between the CO_2 and the oil creates a gravity driving force for oil drainage. That force is opposed by capillary forces which depend on the interfacial tension of the gas/oil system. That interfacial tension changes as components transfer between the phases and the oil swells as the CO_2 dissolves in it. Thus, the experiment determines whether the component transfers lead to significant recovery of crude oil.

5.2.2 Results

We conducted two drainage experiments at different temperatures and pressures. Fig. 5.11 shows the crude oil recovery curves. Experiment 1 was performed at room temperature (72.5 °F) and relatively low pressure (900 psi) in a 500 md sandstone core. After three weeks of drainage, there was about 27% of original oil in place (OOIP) recovered. The experiment was stopped after six weeks of drainage. There was little additional oil recovered in the last three weeks. No additional oil was recovered when we blew down the system to ambient pressure. The calculations of the phase properties presented below show that the interfacial tension was relatively high (about 4.0 mN/m). Therefore, this low recovery is not surprising.

In Experiment 2, the temperature was elevated to 120°F, and the pressure was kept at 1500 psia for the first five weeks and jumped to 1700 psia in the last week of the experiment. Two recovery periods were observed in this experiment. Drainage was fast in the first week of drainage, and then it slow down in the remaining four weeks. That behavior is consistent with the observations of Schechter *et al.*[165]. Comparison of Experiments 1 and 2 suggests that gravity drainage is faster and more efficient at the higher temperature and pressure. At same temperature, we recovered additional 6 % OOIP when the pressure was increased from 1500 psia to 1700 psia. This additional recovery indicates that gravity drainage at high pressure is more efficient in the pressure range of the experiments, presumably because interfacial tension was lower at the higher pressure, and

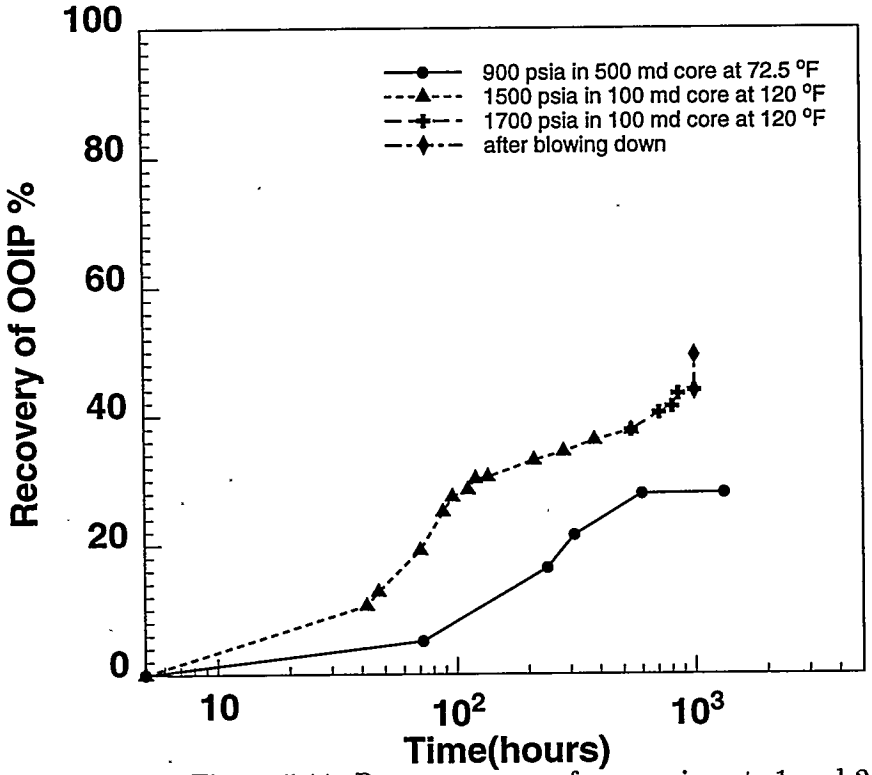

Figure 5.11: Recovery curves for experiments 1 and 2

because solubility of CO_2 in the oil increased somewhat. Experiment 2 was terminated by blowing down the pressure from 1700 psia to ambient pressure in about 20 minutes. We collected additional 5% of oil with a lighter color than the crude oil. Thus, we recovered 50% of OOIP from Experiment 2.

5.2.3 Discussion

Oil recovery from gravity drainage is the result of interactions between capillary forces created by interfacial tension and gravity forces from the density difference of the gas and oil phases. The relative magnitudes of capillary and gravity forces determine the efficiency of a drainage process. The ratio of the capillary to gravity forces can be represented by the inverse Bond number N_B^{-1}, defined here as

$$N_B^{-1} = \frac{c\sigma\sqrt{\frac{\phi}{k}}}{\Delta\rho g H} \tag{5.38}$$

where c is a scaling constant for a given medium (c is about 0.2 for most of the media), σ is interfacial tension, $\Delta\rho$ is the density difference between oil and gas phases, k and ϕ are the permeability and porosity of the medium, and H is the height of the core.

Fayers and Zhou [62] proposed the following equation to correlate the remaining oil saturation (S_{rm}) at the end of a drainage process to the corresponding value of N_B^{-1} by scaling the capillary pressure curves.

$$S_{rm} = N_B^{-1}\left(2 - N_B^{-1}\right)(1 - S_{or}) + S_{or} \tag{5.39}$$

where S_{or} is the irreducible oil saturation. They used 0.25 as S_{or} in correlating their experimental data collection.

To estimate the corresponding values of N_B^{-1} for our experiments, we performed calculations of the phase properties for the Means/CO_2 system. The Peng-Robinson equation of state (PR-EOS) was used to calculate phase densities. Interfacial tensions were calculated with the Parachor

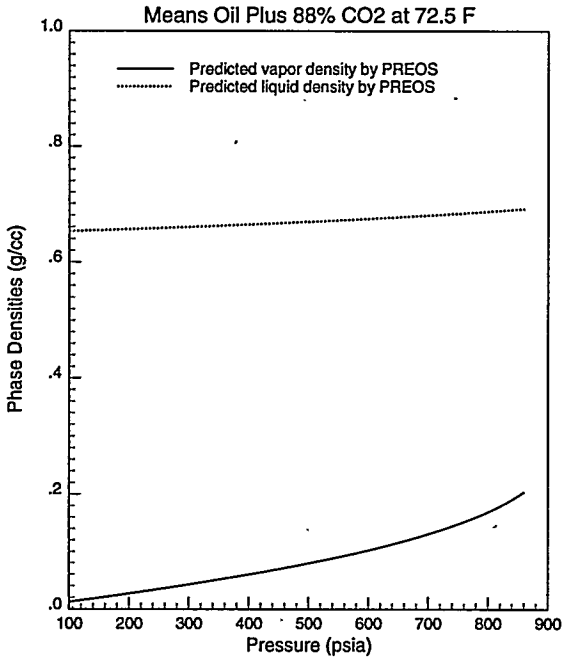

Figure 5.12: Calculated densities of Means/CO_2 mixture at 72.5°F and various pressures

methods. Detailed compositions of stock tank Means reported by Stessman [174] were used in these calculations. Figs. 5.12 and 5.13 show the calculated densities and interfacial tensions of the oil-rich and CO_2-rich phase at 72.5°F and various pressures. Figs. 5.14 and 5.15 show the same calculation for the high temperature and pressure experiment. Our calculations indicate that the interfacial tensions were not ultra-low (10^{-3} mN/m) but were about 1 mN/m. Using $\sigma = 4.0$ mN/m, $\Delta\rho =$ 400 kg/m^3 for experiment 1 and $\sigma = 0.5$ mN/m, $\Delta\rho = 180$ kg/m^3 for experiment 2, we obtained the corresponding N_B^{-1} values as 0.23 and 0.14 for experiments 1 and 2 respectively. Fig. 5.16 shows the comparison of the two experiments and the correlation proposed by Fayers and Zhou. Although the remaining oil saturation is slightly larger than the correlation, the trend agrees well with the earlier comparisons.

The recovery results shown in Fig. 5.16 suggest that substantial recovery of oil from fractured reservoirs is possible by CO_2 injection. If fracture heights larger than 2 ft exist, for example, inverse Bond numbers will be lower still and better recovery efficiency can be expected. Furthermore, if the porous medium is not strongly water wet, then injection of water will yield poor recovery, because imbibition will be relatively inefficient. Even if the porous medium is water wet, the film drainage mechanisms discussed in this chapter can lead to improved recovery after water injection. Thus, there is considerable evidence that the use of gas injection processes in fractured reservoirs should be investigated further.

5.2.4 Conclusions

From the experimental results and calculations of the phase properties of Means/CO_2 systems, we draw the following conclusions.

(i) Crude oil can be efficiently recovered by gravity drainage in the presence of CO_2 at relatively low pressure (1500 psia), in which the interfacial tension between oil and CO_2 rich phase is not necessarily ultra-low.

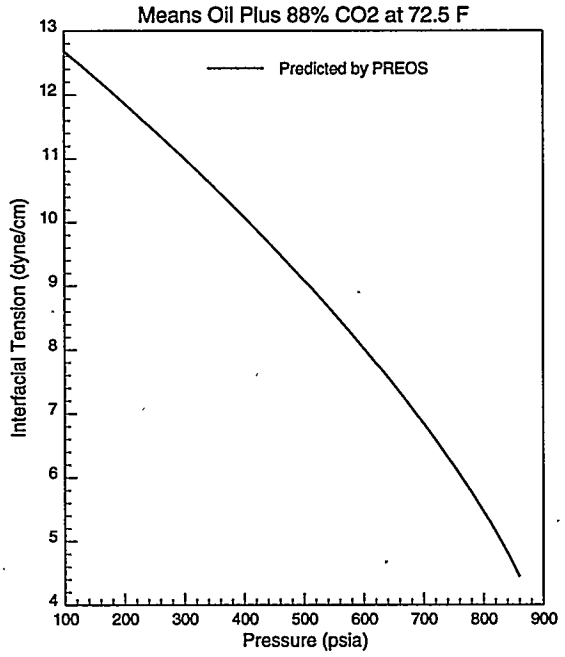

Figure 5.13: Calculated interfacial tension of Means/CO_2 mixture at 72.5°F and various pressures

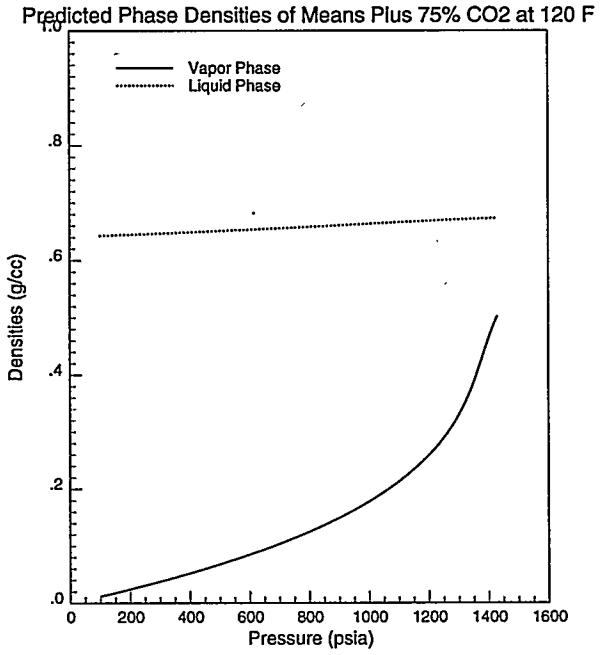

Figure 5.14: Calculated densities of Means/CO_2 mixture at 120°F and various pressures

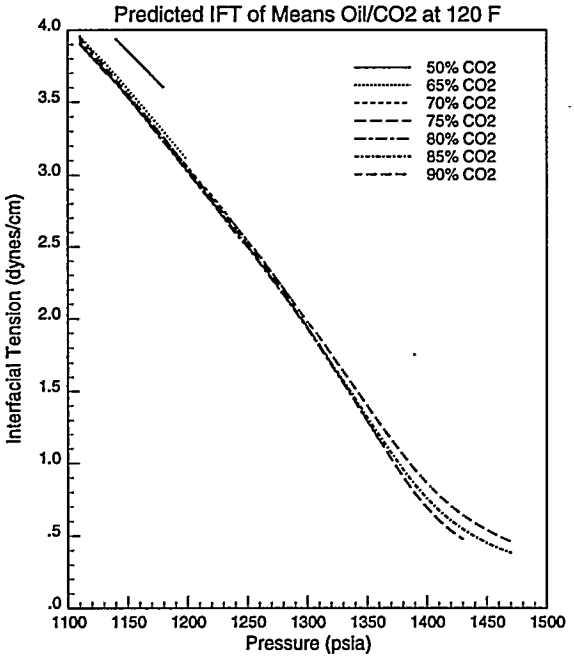

Figure 5.15: Calculated interfacial tension of Means/CO_2 mixture at 120°F and various pressures

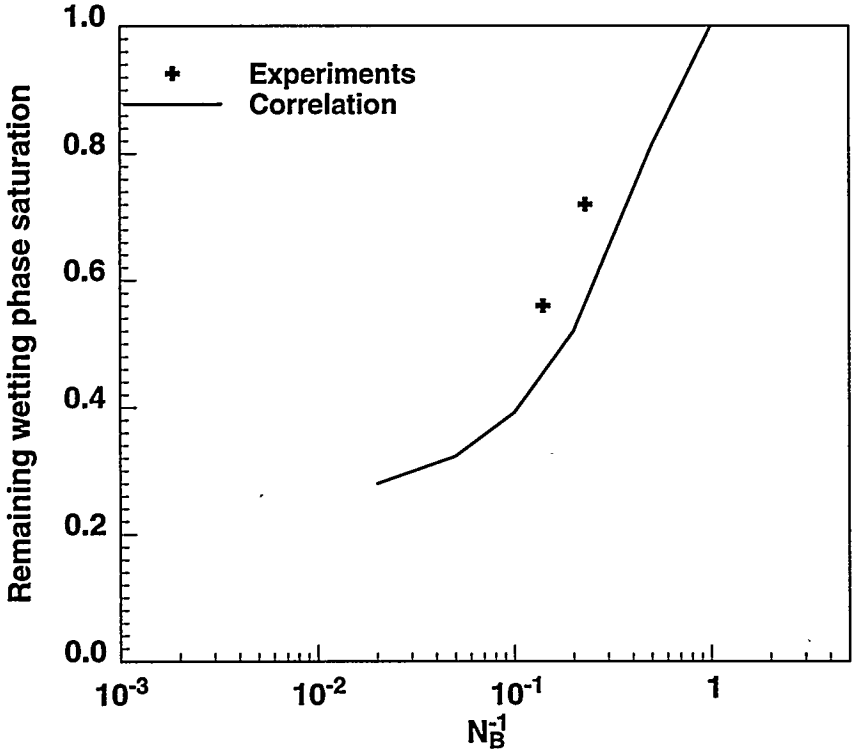

Figure 5.16: Correlation of the remaining crude oil saturation with the inverse Bond numbers

(ii) Final crude oil recovery can be related to the inverse Bond number of the model systems, although the Means/CO_2 fluids were not pre-equilibrated.

(iii) Additional oil can be recovered by blowing down the system pressure after a drainage process, and the recovered oil is lighter than the original crude oil.

5.3 Scaling Multiphase Flow in Simple Heterogenous Porous Media

D. Zhou, F. J. Fayers, and F. M. Orr, Jr.

In this section, we examine the scaling laws and flow regions controlling various types of flow behavior in systems with simple forms of heterogeneity. If we imagine displacement of oil by water in a two-dimensional, vertical cross-section of two layers with differing permeability, the distribution of oil and water at any time during the displacement will be controlled by a combination of physical phenomena. Water will usually flow faster in the high permeability layer. If the water is less viscous than the oil, then viscous fingering may influence the flow pattern. Gravity segregation will induce vertical flow, with very different effects depending on whether the high permeability layer is above or below the low permeability layer. Capillary forces will also cause transverse flow or crossflow, as water imbibes from the high permeability layer into adjacent low permeability zones (in a water-wet porous medium). The relative importance of each flow mechanism depends on the flow rate, the density difference between oil and water, the mobility ratio, permeabilities and capillary pressure curves for the layers, and so on. At low flow rate, for example, capillary and gravity forces will dominate the flow pattern, but at high flow rate, viscous forces will control fluid distributions.

We consider scaling of viscous, gravity, and capillary forces for displacements in homogeneous porous media and in systems that contain some simple heterogeneity such as layers and fractures. We do so by making the material balance equation dimensionless, thereby deriving a set of dimensionless groups that describe the relative magnitudes of the various forces. While many investigators [167, 198, 54, 156, 66] have used the same approach for subsets of the flow problems examined here, there has not previously been a comprehensive analysis which attempts to include a wide range of experimental data covering the combined effects of viscous, gravity, and capillary forces with the effects of permeability variation. We have analyzed many sources of experimental and simulation data to identify limiting flow regimes and to establish the range of values of the dimensionless groups over which transitions from one region to another occur. We find that the experimental information confirms consistent boundaries for the flow domains, and thus our results give a comprehensive mapping of the overall flow behavior.

The analysis and delineation of dimensionless transition regions given here will find a variety of applications. It will establish when concepts such as "vertical equilibrium" can be used to calculate average transport functions (pseudofunctions), and it will help to determine how much resolution is required in description of permeability heterogeneity in a reservoir. For example, if capillary pressure dominates local flow, then capillary crossflow will eliminate the effects of local permeability heterogeneity variations as capillary forces move water from high permeability to low-permeability zones. In such cases, the details of the local variations need not to be resolved in simulation representations of the flow. Thus, this analysis given here will permit more effective use of approximate simulation techniques that are an inevitable part of current simulation approaches for field-scale flows.

5.3.1 Analysis

For two-phase flow in a heterogeneous two-dimensional cross-section, we commence by expressing the equations of motion in a dimensionless form similar to that adopted by Yortsos [198] and Ekrann [54]. This form of analysis is referred to as Inspectional Analysis by Shook *et al.* [167]. While the approach we use is similar, the dimensionless groups we will define differ from those obtained by Shook *et al.* [167]. Material balance equations for incompressible flow are

$$\phi\frac{\partial S_w}{\partial T}+\frac{\partial U_w}{\partial X}+\frac{\partial V_w}{\partial Y}=0, \tag{5.40}$$

$$\frac{\partial}{\partial X}(U_w+U_o)+\frac{\partial}{\partial Y}(V_w+V_o)=0, \tag{5.41}$$

and the Darcy flow velocities for both phases are given by

$$U_j=-k_h(X,Y)\frac{k_{rj}}{\mu_j}\frac{\partial \Psi_j}{\partial X}, \tag{5.42}$$

$$V_j=-k_v(X,Y)\frac{k_{rj}}{\mu_j}\frac{\partial \Psi_j}{\partial Y}, \tag{5.43}$$

where Ψ_j is the flow potential in phase j, U_j and V_j are the flow velocities of phase j in the horizontal and vertical directions, and k_v and k_h are the permeability distribution functions in the vertical and horizontal directions. By defining $x=X/L$, $y=Y/H$, $t=Tq/L$, $u_j=U_j/q$, $v_j=(LV_j)/(qH)$, $k_v=k_{av}K_V(x,y)$, $k_h=k_{ah}K_H(x,y)$, $\Phi_j=(\Psi_j k_{ah})/(Lq\mu_o)$, and $\lambda_j=(k_{rj}\mu_o)/\mu_j$, we obtain the following dimensionless equations

$$\phi\frac{\partial S_w}{\partial t}+\frac{\partial u_w}{\partial x}+\frac{\partial v_w}{\partial y}=0, \tag{5.44}$$

$$\frac{\partial}{\partial x}(u_w+u_o)+\frac{\partial}{\partial y}(v_w+v_o)=0, \tag{5.45}$$

$$u_j=-K_H(x,y)\lambda_j\frac{\partial \Phi_j}{\partial x}, \tag{5.46}$$

$$\left(\frac{H}{L}\right)^2\frac{k_{ah}}{k_{av}}v_j=-K_V(x,y)\lambda_j\frac{\partial \Phi_j}{\partial y}, \tag{5.47}$$

where H and L are the width and length of the medium, k_{av} and k_{ah} are the average permeabilities of the medium in vertical and horizontal directions, and q is the total flow velocity in the horizontal direction. Note that the flow potentials Φ_o are dimensionless and expressed relative to the oil viscosity, and that the dimensionless mobilities also contain oil viscosity as a factor.

In the four dimensionless equations, $(L/H)^2(k_{av}/k_{ah})=R_l{}^2$ appears in Eq. 5.47 as the only scaling group, which can be rearranged as

$$\left(\frac{L}{H}\right)^2\frac{k_{av}}{k_{ah}}=\frac{L}{H}\frac{\frac{k_{av}\Delta\Phi}{H\mu}}{\frac{k_{ah}\Delta\Phi}{L\mu}}=\frac{L}{H}\frac{q_v}{q_h}=\frac{T_h}{T_v}, \tag{5.48}$$

which is the time ratio for a fluid to flow a distance (L) in the horizontal direction to the distance (H) in the vertical direction with the same potential difference across the distance. R_l is also called the effective shape factor, which is the shape factor L/H weighted by the permeability anisotropy. The shape factor ($R_l{}^2$) represents the relative flow capacities of the medium in vertical and horizontal directions.

In this section, our objective is to identify flow regions where certain forces dominate fluid movement in the transverse direction. Thus, we will focus our attention on the flow velocity in the transverse direction. Combining the Darcy equations for each phase gives

$$\frac{1}{(R_l)^2}(v_w + v_o) = -K_V(x,y)\left(\lambda_o \frac{\partial \Phi_o}{\partial y} + \lambda_w \frac{\partial \Phi_w}{\partial y}\right). \tag{5.49}$$

In order to define the relation between Φ_o and Φ_w, we use the definition of capillary pressure to obtain

$$\Phi_w = \Phi_o + \frac{\Delta\rho g H k_{ah}}{Lq\mu_o} y - \frac{{p_c}^* k_{ah}}{Lq\mu_o} J(S_w), \tag{5.50}$$

where transverse capillary pressure is defined as $p_c = {p_c}^* J(S_w)$, and ${p_c}^*$ is a characteristic transverse capillary pressure of the medium, ${p_c}^* = \int_{S_{wc}}^{1-S_{or}} p_c(S_w) dS/(1 - S_{or} - S_{wc})$. Substituting Eq. 5.50 into Eq. 5.49 yields

$$R_l{}^2 \frac{\partial \Phi_o}{\partial y} = \frac{-(v_o + v_w)}{\lambda_o K_V(x,y)(1+M)} - \frac{M}{1+M}\left(N_{gv} - N_{cv}\frac{\partial J}{\partial y}\right), \tag{5.51}$$

where

$$N_{gv} = \frac{\Delta\rho g L k_{av}}{Hq\mu_o}, \tag{5.52}$$

$$N_{cv} = \frac{L{p_c}^* k_{av}}{H^2 q\mu_o}, \tag{5.53}$$

and

$$M = \frac{\lambda_w}{\lambda_o}. \tag{5.54}$$

N_{gv} and N_{cv} are the characteristic time ratios for fluid to flow in the transverse direction due to gravity or capillary forces to that in horizontal direction due to viscous forces as shown by Eqs. 5.55 and 5.56.

$$N_{gv} = \frac{\Delta\rho g L k_{av}}{Hq\mu_o} = \frac{L}{q}\frac{\frac{\Delta\rho g k_{av}}{\mu_o}}{H} = \frac{T_h}{T_{gv}}, \tag{5.55}$$

and

$$N_{cv} = \frac{L{p_c}^* k_{av}}{H^2 q\mu_o} = \frac{L}{q}\frac{\frac{{p_c}^* k_{av}}{H\mu_o}}{H} = \frac{T_h}{T_{cv}}. \tag{5.56}$$

Note the differences of the gravity and capillary numbers defined here from the conventional gravity (N_g) and capillary (N_c) numbers in the past studies [167, 198, 5], except Fayers and Muggeridge [64] used N_{gv}, and Yokoyama and Lake [197] used N_{cv} in their studies. The conventional capillary (N_c) and gravity (N_g) numbers are defined and related to the new numbers as

$$N_g = \frac{\Delta\rho g H k_{ah}}{Lq\mu_o} = \frac{N_{gv}}{R_l{}^2}, \tag{5.57}$$

and

$$N_c = \frac{{p_c}^* k_{ah}}{Lq\mu_o} = \frac{N_{cv}}{R_l{}^2}. \tag{5.58}$$

The advantage of using N_{gv} and N_{cv} is that they represent the relative magnitudes of the gravity and capillary forces to the viscous forces in the transverse direction including the fact of aspect ratio as reflected by the shape factor ($R_l{}^2$).

We will treat $M/(1+M)$ as a constant in the system, although in principle, the mobility ratio M is a function of saturation. For a number of the applications to be considered, we will

Table 5.3: Summary of the limiting cases

Flow region	Simplified expression	Conditions
Capillary-dominated	$R_l{}^2 \frac{\partial \Phi_o}{\partial y} = \frac{MN_{gv}}{1+M} \frac{\partial J}{\partial y}$	$N_{cv} >> N_{gv}$ and $\frac{MN_{cv}}{1+M} >> 1.0$
Gravity-dominated	$R_l{}^2 \frac{\partial \Phi_o}{\partial y} = -\frac{MN_{gv}}{1+M}$	$N_{gv} >> N_{cv}$ and $\frac{MN_{gv}}{1+M} >> 1.0$
Capillary-gravity equil.	$\frac{\partial J}{\partial S} \frac{\partial S}{\partial y} = -\frac{\Delta \rho g H}{p_c{}^*}$	$N_{gv} \approx N_{cv}$ and $\frac{MN_{gv}}{1+M} >> 1.0$
Viscous-dominated	$R_l{}^2 \frac{\partial \Phi_o}{\partial y} = \frac{1}{(1+M)} \frac{v_o+v_w}{\lambda_o K_V(x,y)}$	$\frac{(N_{gv}+N_{cv})M}{1+M} << 1.0$
Vertical crossflow equil.	$\frac{\partial \Phi_o}{\partial y} \approx 0$	$\frac{(N_{gv}+N_{cv})M}{1+M} << 1.0$ and $R_l{}^2 >> 1.0$
No-communication	$\frac{\partial \Phi_o}{\partial y} \approx \infty$	$\frac{(N_{gv}+N_{cv})M}{1+M} << 1.0$ and $R_l{}^2 << 1.0$

be concerned with crossflow mechanisms in vertical sections for which the boundary conditions are $v_o = v_w = 0$ at top and bottom. We therefore expect that v_o and v_w will be relatively small at intermediate locations.

Eq. 5.51 shows that the potential gradient in the vertical direction of a cross-section consists of three parts: viscous, gravity and capillary forces. The relative magnitudes of these forces are defined by two dimensionless numbers: a modified gravity number $(N_{gv}M)/(1+M)$, and a modified capillary number $(N_{cv}M)/(1+M)$. Thus, the mobility ratio has been included in the capillary and gravity numbers, because the definitions of capillary and gravity numbers are based only on oil viscosity. The shape factor $(R_l{}^2)$ defines the magnitude of the potential gradient of the system in the transverse direction. In addition to the three scaling numbers, the scaled permeability distribution function $K_V(x,y)$ and scaled capillary pressure function $J(S_w)$ represent the effects of heterogeneity of the medium. $\partial S_w/\partial y$ shows the influence of the phase distribution in the medium.

The scaling properties of a heterogeneous medium can be categorized as the average scaling parameters, such as the shape factor $R_l{}^2$, capillary number $(MN_{cv})/(1+M)$, gravity number $(MN_{gv})/(1+M)$, and the mobility ratio M, and the detailed scaling properties as the scaled permeability distribution function $K_V(x,y)$, capillary pressure function $J(S_w)$, and phase distribution $\partial S_w/\partial y$. This work will examine the average scaling parameters to identify flow regions where certain forces dominate. We will consider media having simple heterogeneity, but will assume that the effects of ordering of layers is secondary to the principal mechanisms controlling the flows. In the following, we will define conditions for four flow regions: gravity-dominated, capillary-dominated, capillary-gravity equilibrium, and viscous-dominated flow regions. In each case, the vertical potential gradient given in Eq. 5.51 is used to obtain limiting conditions for the crossflow behavior. The limiting forms of expression for vertical potential gradients to be derived in the next section are summarized in Table 5.3.

Gravity-Dominated Crossflow. Gravity-dominated flow occurs if $N_{gv} >> N_{cv}$, so that Eq. 5.51 can be reduced to

$$R_l{}^2 \frac{\partial \Phi_o}{\partial y} = \frac{-(v_o + v_w)}{\lambda_o K_V(x,y)(1+M)} - \frac{MN_{gv}}{1+M}. \tag{5.59}$$

Furthermore, if $(N_{gv}M)/(1+M) >> F_{vis}$, Eq. 5.59 can then be reduced to

$$R_l{}^2 \frac{\partial \Phi_o}{\partial y} = -\frac{MN_{gv}}{1+M}. \tag{5.60}$$

where $F_{vis} = -(v_w + v_o)/(\lambda_o(1+M)K_V(x,y))$. F_{vis} should be small and in the magnitude of unity for this case. Thus, the conditions for Eq. 5.60 to be valid are that $N_{gv} >> N_{cv}$ and $MN_{gv}/(1+M) >> 1.0$. Eq. 5.60 has been derived such that the system is dominated by gravity segregation.

Capillary-Dominated Crossflow. If capillary effects dominate, then Eq. 5.51 reduces, when $N_{cv} >> N_{gv}$ to

$$R_l{}^2 \frac{\partial \Phi_o}{\partial y} = \frac{-(v_o + v_w)}{\lambda_o K_V(x,y)(1+M)} + \frac{M}{1+M} N_{cv} \frac{\partial J}{\partial y}. \tag{5.61}$$

When $(N_{cv}M)/(1+M) >> 1.0$, Eq. 5.61 simplifies to

$$R_l{}^2 \frac{\partial \Phi_o}{\partial y} = \frac{M N_{cv}}{1+M} \frac{\partial J}{\partial y}, \tag{5.62}$$

Thus, the driving force for fluid to flow in the transverse direction is the capillary force. The conditions for such a case are that $(N_{cv}M)/(1+M) >> 1.0$ and $N_{cv} >> N_{gv}$.

Capillary-Gravity Equilibrium. If $(N_{gv}M)/(1+M) >> 1.0$, Eq. 5.51 can be reduced to

$$R_l{}^2 \frac{\partial \Phi_o}{\partial y} = \frac{M N_{gv}}{1+M} \left(1 - \frac{N_{cv}}{N_{gv}} \frac{\partial J}{\partial y}\right). \tag{5.63}$$

If $(MN_{gv})/(1+M) >> 1.0$, and $N_B = N_{gv}/N_{cv}$ is intermediate, the value of $(1-(N_{cv}/N_{gr})(\partial J/\partial y))$ should be small, which means that

$$\frac{\partial J}{\partial S} \frac{\partial S}{\partial y} \approx \frac{N_{gv}}{N_{cv}} = \frac{\Delta \rho g}{p_c{}^*}. \tag{5.64}$$

Eq. 5.64 indicates that the system is in capillary-gravity equilibrium. Thus, if $(N_{gv}M)/(1+M) >> 1.0$ and N_{gv}/N_{cv} is moderate, the system can be considered to be in capillary-gravity equilibrium.

Viscous-Dominated Crossflow. In Eq. 5.51, the net effects of capillary and gravity forces are controlled by the sign of $\partial S_w/\partial y$. Since $\partial J/\partial S_w$ is negative, if $\partial S_w/\partial y$ is negative, the gravity and capillary forces tend to offset each other's effects. However, they will enhance each other's effects if $\partial S_w/\partial y$ is positive. In order to reach a viscous-dominated flow region, the viscous force should be much greater than the maximum effects of capillary and gravity forces, that is

$$(1 + \frac{N_{cv}}{N_{gv}}) \frac{N_{gv} M}{1+M} << 1.0. \tag{5.65}$$

Eq. 5.51 can then simplify to

$$R_l{}^2 \frac{\partial \Phi_w}{\partial y} = R_l{}^2 \frac{\partial \Phi_o}{\partial y} = \frac{-(v_w + v_o)}{\lambda_w K_V(x,y)}. \tag{5.66}$$

If $R_l{}^2 >> 1.0$, the value of $\partial \Phi_o/\partial y$ should be very small, because $F_{vis} = -(v_o + v_w)/(\lambda_o(1+M)K_V(x,y))$ has a finite value. Thus,

$$\frac{\partial \Phi_o}{\partial y} \approx 0 \approx \frac{\partial \Phi_w}{\partial y}. \tag{5.67}$$

Crossflow under such condition is referred as viscous crossflow equilibrium (VCE). It is obvious that VCE is valid only if $(N_{gv}G + N_{cv})M/(1+M) << 1.0$, and also $R_l{}^2 >> 1.0$.

Eq. 5.66 indicates that if the viscous forces dominate flow, both phases should crossflow in the same direction at any point of the medium. Furthermore, if $R_l{}^2 << 1.0$, $\partial \Phi_o/\partial y$ should be very large, that is,

$$\frac{\partial \Phi_o}{\partial y} = \frac{\partial \Phi_w}{\partial y} \rightarrow \infty. \tag{5.68}$$

Eq. 5.68 indicates that for finite crossflow velocities $(v_o + v_w)$ and $R_l^2 << 1.0$, there would need to be an infinitely large potential gradient. Since this is not plausible, there should be little crossflow in the transverse direction.

In summary, if $(N_{cv} + N_{gv})M/(1+M) << 1.0$, the system is dominated by the viscous forces. At the same time, if $R_l^2 << 1.0$, viscous crossflow can be neglected, and if $R_l^2 >> 1.0$, the system is in VCE.

5.3.2 Discussion and Comparison with Existing Experimental and Simulation Results

Three independent dimensionless groups have been derived for the average scaling properties of a flow system: $(N_{gv}M)/(1+M)$, $(N_{cv}M)/(1+M)$ and R_l^2. We then defined the conditions for certain forces to dominate fluid flow in a medium. However, the conditions defined in the above section are mathematically infinitely small or large. In practice, we would ask, how large (or small) is large (or small) enough for these conditions to hold. To answer this question, we examined existing experimental and numerical simulation results to identify flow regions. In the following, we define a flow with a single gravity tongue as gravity-dominated flow, a flow which is faster in the low-permeable region than in high-permeable region as capillary-dominated, and a flow where recovery varies little with increase in flow rates as viscous-dominated.

Previous studies of scaling behavior in multiphase flow in porous media have usually concentrated on one of the following three situations: miscible displacements, immiscible displacements with minimal gravity effects, and flow in fractured reservoirs. Although the existing experimental and numerical simulation results for each case do not cover all parameters derived above, combining these three different situations gives us a reasonably clear picture of the flow regions in general. A summary of the principal sources of data and their estimated ranges of scaling parameters is given in Table 5.4.

Miscible Displacements($N_{cv} \approx 0$). The term miscible displacement here refers to displacements with negligible capillary effects ($N_{cv} \approx 0$), which can also include two-phase flow. Much research effort has been applied to flow in such systems [5, 66, 23, 93]. When the capillary force is neglected, only gravity and viscous forces contribute to flow. Dispersion and diffusion can influence to some degree the performance of miscible and near-miscible displacements [63], since they affect mixing and the contrasts in viscosity and density differences. However, dispersion can usually only be a significant contributor in displacements where capillary and gravity forces are small and injection rates are also relatively small. Dispersion effects will not be included in this work, and we retain the unmixed viscosities and densities to analyze miscible scaling behavior.

Studies of crossflow in heterogeneous media have commonly been carried out on stratified media [149, 201, 202, 93]. The complexity of the problem has progressed from studying viscous crossflow alone [202, 201] to including gravity effects [54, 93]. Zapata and Lake's fine-grid simulation results on stratified reservoirs concluded that for systems without gravity and capillary effects, when R_l^2 was larger than 100, the viscous-crossflow equilibrium assumption was valid [202]. Continuation of their work by Thiele [182] showed that for practical purposes, if R_l^2 was larger than 10, the VCE assumption held, and if R_l^2 was smaller than 0.01, the system could be assumed to have no communication (vertical crossflow can be neglected).

Both experimental and numerical simulation results have been reported for gravity effects on displacement performance in vertical cross-sections [5, 66, 93]. Fayers and Muggeridge [66] performed very fine-grid simulations for homogeneous vertical cross-sections and found that the transition of viscous-dominated flow to gravity tonguing occurs in the range of $0.2 < (N_{gv}M)/(1+M) < 2$. Pozzi's [156] experimental results for uniform bead-packs showed that a single-gravity tongue would form if $(N_{gv}M)/(1+M) > 2.5$, which agrees well with Fayers and Muggeridge's

Table 5.4: Summary of data used to identify flow regions

Source	Flow type (medium)	Scaling numbers N_B	$\frac{MN_{cv}}{1+M}$	$\frac{MN_{gv}}{1+M}$	${R_l}^2$	Flow regions
Du Prey [49]	imbibition (sandstone)	$0.05 - 10$			0.59	transition $0.2 < N_B < 5.0$
Hamon [80]	Imbibition (sandstone)	$10^{-3} - 10^{-1}$			$10^{-2} - 0.5$	capillary-dominated $N_B < 0.05$
Cuiec [37]	Imbibition (chalks)	$10^{-3} - 10^{-2}$			0.56	capillary-dominated $N_B < 10^{-2}$
Schechter [165]	imbibition drainage (sandstone)	$10^{-2} - 20$			0.01	transition $0.2 < N_B < 5.0$
Fayers [66]	miscible (simulation)		0	$10^{-4} - 10^{2}$	$10^{2} - 10^{3}$	transition $0.2 < \frac{MN_{gv}}{1+M} < 2.0$
Araktingi [5]	miscible (simulation)		0	$10^{-4} - 1.0$	$10^{2} - 10^{3}$	viscous-dominated $0.25 < \frac{MN_{gv}}{1+M}$
Ingsoy [93]	miscible (bead-packs)		0	$8.0 - 14.0$	20	gravity-dominated $\frac{MN_{gv}}{1+M} > 5.0$
Pozzi [156]	miscible (bead-packs)		0	$10^{-5} - 10^{-1}$	$10 - 10^{5}$	gravity-dominated $\frac{MN_{gv}}{1+M} > 5.0$
Zapata [202]	viscous flow (simulation)		0	0	0.1–?	VCE ${R_l}^2 > 10^2$
Thiele [182]	viscous flow (simulation)		0	0	$10^{-2} - 10^{3}$	transition $0.1 < \frac{1}{{R_l}^2} < 10^2$
Yokoyama [197]	imbibition (simulation)		$0 - 57.4$	0	$0 - 10^{4}$	capillary-dominated $\frac{N_{cv}M}{1+M} > 4.1$
Dawe [39]	imbibition (bead-packs)		$13.1 - 250$	0	25	capillary-dominated $\frac{N_{cv}M}{1+M} > 13.1$
Ahmed [3]	imbibition (bead-packs)		$0.29 - 14.3$	0	14.3	transition $0.2 < \frac{N_{cv}M}{1+M} < 6.1$
Pavone [153]	drainage (carbonate)		$0.2 - 20$	0	11.1	transition $0.2 < \frac{N_{cv}M}{1+M} < 10$

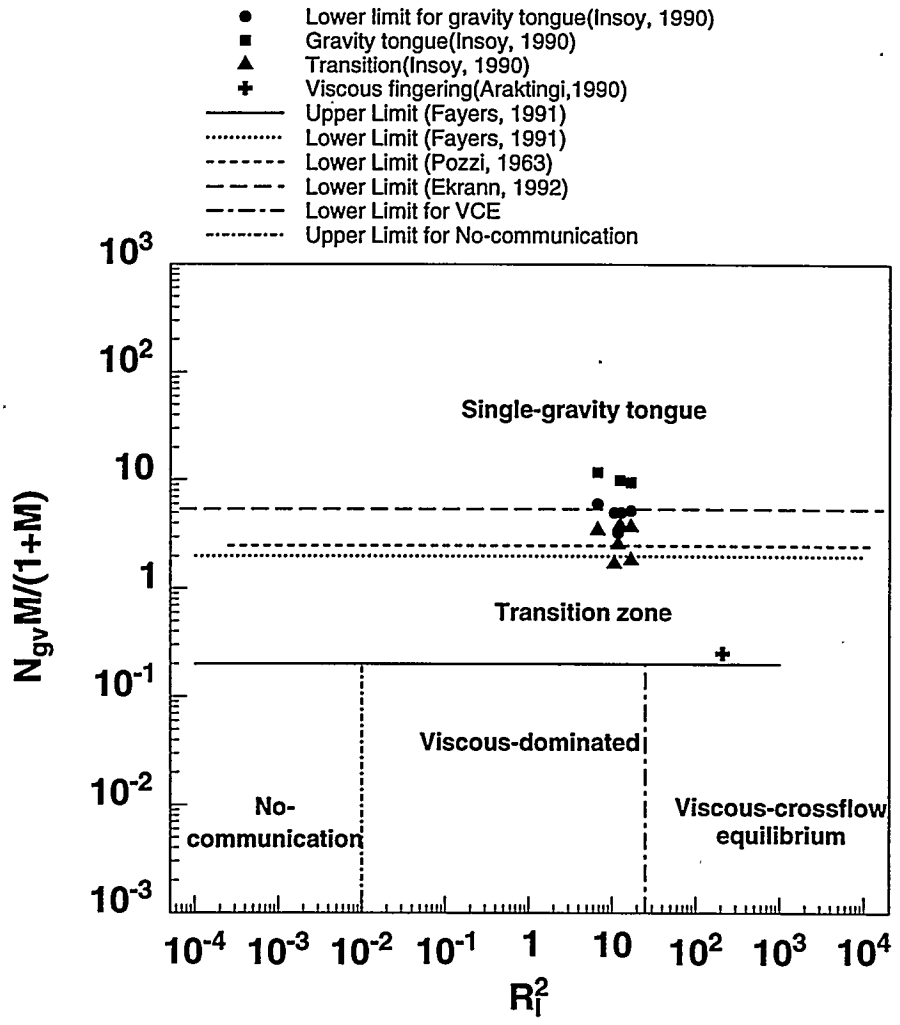

Figure 5.17: Flow regions in miscible displacements

simulation results. Araktingi and Orr's simulation results from a particle-tracking simulator for both homogeneous and stratified vertical cross-sections indicates that flow was viscous-dominated if $N_{gv}M/(1+M) < 0.25$ [5], which also agrees very well with the above results.

Experimental results were reported by Insoy and Skjaeveland [93] to examine the theory by Ekrann for development of a gravity tongue in a stratified porous medium. Ekrann's theory assumed that vertical equilibrium and pressure continuity along the displacement front are the criteria for development of a single gravity tongue. The predicted critical value of a system for a single gravity tonguing is $(MN_{gv})/(1+M) > 5.0$. Their experimental data showed that when $(MN_{gv})/(1+M) = 11.5$, there was a gravity-stable tongue.

Fig. 5.17 shows the flow regions in miscible displacements in layered and homogeneous media. The lines are the boundaries between flow regions reviewed in this section. Although the results are from both layered and homogeneous media, the transition from the gravity-dominated to the viscous-dominated region agrees well between investigators. The transition is in the range of $0.2 < (N_{gv}M)/(1+M) < 5.0$. In the viscous-dominated region, the boundaries of transition from no communication to VCE regions are based on Thiele's results. The transition in this case in the range of $0.01 < R_l{}^2 < 10$.

Immiscible Displacements without Gravity Effects ($N_{gv} \approx 0$). Capillary-dominated cross-flow has been demonstrated as an important oil recovery mechanism, and therefore it receives

considerable attention in oil recovery research. Several studies were carried out to investigate capillary crossflow in the absence of gravity effects [55, 197, 39]. Yokoyama and Lake [197] simulated the effects of capillary pressure on displacements in stratified porous media. Their results show that with increased injection rate, less oil was recovered at the same pore volume injected [197]. They varied the transverse capillary number (N_{cv}) from 0 to 57.4. From their simulated fractional flow curves, we can see that at $N_{cv} = 0$, there was no crossflow between layers, while with increase of N_{cv}, more crossflow occurred from the high-permeable layer to the low-permeable layer. When $MN_{cv}/(1+M) = 4.1$, the displacement front in the stratified system was close to uniform. When $(MN_{cv})/(1+M) = 57.4$, the displacement front was completely uniform, which indicated capillary-dominated flow.

An experimental study of capillary crossflow on a bead-pack by Ahmed *et al.* [3] showed that crossflow changed significantly with changes in injection rates, although the production curves did not vary so much. At their high injection rate ($MN_{cv}/(1+M) = 0.35$), a viscous flow regime existed in the most permeable layer, with breakthrough occurring in that layer. At low injection rate ($MN_{cv}/(1+M) = 8.5$), flow advanced faster in the low-permeability layer, which indicates a capillary-dominated flow. At intermediate flow rates ($(MN_{cv})/(1+M) = 0.57$), displacements occurred in both the high-permeability layer and the low-permeability layer.

In the waterfloods by Dawe *et al.* [39] in layered bead-pack systems at low rates, the water front in the low-permeability layer advanced faster than that in the high-permeability layer [39]. Thus, the displacements were capillary-dominated. The corresponding value for $(MN_{cv})/(1+M)$ varied from 13.1 to 105.

The studies discussed above were for imbibition processes. Pavone's study [153] of viscous fingering in carbonate porous media was for drainage processes, however. The physical parameters of the system were not well defined, although the author listed the permeabilities and porosities of the samples. In order to use Pavone's experimental results, the measured maximum pressures were used to estimate the capillary entry pressures and the viscous pressure drops for similar media. For each viscous ratio, media with reported permeability differences of no more than 0.1 Darcy were considered as similar media. The corresponding values of $(MN_{cv})/(1+M)$ can then be estimated for all displacements. From the moldings of the displacement fronts in the porous media, it can be seen that the displacement in RUN 9 is capillary-dominated, since it had a stable front with unfavorable mobility ratio. For RUN 9, $(MN_{cv})/(1+M) = 10$.

Combining the experimental and simulation data, we can approximately determine the transition region from capillary- to viscous-dominated flow as shown in Fig. 5.18. The lower limit for the capillary-dominated flow is the intermediate rate displacement of Yokoyama and Lake's simulations $MN_{cv}/(1+M) = 4.1$. The dashed line in Fig. 5.18 is the estimated lower limit for the capillary-dominated region. The upper limit (solid line) for the viscous-dominated region is drawn through the highest rate of Ahmed *et al.*'s experiments. In summary, the transition between capillary-dominated and viscous-dominated flow occurs in the range of $0.35 < N_{cv}\frac{M}{1+M} < 4.1$. Within the viscous-dominated flow regions (i.e. capillary and gravity forces are negligible), the no-communication and viscous crossflow equilibrium flow regimes should be the same as in the miscible displacement cases.

Flow in Fractured Reservoirs. In studies of flow in fractured reservoirs, imbibition or drainage cells are commonly used to simulate the behavior of oil recovery from reservoirs with vertical fractures [165, 37, 49]. In such cases, the flow in the horizontal direction is relatively small and the values for N_{cv} and N_{gv} become very large. Therefore, the ratio of the gravity to capillary forces ($N_B = N_{gv}/N_{cv}$) is an important parameter in scaling flow in fractured media. Thus, flow in vertically fractured reservoirs is a special case in using the scaling equation. The calculation of the Bond number (N_B) requires the value of capillary pressure. However, in some of the studies, capillary pressure curves are not available. In the following discussion, $p_c{}^*$ is taken to be the

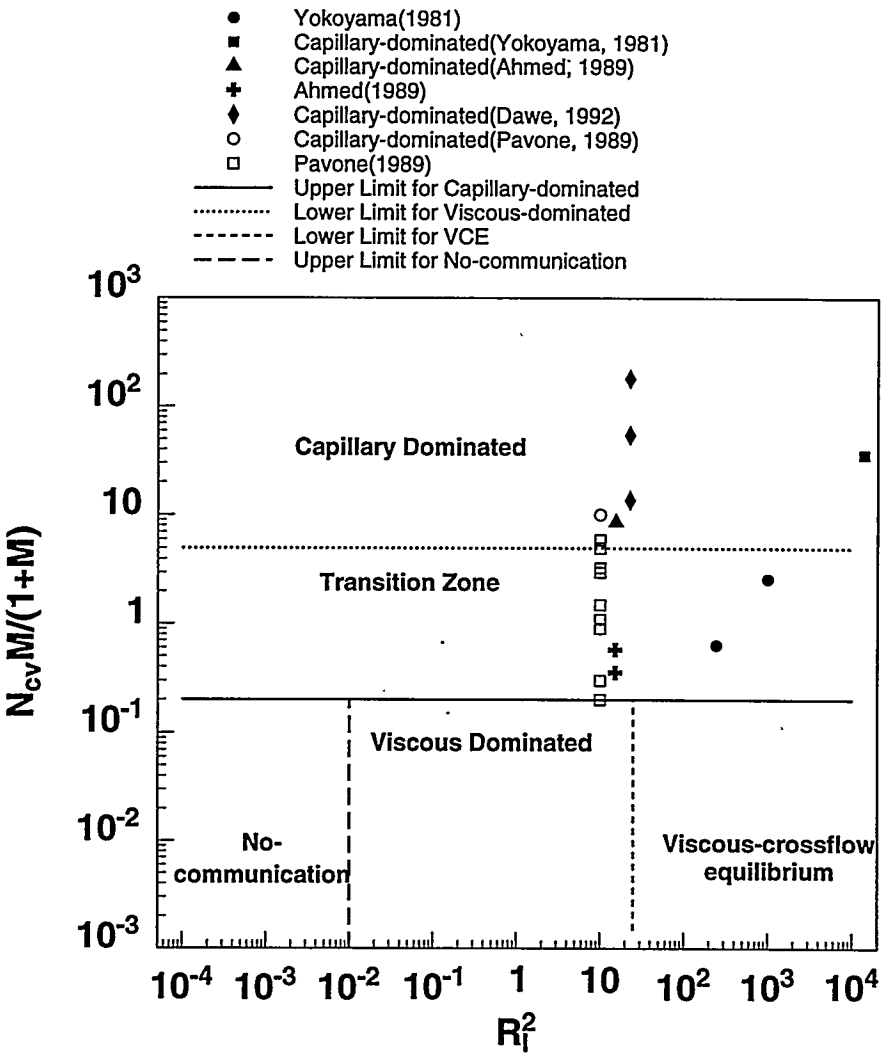

Figure 5.18: Flow regions in immiscible displacements

average threshold capillary pressure of the medium and is estimated by the following equation for cases without capillary pressure data:

$$p_c^* = 4\sigma \cos\theta \left(\frac{c\phi}{k}\right)^{1/2} \tag{5.69}$$

where c is a constant depending on the medium, $c = 0.02$ is used for glass bead-packs, θ is the contact angle depending on the wettability of the system. The glass bead-packs can be considered as strongly water-wet ($\cos\theta = 1$) .

Early studies of imbibition were carried out on small reservoir samples and at high interfacial tension (IFT). Cuiec's results [37] for low-permeability chalks indicates that production curves could be scaled according to imbibition theory (i.e. capillary force is the driving force). The Bond numbers were small and varied from 10^{-4} to 10^{-2} in Cuiec's study. On the other hand, du Prey's centrifuge imbibition tests [49] for sandstone samples showed that production curves could not be successfully scaled with an imbibition model when the Bond number changed from 10^{-2} to 10. Careful examination of the production curves shows that they can be scaled well by imbibition theory if $N_B < 0.2$. Production curves with Bond numbers between 0.2 to 10 cannot be scaled by either capillary-dominated or gravity-dominated theory.

Schechter *et al.* [165] reported low IFT imbibition and drainage results, which showed that imbibition processes changed from capillary-dominated to gravity-dominated when IFT was

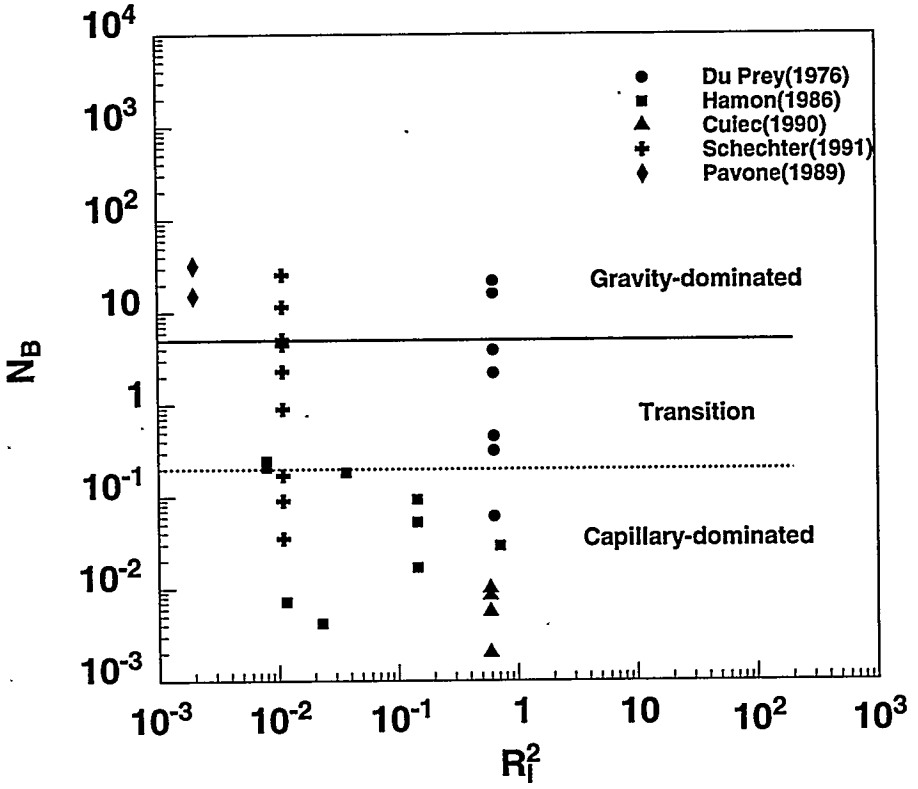

Figure 5.19: Flow regions in fractured reservoirs

changed from 38.1 mN/m to 0.1 mN/m. Their characteristic time scaling shows that if $N_B < 0.2$ the flow could be considered to be capillary-dominated, and if $N_B > 5$ the flow was gravity-dominated.

Imbibition studies by Iffly *et al.* [92] concluded that gravity influenced imbibition in the tests with the cylindrical sides sealed when the Bond number changed from 0.05 to 10^{-3}. This seems a contradiction to the results reviewed above. However, the characteristic length used in their scaling was based on countercurrent flow. The flows in the test could have been cocurrent flow. Thus, an explanation is that water imbibed in from the bottom of the media and oil flowed out from the top of the samples. Scaling of their results improves significantly with the characteristic length for cocurrent flow. The improvement suggests that the imbibition processes were capillary-dominated, but the flow was cocurrent.

Fig. 5.19 summarizes the experimental results reviewed in this section. Most of studies were focused on the capillary-dominated region with only the work by du Prey [49] and Schechter *et al.* [165] covering the transition region. The transition boundaries from the capillary-dominated to gravity-dominated regions are determined from Schechter *et al.*'s results, which are in the range of $(0.2 < N_B < 5)$.

Discussion. In previous sections, we have reviewed data from three types of situations: miscible displacements, immiscible displacements, and flow in fractured reservoirs. Although the data are limited, approximate bounds can be set up between flow regions for the media reviewed here. From miscible displacements, we find the transition between viscous-dominated to gravity-dominated is in the range of $0.2 < (MN_{gv})/(1+M) < 5.0$. Immiscible displacement results indicates the transition between viscous-dominated to capillary-dominated is in the range of $0.35 < (MN_{cv})/(1+M) < 4.1$, and the transition from capillary- to gravity-dominated flow in vertically fractured reservoirs is in the range of $0.2 < N_B < 5.0$. It is interesting to note that the transitions from capillary to gravity, from viscous to capillary, and from viscous to gravity flow regions occur in a similar range for the different scaling numbers. We can generalize the conditions for the transitions as: $0.2 < Sc < 5.0$,

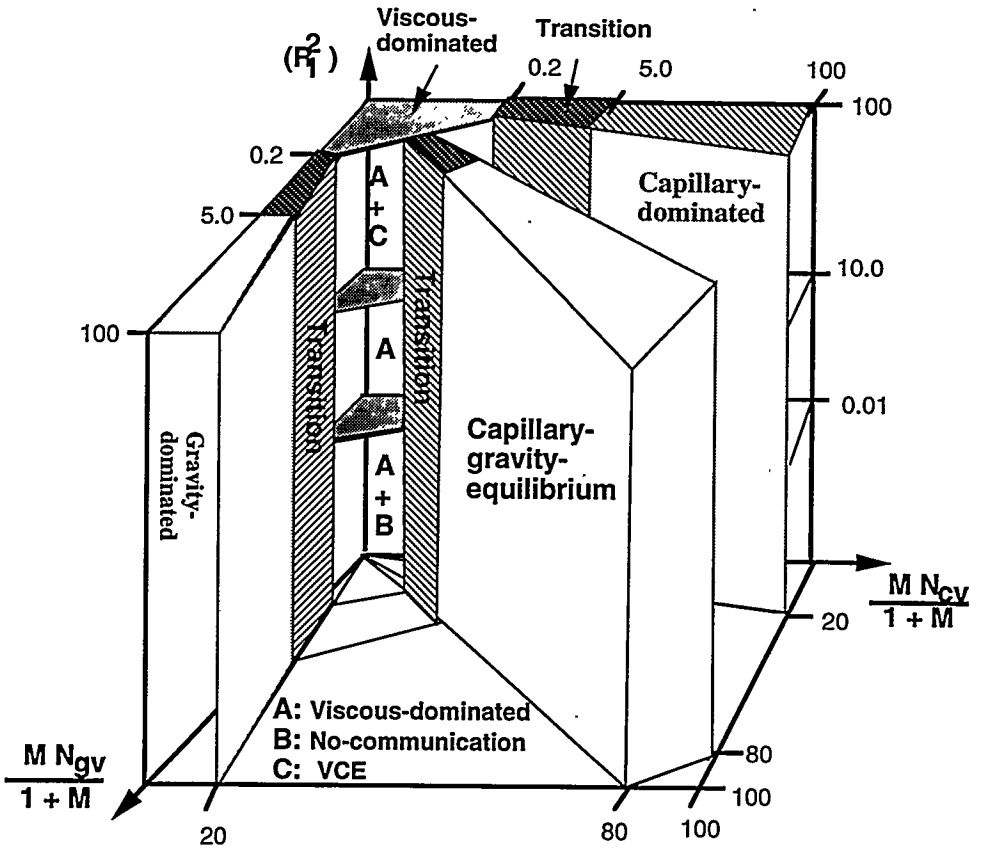

Figure 5.20: Schematic of flow regions in simple heterogeneous porous media

where Sc can be either $MN_{cv}/(1+M)$, or $MN_{gv}/(1+M)$, or N_B.

Fig. 5.20 shows the combined results of the flow regions for all three scaling numbers. The boundaries are determined based on the general results discussed above. In determining the viscous-dominated region with both gravity and capillary effects, we assume that $0.2 < (M(N_{cv} + N_{gv})/(1+M) < 5.0$. In the viscous-dominated region, the bounds of the transition from viscous crossflow equilibrium to no-communication regions are based on Thiele's simulation results.

For slightly immiscible systems approaching a critical condition, the ratio $\Delta\rho/\sigma$ determined from critical scaling theory increases rapidly near the critical point, and thus the Bond number of the system can increase dramatically. Therefore, in systems approaching miscibility as injection pressure or solvent enrichment increases, gravity effects will dominate as the capillary forces are reduced. In such situations, simulation models of near-miscible processes must handle the phase behavior and the density difference with care if the interplay of capillary and gravity forces is to be modeled accurately.

Since there are difficulties in determining the capillary pressure and mobility ratio, the bounds set from this work for immiscible displacements may have relatively large uncertainty regarding to the Bond number and capillary numbers. Capillary pressure curves should be measured to obtain reliable scaling for reservoirs, using either the imbibition or drainage mode appropriate to the type of displacement. Further investigation is needed to be sure that the end-point mobility ratio used here is valid for immiscible displacements with unfavorable mobility ratios.

5.3.3 Conclusions

In this study, we have defined three important dimensionless numbers that govern fluid flow in porous media with simple heterogeneities, and we have established approximate bounds for the transitions between regions. The dimensionless numbers can be easily extended to specific flow

systems as shown in the discussion section. A diagram of flow regions (Fig. 5.20) was drawn from the above discussion. This diagram can be very useful in identifying a flow situation in a given reservoir. From this work, the following conclusions can be drawn:

(i) Transverse gravity (N_{gv}) and capillary (N_{cv}) numbers have been defined from this analysis for identifying flow regions in heterogeneous porous media. These numbers are the characteristic time ratios for fluid to flow in the transverse direction due to gravity or capillary forces to that in horizontal direction.

(ii) Mobility ratio should be considered in the scaling process. With decreasing mobility ratio for a given medium, the viscous crossflow increases.

(iii) Miscible displacements can be very different in behavior depending on the system properties. Even for a system with an aspect ratio less than 0.1, the flow region can vary from viscous-dominated, to gravity-dominated regions depending on the gravity number.

(iv) Viscous-dominated flow in layered porous media can be in the vertical crossflow equilibrium region or the no-communication region depending upon the shape factor of the media and the gravity or capillary number of the system.

(v) In near-miscible displacements, increases in injection pressure or enrichment will cause the gravity effects to increase.

(vi) In fractured systems, the capillary to gravity force ratio defines the recovery mechanisms of oil from the matrix. Hence, identifying the flow regions is important in the simulation of fractured reservoirs.

5.4 Simulation Results for Imbibition Experiments

D. H. Fenwick and F. M. Orr, Jr.

Imbibition by a combination of capillary and gravity forces occurs often in multiphase flow. One example is the imbibition of water into oil-filled matrix blocks in fractured reservoirs. In this case, high capillary forces dominate over gravity forces and cause rapid imbibition into the water-wet rock, which forces the oil out of the matrix and into the fracture. Imbibition by capillary forces is the primary mechanism of oil production when waterflooding fractured reservoirs.

Capillary and gravity forces also operate in enhanced oil recovery, where interfacial tension (IFT) and density differences between the phases vary according to the compositions of the phases. Compositional variation makes the interplay between gravity and capillary forces more complex, and could significantly effect the recovery of oil from fractured reservoirs. Schechter *et al.* [164] performed core displacement experiments where the IFT was varied in imbibition. Four cores with varying permeability were filled with oil, and the entire core was immersed in water and allowed to contact all faces of the core. The experiments were performed with three different interfacial tensions, 38.1 mN/m, 1.07 mN/m, and 0.10 mN/m. Fig. 5.21 shows the results of the experiments on the 500 md Berea sandstone for the three interfacial tensions. Note that the recovery rate increased as the IFT was reduced. The results in Fig. 5.21 demonstrate recovery behavior that is inconsistent with scaling rules. (For a discussion of scaling see [164], [165], and Section 5.2). Increased recovery rate for lower IFT's is a surprising result, because as IFT is reduced, both capillary and gravitational driving forces for imbibition are reduced. Schechter *et al.* [164] explained the increase in rate by the fact that as IFT is reduced, gravity forces became more significant, which brought about a transition from countercurrent flow to cocurrent flow.

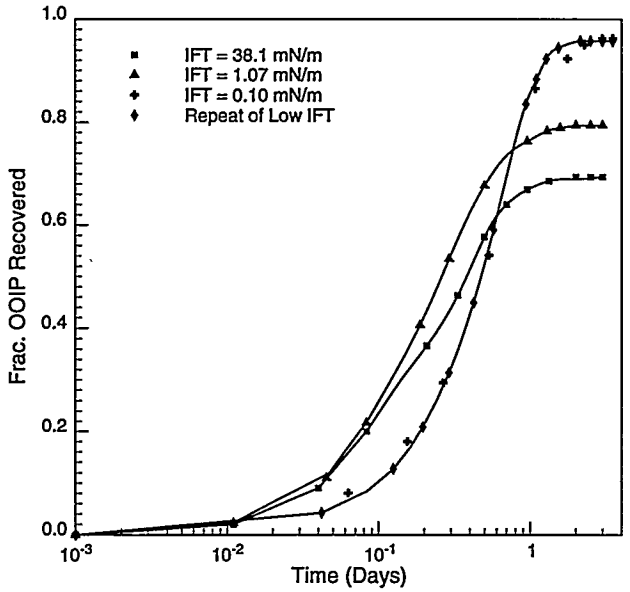

Figure 5.21: Imbibition Oil Recovery for 500 md Berea Sandstone [164]

The experimental results of Schechter *et al.* bring up many new questions about scaling of imbibition as IFT is reduced. For very small blocks, capillary forces will dominate for all but the extremely low IFT's. As the blocks become larger gravitational forces will become more significant, and the transition from countercurrent to cocurrent flow will occur at higher IFT's. The understanding of the transition from countercurrent to cocurrent flow would be particularly useful for design of recovery processes for reservoirs containing vertical fractures. The implication of this work is that if cocurrent flow can be obtained in a vertically fractured reservoir, then a significant increase in recovery efficiency would be achieved at a potentially more rapid rate.

In this section we use a numerical simulator (ECLIPSE) to obtain insight into the results of Schechter *et al.* The results of the simulations reveal what physical mechanisms are dominant and how scaling of these imbibition experiments behaves. The results also demonstrate certain limitations of the numerical simulator for simulation of imbibition.

5.4.1 Simulation of Imbibition Experiments

Input Data. Appropriate rock and fluid data property must be used in simulations if the physics of the experiments are to be captured. Hamon and Vidal demonstrated that characterization of the heterogeneity on the core is needed for scaling to be done properly. In fact, a complete description of the varying relative permeabilities and capillary pressures along the core is necessary. This point was also emphasized by Bourbiaux and Kalaydjian [21], who found that countercurrent imbibition relative permeabilities were quite different than cocurrent imbibition relative permeabilities. According to the arguments of Bourbiaux and Kalaydjian, the type of flow regime must be understood before appropriate relative permeability functions can be specified. Unfortunately, these functions are not well known for the experiments of Schechter *et al.* [164]. The heterogeneity of the cores was not characterized, and only single values of the permeability were given. However, Berea is a fairly homogeneous sandstone, so the assumption of constant permeability throughout the Berea cores may be acceptable. Hence, the 500 md Berea core results were selected to be investigated. The experiments done at high IFT (38.1 mN/m) on the 500 md Berea core will subsequently be

referred to as the high IFT case, and the low IFT (0.1 mN/m) experiments will be referred to as the low IFT case.

Capillary Pressure. Because the imbibition experiments were done without initial water in the core, primary imbibition capillary pressure curves are needed. Unfortunately, they cannot be found in the literature for Berea. Capillary pressure curves were obtained by extrapolating secondary imbibition curves to zero water saturation. This process does not obtain the correct curve, but the emphasis of this work is not to find an exact match to the imbibition recovery curve. It is the understanding of the physical mechanisms behind imbibition as the IFT is varied that is of interest.

Fig. 5.22 shows the positive values of capillary pressure used for three different simulations. The high IFT and low IFT capillary pressure curves are shown, as well as the capillary pressure curve for a low IFT experiment run with 19% initial water saturation (IWS) in the core. This experiment will be introduced in the Discussion. A logarithmic scale is used to demonstrate how the low IFT curve is over two orders of magnitude smaller in value than the high IFT curve. The difference in capillary forces will become important later when the effects of gravity on the imbibition behavior are considered. The Berea core was assumed to be strongly water wet, so the negative portion of the capillary pressure curves was essentially a vertical line.

Relative Permeability. The relative permeabilities for the low IFT and high IFT experiments were determined by a history match of the experimental recovery curve. Fig. 5.23 gives three different sets of relative permeability curves which were used to match the high IFT case recovery curve. The oil relative permeability curve was kept the same throughout the different simulation runs. Note that the three water relative permeability curves have extremely low values even up to high water saturations. Those low values will be important for the scaling of these experiments. The values of the k_{rw} III curve defined in Fig. 5.23 were used to produce the oil saturation profiles in Fig. 5.26, which will be discussed later.

Fig. 5.24 shows two different sets of relative permeability curves used for the low IFT case. These values for relative permeability were over two orders of magnitude larger at lower water saturations than the values for the high IFT case. The values of the k_{rw} I and k_{ro} I curves in Fig. 5.24 were used in generating the oil saturation profiles in Fig. 5.30 to be discussed later.

Gridding Techniques. Sensitivity of computed results to the effects of gridding was investigated. Cylindrical coordinates were used to grid the core and annulus region. For the high IFT case, the core was separated into 59 vertical regions, with the top and bottom region representing the annulus above and below the core. The middle 57 regions were 1 cm in length covering the full length of the core. The core was divided up radially into 27 parts, logarithmically distributed over the core diameter (6.35 cm) such that the finest grid blocks were closest to the annulus. The annulus outside the core was represented by one radial block, so there were a total of 28 radial grid blocks for the high IFT simulations. This configuration was tested against simulations with 8 radial grid blocks and 57 radial grid blocks. The 28 radial grid block results were indistinguishable from the 57 radial grid block results, but were quite different than the 8 radial grid block simulation. It was then considered that 28 radial grid blocks were sufficient to grid the radial flow of the high IFT case accurately .

The low IFT case contained 122 vertical sections to capture more easily the significant vertical component of flow found in the low IFT experiments. Radially the core was set up into 15 sections in a similar manner as for the high IFT case.

High IFT Simulation Results. The simulations showed a very high sensitivity to relative permeability. Fig. 5.25 shows the results for the three different cases of water relative permeability. Note that none of the curves show a good match to the experimental data. The very low relative permeabilities of the k_{rw} II curve matched the very early recovery time, but the curves of k_{rw} I and k_{rw} III match the recovery better at later times. Attempts to achieve a better match were unsuccessful. There is evidence that simulation of primary imbibition is a very difficult task.

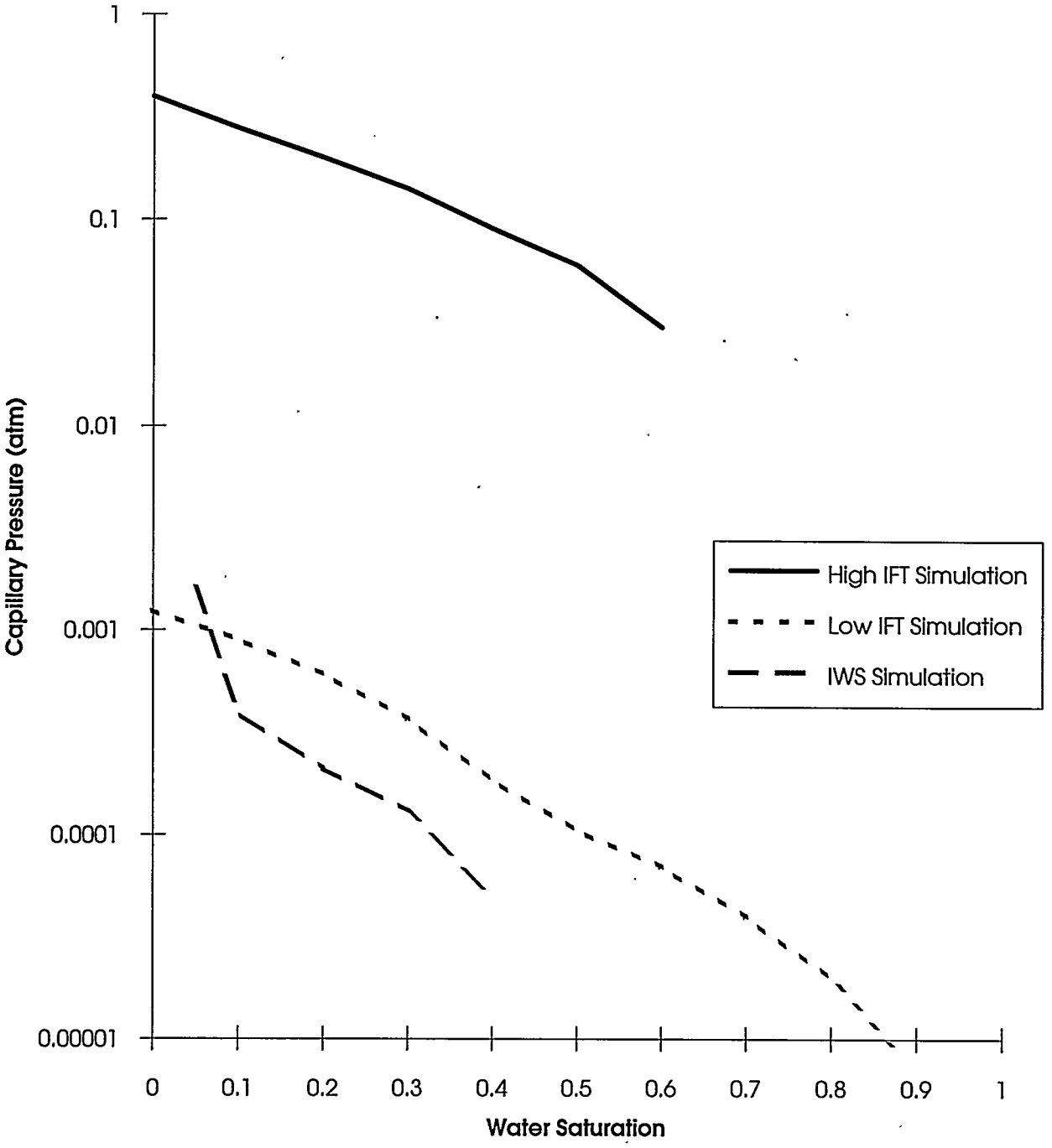

Figure 5.22: Capillary pressure curves for simulations of imbibition experiments.

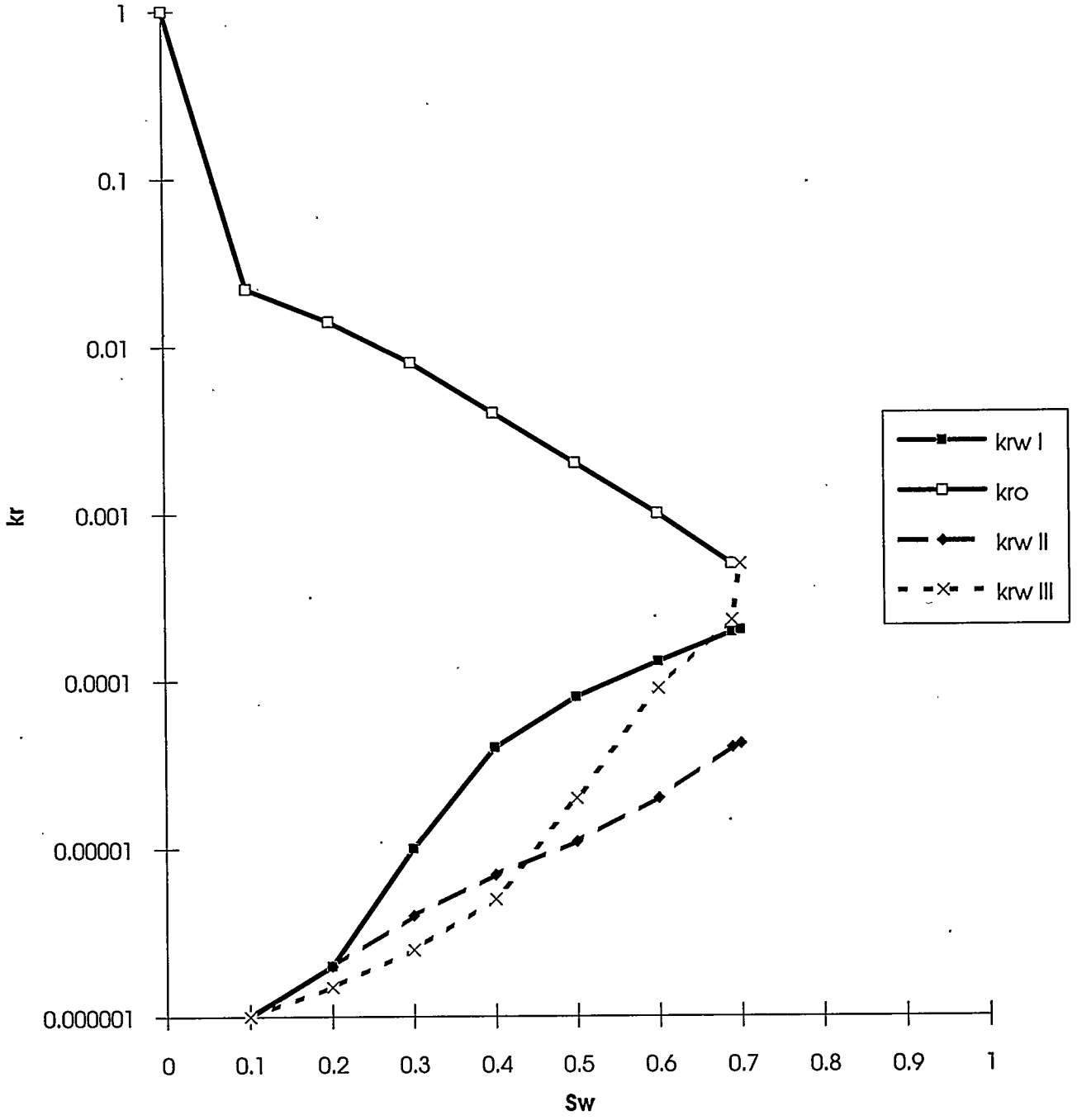

Figure 5.23: Relative permeability functions for high IFT imbibition.

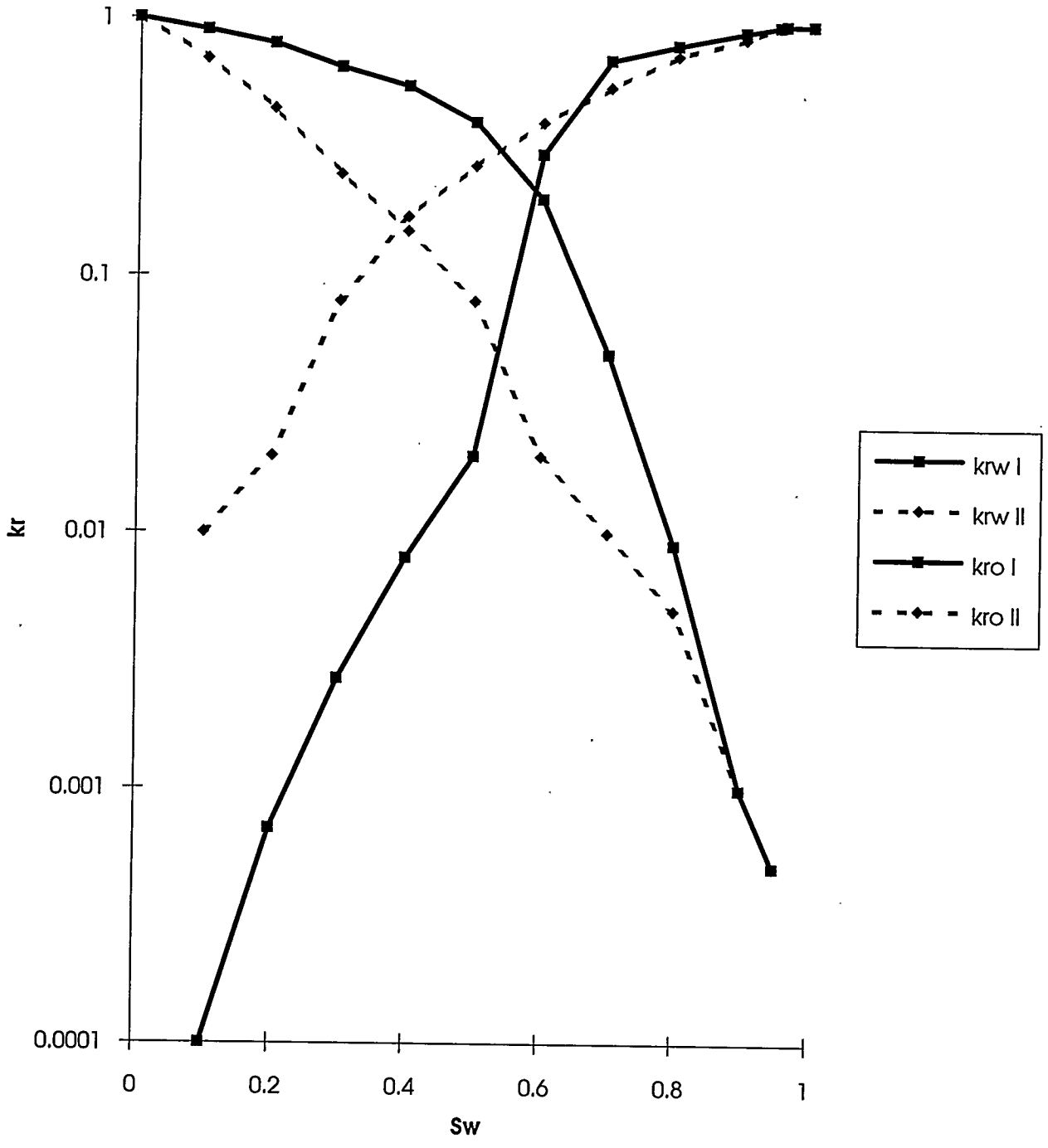

Figure 5.24: Relative permeability functions for low IFT imbibition

Kazemi and Merril [110] had to add a second capillary pressure curve to match the experimental results. The second curve was supposed to account for a "time delay" in the experimental recovery rate. They provided no physical justification for the addition of a second capillary pressure curve. Most important to note is that even for the very low relative permeabilities found in k_{rw} I and k_{rw} III, the simulations had orders of magnitude faster recovery at early times.

Because the k_{rw} III curve matched best the experimental recovery values, the average oil saturation profile along the core was plotted at selected intervals. These values simply averaged the oil saturation for each vertical layer of the core. Fig. 5.26 shows the results. Evidently, the oil saturation decreased in a uniform fashion, with the top and bottom part of the core showing equal additional reductions. The oil saturation decreased faster here than in the rest of the core due to the increased surface area in contact with the water-filled annulus. Note that at 0.1 hour (6 minutes) the average oil saturation was already down to 50% along the core, a very fast recovery rate. The lack of evidence for the segregation of oil and water in the core indicates that the flow was radial and countercurrent in nature.

Low IFT Simulation Results. Schechter *et al.* [165] proposed that in the scaling of the low IFT experiments, capillary effects can be neglected and the recovery is dominated by vertical gravity-driven flow. To examine this assertion, a simulation run was performed where the IFT was set to zero and straight line relative permeability curves were used. The recovery is then due only to the difference in gravity between the oil and water. Fig. 5.27 indicates that the experimental recovery rate was in fact influenced significantly by capillary forces, because the density difference was insufficient to maintain the recovery rate at the level of the experiment. Therefore, capillary pressure must be considered as an important driving force even for these low IFT experiments. The average oil saturation profile for the gravity-driven displacement (Fig. 5.28) shows a very distinct water front advancing from the bottom of the core upward, with original oil saturations ahead of the front. The top of the core shows some oil desaturation due to the top annulus imbibing into the core due to gravity. As expected, the oil saturation profile shows segregation between the oil and water, resulting in largely cocurrent flow.

When the low IFT capillary pressure curve (shown in Fig. 5.22) is incorporated into the simulation, the relative permeability curves in Fig. 5.24 result in the recovery curves in Fig. 5.29. Note that as for the high IFT case, the early time recovery behavior does not match well. Note also that the poor match was obtained even though the water relative permeabilities at low water saturations were quite low, especially for the k_{rw} I curve. In addition, the late time recovery behavior also does not match the experimental results. Attempts to match the experiment better were unsuccessful.

Despite the poor agreement, some important conclusions can be constructed from these simulation runs. Fig. 5.30 shows the average oil saturation profile at different times for the low IFT displacement. Comparison of Fig. 5.30 to Fig. 5.26 indicates that there is an important distinction between the low and high IFT displacements. The low IFT case profile shows aspects of both the high IFT case profile and the gravity-driven flow saturation profile of Fig. 5.28. An advancing water front is evident, as well as a fairly uniform decrease in the oil saturation away from the advancing water front, indicating radial flow. Thus it seems likely that both radial and vertical flow contributed to recovery in the low IFT displacements.

5.4.2 Discussion

In the experiments in Schechter *et al.* [164] imbibition is driven by a combination of capillary and gravity forces. The capillary-to-gravity-force ratio, given by the inverse bond number N_B^{-1}, describes the type of flow that is exhibited in these experiments. Here, N_B^{-1} is given by,

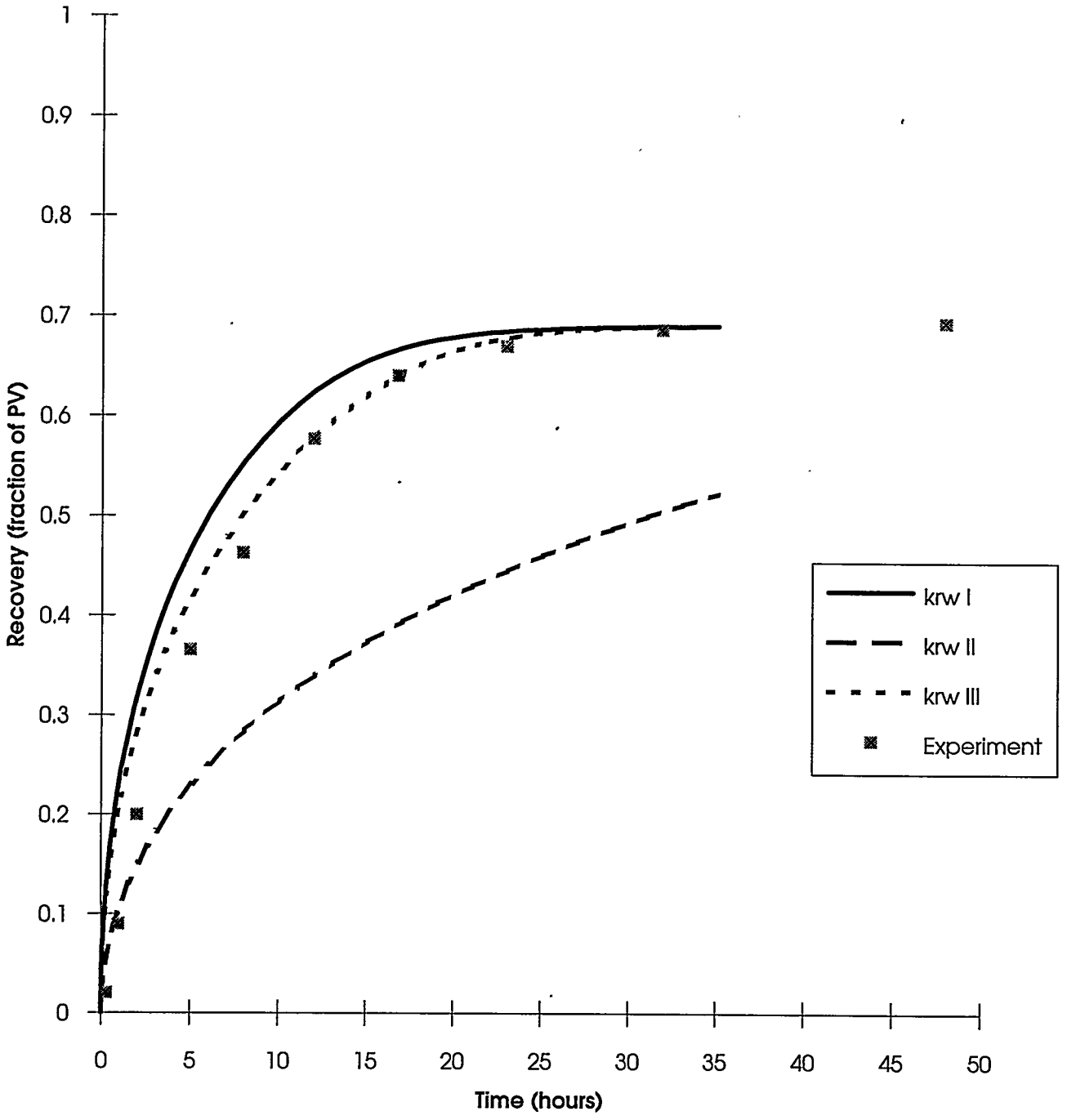

Figure 5.25: Comparison of simulation and experiment for recovery of oil by imbibition at high IFT.

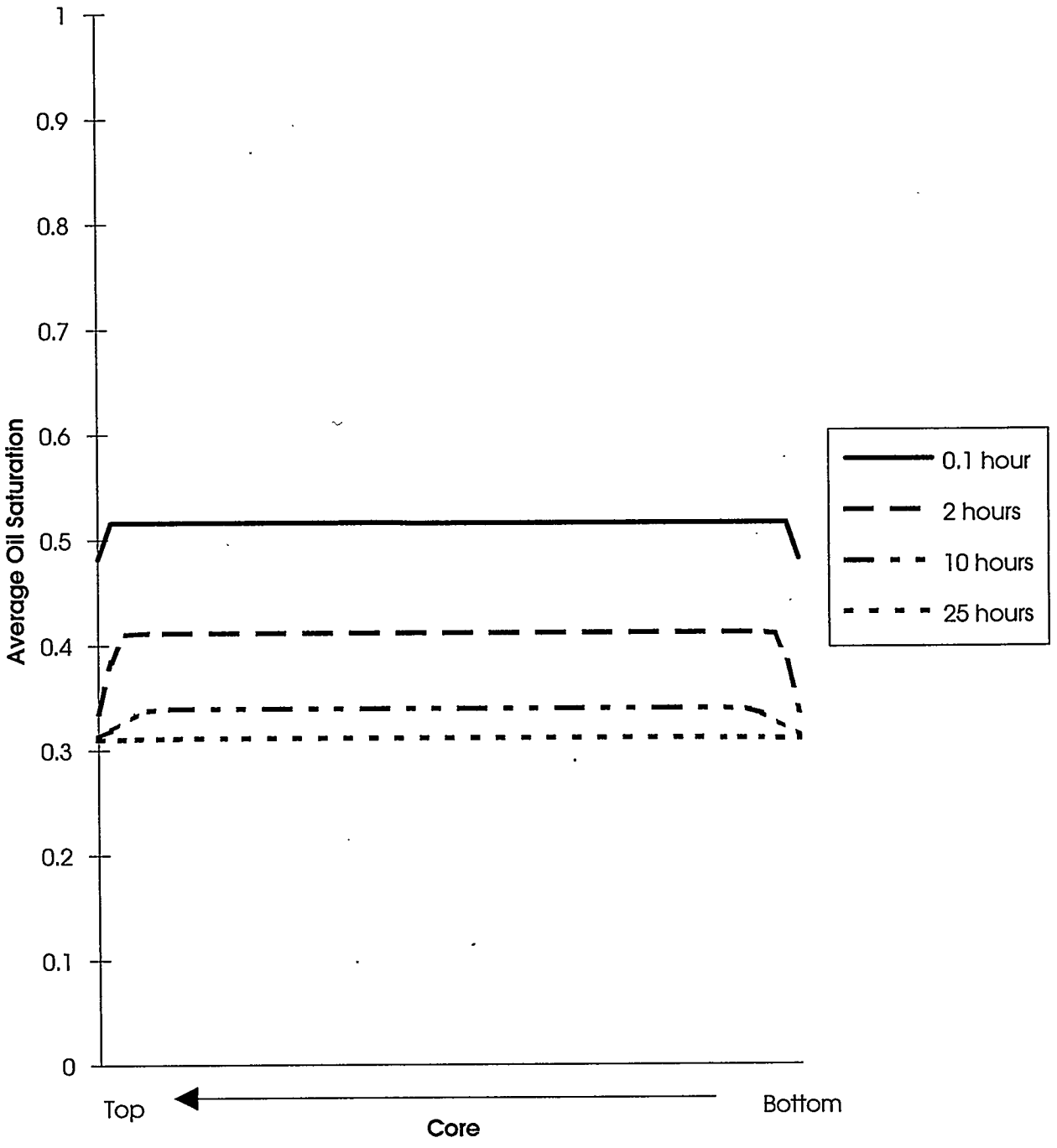

Figure 5.26: Oil saturation profiles during imbibition at high IFT.